

Optical Injection Locking on Vertical-Cavity Surface-Emitting Lasers (VCSELs): Physics and Applications

Xiaoxue Zhao



Electrical Engineering and Computer Sciences
University of California at Berkeley

Technical Report No. UCB/EECS-2008-96

<http://www.eecs.berkeley.edu/Pubs/TechRpts/2008/EECS-2008-96.html>

August 15, 2008

Copyright 2008, by the author(s).
All rights reserved.

Permission to make digital or hard copies of all or part of this work for personal or classroom use is granted without fee provided that copies are not made or distributed for profit or commercial advantage and that copies bear this notice and the full citation on the first page. To copy otherwise, to republish, to post on servers or to redistribute to lists, requires prior specific permission.

**Optical Injection Locking on Vertical-Cavity Surface-Emitting Lasers (VCSELs):
Physics and Applications**

by

Xiaoxue Zhao

B.S. (Peking University) 2003

A dissertation submitted in partial satisfaction of the

requirements for the degree of

Doctor of Philosophy

in

Engineering – Electrical Engineering and Computer Sciences

in the

Graduate Division

of the

UNIVERSITY *of* CALIFORNIA, BERKELEY

Committee in charge:

Professor Constance J. Chang-Hasnain, Chair

Professor Ming C. Wu

Professor Peter Y. Yu

Fall 2008

The dissertation of Xiaoxue Zhao is approved:

Professor Constance J. Chang-Hasnain, Chair

Date

Professor Ming C. Wu

Date

Professor Peter Y. Yu

Date

University of California, Berkeley

Fall 2008

Optical Injection Locking on Vertical-Cavity Surface-Emitting Lasers (VCSELs):
Physics and Applications

© 2008

by Xiaoxue Zhao

ABSTRACT

Optical Injection Locking on Vertical-Cavity Surface-Emitting Lasers (VCSELs): Physics and Applications

by

Xiaoxue Zhao

Doctor of Philosophy in Engineering – Electrical Engineering and Computer Sciences

University of California, Berkeley

Professor Constance J. Chang-Hasnain, Chair

The revolutionary achievements on both digital and analog fiber-optic communications have shown their powerful functions and significant influences on our everyday life – from the Internet to cable TV. Semiconductor optoelectronic devices, as major enabling components in the physical layer of the optical communication network, are being explored extensively for various high-speed applications.

Direct modulated semiconductor lasers, particularly vertical-cavity surface-emitting lasers (VCSELs), with their great advantages on cost and size, are attractive for optical data transmission along both analog and digital links. However, these devices have limited modulation performance that prevents them from being widely employed as data transmitters in various communication systems. Other than novel device design and engineering, an alternative technique to help improve the laser modulation properties is optical injection locking, which refers to a state when the frequency and phase of one

laser oscillator, known as the slave laser, are locked through the direct coupling to the light injection from another laser oscillator, known as the master laser.

In this dissertation, optical injection locking induced laser dynamics in a VCSEL is investigated in detail both theoretically and experimentally. A hybrid model based on a Fabry-Perot amplifier structure for the VCSEL and the well-formulated injection-locking laser rate equations is established, which can be used to intuitively explain the physics of various experimental phenomena. Systematic experimental study on the modulation characteristics of injection-locked VCSELs is conducted, showing significant performance improvement, such as record resonance frequency > 100 GHz and 3-dB bandwidth of 66 GHz for small-signal modulation, and 10 times chirp reduction and > 10 times transmission distance enhancement for large-signal modulation. A number of intriguing applications are discussed, including a microwave optoelectronic oscillator (OEO), pre-chirp technique for digital data transmission and wavelength-division-multiplexed (WDM) passive optical networks (PONs), all of which appear exceptionally good performance. Finally, future work and projections of the technology are briefly mentioned to encourage further study and development on this research topic.

Professor Constance J. Chang-Hasnain
Dissertation Committee Chair

TABLE OF CONTENTS

TABLE OF CONTENTS.....	i
LIST OF FIGURES.....	iii
LIST OF TABLES.....	ix
ACKNOWLEDGEMENT	x
Chapter 1 Introduction to Optical Injection Locking	1
1.1 Brief History of Injection Locking.....	1
1.2 Optical Injection Locking on Semiconductor Lasers.....	2
1.3 Advantages of Vertical-Cavity Surface-Emitting Lasers (VCSELs).....	3
Chapter 2 Basic Principles of Optical Injection Locking	7
2.1 Optical-Injection-Locking Rate Equations	8
2.1.1 Analytical Solutions to OIL Rate Equations.....	10
2.1.2 Numerical Simulation of OIL Rate Equations	17
2.2 Physics of Optical-Injection-Locking Dynamics	18
2.3 Fabry-Perot Amplifier Model	21
Chapter 3 Small-Signal Modulation Characteristics	25
3.1 Resonance Frequency Enhancement	26
3.1.1 Experimental Demonstration	26
3.1.2 Physical Explanation of Resonance Enhancement Using the Fabry-Perot Amplifier Model	31
3.2 Intrinsic Modulation Bandwidth Enhancement	37
3.3 Cascaded Optical Injection Locking for Broadband Modulation	40
3.3.1 Slave-Modulated Cascaded Optical Injection Locking	41
3.3.2 Master-Modulated Cascaded Optical Injection Locking.....	47
3.3.3 Scaling Using a Daisy Chain Structure	49
Chapter 4 Large-Signal Modulation Characteristics	51
4.1 Chirp Reduction	53
4.1.1 Frequency Chirping of Semiconductor Lasers	53
4.1.2 Chirp Reduction by OIL.....	55
4.2 Data Pattern Inversion and Negative Chirp.....	58
4.2.1 Pre-Chirp Using Data Pattern Inversion	59
4.2.2 OIL-Induced Data Pattern Inversion.....	60
4.2.3 Negative Chirp	66
4.2.4 Transmission Distance Enhancement	70
Chapter 5 Analog Applications of Injection-Locked VCSELs.....	74
5.1 Microwave Performance for Analog Fiber-Optic Link	74
5.1.1 RF Gain	76
5.1.2 Nonlinearity and Dynamic Range	81
5.1.3 Relative Intensity Noise	86
5.1.4 Summary of Microwave Performance	88
5.2 Optoelectronic Oscillator (OEO)	90
5.2.1 Open-Loop Characterization.....	92
5.2.2 Close-Loop Characterization.....	97

5.3 Slow Light.....	101
5.3.1 Master-Modulated Injection-Locked VCSELs	102
Chapter 6 Digital Applications of Injection-Locked VCSELs.....	111
6.1 Wavelength-Division-Multiplexed Passive Optical Network (WDM-PON)	112
6.1.1 Injection-Locked VCSELs as Upstream Transmitters.....	114
6.1.2 Rayleigh Backscattering and Extinction Ratio Study	122
6.1.3 Fault Monitoring and Localization Scheme	127
Chapter 7 Optical Injection Locking of Multimode VCSELs	139
7.1 Experimental Results of Small-Signal Frequency Response.....	141
7.1.1 Resonance Frequency and Bandwidth Enhancement	141
7.1.2 Spatial Detuning.....	145
7.2 Experimental Results of Large-Signal Modulation, Chirp Reduction and Transmission Characteristics	147
7.2.1 Large-Signal Modulation	148
7.2.2 Chirp Reduction and Negative Chirp	151
7.2.3 Transmission Distance Enhancement	153
7.3 Numerical Simulations of Injection-Locking Dynamics of a Two-Mode VCSEL	155
7.4 Outlook	161
Chapter 8 Conclusion and Future Work	163
Appendix 1 MATLAB Code.....	167
A1.1 Single-Mode OIL Stability Plot – Frequency Domain Method.....	167
A1.2 Single-Mode OIL Stability Plot – Time Domain Method	168
A1.3 Fabry-Perot Amplifier Model for Frequency Response	171
A1.4 Parasitic De-embedding from Measured Frequency Response	173
A1.5 Amplifier Model for Data Pattern Inversion.....	180
A1.6 Spectrogram Plotting	183
A1.7 LI Curve of a Two-Mode VCSEL	184
A1.8 Two-Mode OIL Stability Plot With Spatial Detuning.....	185
BIBLIOGRAPHY	189

LIST OF FIGURES

Figure 1.1 Christaan Huygens and his record of discovering the synchronization of two pendulum clocks in 1665 [5].	2
Figure 1.2 Schematic showing a standard VCSEL structure.	4
Figure 2.1 Typical experimental setups for (a) edge-emitting laser as a slave laser (b) surface-emitting laser as a slave laser.	7
Figure 2.2 Locking stability plot (a) calculated from Eqn (2.8) and (b) measured from experiment.	13
Figure 2.3 Locking stability plot calculated from Eqn (2.8) (solid blue line) and from frequency domain method (red dots). See Appendix A1.1 for MATLAB code.	14
Figure 2.4 Experimentally measured optical spectra of injection locking at a fixed ultra-high injection ratio but various detuning values over the locking range.	15
Figure 2.5 Phasor diagram showing the dynamics of injection locking.	16
Figure 2.6 Simulated locking stability plot using time domain method by solving Eqn (2.9a-c). See Appendix A1.2 for MATLAB code.	18
Figure 2.7 (a) Optical spectra of an OIL VCSEL at various detuning values. (b) Zoom-in of the amplified spontaneous emission (ASE) of the VCSEL cavity at various detuning values.	19
Figure 2.8 Schematic of the gain/loss spectrum and the optical spectrum as well as a flow chart to illustrate the OIL dynamic process and its detuning dependence.	21
Figure 2.9 Experimental setup and measurement results of the reflection spectra of a VCSEL amplifier at various bias (gain) levels.	22
Figure 2.10 Experimental setup and measurement results of the reflection spectra of an OIL VCSEL at various detuning (gain) values.	23
Figure 3.1 Experimental Setup. (VNA: vector network analyzer, PD: photo-detector, OSA: optical spectrum analyzer)	28
Figure 3.2 (a) Frequency response and (b) optical spectra of an OIL VCSEL at various detuning values. A record resonance frequency of 107 GHz is shown. The master laser wavelength is tuned. The frequency spacing between the master mode and the cavity mode in the optical domain is equal to the resonance frequency in the electric domain.	29
Figure 3.3 Frequency response and (b) optical spectra of an OIL VCSEL at various injection ratios. The resonance frequency increases with injection ratio.	30
Figure 3.4 Schematic optical spectrum of a modulated OIL laser. The modulation frequency ω_m is being scanned when frequency response measurement is performed.	32
Figure 3.5 A simple F-P amplifier model used to simulate the OIL VCSEL. E_i is the incident light field, E_r is the reflected light field, L is the cavity length, r_1 and r_2 are the mirror field reflectivity, γ and α_i are the gain and the distributed loss of the active medium.	32
Figure 3.6 Flow chart of the simulation process of a hybrid model using both steady-state solutions to OIL rate equations and the Fabry-Perot amplifier structure.	34
Figure 3.7 Simulated optical spectra and frequency response of an OIL VCSEL at three detuning conditions. (FR: free-running, SL: slave laser, ML: master laser) See Appendix A1.3 for MATLAB code.	35

Figure 3.8 Measured optical spectra and frequency response of an OIL VCSEL at three detuning conditions. The frequency response is raw data without removing detector responsivity, and VCSEL parasitics (estimated cutoff at 10 GHz).	36
Figure 3.9 Measured optical spectrum and frequency response showing a double-resonance phenomenon. The two resonance peaks are due the two polarization modes of the VCSEL under strong injection locking.	37
Figure 3.10 Flow chart of the de-embedding procedures to obtain OIL laser intrinsic response. See Appendix A1.4 for MATLAB code.	40
Figure 3.11 A schematic explaining the idea of cascaded optical injection locking (COIL).	42
Figure 3.12 Experimental setup. Orange lines are optical paths, while blue lines are electrical paths. (ML: master laser, PC: polarization controller, OSA: optical spectrum analyzer, VNA: vector network analyzer, PD: photodetector.)	43
Figure 3.13 Frequency response of COIL. The first modulated VCSEL is red-detuned to provide a flat response while the second VCSEL is locked at a longer wavelength to extend the bandwidth. 3-dB bandwidth of 66 GHz is obtained.	45
Figure 3.14 Frequency response of COIL. (a) The first modulated VCSEL is blue-detuned. Cascading effect is clearly shown by the two resonance peaks. (b) The first modulated VCSEL is red-detuned. A flat response with 3-dB bandwidth of 50 GHz is achieved.	46
Figure 3.15 Experimental setup of master-modulated COIL. MZM: Mach-Zehnder modulator.	48
Figure 3.16 Frequency response of master-modulated COIL where signal is from external modulation of the master light. Bandwidth of ~ 47 GHz is achieved using two OIL-VCSELS.	49
Figure 3.17 Schematic of a multiple COIL transmitter with optical spectra and frequency response shown after each cascaded stage. The modulation signal can be applied to the master laser or directly to the first slave laser only or to all the slave lasers simultaneously for an integrated device. (ML: master laser, SL: slave laser).	50
Figure 4.1 Input pulse with positive chirp will be broadened monotonically as it propagates along 1550-nm standard single-mode fiber (SSMF), because high frequency (blue) components travel faster than low frequency (red) components. Transmission distance is severely limited by pulse broadening.	52
Figure 4.2 Frequency chirping of semiconductor lasers. Positive chirp exhibits for all types of semiconductor lasers due to the existence of linewidth enhancement factor.	54
Figure 4.3 Signal amplitude (black) and chirp (blue) waveforms at 10 Gb/s for (a) free-running VCSEL and (b) injection-locked VCSEL. Chirp data plotted on the same scale for both figures on the right. OIL removes adiabatic chirp and reduces transient chirp by 10X.	57
Figure 4.4 Optical spectra of both free-running and injection-locked VCSEL under 10 Gb/s large-signal modulation.	58
Figure 4.5 Concept of pre-chirping using negative-chirped pulse that can compensate fiber dispersion till the optimal distance is reached, where the pulse is mostly compressed. Transmission distance can be greatly enhanced by employing pre-chirp technique.	59
Figure 4.6 Negative chirp can be obtained by inverting intensity modulation signal pattern without changing carrier modulation.	59
Figure 4.7 VCSEL amplifier reflection spectra at various bias levels. If all spectra are considered at a fixed wavelength (dashed line), an electric-to-optical transfer function (reflection output vs. bias current) can be obtained.	61
Figure 4.8 Electric-to-optical transfer function extracted from Figure 4.7. Inversion occurs in the loss regime.	61

Figure 4.9 Experimentally measured square wave showing detuning-controlled inversion phenomenon of an OIL VCSEL. Free-running VCSEL waveform is also shown as a reference. Transition from non-inversion to Inversion occurs at detuning of 0.2 nm.....	63
Figure 4.10 Simulated modulation output of an OIL VCSEL at various wavelength detuning values using the hybrid model combining OIL rate equations and a Fabry-Perot amplifier structure as shown in Chapter 3. Modulation on VCSEL gain is also shown on the left to illustrate the gain/loss regime that the VCSEL amplifier is in as detuning varies. See Appendix A1.5 for MATLAB code.	64
Figure 4.11 Inversion occurs at horizontal displacement of the coupling lensed-fiber that changes the gain/loss regime of the VCSEL. The VCSEL is directly modulated at 2.5 Gb/s and the detuning is adjusted to the blue side to have minimum carrier reduction. (a) Experimental setup. (b) Measured waveforms for both free-running and injection-locked conditions with lensed-fiber at different locations (i), (ii) and (iii).....	65
Figure 4.12 Time-resolved chirp waveforms and the intensity waveforms for a free-running (top) and injection-locked (bottom) VCSEL. The detuning is adjusted so that pattern inversion occurs. Negative chirp obtained in OIL case and peak-to-peak chirp is reduced by 10X.....	66
Figure 4.13 Spectrogram of two consecutive bits from a pseudorandom bit sequence (PRBS) at 10 Gb/s output from a VCSEL. Color map represents signal intensity. (a) Free-running VCSEL. Large positive frequency chirp is indicated by the leftward skew of the bits. (b) Injection-locked VCSEL. Detuning is adjusted so that data inversion occurs. Total peak-to-peak chirp is greatly reduced. A slight right skew indicates negative chirp. See Appendix A1.6 for MATLAB code.	67
Figure 4.14 Experimental measurement of time-resolved chirp and intensity waveforms at 10 Gb/s for (a) free-running VCSEL, (b-d) OIL VCSEL with injection ratios of (b) 6.21 dB (c) 8.58 dB (d) 11.12 dB. Transient peak-to-peak is reduced from (a) 30 GHz to (b) 3.1 GHz (c) 2.7 GHz (d) 1.55 GHz as injection ratio increases.	68
Figure 4.15 Peak-to-peak chirp and extinction ratio at 10-Gb/s as functions of injection ratio. Injection ratio needs to be optimized due to the trade-off between the two.	69
Figure 4.16 Experimental setup for testing transmission performance. (Tx: transmitter, VOA: variable attenuator, BPF: band-pass filter, Rx: receiver.).....	70
Figure 4.17 Bit-error-rate measurements and error-free eye diagrams of an OIL VCSEL after back-to-back, 25-km and 100-km SSMF transmission.	72
Figure 4.18 Power penalty versus SSMF transmission distance for a free-running VCSEL, a commercial DFB DML and an OIL VCSEL. More than 10X transmission distance is obtained on the OIL VCSEL with negative chirp.....	72
Figure 5.1 De-embedded frequency response of an OIL VCSEL at various detuning values. RF gain up to 20 dB is obtained when the master laser is red-detuned.	77
Figure 5.2 RF gain measured at 1 GHz for four different VCSELs vs. wavelength detuning. 20-dB RF gain is found for large detuning cases. (FR: free running, decibel values are injection ratios).	78
Figure 5.3 Maximum RF gain enhancement vs. injection ratio for an OIL VCSEL.	78
Figure 5.4 Contour plot of RF gain enhancement as a function of both wavelength detuning and injection ratio.	79
Figure 5.5 (a) Optical spectrum of an OIL VCSEL under a single-tone modulation at 10 GHz. Sidebands and the cavity mode ASE can be observed. (b) A series of spectra at different detuning values of an OIL VCSEL under a single-tone modulation at 10 GHz.	80
Figure 5.6 Schematic defining IMD3-limited spur-free dynamic range (SFDR).	82

Figure 5.7 Two-tone spur-free dynamic range (SFDR) improvement at 1-GHz modulation by OIL. Inner lines are for a free-running VCSEL.....	83
Figure 5.8 Measured frequency response of the fundamental tone and two-tone IMD3 distortion at different injection ratios.	84
Figure 5.9 Experimental and simulated spur-free dynamic range (SFDR) enhancement vs. injection ratio at half of the resonance frequency.	85
Figure 5.10 Numerical simulation of frequency response of both the fundamental tone and the two-tone IMD3 distortion at different injection ratios.	86
Figure 5.11 Experimental demonstration of relative intensity noise (RIN) reduction of an OIL VCSEL at various injection-locking conditions compared with free-running VCSEL.....	88
Figure 5.12 Schematic of (a) standard optoelectronic oscillator (OEO) and (b) OEO using optically injection-locked semiconductor lasers. Closed-loop optical spectrum of optically injection-locked OEO exhibits a significant enhancement of the longer-wavelength modulation sideband due to the cavity resonance amplification in the injection-locked lasers.....	92
Figure 5.13 Experimental setup (OSA: optical spectrum analyzer, PD: photodetector, RFSA: RF spectrum analyzer). Solid lines: optical path, dashed lines: electrical path. Switch controls open-loop and closed-loop characterization.....	94
Figure 5.14 Small-signal frequency response of an OIL VCSEL. (a) Detuning dependence. (b) Injection ratio dependence.	94
Figure 5.15 Optical spectra of an OIL VCSEL at different detuning values labeled by cavity mode suppression ratio (CMSR). (a) CMSR of 8 dB. (b) CMSR of 20 dB. (c) CMSR of 35 dB.....	95
Figure 5.16 CMSR versus wavelength detuning. The laser should be operated at the onset of the locking range.....	96
Figure 5.17 RF gain of the open-loop link at various CMSR values. The slave laser is modulated by a single tone corresponding to the spacing between the OIL mode and the cavity mode.	97
Figure 5.18 Pictures of the actual experimental setup. Foam board and plexiglass are used to provide temperature and vibration isolation.....	98
Figure 5.19 Optical spectra of open-loop and close-loop operation. The open-loop spectrum shows a locking condition with 35-dB CMSR, and a mode spacing of 20 GHz between the master and the slave cavity mode to match the RF filter center frequency. Cavity mode is enhanced dramatically when oscillation is achieved.....	100
Figure 5.20 Measured phase noise performance of an OIL-OEO generated signal and an HP 83650B generated signal with center frequency at 20 GHz by Agilent 5052A. Phase noise of the 20-GHz signal produced by an OIL VCSEL OEO is 38 dB lower at 5-kHz offset.....	100
Figure 5.21 Experimental Setup. (PM: Polarization Maintaining, EDFA: Erbium-Doped Fiber Amplifier, OSA: Optical Spectrum Analyzer).....	102
Figure 5.22 Amplitude frequency response of a modulated-master OIL VCSEL under a fixed injection power at various detuning values. (a) Raw data. (b) Calibrated data reference to the free-running frequency response.....	103
Figure 5.23 Phase change response of a modulated-master OIL VCSEL under a fixed injection power at various detuning values. For a bandwidth of ~ 2 GHz centered at f_c , the slope $d\phi/d\omega$, equivalent to the delay time τ for each detuning, changes from -0.2 ns to 0.2 ns, representing slow and fast light regimes.....	105
Figure 5.24 Amplitude and phase change response of a modulated-master OIL VCSEL at a fixed detuning but at three different injection power levels. RF gain and phase change is possible for even higher frequencies with higher injection power levels.....	106

Figure 5.25 (a) Phase change response at two different detuning values with single-tone modulation frequencies indicated. (b) Time-domain traces at two detuning conditions showing both slow and fast light at three single-tone modulating frequencies.	109
Figure 6.1 Proposed scheme of WDM-PON using directly modulated OIL-VCSELs as upstream transmitters. Each slave VCSEL is injection-locked by modulated downstream signal transmitted from a master DFB laser located at the CO.	115
Figure 6.2 Experimental setup of single channel demonstration.	116
Figure 6.3 Stability plot for a CW VCSEL injection-locked by a master DFB laser modulated at 1.25 Gb/s.	118
Figure 6.4 Superimposed optical spectra of an externally modulated master DFB laser at 2.5-Gb/s and a directly modulated VCSEL at 2.5-Gb/s when it is both free-running and injection-locked by the modulated DFB.	119
Figure 6.5 Upstream BER of a VCSEL in free-running mode and injection-locked by a CW, 1.25- and 2.5-Gb/s modulated master laser with -23 and -20-dBm absolute injection power levels.	120
Figure 6.6 Single-channel experimental setup to study upstream performance dependence on Rayleigh backscattering and downstream optical extinction ratio in bidirectional WDM-PON using a 1.55- μ m OIL VCSEL as upstream transmitter.	123
Figure 6.7 Upstream BER curves for different values of (a) SRR at a constant downstream ER of 4.5 dB and (b) downstream ER at a constant SRR of 13.4 dB.	124
Figure 6.8 Characteristics of received optical power at error-free versus downstream extinction ratio in both unidirectional and bidirectional network configurations.	125
Figure 6.9 Small-signal frequency response of OIL VCSEL while the master laser is externally modulated at various detuning values, namely at -0.012, 0.018, 0.036 nm.	126
Figure 6.10 Novel fault monitoring and localization scheme in a WDM-PON with OIL VCSELs and lock-in-amplifiers.	131
Figure 6.11 Experimental setup. Inset is the reflection spectrum of a tunable laser beam from the VCSEL top mirror when the VCSEL is off.	132
Figure 6.12 Optical spectra measured at locations A (Fig. 3(a)) and B (Fig. 3(b)-(f)) of the experimental setup in Figure 6.11: (a) broadband light + downstream channel (b) no failure (c) transmitter failure (d) feeder fiber failure at 20 km (e) distribution fiber failure at 2.2 km after AWG2 (f) monitoring channel in detail.	134
Figure 6.13 DC signal of monitoring channel measured at lock-in amplifier as a function of optical power received at the low bandwidth receiver. The inset shows DC measurements over a wider range of received optical power from -67 dB to -35 dB in this case, highlighting the ability to detect signals over a large dynamic range.	136
Figure 6.14 BER of upstream signals, repeated for experiments in back-to-back (B2B) and 22.25 km transmission configurations, with and without implementing the monitoring scheme. The eye diagrams measured at BER = 10^{-9} for the 22.25 km transmission case are shown as insets.	137
Figure 7.1 Frequency response and optical spectra of a free-running and the corresponding OIL multimode VCSEL with aperture size of 10 μ m at various injection ratio and detuning conditions. (a) Small-signal frequency response. Resonance frequency increases from 3 GHz up to 54 GHz and 3-dB bandwidth of 38 GHz is obtained. Response can be tailored by adjusting the locking parameters. The system parasitic is included such as the electric probe (40 GHz), photo-detector (50 GHz) and the bias-Tee (50 GHz). (b) Optical spectra. Master laser locks on the fundamental mode. The higher-order (1st) transverse modes are suppressed under external light injection.	142

Figure 7.2 Frequency response and optical spectra of a free-running and the corresponding OIL multimode VCSEL with aperture size of 15 μm at various injection ratio and detuning conditions. (a) Small-signal frequency response. Smaller enhancement observed results from the reduced injection ratio caused by larger coupling loss. (b) Optical spectra. Master laser locks on the fundamental mode. The higher-order transverse modes are suppressed under external light injection.	144
Figure 7.3 (a) Frequency response and (b) optical spectra of another free-running and the corresponding OIL multimode VCSEL with aperture size of 15 μm at various injection ratio and detuning similar as shown in Figure 7.2.	144
Figure 7.4 (a) Optical spectrum of a multimode VCSEL with 15- μm aperture size. The spatial profile of each transverse mode is labeled. (b) Schematic showing spatial mode selection by moving coupling lensed-fiber.	146
Figure 7.5 shows (a) frequency response and (b) optical spectra of the same 15- μm VCSEL used for the measurement shown in Figure 7.3 but with locking occurs on the 1 st order mode. Double resonance is observed in the frequency response due to two polarization modes belonging to the 1 st order mode.	147
Figure 7.6 Optical spectra showing highly multimode device becomes a single-mode device after injection locking. 10-Gb/s PRBS modulation is applied directly to the VCSEL.	149
Figure 7.7 Eye-diagrams taken at the same oscilloscope settings and receiver power when the multimode VCSEL is modulated with 10-Gb/s 2^{15} -1 PRBS. (a) Free-running condition. The nearly closed eye indicates inter-symbol interference caused by beating noise between different modes. (b) Injection-locked with 3-dBm injection power. The single-mode emission results in much cleaner eye-opening.	149
Figure 7.8 Back-to-back BER showing performance improvements as a function of injection power levels.	151
Figure 7.9 Chirp reduction by OIL on a 15- μm aperture multimode VCSEL without data pattern inversion. (a) Free-running with 10-GHz peak-to-peak positive chirp and non-zero adiabatic chirp. (b) OIL at 3-dBm injection power with 5-GHz peak-to-peak positive chirp and zero adiabatic chirp. (c) OIL at 4-dBm injection power with 4-GHz peak-to-peak positive chirp and zero adiabatic chirp. (d) OIL at 6-dBm injection power with 3-GHz peak-to-peak positive chirp and zero adiabatic chirp.	152
Figure 7.10 Reduced negative chirp by OIL on a 10- μm aperture multimode VCSEL. (a) OIL at 3-dBm injection power with 4-GHz negative chirp. (b) OIL at 6-dBm injection power with 2-GHz negative chirp.	153
Figure 7.11 Transmission characteristics comparison between free-running and injection-locked multimode VCSELs with different values of peak-to-peak positive as well as negative chirp.	155
Figure 7.12 Simulated LI curves of a two-mode VCSEL using the parameters listed in Table 7.1. See Appendix A1.7 for MATLAB code.	157
Figure 7.13 Schematic showing frequency relations between master laser and the two modes for calculating frequency detuning values.	159
Figure 7.14 OIL stability plots of a two-mode VCSEL at different spatial detuning conditions. (a) $\kappa_1 = 0.7 \times 10^{12} \text{ s}^{-1}$ and $\kappa_2 = 0.3 \times 10^{12} \text{ s}^{-1}$ (b) $\kappa_1 = 0.3 \times 10^{12} \text{ s}^{-1}$ and $\kappa_2 = 0.7 \times 10^{12} \text{ s}^{-1}$. Different colors represent different locking conditions: black – unstable, red – stable locking on mode 1, blue – stable locking on mode 2, and green – stable but no locking. See Appendix A1.8 for MATLAB code.	160

LIST OF TABLES

Table 3.1 Parameters for simulations using the amplifier model.....	34
Table 5.1 Microwave performance of OIL VCSELs for analog transmission.....	90
Table 5.2 Amplitude and phase change frequency response of different modulated-master OIL VCSELs.....	107
Table 5.3 Amplitude and phase change frequency response at various detuning values using VCSEL 4 as master and VCSEL 5 as slave at three different power levels.....	108
Table 7.1 Parameter values for free-running VCSEL simulation.....	157

ACKNOWLEDGEMENT

Pursuing a Ph.D. degree at UC Berkeley EECS over the past five years has been the most memorable and significant experience of my life. I am deeply indebted to many people who have guided, helped and supported me along this arduous but incredibly far-reaching journey.

My foremost gratitude and appreciation must go to my Ph.D. advisor Prof. Connie Chang-Hasnain, for being a constant source of inspiration and encouragement. What I learnt from her was much more than the math, the physics and the techniques of doing research, but the qualities that makes one a great researcher – the passion, the optimism, the dedication, and the respect for your work. Without her teaching, guidance and mentorship, I would not have reached this far.

I am grateful to former group members Lukas Chrostowski and Chih-Hao Chang, for their patience in training me lab skills and leading me into this research topic. I am also thankful to current members Michael Moewe, Mervin Ye Zhou, Bala Pesala and Devang Parekh, with whom I worked and shared, not only the joy and satisfaction of our accomplishments, but also the stress and frustration of failure. I like to thank all the group members, not only for the many stimulating discussions and their invaluable assistance in the labs, but more importantly, for the fellowship we have established.

I am very grateful to have collaborated intimately with Prof. Ming C. Wu's group at Berkeley, working closely with Dr. Erwin K. Lau, and Dr. Hyuk-Kee Sung on the high-speed and the OEO projects. My special thanks and appreciation go to Prof. Markus C. Amann and Werner Hofmann at Technical University of Munich for providing us with the best experiment devices over the years. I am pleased to have had the chance to work

with two visitors from the University of Melbourne – Prof. Rod S. Tucker on the injection-locking theory, and Dr Elaine Wong on the WDM-PON project; both were amazing intellectual experiences. I am also grateful to having had the opportunities to work with Prof. Alan E. Willner’s group at University of Southern California: Bo Zhang, Louis Christen and Yang Yue were invaluable in making all the chirp and transmission measurements possible. I also like to express my gratitude and respect to Prof. Koyama at Tokyo Institute of Technology, for fruitful collaborations and his insightful questions.

I benefited enormously from frequent interactions with Prof. Ivan Kaminow, Dr. Tingye Li, Dr. T. P. Lee, and Dr. Hao-Lin Chen, who were always generous in sharing their knowledge, wisdom and experiences on their lifelong academic career.

I thank Prof. Peter Y. Yu and Prof. T. K. Gustafson for finding time serving on my qualifying exam committee and reading my dissertation. Their thought-provoking questions and comments were the impetus to my research progress.

For his companionship and encouragement till the journey’s end, I thank David Sun.

Lastly, to my parents, I am forever indebted to their unyielding love, patience and support; I couldn’t have done it without them.

Chapter 1

Introduction to Optical Injection Locking

1.1 BRIEF HISTORY OF INJECTION LOCKING

Optical injection locking of semiconductor lasers has been studied for more than two decades and demonstrated as an efficient and robust technique to improve the spectral and dynamic performance of a directly modulated diode laser. The concept “injection locking” refers to a state when the frequency and phase of an oscillator, often known as the slave oscillator, are locked via direct coupling or injection by another oscillator, known as the master oscillator. This concept applies to all kinds of oscillators – from mechanical oscillators to electronic oscillators and to optical oscillators, as one will see in the brief history stated below.

The concept of injection locking was first observed and described by Huygens in 1665 [1]. He recorded the phenomenon that two pendulum clocks (mechanical oscillators) hanging on the same wall could synchronize to each other even when they started with different frequencies and phases (Figure 1.1). Van der Pol [2] used this phenomenon to create forced oscillator circuit (electronic oscillators) in 1927. Adler [3] further developed the technique in electronics and communications in 1945. In 1960s, after the invention of lasers (optical oscillators), Stover and Steier [4] studied injection locking on He-Ne lasers in 1966, which is considered the first demonstration of optical

injection locking (OIL). Up to this point, no matter which type of oscillator is under investigation, the primary interest was locking or synchronization of oscillator frequency and phase. With the development of semiconductor diode lasers in the 80s, which stimulated the revolutionary change in telecommunication technology, optical injection locking as well entered a new era – additional properties of the laser were found to be strongly dependent on external light injection, particularly the dynamic modulation characteristics, which are critical for communication applications.

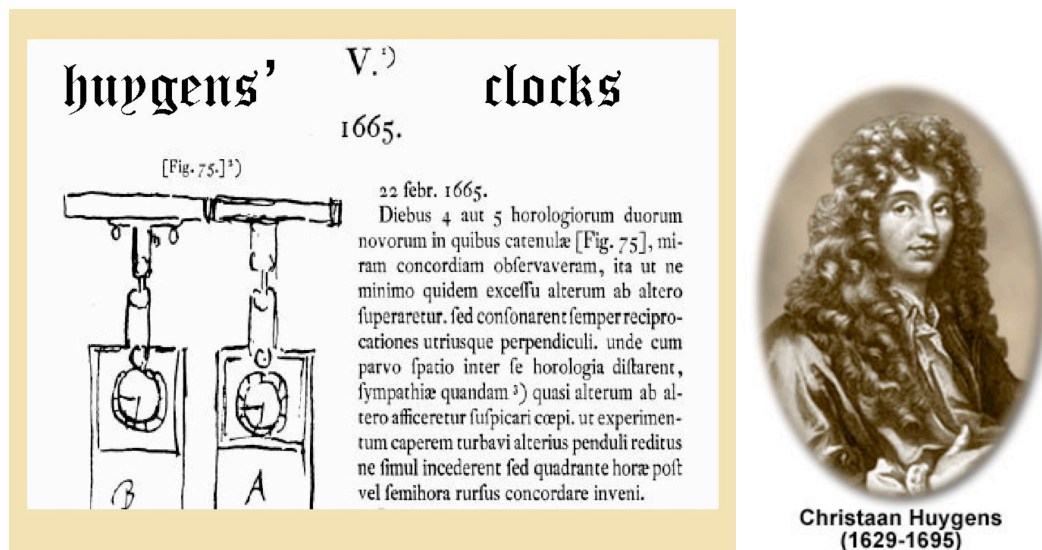


Figure 1.1 Christaan Huygens and his record of discovering the synchronization of two pendulum clocks in 1665 [5].

1.2 OPTICAL INJECTION LOCKING ON SEMICONDUCTOR LASERS

In the late 1970s, the emerging of semiconductor lasers started the revolution of lightwave telecommunication. Numerous investigations were carried out to push the performance, especially the modulation performance, of diode lasers, which would serve as data transmitters in a communication link. Kobayashi and Kimura [6] reported the first

demonstration of OIL in 1980 on an AlGaAs semiconductor laser, which showed frequency stabilization. Iwashita and Nakagawa [7] subsequently demonstrated side mode suppression of a Fabry-Perot laser diode by injection locking, turning a multimode laser to a single-mode laser with much reduced mode partition noise. Lang [8] published the first theory paper on injection locking of semiconductor lasers in 1982, which established the theoretical framework, and later became the foundation of various subsequent theoretical predictions and studies. Over the past two decades, significant progress was made on numerical simulations and experimental demonstrations of chirp reduction [9, 10, 11], modulation bandwidth enhancement [12-15], and broadband noise reduction [12, 16, 17].

1.3 ADVANTAGES OF VERTICAL-CAVITY SURFACE-EMITTING LASERS (VCSELS)

Optical injection locking was initially studied on Fabry-Perot lasers in the early 1980s as a technique to attain single-longitudinal-mode lasers [6] for improved transmission performance in single-mode fibers (SMFs). As laser technology advances, single-mode lasers, namely distributed feedback (DFB) lasers, became commercially available. Then OIL was revisited as a technique to improve various dynamic performances of these lasers rather than simply frequency selection and stabilization.

The vertical-cavity surface-emitting laser (VCSEL) was invented by Iga in 1977 [18], and soon was proven to have a number of unique advantageous features over other types of semiconductor lasers. For VCSELS, the electric field (light) is traveling and bouncing in the vertical direction inside the laser cavity and emitting typically from the top surface of the device as opposed to its edge-emitting counterpart where light moving in the lateral direction and emitting from both facets on the sides. Figure 1.2 shows a

standard VCSEL structure. The active gain region composed of a few layers of quantum wells are sandwiched between stacks of distributed Bragg reflectors (DBRs) serving as high-reflectivity mirrors. Since the cavity length of VCSELs is in the order of $1\ \mu\text{m}$, the large free spectral range (FSR) results in only one cavity mode in the gain spectrum, producing excellent single-longitudinal-mode behavior. Single-transverse-mode emission can be obtained at the same time by controlling the size of the laser aperture. The laser beam emitting from the symmetric aperture is in a narrow circular shape with only a small amount of divergence, which is ideal for direct fiber coupling. In addition, the surface-normal geometry enables very cost-effective fabrication and wafer-scale testing processes. Besides many well-known sensing and display applications, the economic manufacturing together with the high-speed device design also made the VCSEL a competitive candidate over copper and coax cables in various communication applications, such as metropolitan area networks (MANs), local area networks (LANs) passive optical networks (PONs), and radio over fiber (RoF) and so on.

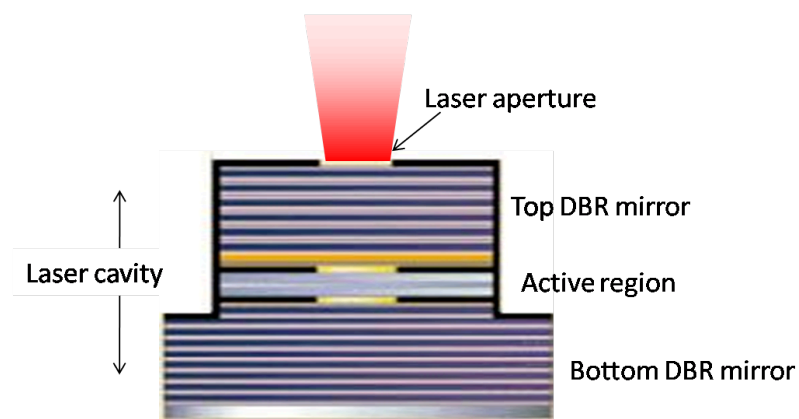


Figure 1.2 Schematic showing a standard VCSEL structure.

However, the thick DBR mirrors as well as the oxide layer around the active region for current and light confinement create large device parasitic impedance, which severely limits the speed of VCSELs under direct current modulation (< 20 GHz). Therefore, it is expected that the modulation properties of VCSELs can be much improved to fit in applications deploying devices with high-speed performance. Much effort has been put into device design and engineering to increase the direct modulation speed of VCSELs. Devices with modulation speed of 35 Gb/s are demonstrated at 980 nm [19] and 30 Gb/s at 850 nm [20]. Wavelength at 1550 nm is much preferred for long-haul transmission due to the low loss window of optical fiber as well as the maturity of the technology of other link components. However, the nonlinear gain effect and the carrier transport lifetime of the material system at 1550 nm are the main hurdles that prevent the modulation speed of long-wavelength VCSELs being engineered even higher. As an alternative, optical injection locking has been demonstrated as an effective technique to drastically improve the dynamic performance of semiconductor lasers, particularly on the resonance frequency and modulation bandwidth. Therefore, it is expected that by applying OIL, the overall modulation characteristics of long-wavelength VCSELs can also be greatly enhanced.

This dissertation studies the physical origin, modulation characteristics and various applications of injection-locked VCSELs both theoretically and experimentally with particular emphasis on high-speed performance for communications. Recent advances of VCSELs under ultrahigh injection locking conditions are discussed with highlights on one order of magnitude increase in resonance frequency, one order of magnitude reduction in chirp, ~ 20 dB increase in both spur-free dynamic range (SFDR) and RF link

gain, ~ 20 dB reduction in laser noise. A record high modulation bandwidth of 66 GHz is also attained by injection locking a 10 GHz VCSEL. These properties can eventually lead to a quantum leap on transmission distance or bandwidth. New applications of injection locking for optoelectronic oscillators and wavelength-division-multiplexed passive optical network (WDM-PON) systems are proposed and demonstrated. Finally, as multimode (transverse mode) VCSELs become more and more appealing for short-reach fiber-optic links, injection locking on multimode VCSELs is investigated, which shows great potential on commercialization of the technique.

Chapter 2

Basic Principles of Optical Injection Locking

Optical injection locking (OIL) refers to a technique of injecting light from one laser (master) to another laser (slave) to result in an apparent locking condition of coherent oscillation of the two lasers. Usually, the master laser is kept under continuous-wave (CW) operation. As the roles of the two lasers are clearly defined, an isolation component is usually in the configuration to achieve unidirectional locking. Figure 2.1 shows the typical OIL experimental setup for either an edge-emitting laser or a surface-emitting laser as a slave laser. An optical isolator or circulator will be used accordingly.

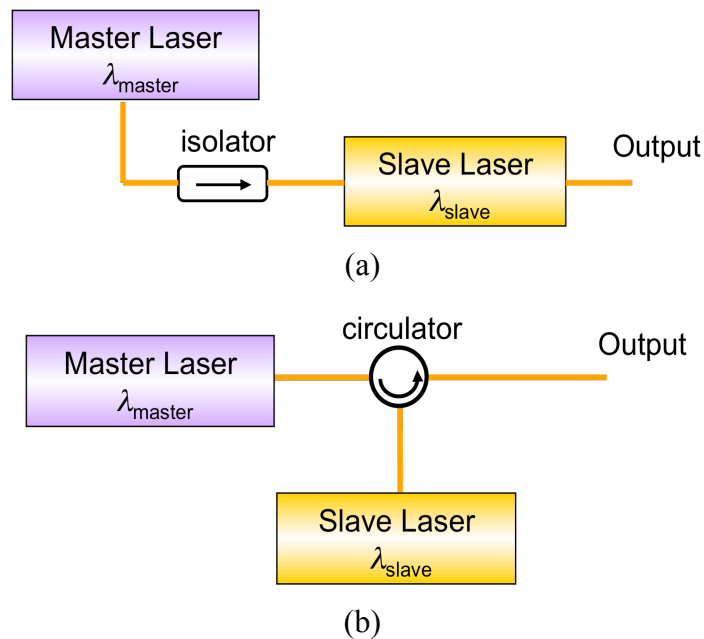


Figure 2.1 Typical experimental setups for (a) edge-emitting laser as a slave laser (b) surface-emitting laser as a slave laser.

2.1 OPTICAL-INJECTION-LOCKING RATE EQUATIONS

The dynamics of injection-locked slave laser can be described by injection-locking rate equations. It was established by modifying the laser master equation within the framework of the semiconductor laser theory developed by Lamb [21] in 1964.

For free-running lasers, based on the laser master equation, the laser field equation can be written as

$$\frac{dE(t)}{dt} = \frac{1}{2}(G - \gamma)E(t) + j\omega E(t) \quad (2.1)$$

$E(t)$ is the laser field, G is the gain from the active material inside the laser cavity, γ is the loss including both material loss and mirror loss, which is equal to the inverse of the photon lifetime $1/\tau_p$, and ω is the cavity resonance frequency. The laser field can be written in a complex form. The amplitude equation together with the carrier conservation equation for electrically injected diode lasers forms the well-known laser rate equations.

If $E(t) = |E(t)|e^{j\phi(t)}$, then

$$\begin{aligned} \frac{d|E(t)|}{dt} &= \frac{1}{2}(G - \gamma)|E(t)| \\ \frac{dN(t)}{dt} &= \frac{I}{q} - \frac{N(t)}{\tau_N} - G|E(t)|^2 \end{aligned} \quad (2.2 \quad \text{a,}$$

b)

where N is the total carrier number in the active region, I is the injected current, q is the electron charge, and τ_N is the carrier lifetime. Note that spontaneous emission term is not included here, which can become important if transient is considered, especially when the laser is being switched on and off.

The first thorough theoretical study on OIL of semiconductor lasers was done by Roy Lang [8] in 1982. By adding in the external light injection term, the master equation changes to

$$\frac{dE_s(t)}{dt} = \frac{1}{2} \left[G(N) - \frac{1}{\tau_p} \right] E_s(t) + j\omega(N)E_s(t) + \kappa E_{inj}(t) \quad (2.3)$$

where $E_s(t) = E(t)e^{j[\omega_{FR} + \phi_s(t)]}$ and $E_{inj}(t) = E(t)e^{j[\omega_{inj} + \phi_{inj}(t)]}$ are the complex fields of the slave and the master laser.

In addition, as the external field enhances the stimulated emission inside the slave laser cavity, which will reduce the carrier number N , the index of refraction, hence the cavity resonance will be red shifted. This is represented by ω as a function of N in Eqn (2.3). It will be seen in the next chapter that this cavity resonance shift plays a very important role in the resonance frequency enhancement of an injection-locked laser under direct modulation.

Plugging the complex form of both the injection field and the slave laser field into the modified master equation and separating the real and imaginary parts using the master laser phase as the reference, a set of three equations can be derived and they are the well-known rate equations for an injection-locked laser [22].

$$\begin{aligned} \frac{dE(t)}{dt} &= \frac{1}{2} G_0 [N(t) - N_{th}] E(t) + \kappa E_{inj} \cos \phi(t) \\ \frac{d\phi(t)}{dt} &= \frac{\alpha}{2} G_0 [N(t) - N_{th}] - \Delta\omega - \kappa \frac{E_{inj}}{E(t)} \sin \phi(t) \\ \frac{dN(t)}{dt} &= \frac{I}{q} - \frac{N(t)}{\tau_N} - \left\{ \frac{1}{\tau_p} + G_0 [N(t) - N_{th}] \right\} E^2(t) \end{aligned} \quad (2.4 \text{ a-})$$

c)

where $E(t)$ is the normalized the filed and $E^2(t) = S$ the total number of photons, N_{th} is the threshold carrier number, $\Delta\omega = \omega_{inj} - \omega_{FR}$ is the frequency difference between the master and the slave laser, often refer to as the frequency detuning, $\phi(t) = \phi_s(t) - \Delta\omega t - \phi_{inj}(t)$ is the relative phase between the master and the slave laser field, α is the linewidth enhancement factor of the slave laser, $\kappa = (v_g/2L)(1-R)^{1/2}$ is the coupling coefficient of the master light into the slave laser depending on the group velocity v_g , the slave laser cavity length L and its mirror reflectivity R , and finally G_0 is the gain coefficient and can be expressed as $G_0 = \Gamma v_g g_n / V_a$ with Γ as the confinement factor describing the overlap between the laser electric field and the active region, v_g as the group velocity of the field inside the cavity, g_n the differential gain and V_a the volume of the active region.

This is a set of simplified rate equations as spontaneous emission, nonlinear gain effects and the noise terms are neglected. However, it can be solved analytically with some physical insights uncovered, which will help understand the dynamics of injection locking as shown in the next subsection. If numerical simulation is to be performed on these equations, all these terms can be included to achieve more accurate solutions as will be shown in the following subsection. Also note that the phase equation, which did not show up in the free-running case, is equally important now as compared to the field and the carrier equations in Eqn set (2.4), indicating that OIL is a coherent process.

2.1.1 Analytical Solutions to OIL Rate Equations

The steady state solution (with subscript $_0$ to the symbol) can be obtained by setting the time derivatives of the three rate equations to zeros. In the amplitude equation, by setting the derivative of (2.4a) to zero, carrier number change can be related to the steady state phase difference as

$$\Delta N = -\frac{2\kappa}{G_0} \frac{E_{\text{inj}}}{E_0} \cos \phi_0 \quad (2.5)$$

Physically, the carrier density is decreased due to the enhanced stimulated emission caused by the external light injection. Therefore, the condition that $\Delta N < 0$ confines the phase term to be $0 < \cos \phi_0 < 1$. In the phase equation, by setting the derivative of the phase to zero and utilizing the equation for (ΔN) , an expression of frequency detuning is derived and given by

$$\Delta \omega = -\frac{E_{\text{inj}}}{E_0} (\alpha \cos \phi_0 + \sin \phi_0) \quad (2.6)$$

The boundaries of injection locking are given by the maximum and minimum of the frequency detuning. By applying the constraints of the trigonometric functions on the above equation, it is straightforward to get

$$(\alpha \cos \phi_0 + \sin \phi_0)_{\text{max}} = \sqrt{1 + \alpha^2} \quad \text{and} \quad (\alpha \cos \phi_0 + \sin \phi_0)_{\text{min}} = -1$$

Therefore, the range within which the slave laser can be locked by the master laser is

$$-\kappa \frac{E_{\text{inj}}}{E_0} \sqrt{1 + \alpha^2} \leq \Delta \omega \leq \kappa \frac{E_{\text{inj}}}{E_0}, \quad (2.7)$$

and the corresponding phase value is $-\pi/2 < \phi_0 < 0$.

However, the experimental detuning values are often presented in wavelength, and the power ratio between the master laser and the slave laser is often referred to as the injection ratio. The ratio of the injection field to the slave laser field can be expressed as the square root of the power ratio of the two quantities. Therefore, the locking range can be rewritten in terms of wavelength as

$$-\frac{\kappa\lambda^2}{2\pi c} \sqrt{\frac{P_{\text{inj}}}{P_0}} \leq \Delta\lambda \leq \frac{\kappa\lambda^2}{2\pi c} \sqrt{\frac{P_{\text{inj}}}{P_0}} \sqrt{1 + \alpha^2} \quad (2.8)$$

where $\Delta\lambda = \lambda_{\text{master}} - \lambda_{\text{slave}}$, c is the speed of light, and P_{inj} / P_0 is the injection ratio. It is interesting to note that the locking range is asymmetric due to the linewidth enhancement factor α . The physical origin of this asymmetry can be explained qualitatively as follows. The external light injection reduces the carrier number, which will in turn reduce the gain of the slave laser. Because the linewidth enhancement factor couples the gain and the phase of the laser field, the gain variation results in a red-shift (shift to longer wavelength) of the slave-cavity wavelength through α . Therefore, the slave laser tends to be locked to a wavelength longer than its lasing wavelength.

A two-dimensional stability plot can be generated with wavelength / frequency detuning as the vertical axis and injection ratio as the horizontal axis, which is usually used to determine the locking condition, including injection regime and locking range. Figure 2.2 shows such a plot both analytically and experimentally by plotting Eqn (2.8) and measuring the injection ratio and locking range, respectively. Locking regimes can be empirically separated into weak, moderate, strong and ultrahigh injection with injection ratio in a range that is below -20 dB, between -20 and -10 dB, greater than, -10 dB, and greater than 0 dB, respectively. The stronger the injection ratio is, the larger the locking range is. This shows the increase of the robustness of the technique with increase of the injection ratio. In addition, as will be shown in the following chapters, the dramatic dynamic performance improvement of the slave laser occurs in the strong or ultrahigh-injection regimes. Hence, these are the regimes where the experiments were performed unless elsewhere stated.

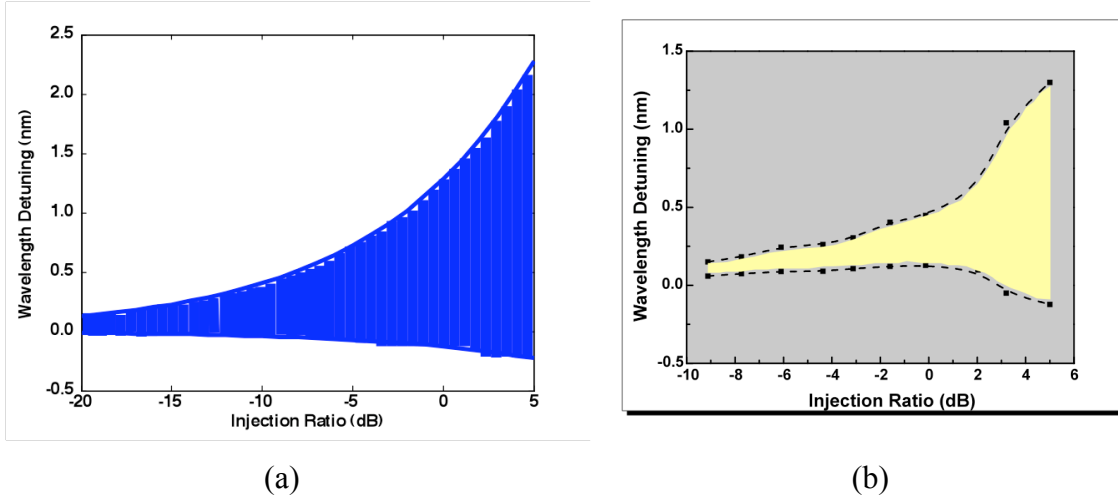


Figure 2.2 Locking stability plot (a) calculated from Eqn (2.8) and (b) measured from experiment.

However, a more rigorous control theory points out that the stability of a system that is initially in the steady state is determined by the response of the system to a small single-frequency perturbation. The system is defined as unstable if the perturbation gets amplified, while the system is stable if the perturbation dies out quickly. Mathematically, this can be examined by linearizing the rate equations (2.4) using small sinusoidal signal as the perturbation. The eigenvalues of the linearized equations provides the stability condition. The imaginary part of the eigenvalues represents the resonance frequency, while the real part represents the associated damping. Therefore, a stable condition is obtained if the damping term is negative. It is also equivalent to say that the stable locking condition is obtained if all the eigenvalues are located on the left half of the complex plane. Detailed derivation on the small-signal linearization of the rate equations can be found in [22, 23]. A locking stability plot generated by this frequency domain method together with the locking range defined by Eqn (2.8) is shown in Figure 2.3. The asymmetry is caused by a large value of $\alpha = 5$ used, which is usually the case for

VCSELs. There is a thin region on the blue detuning side (bottom in Figure 2.3) within the locking range defined by Eqn (2.8) but is not stable according to the control theory stated above. In this region, various nonlinear phenomena could take place, such as four-wave mixing, pulsation, and chaos. These effects have been studied by a number of groups [24-27]. However, to achieve performance improvement, which is the main focus here, usually the injection-locked laser is operated in the stable locking region.

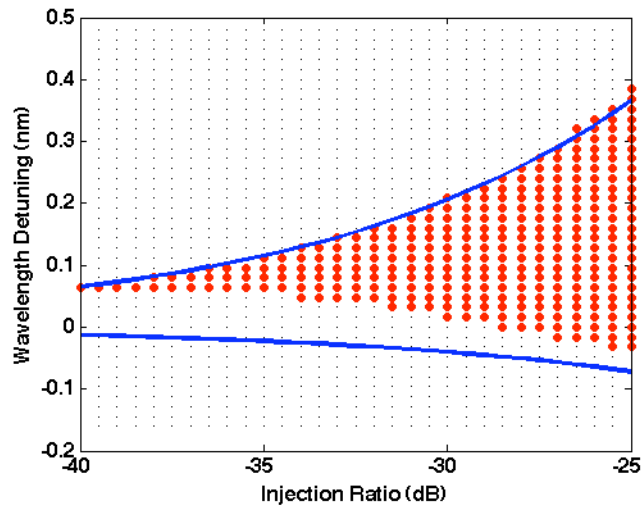


Figure 2.3 Locking stability plot calculated from Eqn (2.8) (solid blue line) and from frequency domain method (red dots). See Appendix A1.1 for MATLAB code.

Experimentally, the locking condition is measured and monitored by an optical spectrum analyzer (OSA). A stream of locking spectra is shown in Figure 2.4 at a particular injection ratio but with various detuning values. It is interesting to see that in the ultra-high-injection regime, even though the slave laser is injection-locked by the master laser and is lasing at the master wavelength; the slave laser mode does not completely disappear. The slave laser cavity-resonance mode can still be seen using a

high-resolution OSA. A rule of thumb to judge the locking range in such a case is that the slave-cavity mode is at least 30 dB below the master mode.

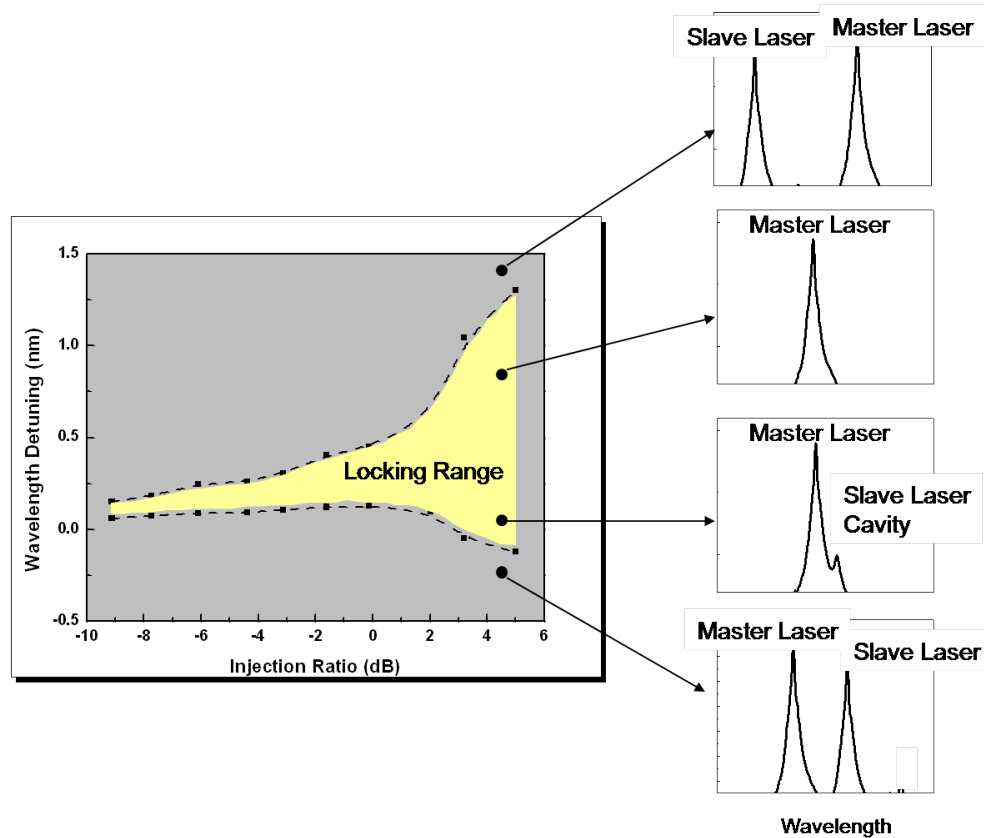


Figure 2.4 Experimentally measured optical spectra of injection locking at a fixed ultra-high injection ratio but various detuning values over the locking range.

An illustrative model to understand the injection-locking dynamics is the phasor model developed by Henry et al. [28] in 1985. This model gives an intuitive description of the coherence interaction between the photons of the two lasers. It also explains the fact that the slave laser will lase at the master laser frequency under injection locking even though the master laser frequency is detuned from the actual cavity resonance frequency of the slave laser. A phasor diagram of a statically injection-locked laser field

is shown in Figure 2.5. The free-running slave laser field is labeled by E_0 . When the slave laser is injection-locked by a master laser field, the locked slave field vector rotates by $\Delta\omega\Delta t$ during each time interval Δt due to the frequency difference between the master and the slave laser, $\Delta\omega$, shown by the black arrow in Figure 2.5. In addition, the external light field contributes to the field as shown by the dashed vector in Figure 2.5 (the coordinate is chosen such that the real part of the electrical field is aligned with the external field merely for calculation simplicity). However, due to the injected external stimulated emission, the slave laser gain is reduced, thus its field amplitude. This introduces the dotted vector shown in the phasor diagram. Therefore, the slave laser field phasor returns to its original position, indicating a steady-state injection-locking condition. It should be noted that the phasor diagram is consistent with the first two OIL rate equations, (2.4a) for amplitude and (2.4b) for phase shown previously. It is also worth mentioning that due to the linewidth enhancement factor and the gain reduction, the slave laser cavity mode will be red shifted under OIL. This will be discussed in detail in the following section.

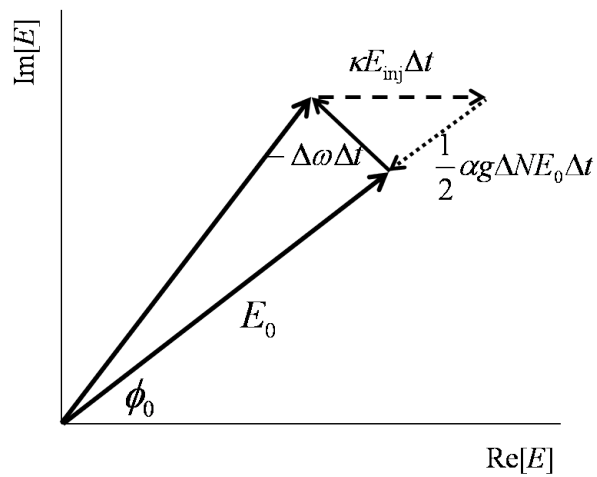


Figure 2.5 Phasor diagram showing the dynamics of injection locking.

2.1.2 Numerical Simulation of OIL Rate Equations

Instead of seeking for analytical solutions, numerical simulation can be performed on the injection-locking rate equations. In this case, a comprehensive model including nonlinear gain effects [29], such as carrier heating and spectral hole burning, and spontaneous emission can be used to describe the locking process. The rate equations used for numerical simulation are as follows

$$\begin{aligned}
 \frac{dS}{dt} &= \left[\Gamma v_g \frac{g_n(N - N_{tr})}{V_a(1 + \varepsilon S)} - \frac{1}{\tau_p} \right] S + \frac{\beta B}{V_a} N^2 + 2\kappa \sqrt{S_{inj}} S \cos(\phi - \phi_{inj}(t)) \\
 \frac{d\phi}{dt} &= \frac{\alpha}{2} \left[\Gamma v_g \frac{g_n(N - N_{tr})}{V_a(1 + \varepsilon S)} - \frac{1}{\tau_p} \right] - 2\pi\Delta f - \kappa \sqrt{\frac{S_{inj}}{S}} \sin(\phi - \phi_{inj}(t)) \\
 \frac{dN}{dt} &= \frac{I_{bias}}{q} - \frac{N}{\tau_N} - \frac{\Gamma v_g g_n(N - N_{tr})}{V_a(1 + \varepsilon S)} S
 \end{aligned} \tag{2.9 a-c}$$

where $S = S(t)$ is the total photon number, ε is the gain compression factor, β is the spontaneous emission rate and B is the recombination coefficient.

Stable locking condition can be tested by solving the set of differential equations numerically and examining the convergence of the results after a reasonably long time period. A stability plot generated by the numerical method is shown in Figure 2.6.

The numerical method is a powerful tool that can simulate various modulation properties of an injection-locked laser. For example, noise performance can be simulated by adding the Langevin noise terms [30], small-signal frequency response [31] and the nonlinearity [32] can be simulated by adding the modulation signal to the current term in Eqn (2.9 c).

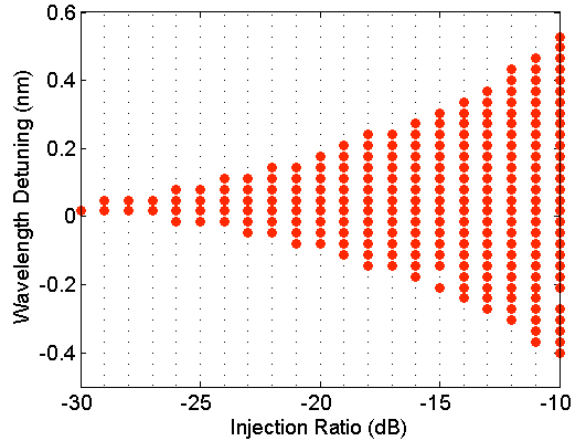


Figure 2.6 Simulated locking stability plot using time domain method by solving Eqn (2.9a-c). See Appendix A1.2 for MATLAB code.

2.2 PHYSICS OF OPTICAL-INJECTION-LOCKING DYNAMICS

Although the rate equations describe injection locking in a fairly accurate and comprehensive way, they still do not sufficiently provide an intuitive picture to understand the dynamics of the locking process. In this section, we combine the analytical solutions to the rate equations with some experimental observations to try to paint a picture showing the physics of OIL dynamics.

Figure 2.7(a) shows the optical spectra of an OIL VCSEL at various detuning values. On the longer wavelength side, a small peak is observed corresponding to the amplified spontaneous emission (ASE) spectrum of the substantially red-shifted VCSEL cavity mode due to the carrier reduction by external optical injection. These features change as $\Delta\lambda$ increases, as shown in a zoom-in picture on the cavity ASE peak in Figure 2.7(b). As $\Delta\lambda$ increases (master wavelength gets to the red side), the cavity resonance peak is more suppressed and closer to the injection-locked lasing mode.

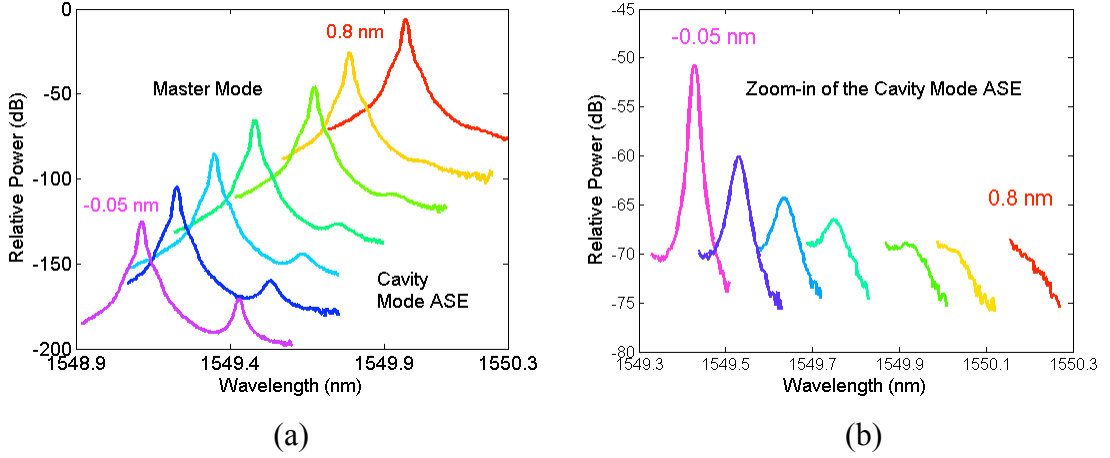


Figure 2.7 (a) Optical spectra of an OIL VCSEL at various detuning values. (b) Zoom-in of the amplified spontaneous emission (ASE) of the VCSEL cavity at various detuning values.

All these experimental observations result from the dynamic coupling between photons and carriers as well as their number change under external light injection. It can be described by the OIL rate equations. From the steady-state solutions to Eqn set (2.4) the steady-state phase as well as the carrier number change (Eqn (2.5), shown again here) is deduced as shown below.

$$\Delta N = -\frac{2\kappa}{G_0} \frac{E_{inj}}{E_0} \cos \phi_0 \quad (2.5)$$

$$\phi_0 = \sin^{-1} \left(\frac{2\pi c}{\lambda_0^2} \frac{\Delta \lambda}{\kappa \sqrt{1 + \alpha^2}} \frac{E_0}{E_{inj}} \right) - \tan^{-1} \alpha \quad (2.10)$$

A simple inspection on the above equation shows that the carrier number of the slave laser under external light injection is reduced. The underlying physics is that the stimulated emission introduced by the external field depletes the carriers of the slave laser. Therefore, the gain of the injection-locked slave laser is lower than its threshold value, which makes the locked slave laser act essentially like a gain-clamped optical

amplifier. Furthermore, the gain level of the OIL laser amplifier can be tuned by the wavelength detuning, $\Delta\lambda$, because the amount of carrier reduction increases with $\Delta\lambda$. However, the stimulated emission from the master laser compensates the gain reduction in the slave laser, and overall the injection-locked slave laser is lasing at the master wavelength. Through the linewidth enhancement factor α , this gain reduction changes the refractive index of the slave laser, thus the cavity resonance frequency. The cavity shift was originally included in the rate equations and clearly pointed out in [22]. The amount of the cavity resonance shift in wavelength can be derived as

$$\Delta\lambda_{\text{cav}}(N) = -\frac{\alpha\lambda_0^2}{2\pi c} G_0 \frac{\Delta N}{2} \quad (2.11)$$

As ΔN is always negative, the cavity resonance will be red-shifted. The steady-state phase difference ϕ_0 can be estimated roughly in the range $(-\pi/2, 0)$ across the locking range of $\Delta\lambda$ according to Eqn (2.10). Therefore, on the blue detuning side, the carrier number only has a small amount of reduction from the threshold value, whereas on the red side, the reduction is larger according to Eqn (2.5). This trend can also be understood by examining the gain reduction change compensated by the same amount of stimulated emission from the master laser at different $\Delta\lambda$. The dynamics and its detuning dependence are visualized in Figure 2.8. It is consistent with the experimental observation shown in Figure 2.7. In essence, the injection-locked VCSEL cavity works as an amplifier with a detuning-controlled gain level.

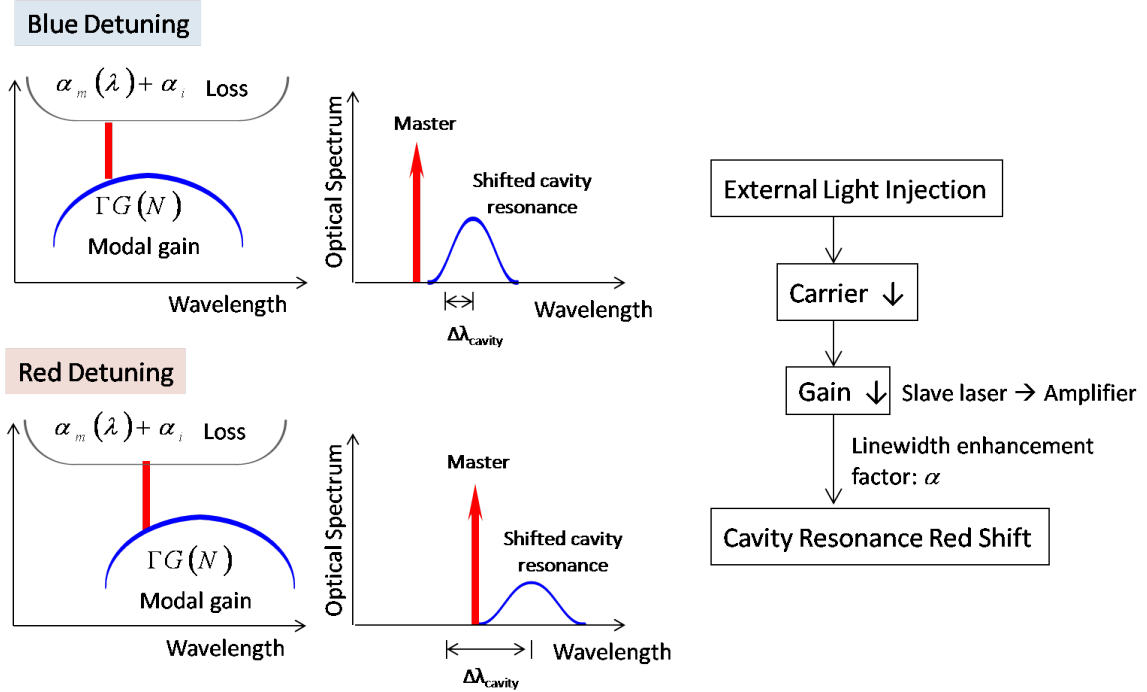


Figure 2.8 Schematic of the gain/loss spectrum and the optical spectrum as well as a flow chart to illustrate the OIL dynamic process and its detuning dependence.

2.3 FABRY-PEROT AMPLIFIER MODEL

Based on the understanding presented in the previous section, the injection-locked VCSEL can be modeled as a simple Fabry-Perot amplifier consisting of two mirrors and active media in between, whose gain level is controlled by the detuning value. To experimentally verify this model, the optical reflection spectrum of a VCSEL amplifier as well as the OIL VCSEL can be measured.

The experimental setup of measuring the reflection spectrum of a VCSEL amplifier and the measurement results are shown in Figure 2.9. By illuminating the light from a broadband optical source, such as an erbium-doped fiber amplifier (EDFA), onto the VCSEL then collecting the reflected light, the reflection spectrum of a VCSEL amplifier at various bias, hence gain levels, below lasing threshold ($I_{th} = 0.6$ mA) can be measured

using an OSA. It is interesting to notice that a minimum reflection power occurs at the cavity transparency ($I = 0.32$ mA for this particular device), where the material gain (γ) is equal to the material loss (α_i), so that the active cavity is equivalent to a cold cavity without any gain medium. Therefore, bias level above cavity transparency is the gain regime ($\gamma > \alpha_i$), whereas bias level below cavity transparency is the loss regime ($\gamma < \alpha_i$). Because of the linewidth enhancement factor, the resonance red shifts as the bias level decreases. This can be calculated simply from the multiple reflections between the two mirrors of the Fabry-Perot amplifier structure. A detailed derivation can be found in [33]. Transmission matrix simulation of a VCSEL amplifier structure generates the same result [34].

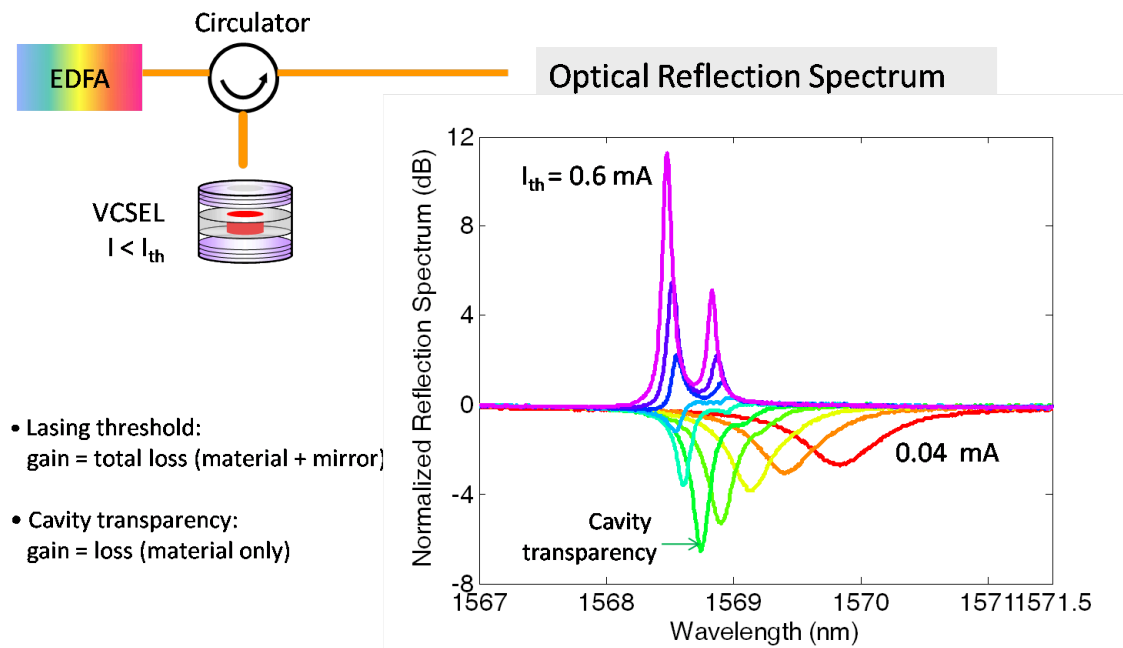


Figure 2.9 Experimental setup and measurement results of the reflection spectra of a VCSEL amplifier at various bias (gain) levels.

Knowing the reflection characteristics of a VCSEL amplifier, one can measure the reflection spectra of an OIL VCSEL and verify that the cavity mode exhibits similar

features. The setup and the results are shown in Figure 2.10. The master light and the broadband light are combined at a 50/50 combiner and shun onto the VCSEL, which is biased above threshold now. Similar as shown in Figure 2.7, the cavity resonance can be observed on the longer wavelength side of the master mode. As detuning increases, the carrier number is reduced further, hence larger reduction in gain level. By examining the zoom-in of the cavity mode reflection as a function of detuning shown in the inset, it is clear that the OIL VCSEL possesses similar characteristics as a VCSEL amplifier. This measurement experimentally proves that the VCSEL becomes a gain-clamped detuning-controlled amplifier under injection locking.

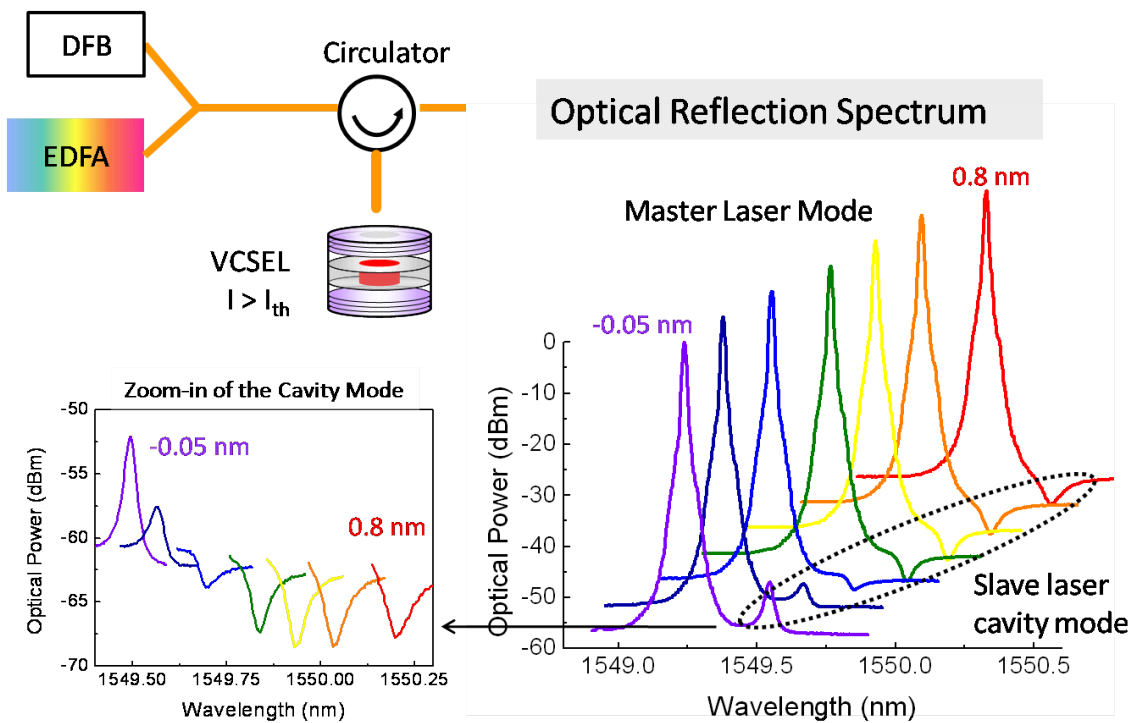


Figure 2.10 Experimental setup and measurement results of the reflection spectra of an OIL VCSEL at various detuning (gain) values.

As will be seen in later chapters, this amplifier model can effectively provide some intuitive understandings thus explanations of the modulation performance improvement of OIL VCSELs, such as the resonance frequency enhancement (Chapter 3) and negative chirp by data pattern inversion (Chapter 4).

Chapter 3

Small-Signal Modulation Characteristics

There is an ever-increasing demand of very high-speed, low-cost optical transmitters to transmit analog and digital signals over optical fibers. High-speed transmitters are enabling components for not only the RF and millimeter-wave applications, but also next generation 100-Gb/s Ethernet and local area networks (LANs). Over the past ten years, much effort has been put into developing wide-bandwidth lasers and modulators. Devices working at wavelength around 1.55 μm are preferred due to more mature technologies of the link and other components. In a typical laser, the relaxation oscillation (resonance) frequency is a figure-of-merit that is a necessary but not sufficient condition for determining its maximum direct modulation bandwidth. The resonance frequency of directly modulated diode lasers at 1.55 μm has been demonstrated up to 30 GHz measured from a multiple-quantum-well laser [35] as well as a DBR laser [36]. Practical limitations, including laser heating and gain compression [29], limit the maximum resonance frequency. Furthermore, increased damping at higher resonance frequencies limit the maximum bandwidth to 30-40 GHz [35, 36]. On the other hand, the external modulators are demonstrated with impressive achievements. Up to 105 GHz and 150 GHz modulation have been shown on a Ti:LiNbO₃ traveling wave modulator [37] and a polymer electro-optic modulator [38], respectively. However, the half-wave voltage, V_{π} ,

is currently still very high, making it difficult for system applications. Long-term stability of polymer materials is still undergoing development. In addition, overall design and fabrication process of these devices are complex and costly. Therefore, a very high-speed, direct-modulated laser is highly desirable for the rapidly growing applications.

Optical injection locking (OIL) has been shown as a very effective technique to increase the laser resonance frequency [23, 39]. A record resonance frequency of 72 GHz was reported on a directly modulated injection-locked DFB laser [23]. High-speed VCSELs are also of great interests for many short-haul communication systems due to their cost-effective fabrication and simple testing process. Although the modulation speed of 1.55- μm VCSELs is limited by device parasitics to < 20 GHz, the dynamic performance can be drastically improved by applying strong optical injection locking [39, 40]. Small-signal frequency response of a laser is the standard measurement to characterize the laser resonance frequency as well as the modulation bandwidth. In this chapter, small-signal characteristics of an OIL VCSEL are studied thoroughly and systematically with the focus on high-speed performance. Physical explanations using the amplifier model developed in Chapter 2 are also discussed.

3.1 RESONANCE FREQUENCY ENHANCEMENT

3.1.1 Experimental Demonstration

One of the predictions made by the OIL theory is that injection locking can increase the resonance frequency of a directly modulated laser, and it was published by a number of groups independently [12, 22, 31]. Experimental results demonstrated at the same time. Systematic experimental study has been done on 1.55- μm VCSELs [39, 40] in the ultra-high injection regime. As mentioned in the previous chapter, there are two

parameters, injection ratio and detuning, to control the locking condition. Therefore, small-signal frequency response is usually examined as a function of both parameters.

The experimental setup is shown in Figure 3.1. A commercial DFB laser is used as the master laser with maximum output power ~ 40 mW. The VCSEL is single-mode (side polarization mode suppression ratio > 40 dB) at $1.55 \mu\text{m}$ with buried tunnel junction (BTJ) structure designed for high-speed operation (3-dB bandwidth of ~ 10 GHz) [41]. The threshold current is 0.6 mA, and the output power is > 1 mW. The VCSEL is mounted on a copper block and temperature controlled by thermal electric coolers (TECs). The emitted light is coupled into tapered fiber, hence can be injection-locked through an optical circulator. Polarization controller is used to match the master polarization to the VCSEL preferred polarization to maximize the locking stability. Biasing and modulation signals are delivered to the VCSELs through high-speed 1-mm coaxial microwave signal-ground probe. A small amount of the output light is sent to an optical spectrum analyzer (OSA) to monitor the locking condition. The majority of the light is detected by a photo-detector (PD) with 3-dB bandwidth of 84 GHz. A 110-GHz vector network analyzer (VNA), Agilent N5250A, is used to test the small-signal frequency response. All the frequency response shown in Figure 3.1 is corrected for RF cable loss only. The VCSEL parasitic response is not de-embedded.

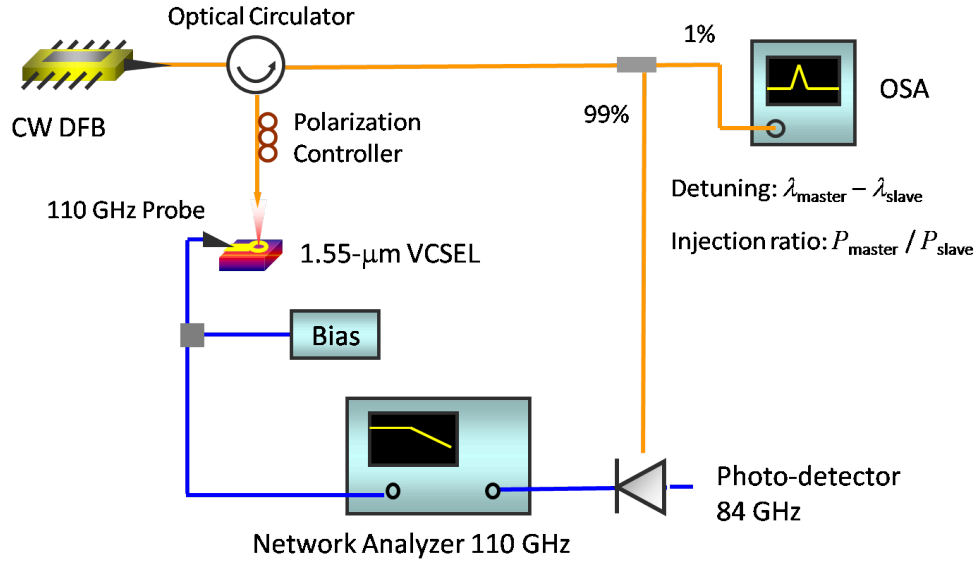


Figure 3.1 Experimental Setup. (VNA: vector network analyzer, PD: photo-detector, OSA: optical spectrum analyzer)

Detuning dependence is tested by keeping the injection ratio at a fixed value within strong or ultra-high injection regime and varying the master wavelength. Figure 3.2 shows the frequency response and optical spectra of the VCSEL at various detuning values under a constant external light injection of 16 dB. Free-running response is also shown as a reference. The VCSEL is biased at 2 mA ($3.3 \times I_{th}$) with 0.43 mW output power and a 6-GHz resonance frequency. As the master wavelength is tuned from detuning values ($\Delta\lambda$) of -0.748 nm to -0.906 nm as shown in Figure 3.2(b), the resonance peak increases from 92 GHz to 107 GHz with a reduced damping factor. The resonance frequency of 107 GHz sets the record for directly modulated diode laser so far. However, this number is currently limited by the measurement instrument but not any fundamental physics. Correspondingly, the cavity mode shown in the optical spectra is suppressed as $\Delta\lambda$ increases. It is interesting but also important to note that the frequency spacing between the master mode and the cavity mode in the optical domain corresponds to the

resonance frequency in the electric / radio frequency (RF) domain. This discovery can be explained very well by the amplifier model as one will see in the next section.

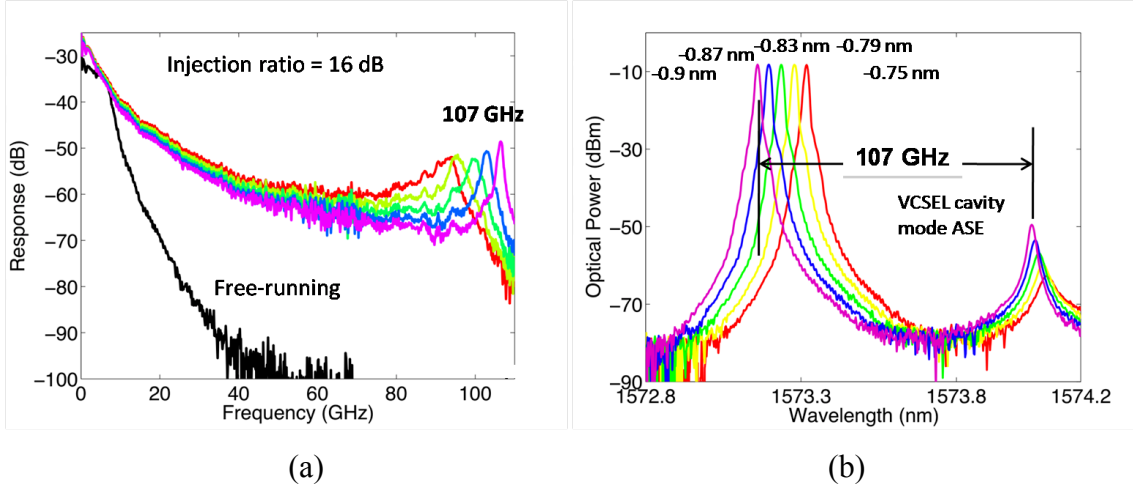


Figure 3.2 (a) Frequency response and (b) optical spectra of an OIL VCSEL at various detuning values. A record resonance frequency of 107 GHz is shown. The master laser wavelength is tuned. The frequency spacing between the master mode and the cavity mode in the optical domain is equal to the resonance frequency in the electric domain.

In strong or ultra-high injection regime, first-order approximation of the linearized rate equations shows that the square of the enhanced resonance frequency of an injection-locked laser is in a linear relationship with the injection ratio [23, 42]:

$$\omega_R^2 \approx \omega_{FR}^2 + \kappa^2 \frac{P_{inj}}{P_0} \quad (3.1)$$

This indicates that an OIL laser resonance frequency is dominated by the injection ratio and continues to increase under stronger injection.

The injection ratio dependence of the frequency response is obtained varying the master laser power. Figure 3.3 shows the frequency response and optical spectra of the OIL VCSEL at different injection ratio levels. At each injection ratio, the detuning is adjusted slightly so that the RF gain of the resonance peak is about ~ 20 dB (thus a

similar damping factor). Correspondingly, in the optical domain, shown in Figure 3.3(b), the cavity modes for different injection ratio conditions are all aligned with similar optical gain. As shown theoretically above in Eqn (3.1), the maximum resonance frequency enhancement increases with injection ratio. Therefore, even higher resonance frequency is expected with a higher injection ratio. However, the ultimate limit of the resonance frequency remains an interesting, important, and unanswered question.

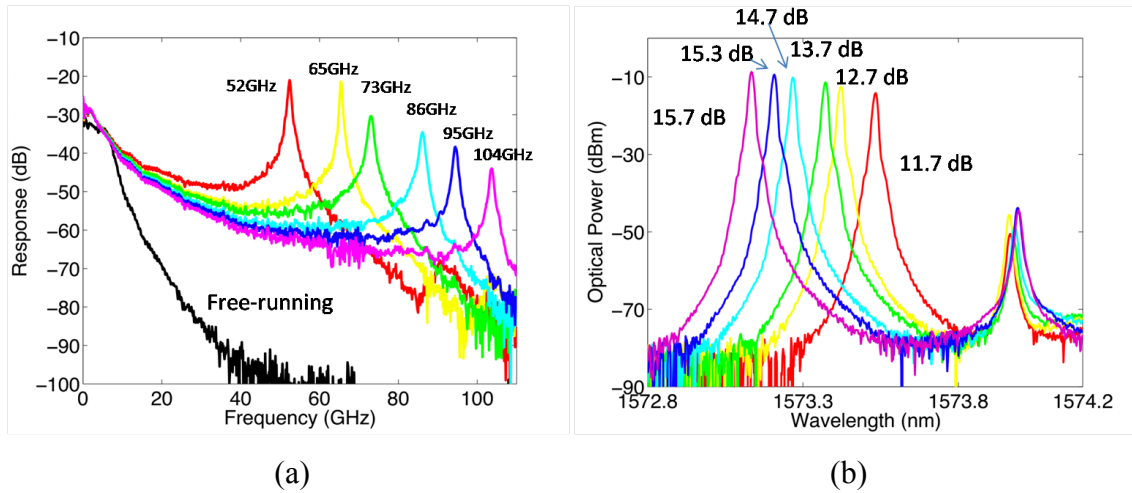


Figure 3.3 Frequency response and (b) optical spectra of an OIL VCSEL at various injection ratios. The resonance frequency increases with injection ratio.

If combine the trend in both detuning and injection ratio dependence, it is clear that to achieve high-resonance frequency, the locking condition should be in a high injection ratio regime with a small wavelength detuning (master wavelength on the blue side relative to the slave laser). Furthermore, by adjusting injection ratio and detuning independently, one can customize the frequency response to have a desired shape of laser transfer function.

3.1.2 Physical Explanation of Resonance Enhancement Using the Fabry-Perot Amplifier Model

The detuning-dependent behavior of the frequency response shown in Figure 3.2(a) was repeatedly observed, not only on OIL VCSELs but also on other types of injection-locked lasers. Although the small-signal modeling using OIL rate equations provides excellent agreement with the measurement, a physically intuitive explanation that is critical to further the understanding is still in need. In this section, we show a hybrid model using the OIL rate equations as the foundation, and then incorporate the amplifier model developed in Chapter 2 to explain the properties of small-signal frequency response of an OIL laser, especially its resonance frequency enhancement and detuning dependence.

When the frequency response of an injection-locked laser is being measured, the modulation sidebands (ω_m) scan over a certain frequency range beside the master mode as shown in Figure 3.4. The sidebands, which work like probes, replicate the features of the VCSEL amplifier gain profile and represent it in the RF domain after detection. Therefore, major features including the gain of the resonance peak and the frequency at which the resonance peak is located in the RF domain, as functions of the detuning, should follow those of the cavity mode in the optical domain. To verify these strong correlations, hence the physical origin of the resonance enhancement, optical spectra and the frequency response of an OIL VCSEL are simulated using an F-P amplifier model.

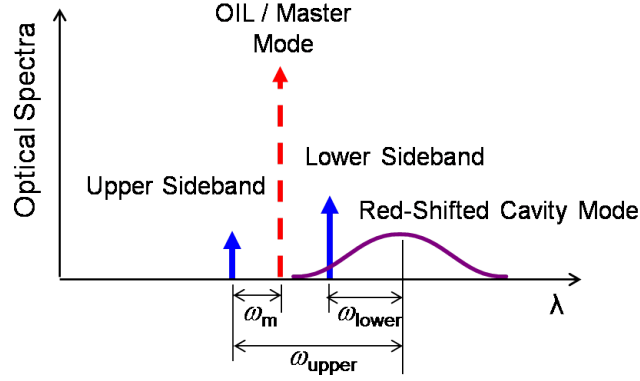


Figure 3.4 Schematic optical spectrum of a modulated OIL laser. The modulation frequency ω_m is being scanned when frequency response measurement is performed.

A simple F-P amplifier structure is shown in Figure 3.5, which consists of two mirrors and active media in between. A reflection spectrum can be obtained from multiple reflections between the front and back mirror,

$$\frac{E_r}{E_i} = \frac{(1 - r_1^2) r_2 e^{(\gamma - \alpha_i)L} e^{-i\phi}}{1 - r_1 r_2 e^{(\gamma - \alpha_i)L} e^{-i\phi}} - r_1 \quad (3.2)$$

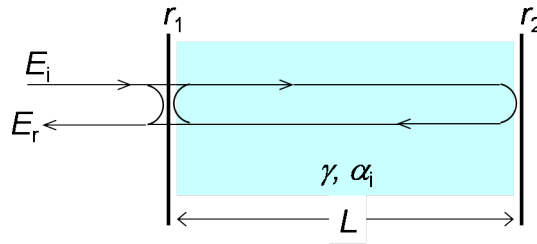


Figure 3.5 A simple F-P amplifier model used to simulate the OIL VCSEL. E_i is the incident light field, E_r is the reflected light field, L is the cavity length, r_1 and r_2 are the mirror field reflectivity, γ and α_i are the gain and the distributed loss of the active medium.

By calculating the reflection spectrum of the two optical sidebands, the RF response in the frequency domain will be attained accordingly. The optical spectrum, which measures the intensity of the field, is the norm square of Eqn (3.2). The frequency

response in the RF domain, including contributions from both the lower and the upper sidebands, can be expressed as

$$20 \log \left| \left(\frac{E_r}{E_i} \right)_u + \left(\frac{E_r}{E_i} \right)_l \right|^2 \quad (3.3)$$

From a particular injection-locking condition, with a known injection ratio and a detuning value, one can calculate the carrier density reduction from Eqn (2.5). This determines the gain of the slave laser through $\gamma = g_n(N_{th} + \Delta N)$, where g_n is the differential gain, and the threshold carrier density, N_{th} , can be obtained from the threshold gain $\gamma_{th} = \alpha_i - (1/L) \ln r_1 r_2$. The cavity resonance shift is attained through Eqn (2.11). This needs to be taken into account when computing the frequency of the modulation sidebands ω_{lower} and ω_{upper} relative to the cavity resonance as labeled in Figure 3.4, thus obtaining RF response from interactions of both sidebands with the cavity mode. Therefore, the phase of the two sidebands needed in Eqn 3.2 are

$$\phi_{lower} = 2kL = 2 \left(\frac{\omega_{lower}}{v_g} \right) L \quad (3.4 \text{ a})$$

$$\phi_{upper} = 2kL = 2 \left(\frac{\omega_{upper}}{v_g} \right) L \quad (3.4 \text{ b})$$

The flow chart of the modeling process is shown in Figure 3.6 as a reference.

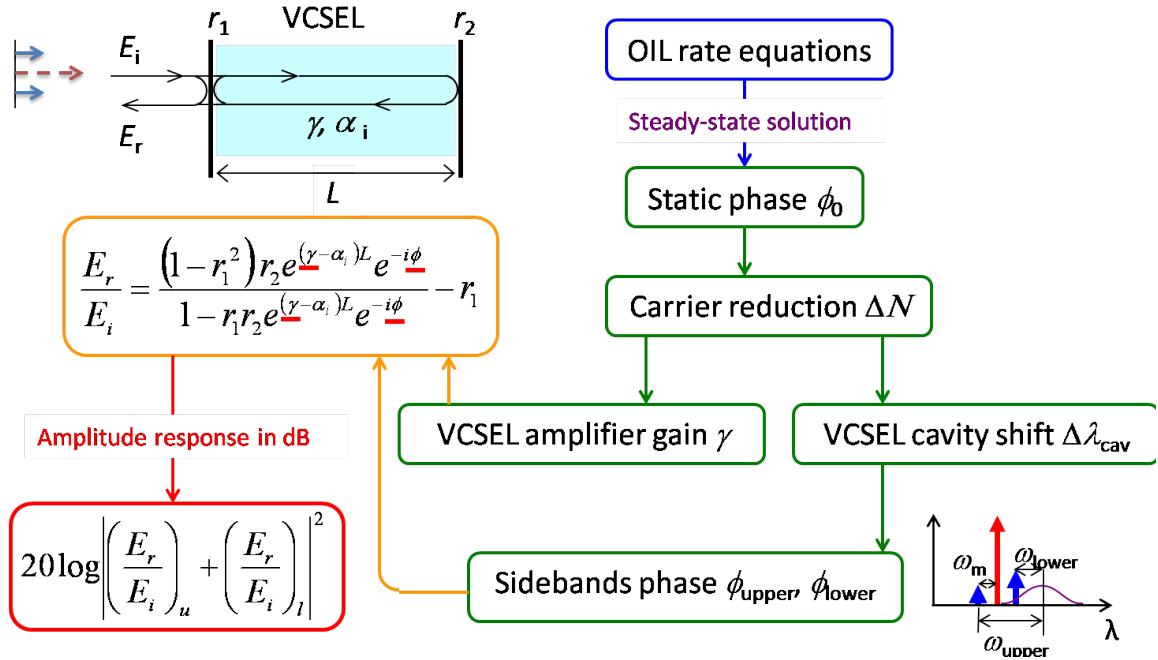


Figure 3.6 Flow chart of the simulation process of a hybrid model using both steady-state solutions to OIL rate equations and the Fabry-Perot amplifier structure.

Table 3.1 Parameters for simulations using the amplifier model.

r_1	99.5%	Top mirror field reflectivity	r_{inj}	0.65	Field injection ratio
r_2	99.9%	Bottom mirror field reflectivity	g	$3 \times 10^{-16} \text{ cm}^2$	Differential gain
L	1 μm	Cavity length	κ	10^{12} s^{-1}	Coupling rate
α_i	10 cm^{-1}	Material distributed loss	γ_{th}	70.13 cm^{-1}	Threshold gain value
λ_0	1550 nm	Emission wavelength	N_{th}	$2.34 \times 10^{17} \text{ cm}^{-3}$	Threshold carrier density
v_g	$8.3 \times 10^7 \text{ m/s}$	Index = 3.6, $v_g = c/n$	α	6	Linewidth enhancement factor

Simulation is performed based on this modeling framework. The values of the parameters are carefully chosen and listed in Table 3.1 so that they resemble the actual values used in the experiment. The simulated optical spectra and frequency response are

shown in Figure 3.7. As $\Delta\lambda$ increases, from -0.35, -0.15 to 0 nm, the carrier density reduces further, resulting in a more and more suppressed amplifier peak. This reduced amplifier peak manifests itself in the RF domain as a more damped resonance peak. Hence, strong correlation between the VCSEL cavity quality factor (Q), the bandwidth of the ASE spectrum and the damping of the RF response are clearly illustrated. In addition, the carrier density reduction further red-shifts the slave cavity mode. However, the overall spacing between the master and the slave laser cavity mode is reduced. This spacing in fact determines the resonance frequency. And the resonance frequency is reduced as $\Delta\lambda$ is increased.

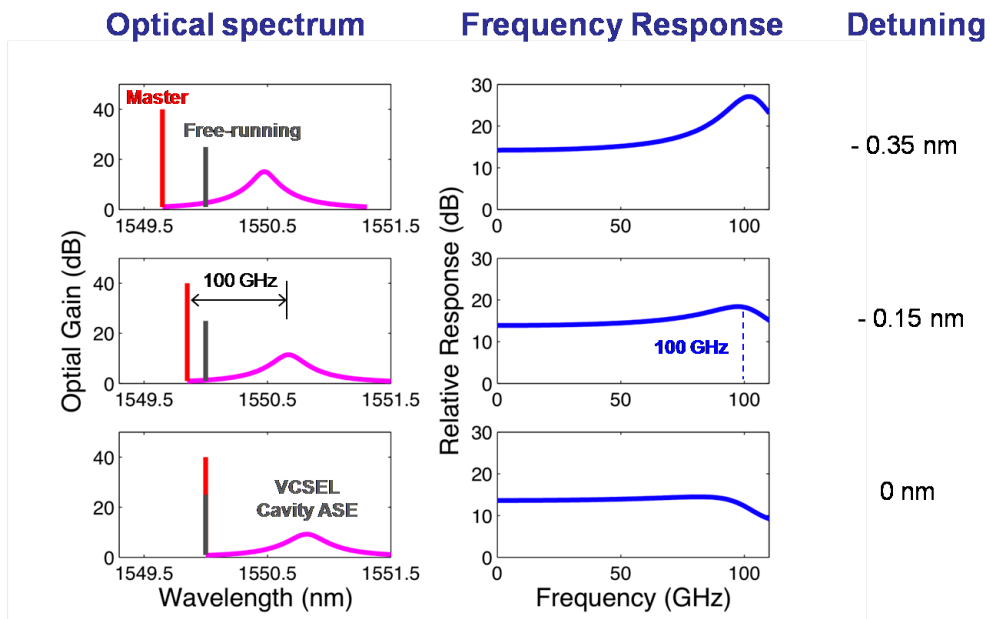


Figure 3.7 Simulated optical spectra and frequency response of an OIL VCSEL at three detuning conditions. (FR: free-running, SL: slave laser, ML: master laser) See Appendix A1.3 for MATLAB code.

Figure 3.8 replots the experimental optical spectra and their corresponding small-signal modulation response shown previously in Figure 3.2 to compare with the simulation results. The experimental results in Figure 3.8 agree well with the simulation

results in Figure 3.7, expect the overall efficiency declination of the RF response, which is due to the parasitic response of the VCSEL (bandwidth ~ 10 GHz).

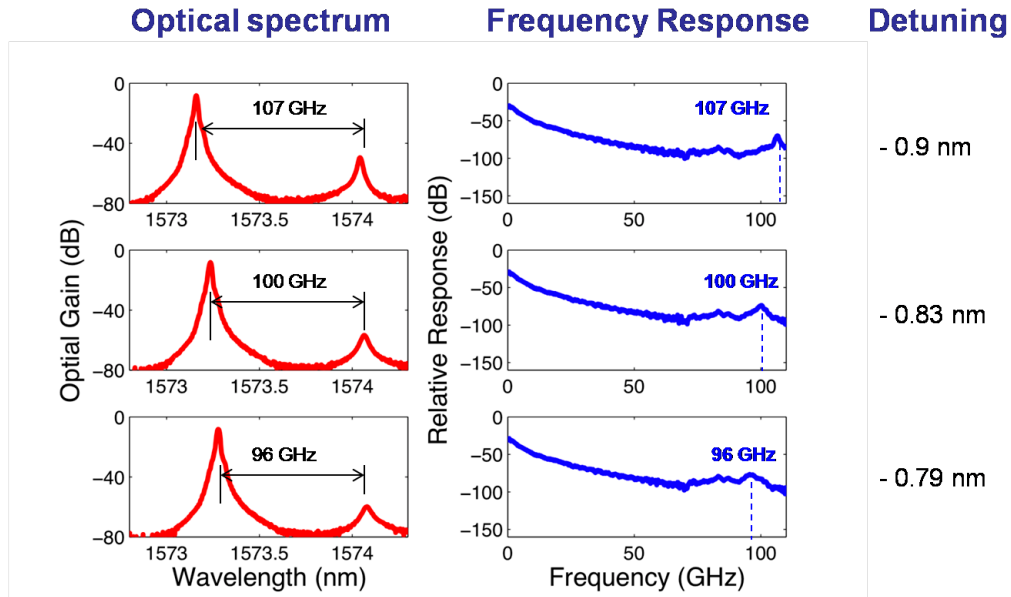


Figure 3.8 Measured optical spectra and frequency response of an OIL VCSEL at three detuning conditions. The frequency response is raw data without removing detector responsivity, and VCSEL parasitics (estimated cutoff at 10 GHz).

A more convincing and interesting observation is the double-resonance on the frequency response as shown in Figure 3.9. The two resonance peaks correspond to the two polarization modes of the VCSEL [43], which are typically 0.3-0.4 nm apart. The master polarization is aligned with the slave lasing mode M1. As labeled in both optical spectrum and the frequency response, the optical mode spacing corresponds to the resonance frequency of both polarization modes. Furthermore, since M2 is not the lasing mode, it possesses a much lower gain, resulting in a broader and more damped peak in the optical domain as well as in the RF domain. This concurs with the amplifier model presented here.

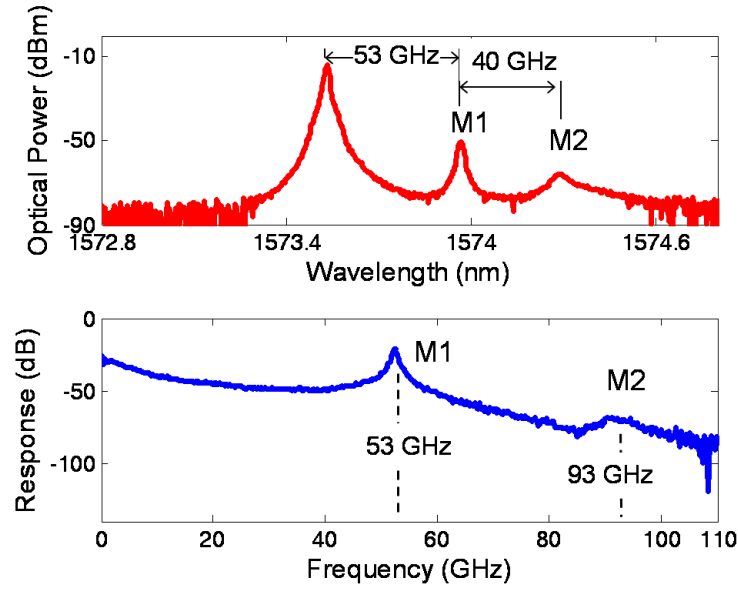


Figure 3.9 Measured optical spectrum and frequency response showing a double-resonance phenomenon. The two resonance peaks are due to the two polarization modes of the VCSEL under strong injection locking.

3.2 INTRINSIC MODULATION BANDWIDTH ENHANCEMENT

All the results of the frequency response measurement shown in the previous section (the rest of the chapter too unless otherwise stated) are raw data with at most only cable loss calibrated. Therefore, the measured frequency response is the total response of the entire system, including the laser intrinsic response (determined by the relaxation oscillation frequency – exchange between carriers and photons), laser parasitic response (determined by the parasitic resistance and capacitance – RC), packaging response (e.g. the bonding wires of the VCSEL), and also the response of the detector, cables, connectors, bias Tees and the testing instrument itself (network analyzer). However, to reveal the features and trends caused by OIL on the laser modulation behavior, only the intrinsic response is of interest here [44]. Since it is usually buried in the parasitic response of the whole system, a set of proper procedures need to be developed to de-

embed the intrinsic response. The procedures described below are similar as presented in [45], but for calibrating an OIL laser response instead of a free-running laser response.

The measured transfer function can be written as the product of system parasitic response and the laser intrinsic response. The system parasitic response lumps together all the components response (RC, packaging, cable, detector, etc) other than the laser intrinsic response. The OIL laser intrinsic response can be obtained by doing small-signal analysis on the rate equations [23]. The square on the transfer function comes from the fact that power is being measured in the experiment while the transfer function is defined using voltage.

$$H_{\text{system}}^2(f) = H_{\text{parasitic}}^2(f) \times H_{\text{intrinsic}}^2(f) \quad (3.5 \text{ a})$$

$$H_{\text{intrinsic}}^2(f) = H_{\text{OIL}}^2(f) = \frac{1 + \left(\frac{f}{f_z}\right)}{1 + \left(\frac{f}{f_p}\right)^2} \cdot \frac{1}{\left(1 - \left(\frac{f}{f_r}\right)^2\right)^2 + \left(\frac{\gamma}{2\pi f_r}\right)^2 \left(\frac{f}{f_r}\right)^2} \quad (3.5 \text{ b})$$

In the experiment, power is usually presented in logarithmic scale. So Eqn (3.5a) can be written as

$$20\log H_{\text{system}}(f) = 20\log H_{\text{parasitic}}(f) + 20\log H_{\text{OIL}}(f) \quad (3.6)$$

So the question here is how one can remove the parasitic response from the measured system response without knowing it either experimentally or mathematically to obtain the intrinsic OIL laser response. Based on the expression in Eqn (3.6), the procedures of de-embedding are stated below with the assistance of the flow chart shown in Figure 3.10.

First, system response curves at different locking conditions are measured experimentally in logarithmic scale labeled as $20\log H_{s1}, \dots, 20\log H_{sN}$. It is reasonable to

assume the system parasitic response stays the same while injection-locking condition (detuning, injection ratio) is being changed since it is mainly from passive electronic components. Then if one takes the difference of any two of the system response curves, the system parasitic term will be cancelled out as shown below.

$$20\log H_{s1}(f) - 20\log H_{s2}(f) = 20\log H_{OIL2}(f) - 20\log H_{OIL1}(f) \quad (3.7)$$

Since the expression of the transfer function of an injection-locked laser is known, one can use the right-hand side of Eqn (3.7) (mathematical expression) to curve-fit the left-hand side of it (measured raw data). From the fitting, parameters such as f_z , f_p , f_r , and γ for each locking condition are available. Next, by plugging these parameters back to Eqn (3.5b), laser intrinsic response for each locking condition is obtained. Now if one subtracts the intrinsic response from the raw data as

$$20\log H_{s1}(f) - 20\log H_{OIL1}(f) = 20\log H_{parasitic}(f), \quad (3.8)$$

the system parasitic is attained. If this process is repeated for any combination of the two measured curves, the system parasitic is finally taken as an average of all of the parasitic response generated. Then, one can subtract this averaged parasitic response from the raw data to get the parasitic-removed OIL laser intrinsic response. Finally, curve-fitting of this de-embedded response is performed to grab important fitting parameters such as f_z , f_p , f_r , and γ etc., and also to check if the whole process is consistent.

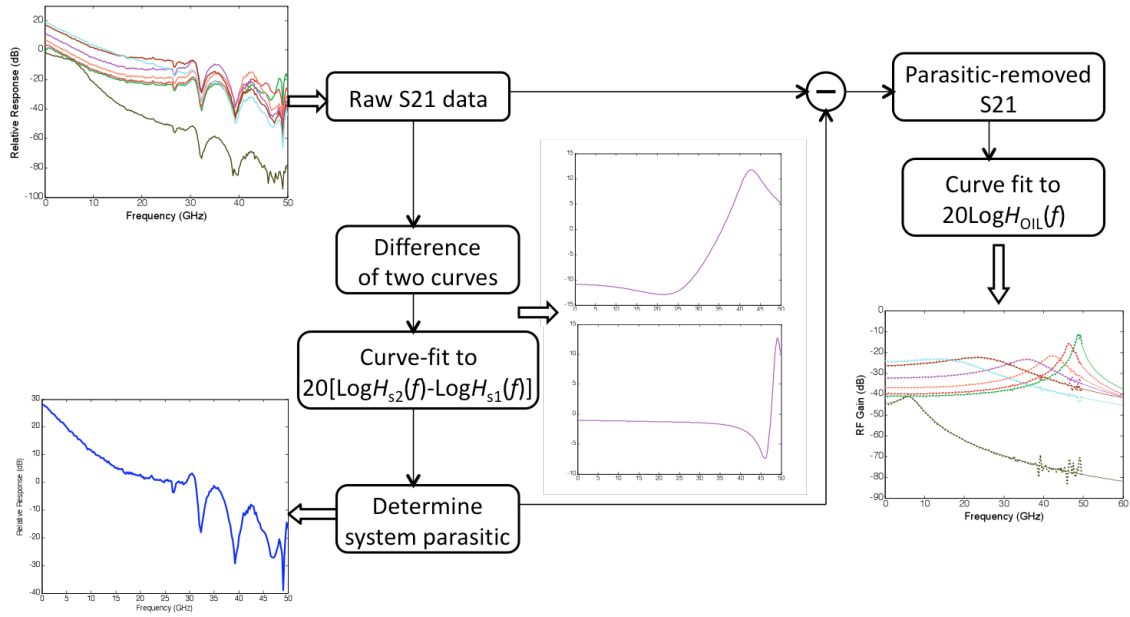


Figure 3.10 Flow chart of the de-embedding procedures to obtain OIL laser intrinsic response. See Appendix A1.4 for MATLAB code.

Comparing the measured system response curves with the de-embedded ones in Figure 3.10, it is obvious that the intrinsic response reveals the detuning dependence much more clearly.

The de-embedding process on frequency response is sometimes controversial, because the actual 3-dB bandwidth without de-embedding is the determining factor for the data rate in a digital fiber-optic link though the de-embedded response shows a high-resonance frequency and a flat response. However, the total response can be improved by engineering the laser and the system parasitics.

3.3 CASCADED OPTICAL INJECTION LOCKING FOR BROADBAND MODULATION

As pointed out already previously that the resonance enhancement not necessarily results in bandwidth enhancement which actually determines how fast the laser can be modulated for communication systems. One factor that bottlenecks the 3-dB bandwidth

of an injection-locked laser is the device parasitics. However, this is not a fundamental limit and can be engineered by modern laser device design. Another factor, which is more closely related to OIL itself, is the 3rd pole of the transfer function introduced by the nonlinear process [23]. A detailed examination of the OIL rate equations shows that the intrinsic bandwidth can be greatly increased by increasing the DC bias of the slave laser in absence of the RC parasitics of the slave laser [44]. In this section, we present a comprehensive study on a cascaded optical injection locking (COIL) technique, which cleverly leverages the resonance amplification using two slave lasers to achieve a wide and tailorable modulation bandwidth in spite of the existence of the RC parasitics of the slave laser.

3.3.1 Slave-Modulated Cascaded Optical Injection Locking

The resonance frequency enhancement of an OIL laser is primarily due to the red-shifted cavity resonance of the slave laser, which resulted in the amplification of the modulation sideband of either the master or the slave laser as explained in section 3.1.2. The frequency difference between the injection-locked laser mode (same as the master mode) and the cavity mode corresponds to the resonance frequency in the RF domain. If we extend the typical OIL configuration by adding one more slave laser, injection-locked by the same master laser but with a different detuning, an even larger difference between the OIL mode and the cavity mode can be achieved. Hence a second resonance peak is created in the modulation response at an even higher frequency.

This cascaded OIL (COIL) idea is schematically illustrated in Figure 3.11. The first slave laser, colored in blue, is injection-locked and directly modulated, while the second slave laser, colored in red, is kept under CW operation while injection-locked by the

output of the first stage. The slave laser is lasing at the master mode when it is injection-locked shown in gray, while its cavity resonance is red-shifted and exhibit amplified spontaneous emission in the optical spectrum, shown in blue and red for the first stage and the second stage, respectively. When the modulation lower sideband (with lower frequency) scans over the cavity mode and experiences the amplification, a resonance peak shows up in the frequency response at the frequency corresponding to the spacing between the OIL mode and the cavity mode as labeled in the Figure 3.11. Since the resonance peak is due to the amplification of the sideband by the slave laser cavity, a second resonance peak exhibits even though the second slave laser is not modulated. Therefore, by repeatedly utilizing the cavity effect based on the understanding of OIL dynamics, it is promising to achieve high-speed devices using COIL.

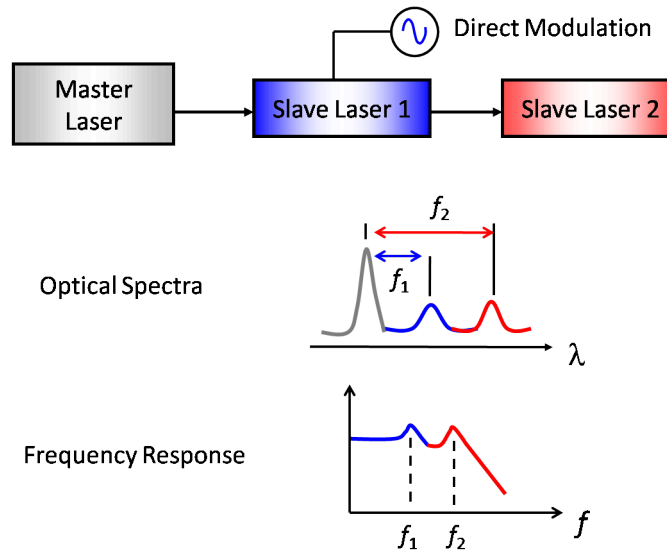


Figure 3.11 A schematic explaining the idea of cascaded optical injection locking (COIL).

Experiments are performed to verify the COIL idea. The measurement setup is shown in Figure 3.12. All the devices, components and measurement instruments are the same as shown in Figure 3.1 except two VCSELs are used here.

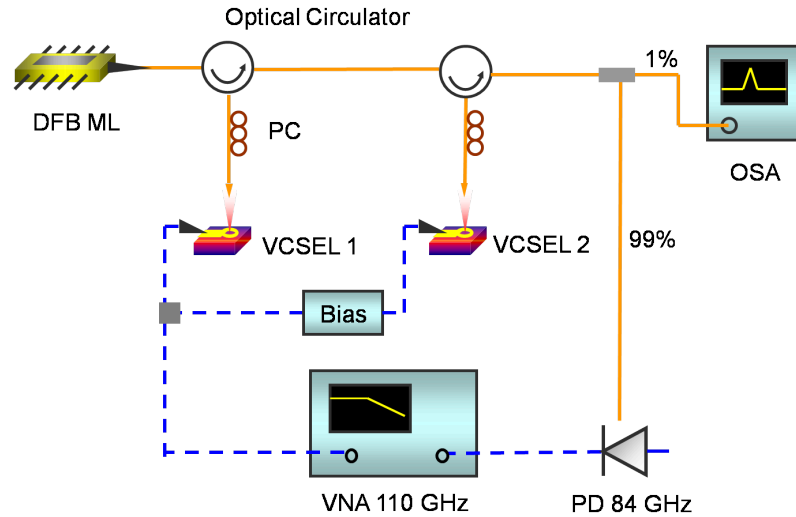


Figure 3.12 Experimental setup. Orange lines are optical paths, while blue lines are electrical paths. (ML: master laser, PC: polarization controller, OSA: optical spectrum analyzer, VNA: vector network analyzer, PD: photodetector.)

It has been demonstrated in section 3.1.1 that the frequency response of an injection-locked laser can be tailored by adjusting the wavelength detuning ($\lambda_{\text{master}} - \lambda_{\text{slave}}$) between the master and the slave laser. On the blue detuning side ($\lambda_{\text{master}} < \lambda_{\text{slave}}$), the frequency response possesses a sharp resonance peak at a high frequency, but usually associated with a droop in the middle frequencies [44]. According to OIL dynamics, a third pole in the transfer function, which can be derived from injection-locking rate equations, causes a significant reduction in the modulation response between low frequencies and the resonance peak. Therefore, even though the resonance frequency can be maximized in this condition, the modulation bandwidth is limited at a relatively low frequency. On the

red detuning side ($\lambda_{\text{master}} > \lambda_{\text{slave}}$), however, the response is flatter and the resonance peak is damped, but at a lower frequency. This would help obtain a better performance in terms of modulation bandwidth, but the ultimate limit is reduced. Therefore, based on the detuning dependence stated above, there could be two possible configurations to realize COIL, both with the purpose to widen the bandwidth.

If one follows the concept described in Figure 3.11 directly, the second stage should be detuned to generate a resonance peak at a higher frequency, thus extending the bandwidth even further. In this case, to alleviate the bandwidth limit caused by the third pole of the first stage, OIL on the first stage should be kept at a red detuning condition to attain a flat response. It should also be noted that the resonance frequency enhancement of OIL laser is determined by the injection ratio ($P_{\text{master}} / P_{\text{slave}}$), the second VCSEL needs to be locked with a higher power. However, due to coupling and other link loss, the master laser power is usually significantly reduced when it reaches the second stage. Therefore, to maintain a high injection ratio for the second stage, the second VCSEL needs to be biased at a low current level, thus emitting less power.

Figure 3.13 shows the frequency response. Dashed gray line is the response from the first OIL stage only, under an injection ratio of ~ 14 dB. Since it is red-detuned, no severe droop is observed. Then the second VCSEL is injection-locked with an injection ratio of ~ 16 dB. As expected, the response of two-stage OIL is ameliorated as shown in the solid red line, and a 3-dB bandwidth of 66 GHz is achieved. This is the highest bandwidth reported of a direct modulated semiconductor laser so far, to the best of our knowledge.

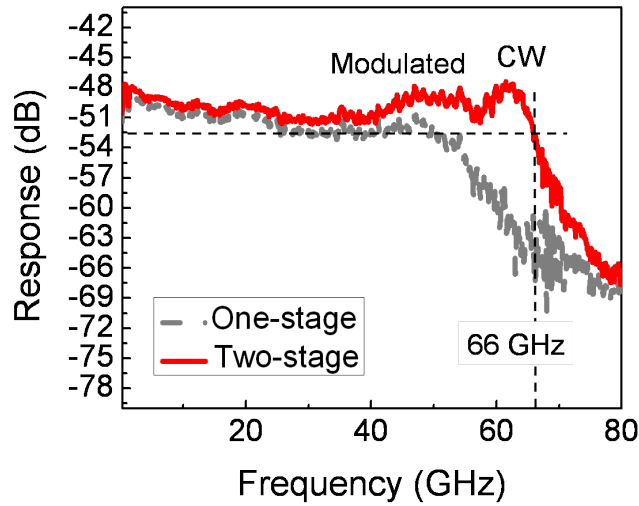


Figure 3.13 Frequency response of COIL. The first modulated VCSEL is red-detuned to provide a flat response while the second VCSEL is locked at a longer wavelength to extend the bandwidth. 3-dB bandwidth of 66 GHz is obtained.

On the other hand, the first stage can be detuned to the blue side to reach a high resonance frequency, and then the second stage is utilized to compensate the efficiency reduction in the middle frequencies caused by the third pole. The frequency response is shown in Figure 3.14. Figure 3.14(a) shows the frequency response of both one-stage (dashed gray) and two-stage (solid red) OIL VCSELs. The first VCSEL is modulated as well as injection-locked by the master laser with an injection ratio of ~ 12.5 dB and a blue detuning so that the resonance peak is pronounced at 60 GHz as indicated by the gray dashed line. However, the modulation efficiency drops about 20 dB up to 40 GHz. As the second VCSEL is biased and injection-locked by the output of the first stage with an injection ratio ~ 11 dB and a proper detuning value, a second peak shows up at a frequency between DC and the first resonance peak, and helps increase the modulation efficiency dramatically in the middle frequencies. Similarly as the first stage, the exact

location and damping of the second peak can be tuned by adjusting the injection ratio and the detuning value of the second stage. Even though the response is improved by putting in a second VCSEL, the 3-dB bandwidth is still limited by the fast roll-off due to the third pole from the first OIL stage. However, there are totally four parameters, injection ratios and detuning values of two OIL stages, can be tuned to tailor the overall response. If the master laser can be red-detuned for the first stage to relieve the dipping at frequencies below the resonance, the compensation brought in by the second stage can be more effective. This is shown in Figure 3.14(b) as the first stage is detuned to exhibit a flatter and damped response. And then with the assist from the second stage, a 3-dB bandwidth of 50 GHz is achieved.

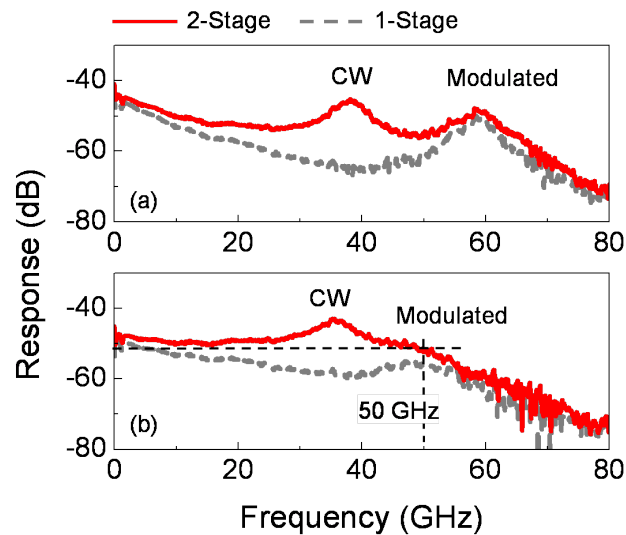


Figure 3.14 Frequency response of COIL. (a) The first modulated VCSEL is blue-detuned. Cascading effect is clearly shown by the two resonance peaks. (b) The first modulated VCSEL is red-detuned. A flat response with 3-dB bandwidth of 50 GHz is achieved.

Therefore, as demonstrated above, the first configuration starts with a flat response of the first stage and extends the bandwidth by adding in a second stage. In this case, the

second slave laser needs to be locked at a longer wavelength to provide the extra bandwidth, which in turn desires a higher injection ratio. Alternatively, the second configuration takes the advantage of the large resonance frequency on the blue detuning side and uses the second stage to compensate the drop in the middle frequencies, thus resulting in an overall wide-bandwidth response. So the first slave laser is locked at a longer wavelength relative to the second one, which requires a higher injection ratio for the first OIL stage. Both configurations show very impressive improvement on the bandwidth enhancement, even though the first one shows larger bandwidth than the second one (66 GHz vs. 50 GHz), but with higher injection ratio too. They open up great flexibility and tunability for COIL to be employed as an effective technique for high-speed applications.

3.3.2 Master-Modulated Cascaded Optical Injection Locking

The previous section demonstrate impressive bandwidth enhancement when the modulation signal is directly applied to the first OIL slave laser stage. Now let's scrutinize the cascaded configuration shown in Figure 3.12 once more. The modulation signal is actually applied to the two VCSELs in slightly different ways. For the first stage, modulation is applied to the slave laser directly through bias current. However, for the second stage, it is actually kept in CW operation, and the modulation signal is provided by the master light. Since no conspicuous difference is seen from the measurement results of the two stages which have different sources of the modulation signal, one would expect that the COIL system would enhance the bandwidth for a completely master-modulated configuration as well.

The revised setup is shown in Figure 3.15. Since the DFB laser used in the experiment is a high-power CW laser, which cannot be directly modulated, a Mach-Zehnder Modulator (MZM) is used to deliver the signal onto the master light which will in turn injection-lock the two VCSELs. The rest of the setup remains the same.

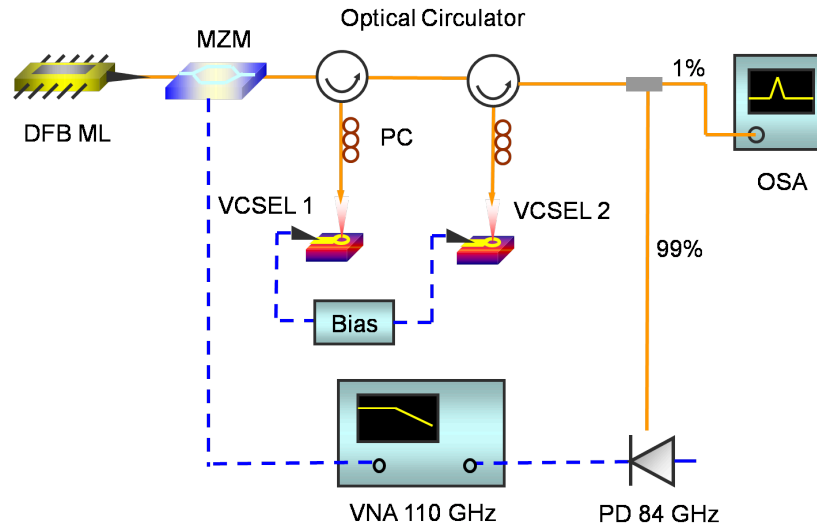


Figure 3.15 Experimental setup of master-modulated COIL. MZM: Mach-Zehnder modulator.

Figure 3.16 shows the frequency response. The dashed dark line shows the link response without any OIL-VCSELs. Since the measurement system and components other than the modulator have a much larger bandwidth, the MZM shows a 3-dB bandwidth of 25 GHz. When the first VCSEL is turned on and injection-locked by the modulated master light, the modulation response is enhanced and bandwidth increases to 36 GHz. Adding a second OIL-VCSEL, the bandwidth is further increased to 47 GHz. The two resonance peaks (first one is more damped) clearly seen in the total frequency response are due the RF amplification from the two shifted VCSEL cavities. The shape of

the resonance peaks and total response can be tailored by adjusting the injection power as well as the detuning values of the two VCSELs as mentioned previously.

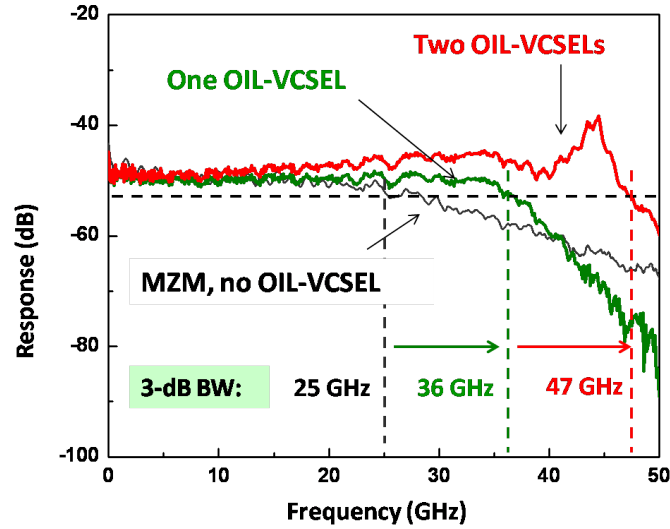


Figure 3.16 Frequency response of master-modulated COIL where signal is from external modulation of the master light. Bandwidth of ~ 47 GHz is achieved using two OIL-VCSELs.

3.3.3 Scaling Using a Daisy Chain Structure

This cascading idea can be simply extended by attaching more slave lasers in a daisy chain structure as long as the master laser has enough power to stably lock the slave laser that has the largest detuning value, as shown schematically in Figure 3.17. If we assume that all the frequency response curves shown in Figure 3.3 (injection ratio dependence) can be cascaded together, it is not hard to imagine that the system has the scaling-up potential to eventually reach ultra-wide band modulation (> 100 GHz).

In such a multi-stage scenario, to further simplify the structure and reduce the size and the cost, the circulators could be possibly replaced by power splitters between different stages. Integration of all the slave lasers on a same chip might be considered as

a more practical solution. For an integrated device, the modulation signal can be applied simultaneously to all the slave lasers rather than only to the first stage. This would provide equal distribution of the RF signal to all the devices, thus avoiding the loss of the signal during transmission from one stage to another. Therefore, the modulation efficiency may possibly be enhanced, especially at high frequencies. There is also no restriction on the laser types for COIL to be implemented even though it is demonstrated on VCSELs. Edge-emitting lasers, or perhaps even micro-ring lasers could also be employed.

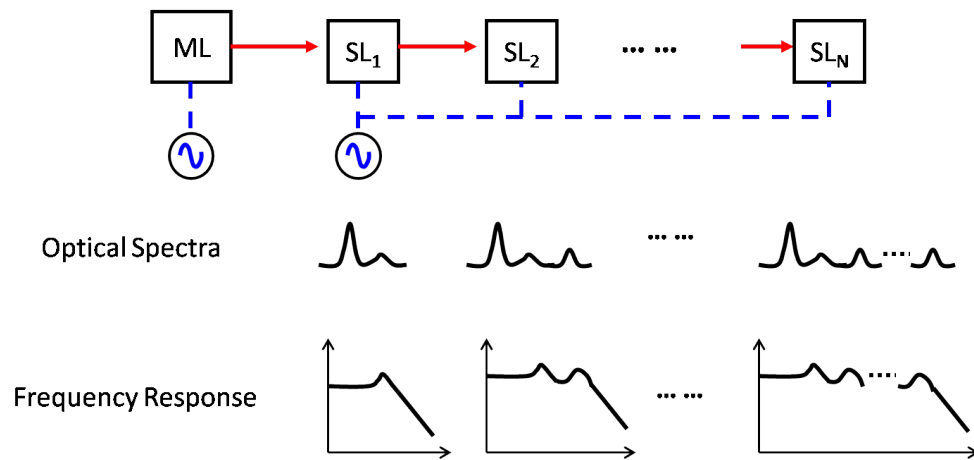


Figure 3.17 Schematic of a multiple COIL transmitter with optical spectra and frequency response shown after each cascaded stage. The modulation signal can be applied to the master laser or directly to the first slave laser only or to all the slave lasers simultaneously for an integrated device. (ML: master laser, SL: slave laser)

Chapter 4

Large-Signal Modulation Characteristics

The development of optical fiber communication, which enables the pervasive accessibility of the Internet, has been revolutionary. Long transmission distance, large data capacity and cost-effective architecture of fiber-optic networks have become necessary features to carry the fast-growing information traffic worldwide. Direct-modulated semiconductor lasers have magnificent advantages over external modulators as a light transmitter because they are 10^7 smaller on size and 10^5 lower on power consumption. Before these devices can be deployed in a data link to transmit digital signals, knowing the large-signal modulation characteristics of them are of great importance in addition to the small-signal frequency response characteristics discussed in the previous chapter. For large-signal modulation, new parameters and figures-of-merit need to be investigated to gauge the device and link performance, such as extinction ratio, dispersion, chirp, bit-error-rate, power penalty etc. In this chapter, we will be focusing on chirp reduction and chirp management on a direct-modulated VCSEL using optical injection locking. Some of the other issues will be addressed in Chapter 6 when digital applications are discussed.

In digital fiber-optic network, high bit rate (data transmission speed) and long transmission distance (without an amplifier) are always desired at the same time. However, the physics that governs the modulated light transmitting through fibers,

unfortunately, does not allow high bit rate and long distance to be achieved simultaneously on a directly modulated laser because of chromatic dispersion from the glass fiber and frequency chirping from the device [46-48]. Chromatic dispersion or more precisely group-velocity dispersion (GVD) in a lightwave system is caused by a variation in the group velocity of an optical pulse in a fiber with changes in the optical frequency. In 1550-nm standard single-mode fiber (SSMF), the short wavelength (blue) components of the pulse travel faster than the longer wavelength (red) components. In short-reach networks, to construct a cost-effective high-speed infrastructure, direct-modulated semiconductor lasers, especially VCSELs, are often deployed as data transmitters, which will generate optical pulses with positive frequency chirp – optical frequency shifts to blue on the rising edge, while red on the falling edge [46-48]. Therefore, such a pulse broadens rapidly as it travels down a 1550-nm SSMF due to GVD, and by the time it reaches the receiver, it may have spread over several bit periods and causes detection errors as illustrated in Figure 4.1.



Figure 4.1 Input pulse with positive chirp will be broadened monotonically as it propagates along 1550-nm standard single-mode fiber (SSMF), because high frequency (blue) components travel faster than low frequency (red) components. Transmission distance is severely limited by pulse broadening.

There are multiple ways to amend this problem, such as different techniques applied to the transmitter, the transmission link (fiber), and the receiver. Dispersion compensation on the link employs dispersion-shifted or dispersion-compensated fiber [49, 50], and

compensation on the receiver is typically accomplished by electronic equalization techniques [51]. For the transmitter, external modulator has been used as an alternative to impose data onto the light carrier despite their bulky size and high cost; pre-chirp techniques using modified modulation formats are also demonstrated [52, 53]; and chirp-managed direct-modulated laser (CML) has recently drawn great attention with their longest transmission distance (> 200 km) reported [54]. It was also demonstrated that optical injection locking could also effectively reduce laser frequency chirping under direct modulation [55, 56]. In this chapter, we will examine the origin of laser frequency chirping, and explore how OIL can help reduce chirp and even change the polarity of chirp to serve the pre-chirp function.

4.1 CHIRP REDUCTION

4.1.1 Frequency Chirping of Semiconductor Lasers

Since frequency chirping exhibits universally for all kinds of semiconductor lasers and severely limits the transmission distance of direct-modulated laser, studies on the origin of chirp dated back to the mid 80s [46-48]. This can be understood by the schematic illustration in Figure 4.2. If the current of a diode laser is modulated by a certain data pattern, the carrier density, which is pumped up by the current, follows the same pattern accordingly. Therefore, the light intensity generated by carrier radiative recombination will also follow the data pattern. However, due to the linewidth enhancement factor of the semiconductor material, the refractive index is coupled to the carrier density, hence the carrier density modulation will result in the index modulation which eventually leads to the residual frequency modulation known as chirp. A thorough

study [57] on semiconductor laser dynamics including the nonlinear gain effect shows that chirp consists of two terms

$$\Delta\nu(t) = \frac{\alpha}{4\pi} \left(\frac{d}{dt} \ln P(t) + \kappa P(t) \right), \quad (4.1)$$

where $\Delta\nu$ is frequency chirp, P is laser power, κ is the a function of the gain compression factor [29]. The first term in Eqn (4.1) represents the transient chirp, which is associated with the fast rising and falling edge of the signal, while the second term represents the adiabatic chirp, which is caused by the nonlinear gain effects, such as carrier heating and spectral hole burning, and determined by the absolute power level. If the intensity waveform is overlaid with the chirp waveform as shown in Figure 4.2, it is seen that positive frequency deviation is on the rising edge while the negative frequency deviation is on the falling edge. By definition, this is known as positive chirp, which is detrimental for transmission as explained in the beginning of the chapter.

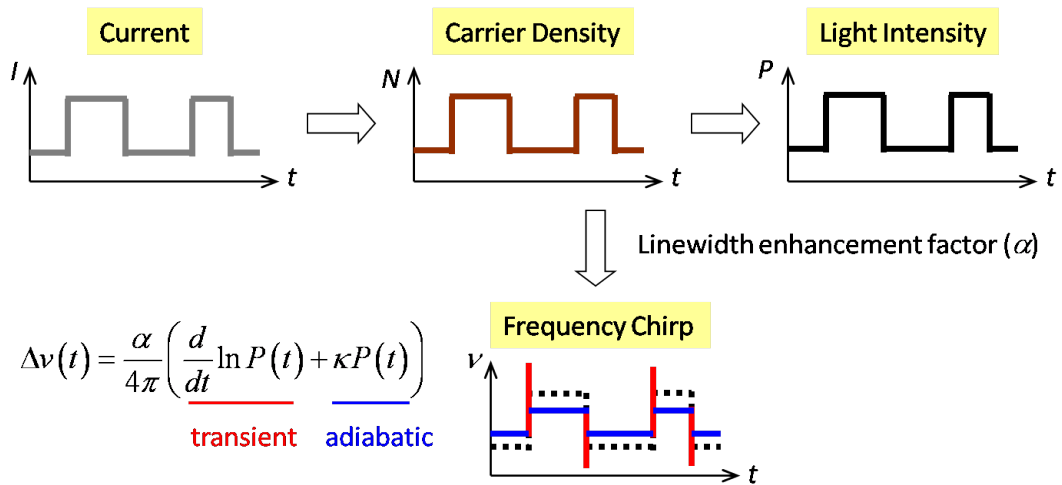


Figure 4.2 Frequency chirping of semiconductor lasers. Positive chirp exhibits for all types of semiconductor lasers due to the existence of linewidth enhancement factor.

4.1.2 Chirp Reduction by OIL

Injection locking was demonstrated to reduce the frequency chirp for a direct amplitude-modulated laser [55, 56]. This technique provides another way to minimize the dispersion penalty without increasing complexity of the laser design. In addition, both the master and the slave laser can be driven with similar electronics without high-power consumption, which greatly simplifies the design of the circuits, hence reduces the cost of the transmitter modules for digital data links.

We start off with an analytical expression of chirp from the OIL rate equations introduced in Chapter 2 to gain a simple and insightful understanding on chirp reduction caused by injection locking. If one recalls the phase equations (2nd in Eqn set 2.9), $d\phi/dt$ on the left hand side of the equation represents frequency of the OIL laser. Therefore, frequency fluctuation – chirp – can be revealed by properly manipulating the terms in this equation. If one arranges terms in Eqn (2.9a), the photon number equation, to express the gain term using other terms, one obtains

$$\frac{G_0(N - N_{tr})}{1 + \epsilon S} - \frac{1}{\tau_p} = \frac{1}{S} \frac{dS}{dt} - 2\kappa \sqrt{\frac{S_{inj}}{S}} \cos \phi(t) \quad (4.2)$$

Plug Eqn (4.2) into Eqn (2.9b), the phase equation, and the expression for chirp of an OIL laser is shown below

$$\nu = \frac{d\phi}{dt} = \frac{\alpha}{2S} \frac{dS}{dt} - \kappa \sqrt{\frac{S_{inj}}{S}} [\alpha \cos \phi(t) + \sin \phi(t)] - \Delta\omega \quad (4.3)$$

Compare Eqn (4.3) with Eqn (4.1), it is interesting to see that the adiabatic chirp term disappears, and there are extra two terms introduced by OIL, however, with opposite signs to the transient chirp. At a first glance, this indicates that OIL induced frequency

change may always reduce the transient chirp, and even completely cancel it out if proper locking condition is chosen. However, notice that detuning value can be either positive or negative. $\phi(t)$ is also a function of both injection ratio and detuning, as discussed in Chapter 2, roughly ranging from $-\pi/2$ to 0. Therefore, the situation is more complex than it seems to be. Chirp reduction will be achieved when proper locking condition is chosen.

In addition, a hand-waving explanation of chirp reduction induced by OIL can be provided. As mentioned in Chapter 3, the injection-locked laser becomes a gain-clamped amplifier. Since the gain level, hence the carrier density of the slave laser is clamped by the external injected light (stimulated emission), the fluctuation of the carrier density due to the current modulation will be reduced. Therefore, the index variation, which is the source of chirp, will also be reduced. An even simpler understanding would be attained from the frequency locking perspective. Since the slave laser is frequency-locked to a CW master laser, the frequency fluctuation of the slave laser will be much reduced and stabilized to it of the master laser.

Numerical simulation using OIL rate equations shows chirp reduction [56]. Experiments on time-resolved chirp measurement concur with the simulation results. Figure 4.3 shows data amplitude waveform as well as chirp waveform at 10 Gb/s on the same plot for a VCSEL in both free-running and injection-locked condition. The scale on the right for chirp is the same for both figures. It is very clear in Figure 4.3(b) that the adiabatic chirp is completely removed as predicted by Eqn (4.3) and the transient chirp is reduced by 10X when OIL is applied. Also notice that positive chirp is measured for the

free-running device as the rising / falling edge has positive / negative frequency deviation, which is consistent with Eqn (4.1).

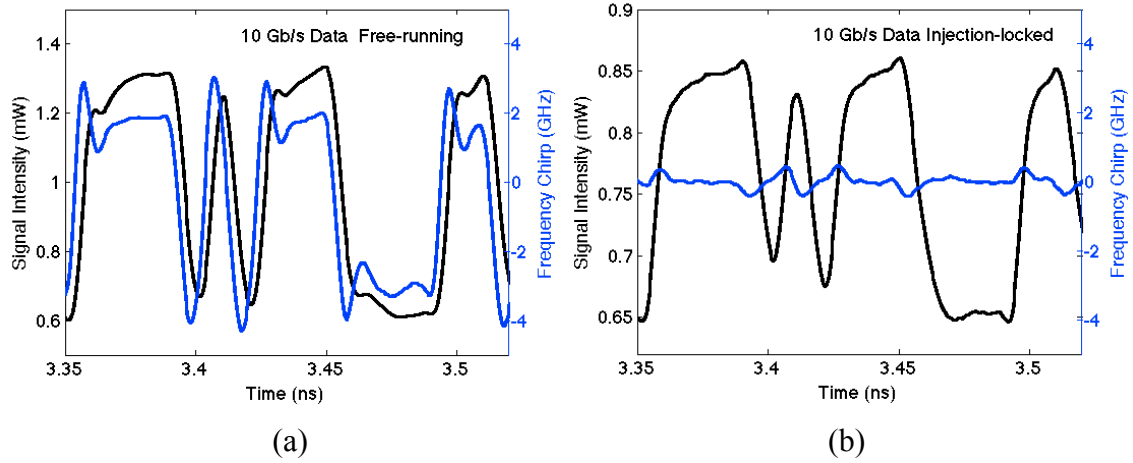


Figure 4.3 Signal amplitude (black) and chirp (blue) waveforms at 10 Gb/s for (a) free-running VCSEL and (b) injection-locked VCSEL. Chirp data plotted on the same scale for both figures on the right. OIL removes adiabatic chirp and reduces transient chirp by 10X.

Optical spectra of the VCSEL under 10 Gb/s large-signal modulation with and without OIL are also measured and shown in Figure 4.4. The VCSEL bias current is optimized at 5.5 mA for free-running and 2.5 mA for OIL. The much broader and asymmetric free-running spectrum indicates the large dominant adiabatic chirp and the unbalanced transient chirp as seen previously in Figure 4.3(a). With injection locking, the spectrum is greatly narrowed due to the chirp reduction. The locked wavelength is also blue-shifted to the master wavelength.

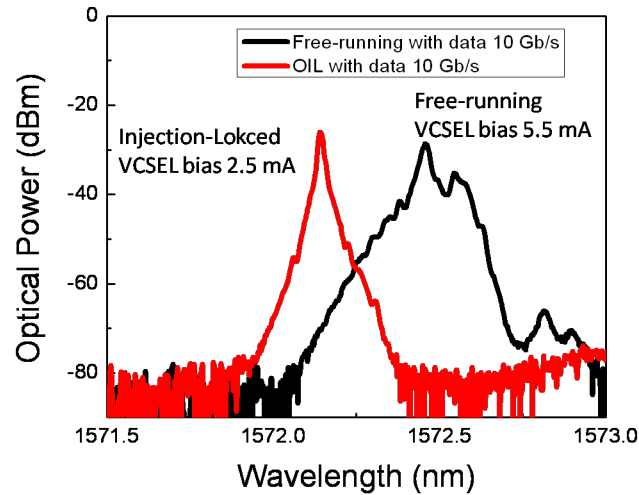


Figure 4.4 Optical spectra of both free-running and injection-locked VCSEL under 10 Gb/s large-signal modulation.

4.2 DATA PATTERN INVERSION AND NEGATIVE CHIRP

Positive chirp interacts with fiber chromatic dispersion constructively so that the transmission distance is limited by the broadening of the optical pulse. However, if the optical pulse can be processed to possess a negative chirp – optical frequency shifts to red (low frequency) on the rising edge, while blue (high frequency) on the falling edge, an optimal transmission distance will appear as the negative chirp compensates the GVD to compress the pulse in the initial transmission stage along the fiber. As shown in Figure 4.5, after passing over the optimal distance where maximum compression occurs, the pulse will be broadened as it propagates, but the overall transmission distance is substantially enhanced. This approach is widely known as the pre-chirp scheme that modifies the characteristics of the input pulses at the transmitter before they are launched into the fiber link. This section discusses how OIL can help obtain negative chirp in order to lengthen the transmission distance.

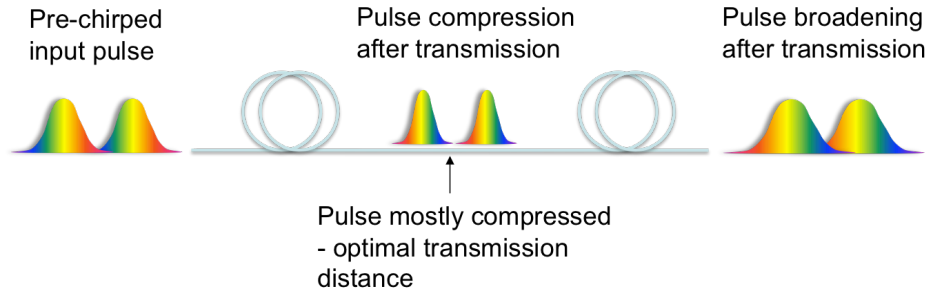


Figure 4.5 Concept of pre-chirping using negative-chirped pulse that can compensate fiber dispersion till the optimal distance is reached, where the pulse is mostly compressed. Transmission distance can be greatly enhanced by employing pre-chirp technique.

4.2.1 Pre-Chirp Using Data Pattern Inversion

According to the definition of negative chirp – negative frequency deviation on the rising edge, while positive frequency deviation on the falling edge, one straightforward and simple way to attain it is to invert the intensity modulation signal pattern without changing the carrier modulation. By doing so, the rising and falling edge of the signal is flipped, while the frequency modulation stays the same. This is illustrated in Figure 4.6, which is similar as Figure 4.2 but with an inverted intensity waveform.

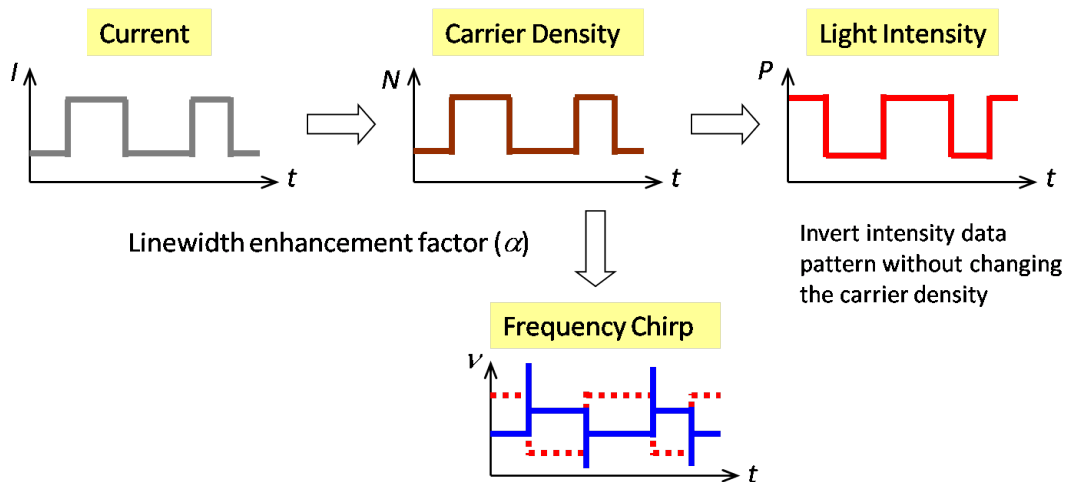


Figure 4.6 Negative chirp can be obtained by inverting intensity modulation signal pattern without changing carrier modulation.

4.2.2 OIL-Induced Data Pattern Inversion

To understand how OIL can help achieve intensity data pattern inversion independently, one needs to revisit the reflection spectrum of a VCSEL amplifier. If a set of reflection spectra at various bias current levels is observed at a fixed wavelength as shown in Figure 4.7, an electrical-to-optical transfer function can be extracted from Figure 4.7 by plotting the reflectivity (power ratio between the reflected and the incident light) at a fixed wavelength versus the bias current, shown in Figure 4.8. It is obvious that if a VCSEL amplifier is biased in the gain regime and under direct current modulation, the optical output will also be modulated following the signal pattern according to a positive slope on the transfer function, but inverted if the VCSEL amplifier is operated in the loss regime with a negative slope. When the data pattern is inverted, rising edge becomes falling edge and vice versa. However, the chirp polarity stays unchanged as the frequency transient follows the carrier density change that is determined by the current modulation. As a result, negative chirp can be obtained through data pattern inversion when a VCSEL amplifier is in the loss regime.

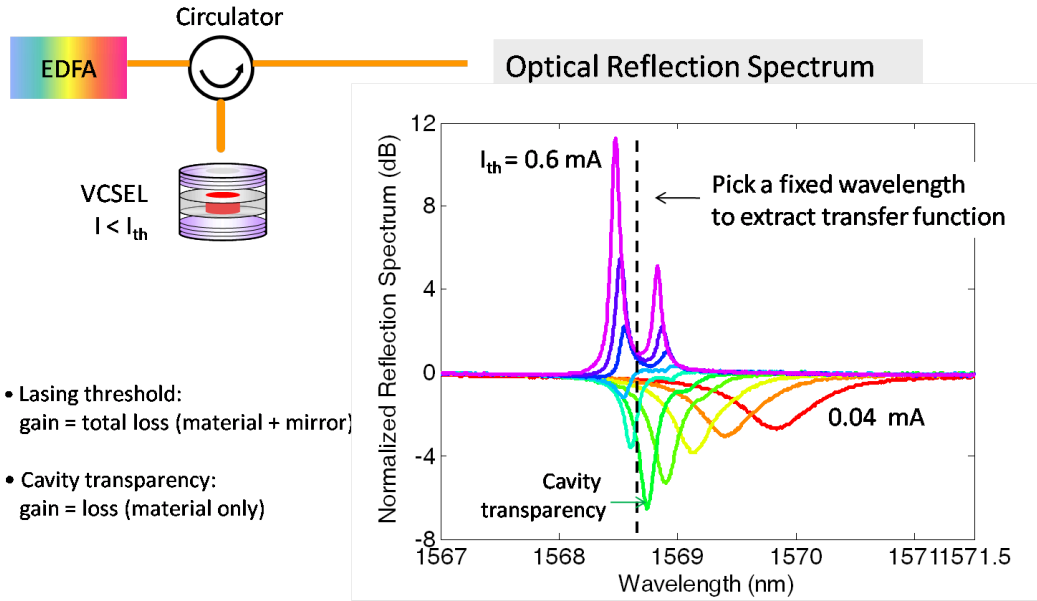


Figure 4.7 VCSEL amplifier reflection spectra at various bias levels. If all spectra are considered at a fixed wavelength (dashed line), an electric-to-optical transfer function (reflection output vs. bias current) can be obtained.

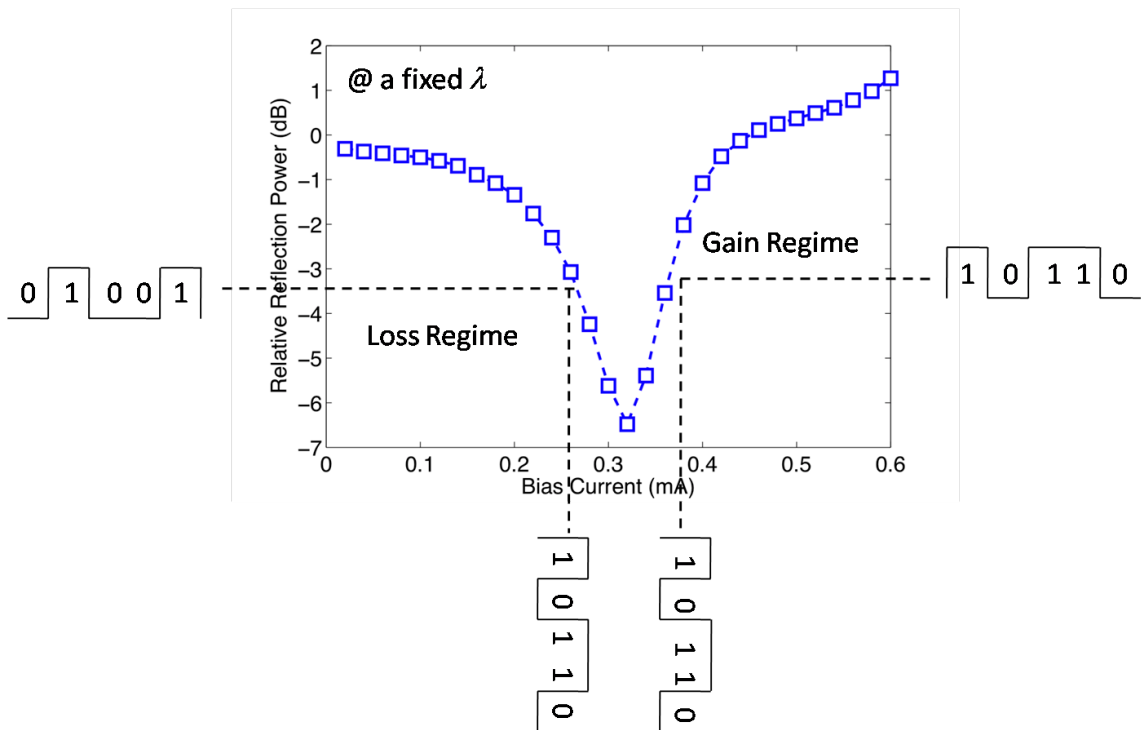


Figure 4.8 Electric-to-optical transfer function extracted from Figure 4.7. Inversion occurs in the loss regime.

However, the VCSEL amplifier itself cannot be used as a transmitter because it is not lasing. To fulfill the pre-chirp function by a VCSEL amplifier, OIL can be applied so that the master light will carry the modulation signal by interacting with the VCSEL cavity, and the VCSEL itself becomes a gain-clamped detuning-controlled amplifier as previously shown in Chapter 2. In addition, detuning dependence shows that the gain level of an OIL VCSEL amplifier is reduced as the master laser wavelength is red-tuned (toward longer wavelength). So the gain-loss regime of an OIL VCSEL can be selected by changing the wavelength detuning ($\lambda_{\text{master}} - \lambda_{\text{VCSEL}}$), thus controlling the phenomenon of data inversion. Detuning-controlled inversion is characterized experimentally by modulating the OIL VCSEL with a 2.5-Gb/s square pulse train and measuring the output at different detuning values as shown in Figure 4.9. The waveform from a free-running VCSEL is shown as a reference. As expected from the VCSEL amplifier characteristics discussed previously, the data pattern goes through a transition from a non-inverted to an inverted state as the wavelength detuning increases (master laser tuned to red) from 0 to 0.34 nm. The spikes appearing on the transition waveform (detuning = 0.2 nm) are induced by the transient chirp associated with the rising and falling edge of the pulse.

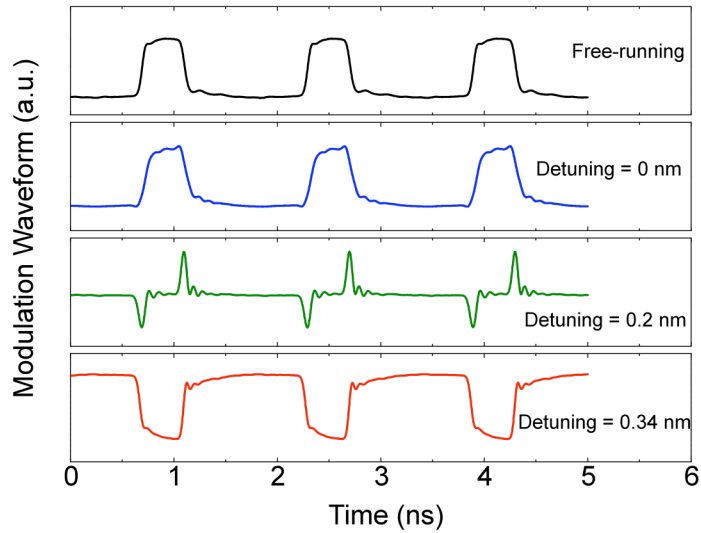


Figure 4.9 Experimentally measured square wave showing detuning-controlled inversion phenomenon of an OIL VCSEL. Free-running VCSEL waveform is also shown as a reference. Transition from non-inversion to Inversion occurs at detuning of 0.2 nm.

A hybrid model combining injection-locking rate equations and a Fabry-Perot amplifier structure to describe the OIL dynamics and the resonance frequency enhancement is established in Chapter 3. Since the data pattern inversion also originates from the amplifier nature of an OIL VCSEL, same model (Eqn 3.2) can be adopted to simulate the phenomenon. Figure 4.10 shows the simulated modulation waveforms imposed on the VCSEL gain as well as the light output at three different detuning conditions, which are in excellent agreement with the experimental results in Figure 4.9.

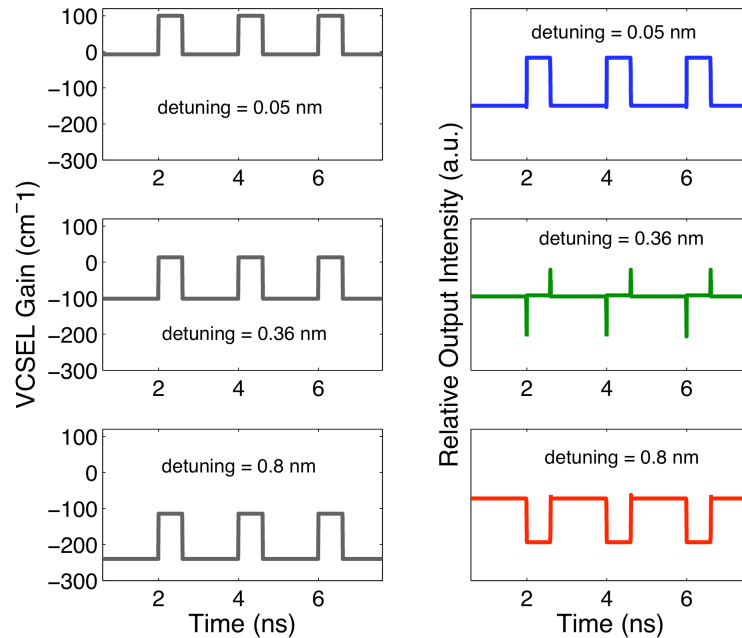


Figure 4.10 Simulated modulation output of an OIL VCSEL at various wavelength detuning values using the hybrid model combining OIL rate equations and a Fabry-Perot amplifier structure as shown in Chapter 3. Modulation on VCSEL gain is also shown on the left to illustrate the gain/loss regime that the VCSEL amplifier is in as detuning varies. See Appendix A1.5 for MATLAB code.

To further prove the signal pattern inversion is closely related to the gain/loss regime of the VCSEL amplifier, a simple experiment that one can conduct is to gradually displace the coupling lensed-fiber in the horizontal plane to misalign the master light and the VCSEL active region. This spatial-dependent gain was previously studied on a multi-transverse-mode VCSEL to realize the function of a nonlinear switch [58]. The experiment is visually illustrated in Figure 4.11(a). Again, the VCSEL is directly modulated by a data sequence at 2.5 Gb/s. The measured waveforms from both free-running and injection-locked conditions are shown in Figure 4.11(b). The lensed-fiber is initially well aligned with the laser aperture. And when the VCSEL is injection-locked,

the detuning is adjusted so that the device is in the gain regime. When the lensed-fiber is in the center location (i), where the active area is located so the gain is large, the signal waveform is found non-inverted. As the lensed-fiber is moving away from the center to location (ii), the gain is then reduced, and the signal waveform turned into a transition stage. Finally when the lensed-fiber is moved even further into the loss region to location (iii), data inversion occurs. This experiment then verifies that the data inversion indeed is determined by and can even be controlled by the VCSEL amplifier gain level.

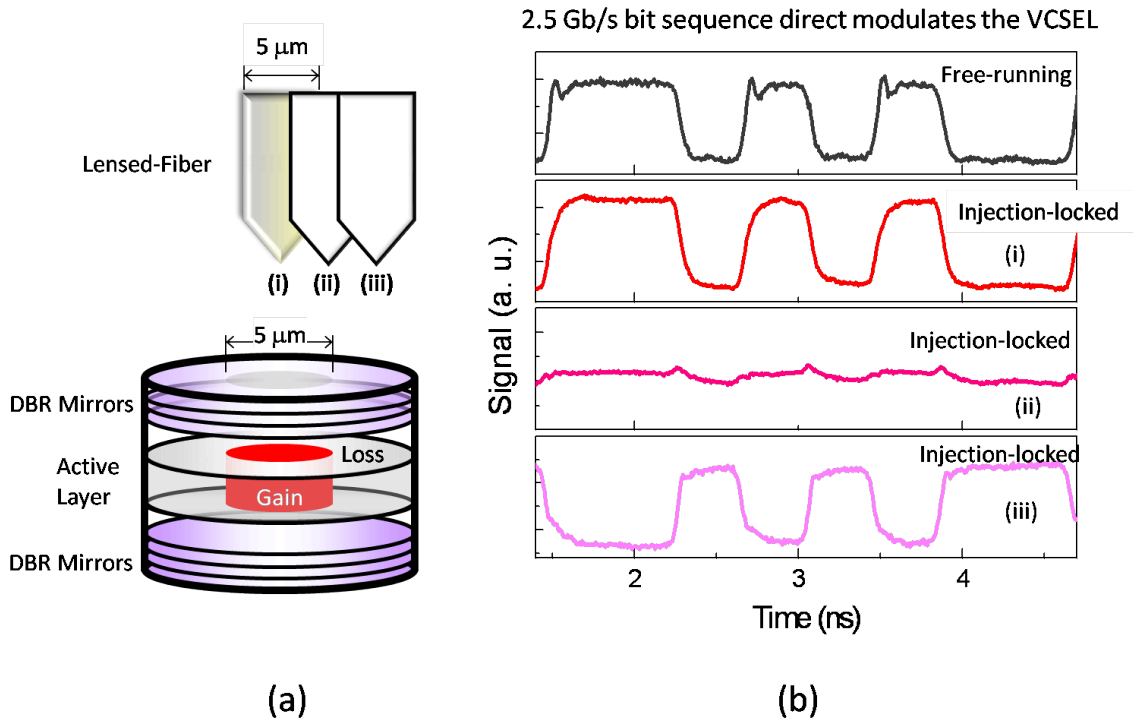


Figure 4.11 Inversion occurs at horizontal displacement of the coupling lensed-fiber that changes the gain/loss regime of the VCSEL. The VCSEL is directly modulated at 2.5 Gb/s and the detuning is adjusted to the blue side to have minimum carrier reduction. (a) Experimental setup. (b) Measured waveforms for both free-running and injection-locked conditions with lensed-fiber at different locations (i), (ii) and (iii).

4.2.3 Negative Chirp

Therefore, associated with the inverted data pattern, negative chirp is expected and can be verified by measuring time-resolved frequency deviation. The VCSEL is directly modulated by 10 Gb/s pseudo-random bit sequence (PRBS). The Advantest Q7606B chirp-form analyzer is used together with a sampling oscilloscope to obtain the time-resolved chirp waveforms and the intensity waveforms. Figure 4.12 shows the results for both free-running (top) and injection-locked (bottom) condition. The detuning value is adjusted so that data pattern inversion occurs.

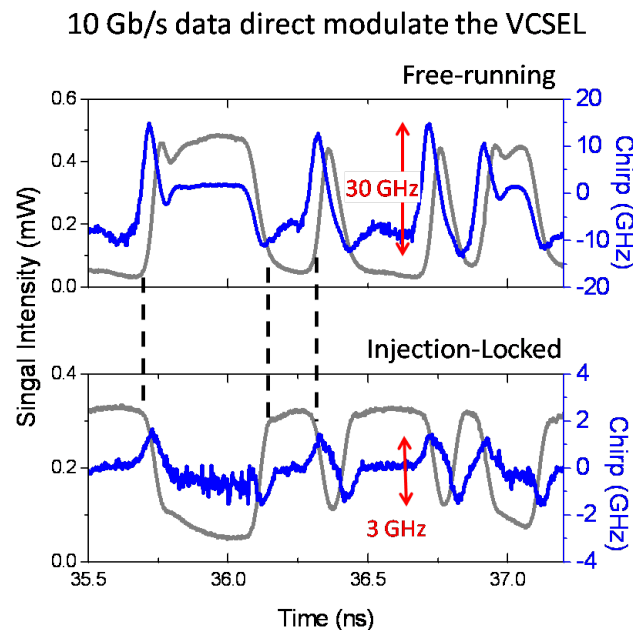


Figure 4.12 Time-resolved chirp waveforms and the intensity waveforms for a free-running (top) and injection-locked (bottom) VCSEL. The detuning is adjusted so that pattern inversion occurs. Negative chirp obtained in OIL case and peak-to-peak chirp is reduced by 10X.

Again, the adiabatic chirp is removed when the VCSEL is injection-locked, and the peak-to-peak transient chirp is reduced from 30 GHz to 3 GHz – 10X smaller. The chirp scale on the right for the OIL case is intentionally zoomed in so that one could see

negative chirp due to pattern inversion – now the falling edge has a small amount of positive frequency shift, while the rising edge has a small amount of negative shift.

Another way of presenting the same data is to use spectrogram. It is a two-dimensional contour plot with chirp and time being the vertical and the horizontal axis, respectively, and the color map is the intensity. A spectrogram of two consecutive bits output from a VCSEL is shown in Figure 4.13. In Figure 4.13(a), for a free-running VCSEL, the leftward skew of the two pulses indicates strong positive frequency chirping of more than 10 GHz. In Figure 4.13(b), however, when the VCSEL is injection-locked, the bits are inverted, shown by the inversion of the color distribution, and the peak-to-peak chirp is reduced to smaller than 1 GHz (same scale used in this case to emphasize the reduction). A slight rightward skew on the middle pulse represents a negative chirp.

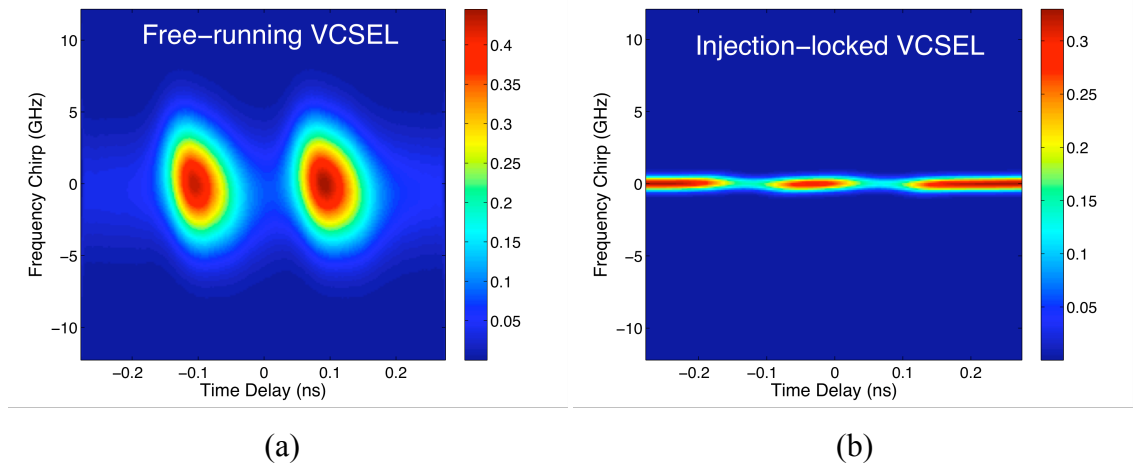


Figure 4.13 Spectrogram of two consecutive bits from a pseudorandom bit sequence (PRBS) at 10 Gb/s output from a VCSEL. Color map represents signal intensity. (a) Free-running VCSEL. Large positive frequency chirp is indicated by the leftward skew of the bits. (b) Injection-locked VCSEL. Detuning is adjusted so that data inversion occurs. Total peak-to-peak chirp is greatly reduced. A slight right skew indicates negative chirp. See Appendix A1.6 for MATLAB code.

Since adiabatic chirp no longer exists in an injection-locked laser, transient chirp becomes dominant. To further reduce the peak-to-peak transient chirp, injection ratio can be used as a tuning knob. Fig. 4.14(a) shows the intensity and chirp waveform when the VCSEL is free-running as a reference, while (b-d) show it is injection-locked at various injection ratios.

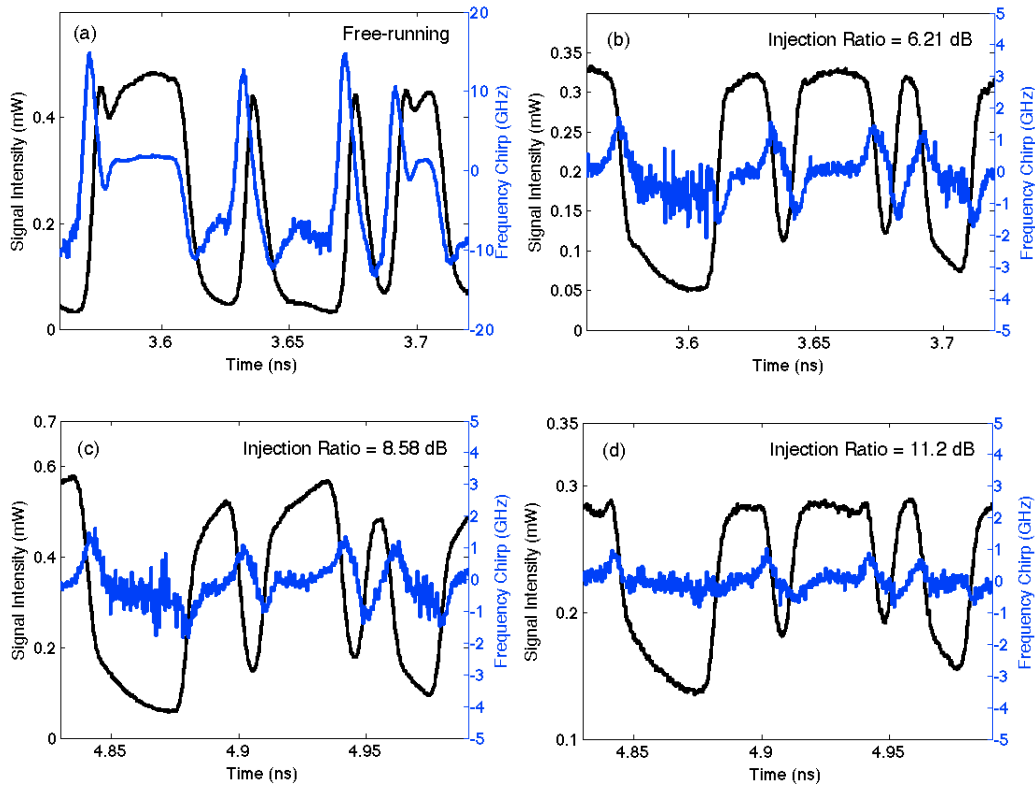


Figure 4.14 Experimental measurement of time-resolved chirp and intensity waveforms at 10 Gb/s for (a) free-running VCSEL, (b-d) OIL VCSEL with injection ratios of (b) 6.21 dB (c) 8.58 dB (d) 11.12 dB. Transient peak-to-peak is reduced from (a) 30 GHz to (b) 3.1 GHz (c) 2.7 GHz (d) 1.55 GHz as injection ratio increases.

The data patterns are all inverted when it is injection-locked even with different injection ratios. By adjusting the power of the DFB laser and the coupling to the VCSEL, the injection ratio is set to 6.21 dB, 8.58 dB and 11.12 dB, the peak-to-peak chirp is

reduced from ~ 30 GHz (free-running) to 3.1 GHz, 2.7 GHz and then 1.55 GHz, respectively. This can be understood from the fact that strong light injection reduces the carrier density change and thus the index variation during the same transition time, as compared to weak injection.

Figure 4.15 quantifies the peak-to-peak chirp tunability as a function of the injection ratio. The chirp can be reduced to half of its original value by increasing the injection ratio from 6.21 dB to 12.07 dB. However, a tradeoff exists between the chirp and the extinction ratio of the signal. The degradation of the extinction ratio is inevitable at strong injection conditions due to the surface normal geometry of the VCSEL, which couples the CW reflection of the injection light to the output. Therefore, the injection ratio needs to be optimized by considering both chirp and extinction ratio.

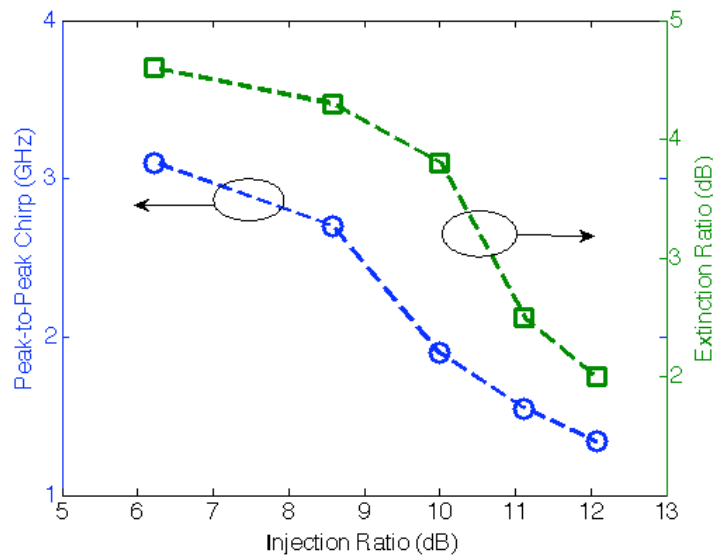


Figure 4.15 Peak-to-peak chirp and extinction ratio at 10-Gb/s as functions of injection ratio. Injection ratio needs to be optimized due to the trade-off between the two.

4.2.4 Transmission Distance Enhancement

In order to demonstrate the benefit of the tunable negative chirp, we can perform chromatic dispersion tolerance comparison between free-running and OIL VCSELs by transmitting 10-Gb/s signals through SSMF with variable lengths. Figure 4.16 shows the experimental setup. Injection locking is performed using the same apparatus as before. The VCSEL current is directly modulated by a bit-error-rate testset (BERT) at 10-Gb/s, with a $2^{15}-1$ PRBS. Both the VCSEL bias and the data driving voltage are optimized. The DFB current is adjusted to control the power injecting into the VCSEL. Chromatic dispersion is emulated using variable lengths of SSMF spools with EDFAs in between. Link power is kept below 3.5 dB to avoid any nonlinearity in the fiber. A preamplified receiver and an error detector are used for BER quantification of the signal with and without fiber transmission. The Advantest Q7606B chirp-form analyzer is also used to monitor the chirp performance.

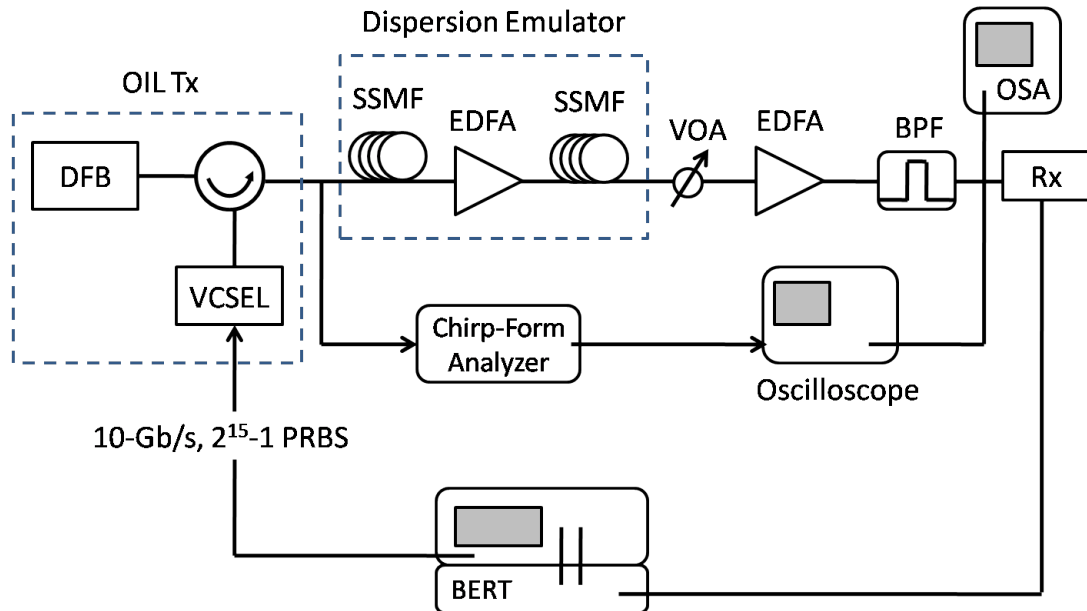


Figure 4.16 Experimental setup for testing transmission performance. (Tx: transmitter, VOA: variable attenuator, BPF: band-pass filter, Rx: receiver.)

Figure 4.17 shows the bit error rate (BER) measurements of an OIL VCSEL at 10 Gb/s. A typical transmission performance metric is the minimum optical power required at the receiver to achieve bit error rate (BER) of 10^{-9} (one error out of a billion bits) or so-called error-free detection, hence the power is also defined as error-free receiver power. In Figure 4.17, after 25-km SSMF transmission, the power penalty (extra receiver power required to achieve error-free detection) reduction reaches its maximum and a 4-dB penalty improvement is achieved at a BER of 10^{-9} . Even 100-km SSMF transmission shows no penalty for a BER of 10^{-9} . These results can be explained by the fact that negative frequency chirping interacts beneficially inside the SSMF as Figure 4.5 illustrated. The pulse initially narrows as it propagates inside the fiber and reaches a minimum width at a certain distance (25-km in this case). After that, the pulse starts to broaden due to the onwards dispersion. The three eye diagrams measured at error-free receiver power in Figure 4.17 clearly show pulse compression after 25-km transmission and distortion after 100 km.

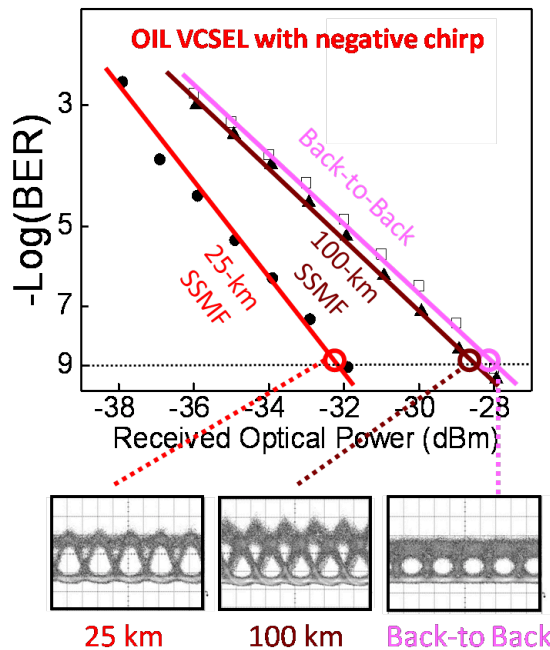


Figure 4.17 Bit-error-rate measurements and error-free eye diagrams of an OIL VCSEL after back-to-back, 25-km and 100-km SSMF transmission.

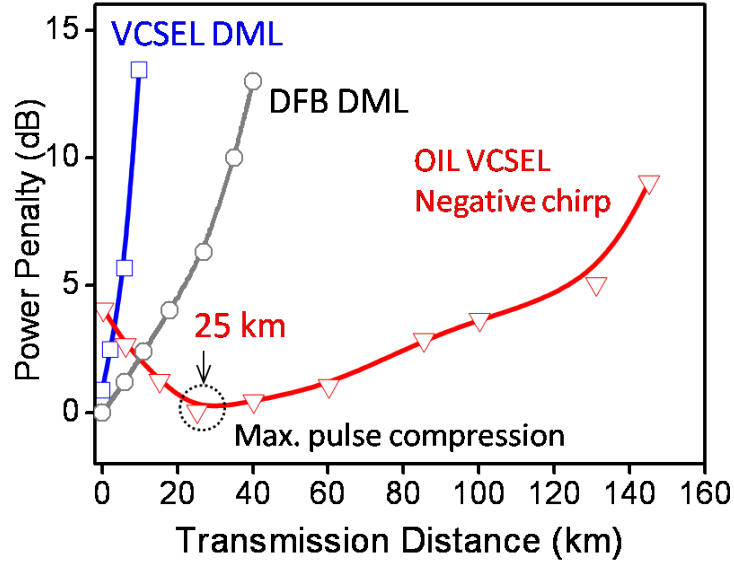


Figure 4.18 Power penalty versus SSMF transmission distance for a free-running VCSEL, a commercial DFB DML and an OIL VCSEL. More than 10X transmission distance is obtained on the OIL VCSEL with negative chirp.

Figure 4.18 quantifies the power penalty with increased SSMF distance for a free-running VCSEL, a DFB laser and an injection-locked VCSEL with negative chirp. Due to the large positive chirp, the 10-Gb/s free-running VCSEL can transmit no more than 5 km with more than 4-dB power penalty. Even for a 10-Gb/s commercial DFB direct-modulated laser (DML) with standard positive chirp, the transmission distance is still limited to be less than 20 km for a 4-dB power penalty. In reality, where the total available power of a network is usually fixed, 2-dB increase in error-free receiver power implies 10-km transmission distance reduction due to fiber attenuation with a coefficient of 0.2 dB/km. For injection-locked VCSELs, even though there is some back-to-back

penalty (due to extinction ratio degradation), the signal is actually regenerated because of the negative chirp, and there is no observed penalty after 125-km of uncompensated SSMF transmission. This performance is more than 10X better than that of a free-running VCSEL or a DFB DML [59].

Chapter 5

Analog Applications of Injection-Locked VCSELs

Other than employed in digital optical fiber communication systems, semiconductor lasers find many applications in analog system as well, just name a few, such as radio-over-fiber (RoF) [60], CATV [61], RF photonics and optical signal processing [62] and so on. Typically very stringent requirements are set for analog applications, because a faithful reproduction of the signal is desired for any process with less tolerance on either distortion or noise. As one could imagine, OIL can also help improve the device performance for these various analog systems. In this chapter, we will first discuss injection-locked VCSELs as transmitters for analog fiber-optic links, with emphases on important figures-of-merit such as RF link gain, distortion and noise. Then we will demonstrate a novel approach using injection-locked VCSEL to create optoelectronic oscillators that generates high frequency microwave signal with high spectral purity. Finally, we close the chapter with an interesting slow light effect found in a master-modulated injection-locking scheme, which generates detuning-controlled RF delays over a full range of 2π .

5.1 MICROWAVE PERFORMANCE FOR ANALOG FIBER-OPTIC LINK

For analog fiber-optic transmission, optical transmitters are usually demanded to have high modulation bandwidth, a high RF link gain, negligible distortion and low

noise. External optical modulators are typically used for high-performance links. This solution, though effective, is costly and bulky. In contrast, directly modulated lasers are more desirable on these two accounts. In particular, VCSELs are very promising for applications where low cost, small size, and low power dissipation are required as much as high signal fidelity. However, directly modulated lasers, including VCSELs, suffer from high distortion near the resonance frequency and can, therefore, only be used at low RF frequencies around 1 GHz [63]. Both the distortion and the intensity noise of a semiconductor laser physically originate from the nonlinear characteristics of the laser, dominated by the carrier–photon interaction, which is also the origin of the laser resonance frequency. Therefore, to avoid performance degradation due to this phenomenon, it is desirable to have the laser resonance frequency greatly exceed the highest RF frequency of use. The modulation frequency response of a diode laser is determined by the rate at which electrons and holes recombine at the laser junction (carrier lifetime), and the rate at which photons are generated and escape from the laser (photon lifetime). To increase the resonance frequency beyond the frequency range in use by most of the applications (0 ~ 60 GHz), optical injection locking could be an effective method for improved microwave performance since it can drastically enhance the laser resonance frequency as demonstrated in Chapter 3. In this section, we conduct a systematic and comprehensive study of the microwave performance of an OIL VCSEL based on various figures-of-merit mentioned above. Since Chapter 3 is dedicated to resonance and bandwidth enhancement, attentions will be put on other parameters.

5.1.1 RF Gain

De-embedded frequency response at detuning values over a full spectrum of locking range at a fixed injection ratio is shown in Figure 5.1. It is interesting to note that very large modulation efficiency (RF gain) enhancement is attained at low frequencies close to DC for large wavelength detuning values (master tuned towards the red). This phenomenon was never predicted by theory before. Experimentally, the larger the $\Delta\lambda$ is, the larger the gain is. Typically, the modulation efficiency of a free-running 1.55- μm VCSEL is $0.2 \sim 0.3$ W/A. For a large injection ratio (14 dB), the low-frequency RF gain enhancement is up to 20 dB at large positive detuning (1.25 nm showing in Figure 5.1), resulting in a modulation efficiency of 2.2 W/A, or an equivalent 2.75 photons generated per electron-hole pair due to the stimulated emission from the external light injection. Under a fixed injection ratio, the RF gain varies with detuning. The minimal value is at a blue detuning associated with frequency response showing a sharp resonance peak. On the other hand, the maxima RF gain is obtained at red detuning accompanied by frequency response highly damped. Hence, there exists a trade off between the resonance frequency and RF gain.

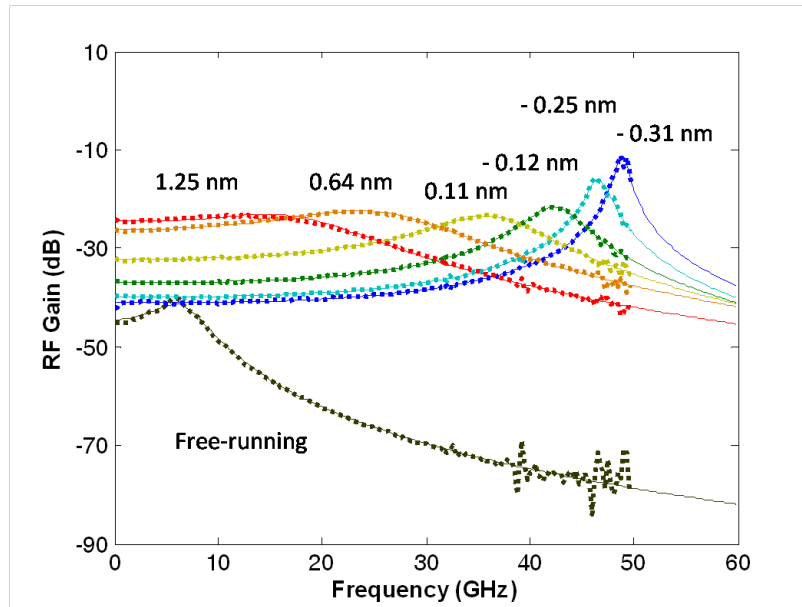


Figure 5.1 De-embedded frequency response of an OIL VCSEL at various detuning values. RF gain up to 20 dB is obtained when the master laser is red-detuned.

Figure 5.2 shows the low-RF gain as a function of wavelength detuning studied on different devices. The correlation between RF gain enhancement and wavelength detuning is clearly visible. Furthermore, the maximum RF gain enhancement obtained at the red edge of the locking range keeps increasing with increasing the injection ratio. Figure 5.3 shows this enhancement versus injection ratio.

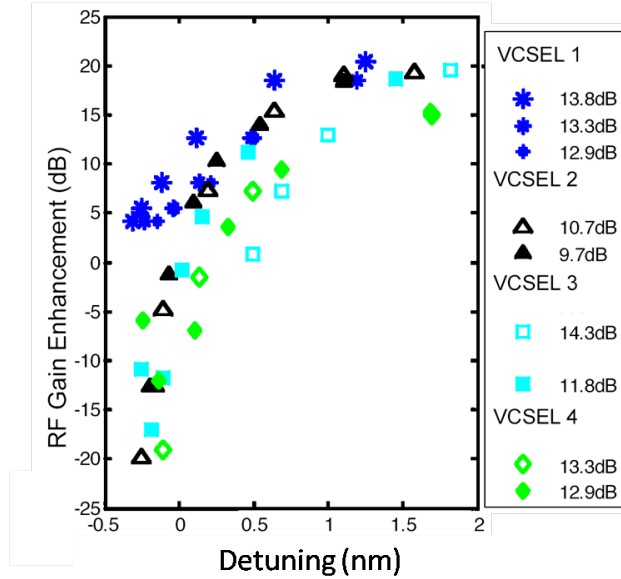


Figure 5.2 RF gain measured at 1 GHz for four different VCSELs vs. wavelength detuning. 20-dB RF gain is found for large detuning cases. (FR: free running, decibel values are injection ratios).

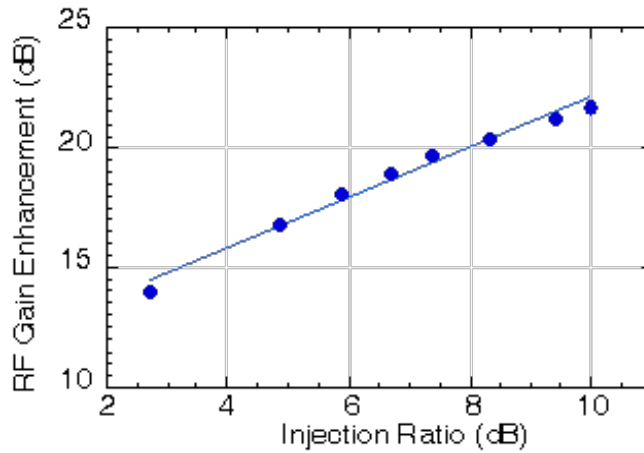


Figure 5.3 Maximum RF gain enhancement vs. injection ratio for an OIL VCSEL.

If we combine the dependence on both the detuning value and injection ratio, the RF gain can also be plotted on the stability plot shown in Figure 5.4. It was measured for a small-signal input of -20 dBm at 1 GHz. A high-RF link gain at low frequencies can be

obtained when operating the OIL laser in the strong injection regime with red detuning values.

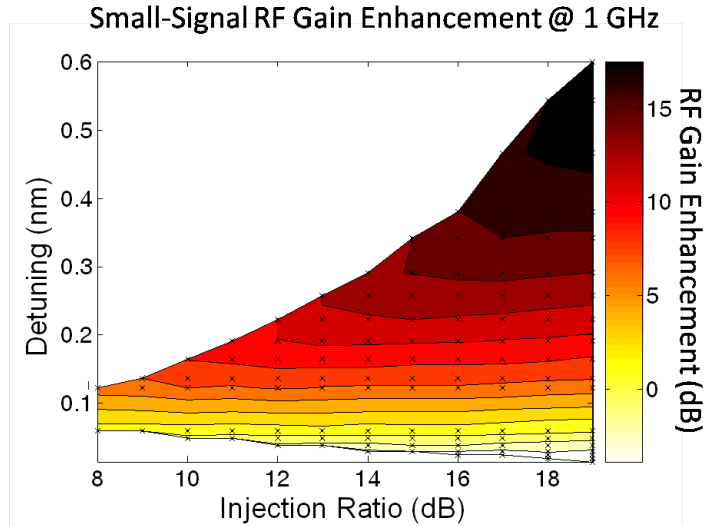


Figure 5.4 Contour plot of RF gain enhancement as a function of both wavelength detuning and injection ratio.

At high frequencies, the RF gain comes primarily from the resonance peak. A high-resonance peak about 20 ~30 dB can be obtained at the blue detuning edge. This high-frequency narrow band RF gain inspired the idea of optoelectronic oscillator, which will be discussed later in the chapter.

In Chapter 3, the amplifier model reveals that the strong resonance peak comes from the resonant amplification of the VCSEL cavity. By measuring a series of optical spectra at different detuning values of an OIL VCSEL under a single-tone modulation at 10 GHz, the low frequency RF gain enhancement can be understood intuitively according to the amplifier model as well. As shown in Figure 5.5(a), the modulation sidebands can be seen on two sides of the optical carrier (master mode) 10 GHz away. Note the lower sideband on the longer wavelength (red) side has substantially greater amplitude, and the

cavity mode ASE is pronounced on the blue detuning side. Therefore, the lower sideband is amplified by the sharp cavity resonance, resulting in a high-frequency resonance peak. These features change as $\Delta\lambda$ increases to the red detuning edge shown in Figure 5.5(b) – the two sidebands are more equal in height while the cavity resonance peak is more suppressed and closer to the master mode. Therefore, the low frequency signals that closer to the carrier get amplified in this case.

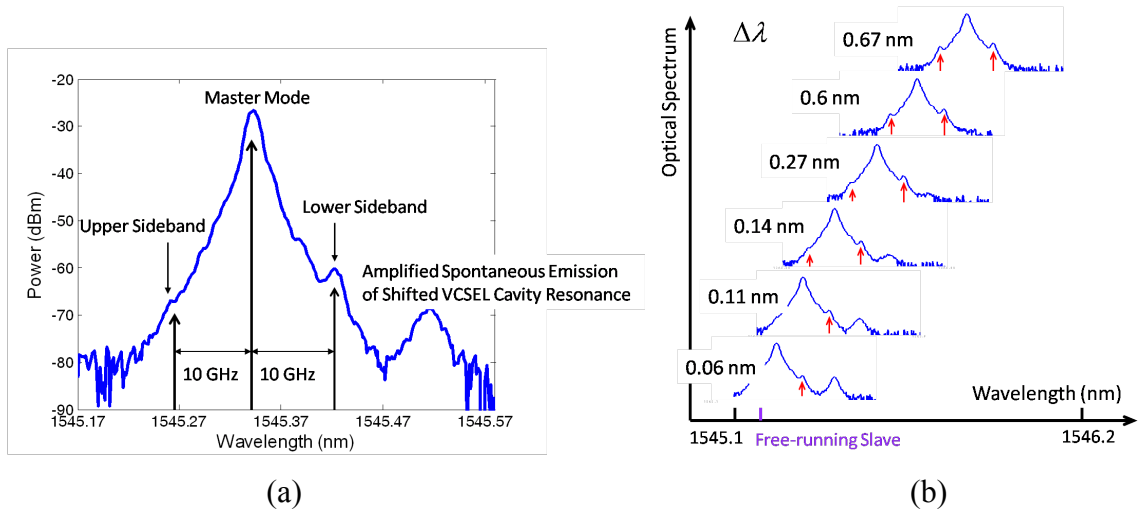


Figure 5.5 (a) Optical spectrum of an OIL VCSEL under a single-tone modulation at 10 GHz. Sidebands and the cavity mode ASE can be observed. (b) A series of spectra at different detuning values of an OIL VCSEL under a single-tone modulation at 10 GHz.

However, a quantitative solution to the drastic RF gain enhancement of an OIL VCSEL still remains undiscovered. And this huge enhancement so far is only reported on VCSELs but not other type of diode lasers, like DFB lasers. Possible directions for future investigations on this topic can be on surface-normal modulators [64] or quantum-confined Stark effect in quantum-wells [65] that are used as the VCSEL gain media.

5.1.2 Nonlinearity and Dynamic Range

Linearity is an important figure-of-merit for analog fiber-optic links, as it represents the faithfulness of reproduction of the modulation signal. Typical optical link linearity is characterized by spur-free dynamic range (SFDR). It is defined as the signal-to-noise ratio at the input RF power for which the system noise floor equals the largest distortion spurious power. Distortion occurs from several sources, including 2nd- and 3rd-order harmonics of the signal and the intermodulation distortion (IMD) between different channels. In actual applications of multichannel signal transmission where baseband signals from different channels are carried on a number of well separated high-frequency carriers, second (or higher) order harmonic distortions generated by signals in a channel are actually of little concern since they generally do not fall within the frequency band of that particular channel or any other channels. The relevant quantity of concern is more on the third order intermodulation (IM) product of the laser transmitter – two signals at different frequencies ω_1 and ω_2 within a certain channel can generate intermodulation products at frequencies $2\omega_1 - \omega_2$ and $2\omega_2 - \omega_1$, which in most likelihood will lie within that particular channel and is thus undesirable. For device characterization, the standard technique is to measure the 3rd order intermodulation distortion (IMD3) by modulating the laser using two single-tone signals at slightly different frequencies. Nonlinear distortion has been shown to be inversely proportional to the resonance frequency [63]. Hence, with the resonance frequency enhancement, injection-locked lasers are promising for exhibiting reduced nonlinear distortion. IMD3-limited SFDR can be evaluated by measuring both the fundamental tone and the IMD3 power at various RF input power levels, as shown by the schematic in Figure 5.6. Since the fundamental tone is the first

order response of the device, it exhibits a slope of one. Therefore, IMD3 as the 3rd order response possesses a slope of three shown in the schematic. It is straightforward to expect three ways to increase the dynamic range of a laser by examining Figure 5.6. One can increase the fundamental tone, which is essentially the RF gain mentioned previously, or reduce the distortion, or reduce the noise floor. However, increasing the fundamental tone or reducing the noise floor could be 3X more effective than reducing IMD3 due to the slope of three. It will be shown below that OIL can help enhance SFDR of a VCSEL in all three ways simultaneously.

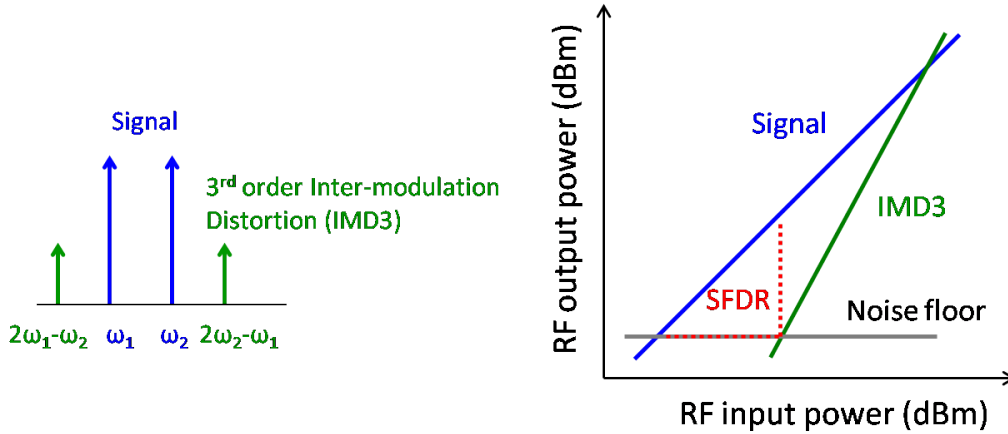


Figure 5.6 Schematic defining IMD3-limited spur-free dynamic range (SFDR).

To measure SFDR, typically two RF synthesizers are used to directly modulate the slave laser, and the output signal is characterized using an RF spectrum analyzer. By pushing out the resonance frequency, OIL VCSEL exhibits a much larger dynamic range than a free-running device. Figure 5.7 shows that a significantly improved IMD3-limited SFDR of $106 \text{ dB-Hz}^{2/3}$ at 1 GHz with channel spacing of 10 MHz [66] was obtained for an injection-locked VCSEL. Due to both the fundamental tone enhancement and IMD3

reduction, 20-dB improvement in the SFDR was attained by using strong OIL. The reduced noise floor of -145 dBm/Hz is used in the calculation. Details on noise reduction measurement will be shown next.

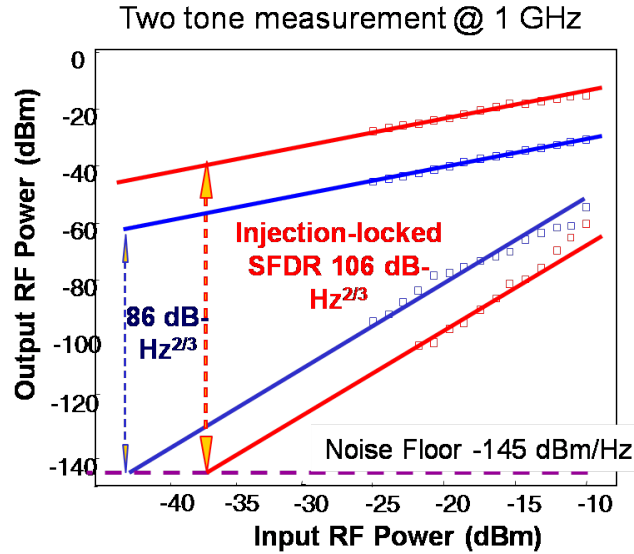


Figure 5.7 Two-tone spur-free dynamic range (SFDR) improvement at 1-GHz modulation by OIL. Inner lines are for a free-running VCSEL.

The frequency response of both the fundamental tone and the IMD3 [66] is shown together in Figure 5.8. This shows that the large SFDR improvement can be achieved for a wide range of modulation frequencies. The fundamental tone response is similar to the small-signal frequency response discussed thoroughly in Chapter 3. The resonance frequency of the free-running VCSEL is about 2 GHz, and with injection locking, it is greatly increased, thus leaving a flat response in the frequency range shown here. For each injection ratio condition, wavelength detuning values were chosen to be close to the red edge where RF gain enhancement is more drastic so as to maximize the SFDR improvement. The IMD3 power, on the other hand, largest at the resonance peak, is reduced with the increasing of the resonance frequency.

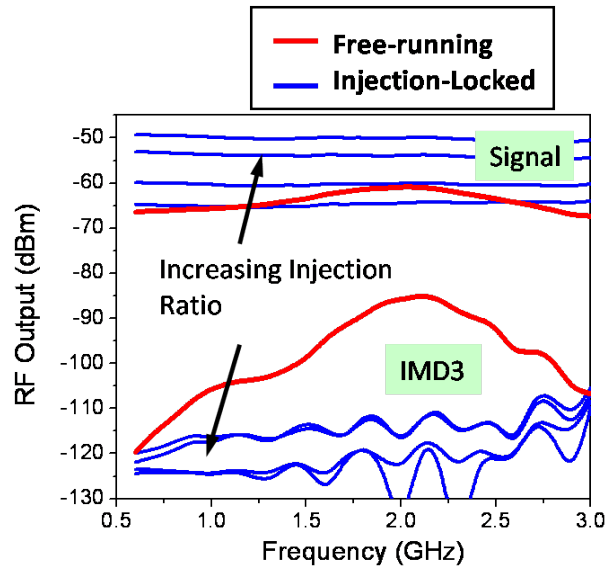


Figure 5.8 Measured frequency response of the fundamental tone and two-tone IMD3 distortion at different injection ratios.

Therefore, the modulation efficiency enhancement with increasing injection ratio ranges from 0.5 to 16 dB, whereas the distortion is reduced from 11 to 19 dB. The SFDR enhancement is determined by the RF gain enhancement plus one-third of the distortion reduction; thus the RF gain significantly contributes to the SFDR enhancement. If we pick the single frequency at 1 GHz (half of the resonance frequency) and plot the SFDR improvement for various injection ratios as shown in Figure 5.9, the experiment demonstrates that an increasing injection ratio leads to an increasing SFDR. It should be mentioned that the measured distortion frequency response in Figure 5.8 is source instrument limited, as evidenced by the similar oscillations observed in the measurement of the IMD3 of the two RF synthesizers.

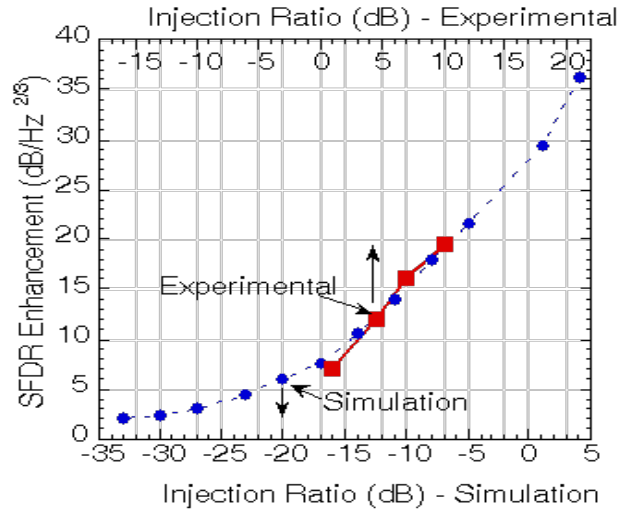


Figure 5.9 Experimental and simulated spur-free dynamic range (SFDR) enhancement vs. injection ratio at half of the resonance frequency.

Theoretical predictions for the distortion of an injection-locked laser have shown that a small reduction in distortion is possible for some injection conditions [32]. The injection conditions studied, however, were for a low-effective injection ratio. In this case, numerical simulations [66] were performed for injection-locked VCSELs under very strong injection conditions and demonstrate that a very large distortion reduction is possible. The OIL laser rate equations were used for numerical simulations.

The simulation results for the SFDR improvement versus injection ratio are also shown in Figure 5.9. They are plotted for the 2.4-GHz signal as a function of injection ratio for a wavelength detuning that is near the red edge of the locking range. For consistency, the comparison between the experimental and numerical results was done at half the resonance frequency. Figure 5.10 shows the simulated results for the signal and distortion frequency response. The thick curves are the (top solid) and IMD3 (bottom dotted) of the free-running laser, whereas the thin curves are those under various injection

ratios. It is interesting to note that, for the free-running laser, a “shoulder” is observed at half of the resonance frequency on the IMD response near the resonance peak, which is also observed in the experimental results shown in Figure 5.8. The wavelength detuning is chosen to be at the red edge of locking range. As can be seen, the modulation efficiency is increased as the injection ratio increases; meanwhile, the IMD3 is suppressed, which is consistent with the experimental results. For very high-injection ratios, substantial suppression of the IMD3 is observed. The experimental and simulation results are comparable in trend. The simulation predicts that a very large dynamic range can be achieved with a high-injection ratio.

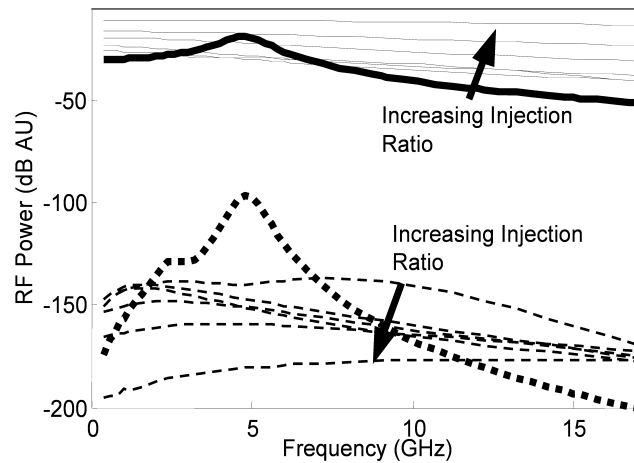


Figure 5.10 Numerical simulation of frequency response of both the fundamental tone and the two-tone IMD3 distortion at different injection ratios.

5.1.3 Relative Intensity Noise

Relative intensity noise (RIN) is defined as the dynamic range between the laser output power and the laser intensity noise power. For laser RIN measurement, the photodetector shot noise and the RF spectrum analyzer thermal noise floor should be lower than the laser intensity noise. Otherwise, the system will be shot-noise limited in a

high detection power situation or thermal-noise limited in a low detection power situation [67]. High laser power would help increase the dynamic range of the measurement to prevent it from being limited by the system noise. Since laser intensity noise originates from the nonlinear interaction between photons and electrons, injection locking has been reported to reduce laser RIN for VCSELs and F-P edge-emitting lasers [16, 17] by pushing the resonance peak out to a much higher frequency. For VCSELs, however, due to the low-emission power (~ 1 mW) and fiber-coupling loss, the average detected optical power is usually too weak to make laser intensity noise surpass the system thermal noise limitation. The solution to this issue is to add an EDFA followed by an optical filter to amplify the average optical power. Then an HP 71400C lightwave signal analyzer is used to measure RIN of an OIL VCSEL. The RIN spectra of the injection-locked VCSEL at different injection conditions are shown in Figure 5.11. The RIN spectrum of the free-running VCSEL is also shown as the reference at a 1-mA bias (2X threshold for this device). The RIN peaks of both free-running and injection-locked conditions are in agreement with resonance frequencies in the small-signal modulation response of the laser. For an injection ratio of 8 dB, RIN data for various detuning values are shown, which also has a similar behavior as the frequency response. A large RIN reduction at the low-frequency regime (0–13 GHz) is observed due to increased resonance peak. However, it is relatively constant over a large frequency span, even at the very low-frequency region. This is attributed to the limit from the amplified spontaneous emission (ASE) noise from the EDFA. At a higher injection ratio (10 dB), the resonance frequency increases beyond the instrument limit, and the noise is reduced over nearly the entire visible frequency band. The RIN reduction can be intuitively understood as the

following: when the laser is injection locked, fewer carriers are needed to achieve lasing threshold. The spontaneous emission of the laser and, therefore, its noise is reduced. However, the increased resonance frequency enhancement is the most important reason that the noise value is decreased at the low-frequency regime as the noise peak is moved to higher frequencies. The combination of these two factors results in the RIN reduction of an injection-locked laser. To model the OIL laser RIN, usually Langevin noise terms are applied [30]. Simulations on RIN reduction by OIL can be found in [16].

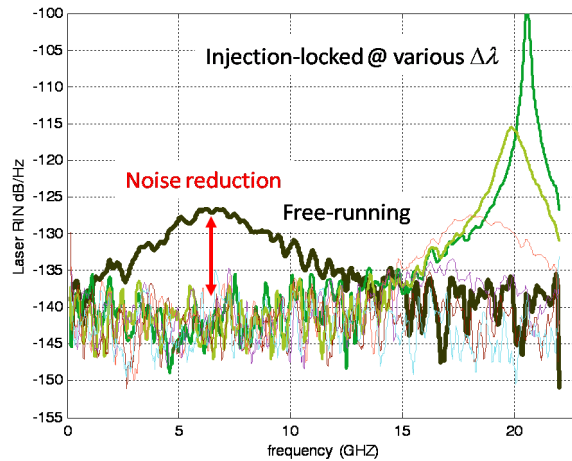


Figure 5.11 Experimental demonstration of relative intensity noise (RIN) reduction of an OIL VCSEL at various injection-locking conditions compared with free-running VCSEL.

5.1.4 Summary of Microwave Performance

As seen from the above subsections so far, the use of an ultrahigh-injection ratio results in a high-resonance frequency, which leads to significant performance improvements including enhancements in bandwidth, RF-link gain, dynamic range, and reduction in laser noise. The performance and enhancements of OIL VCSELs is summarized in Table 5.1. All enhancements, except the large sharp resonance frequency,

were obtained for a red wavelength detuning, for high-injection ratio, and are observable simultaneously. For the red detuning values, the resonance frequency is damped but still enhanced up to 30 ~ 40 GHz. Very high-resonance frequency (~ 100 GHz) is achieved for different devices with all devices showing an initial free-running resonance frequency below 10 GHz. Under the ultra-strong injection conditions, we attain up to 20-dB RF link gain enhancement. This corresponds to a modulation efficiency enhancement from 0.22 to 2.2 W/A. The modulation efficiency increases with increasing injection ratios as well. Furthermore, injection locking is effective in reducing distortion, thereby improving the SFDR of a directly modulated laser, both experimentally and numerically. An OIL VCSEL with an IMD3 SFDR of 106 dB-Hz^{2/3} at 1 GHz was achieved, representing an SFDR increase of 20 dB. A large dynamic range was observed as well over a wider frequency band of 0.6 ~ 3.0 GHz. The SFDR improvement is also shown to linearly increase with injection ratio. Similarly, the SFDR enhancement increases with increasing resonance frequency and RF gain. Due to the resonance frequency enhancement, OIL can reduce laser noise too.

These results suggest that OIL VCSELs are a promising high-performance solution for microwave photonic applications. OIL VCSELs may find applications in low-cost radio-over-fiber (RoF) distribution systems such as cellular telephone signals (global system for mobile communications (GSM) requires 90 dB-Hz^{2/3} dynamic range) and wireless local area networks (WLANs) (802.11x). For injection locking to offer the enhancements described here, the resonance frequency must be increased to a very high value, which is achieved by using an ultra-high injection ratio.

Table 5.1 Microwave performance of OIL VCSELs for analog transmission.

Figure of Merit	OIL VCSEL	Improvement
<i>Resonance Frequency</i>	100 GHz*	10X
<i>Modulation Efficiency</i>	2.2 W/A	10X
<i>RF Link Gain</i>	-19 dB	20 dB
<i>Relative Intensity Noise (RIN)</i>	-145 dB/Hz*	15 dB
<i>Spur-Free Dynamic Range (SFDR)</i>	106 dB-Hz ^{2/3}	20 dB

*Limited by available instrumentation

5.2 OPTOELECTRONIC OSCILLATOR (OEO)

Low phase noise frequency sources are highly demanded in various optical and radio-frequency (RF) systems. The applications cover a wide range of photonic and RF systems such as microwave frequency standards, radars, RF photonics and optical signal processing. Typically, microwave oscillators with high performance are made from either microwave energy storage element, for example dielectric resonators, or acoustic energy storage element, like quartz resonators. However, the carrier frequency generated by these resonators is limited usually in the MHz regime, which really prevents their applications in high-speed systems. In the mid 90s, Maleki [68-70] and his colleagues at JPL first demonstrated optoelectronic oscillator (OEO), which is considered a new paradigm that uses optical energy storage element to generate microwave signal with high spectral purity, low phase noise, and at GHz high frequency regime too.

The phase noise performance of the OEO can be greatly improved by introducing a long delay in the oscillator loop, which is usually provided by a low-loss optical fiber loop with a high quality factor (Q -factor). Yao and Maleki successfully demonstrated several types of OEOs, generating RF signal in the X-band with low phase noise [71-74]. Recently, Zhou et al. demonstrated a dual-loop OEO by using two standard OEO loops with different fiber lengths to eliminate spurious OEO signals [75]. The schematic of a standard OEO originally invented by Maleki is shown in Figure 5.12(a). The CW laser is coupled into the external modulator and fiber loop, which is detected by the high-speed photo-detector. The detected RF signal is amplified and fed back to the modulator. Provided with high enough RF amplification (loop gain > 1), this configuration results in an RF oscillator starting from the noise. The long but low-loss fiber loop resulted in a high- Q cavity, leading to very low phase noise. However, in this configuration, a very high gain (60 dB) RF amplifier chain is necessary to reach the oscillation threshold. The RF amplifiers and external modulator present an upper limit of the RF signal frequency; it is challenging to achieve > 10 GHz oscillation. However, direct-modulated semiconductor lasers under strong optical injection offers an attractive alternative for OEO because of their superior high frequency performance. A tunable microwave source has been demonstrated using semiconductor laser dynamic [76]. We have also shown that OIL VCSELs exhibit high-speed frequency response (~ 100 GHz) and large tunability of the resonance peak by adjusting locking parameters under direct modulation. In addition, the red-shifted OIL VCSEL cavity amplifies the modulation sideband, which enhances the modulation efficiency at the resonance frequency, which could alleviate the amount of RF threshold gain necessary for loop oscillation. Therefore, a novel OIL OEO

configuration leveraging the high frequency and high gain resonance peak of an OIL laser is shown in Figure 5.12(b). The oscillator is composed of a master and slave laser instead of a pump laser and an external modulator. The rest of the setup remains the same. However, the oscillator now can be initiated from the coherent beating between the master and the slave laser cavity mode now rather than noise. So the RF signal frequency generated by OIL OEO is determined by the spacing between the master and the cavity mode, which is obviously tunable. The optical gain provided by the slave laser cavity is also expected to relax the requirement on the RF amplifier to reach oscillation threshold.

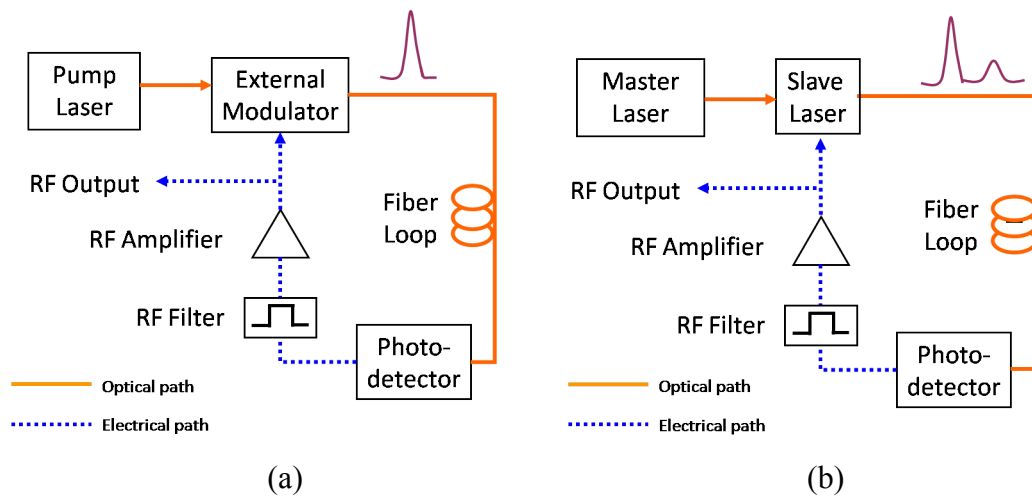


Figure 5.12 Schematic of (a) standard optoelectronic oscillator (OEO) and (b) OEO using optically injection-locked semiconductor lasers. Closed-loop optical spectrum of optically injection-locked OEO exhibits a significant enhancement of the longer-wavelength modulation sideband due to the cavity resonance amplification in the injection-locked lasers.

5.2.1 Open-Loop Characterization

The OIL OEO idea applies to different kind of semiconductor lasers, just as injection locking itself does. In our case, VCSEL is used as usual. A detailed experimental setup is shown in Figure 5.13. A 1.55- μm VCSEL is injection-locked by a DFB laser through an optical circulator. Polarization controller is used to match the polarization of the DFB and

the VCSEL. The VCSEL is coupled through a lensed-fiber, which gives coupling efficiency about 70%. 1% of the output light goes in to an optical spectrum analyzer (OSA) to monitor the locking condition, while 99% of the output runs through a fiber loop of 17 km and is delivered to a photodetector. After going through an RF filter centered at 20 GHz and an RF amplifier, the detected RF signal is subsequently fed back to modulate the VCSEL via a bias Tee. Half of the RF signal is tapped off as the output for characterization.

The target frequency of the RF signal is around 20 GHz (determined by the filter center frequency), open-loop characterization is conducted first based on various injection locking parameters to determine the appropriate operating condition for optimized closed-loop performance. The output of the loop is analyzed with no OEO feedback applied to the laser. The frequency response depending on both detuning and injection ratio of the OIL VCSEL is first measured shown in Figure 5.14. The locking parameters are tuned to have resonance frequencies around 20 GHz. The results demonstrate again that not only the resonance frequency can be increased to a much higher value, but also the efficiency of the resonance peak can also be tuned by adjusting the wavelength detuning. Typically 20-dB gain can be fairly easily achieved. In addition, the resonance frequency can be tuned by changing the injection ratio, while maintaining the 20-dB efficiency. Therefore, features of high gain, high speed and great tenability from the resonance peak of an OIL laser can be transferred to an OIL OEO system.

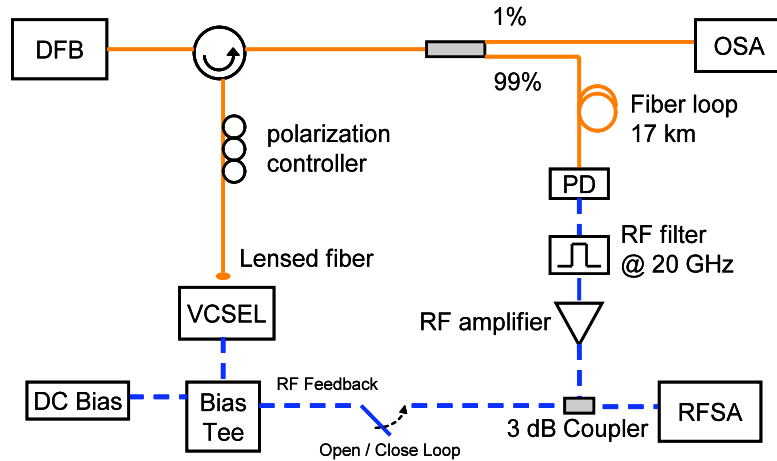


Figure 5.13 Experimental setup (OSA: optical spectrum analyzer, PD: photodetector, RFSA: RF spectrum analyzer). Solid lines: optical path, dashed lines: electrical path. Switch controls open-loop and closed-loop characterization.

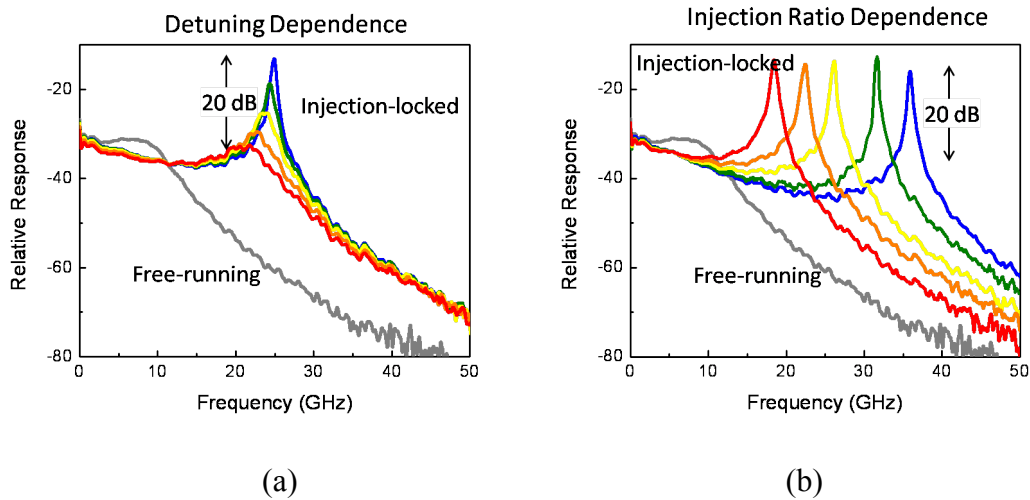


Figure 5.14 Small-signal frequency response of an OIL VCSEL. (a) Detuning dependence. (b) Injection ratio dependence.

Under strong injection, when the master laser is on short wavelength side, the cavity mode is very pronounced. Before the slave laser is stably locked, it is in the four-wave mixing regime, as shown by Figure 5.15(a). As the master is tuned towards the long wavelength side, the slave laser cavity mode is more and more suppressed, shown by

Figure 5.15 (b) and (c). This results in a more stable locking condition, but lower RF gain or amplification at the resonance frequency. Therefore, the wavelength detuning monotonically translates into cavity mode suppression ratio (CMSR), defined as the power ratio between the OIL mode (master mode) and the slave laser cavity mode. On the blue detuning side, the CMSR is small, and it increases with the wavelength detuning. So if one plots CMSR versus wavelength detuning in Figure 5.16, CMSR increases as the locking condition changes from wave mixing to stable locking regime. Obviously, one would like to operate the laser in the stable locking regime, because coherence will be achieved when the slave laser is stably locked. However, if the master laser is tuned too far into the locking regime, the cavity mode will be highly suppressed, hence, one cannot take advantage of the high gain resonance to achieve oscillation. Trade-off exhibits between low phase noise and low RF gain simultaneously. Therefore, according to the optical characterization, the system should be operated at the onset of the locking range.

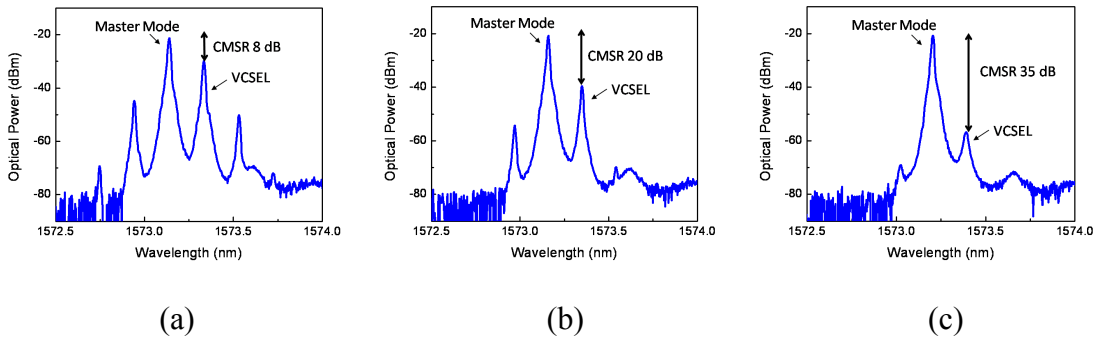


Figure 5.15 Optical spectra of an OIL VCSEL at different detuning values labeled by cavity mode suppression ratio (CMSR). (a) CMSR of 8 dB. (b) CMSR of 20 dB. (c) CMSR of 35 dB.

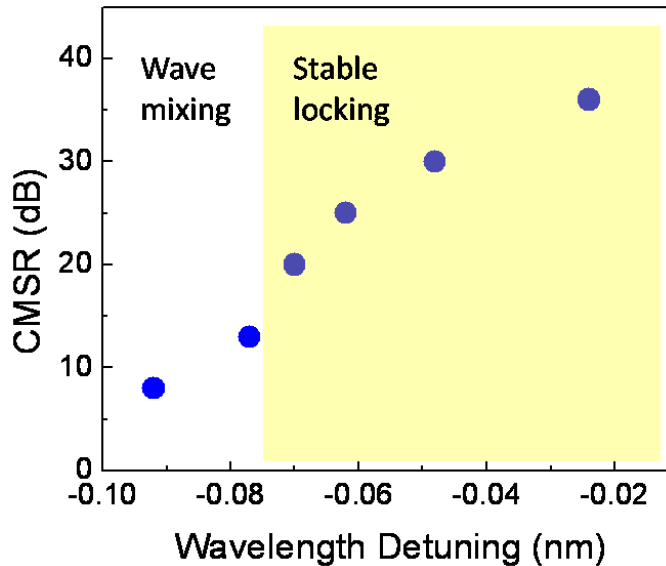


Figure 5.16 CMSR versus wavelength detuning. The laser should be operated at the onset of the locking range.

Next the open-loop RF gain (RF output versus RF input power) at different CMSR can be characterized. The VCSEL is modulated by a synthesizer at a frequency corresponding to the spacing between the master and the cavity mode. At each fixed CMSR, RF output power is measured according to each RF input power level. The results are shown in Figure 5.17. The separation of unlocked and locked regimes can be clearly seen. The laser does not show a plausible RF performance in the wave-mixing regime – a significant drop in RF gain, even though the beating signal is strong.

Therefore, based on all the above open-loop characterization, the system should be operated within the locking range with a CMSR between 20 ~ 40 dB for a closed-loop oscillation.

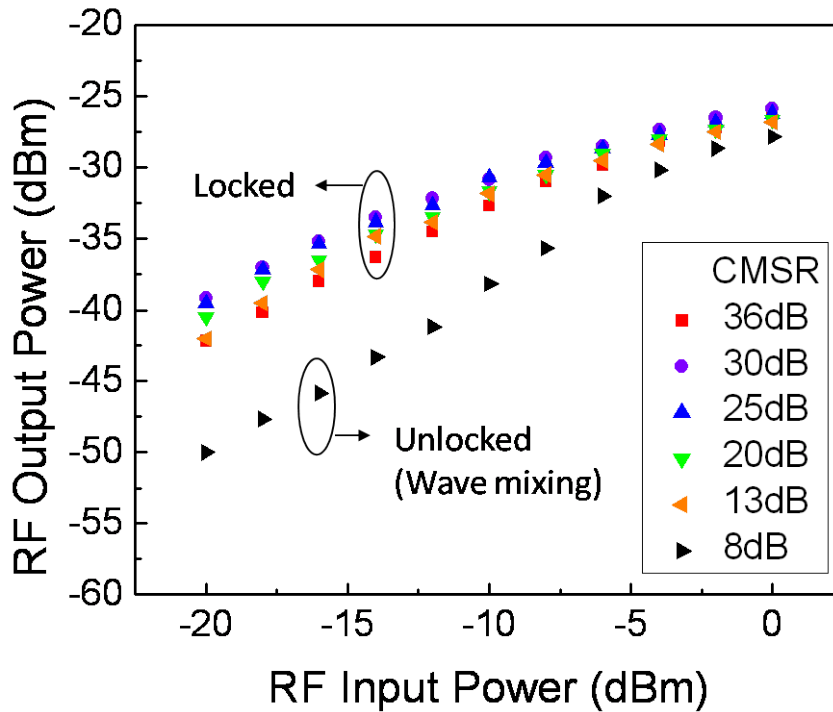


Figure 5.17 RF gain of the open-loop link at various CMSR values. The slave laser is modulated by a single tone corresponding to the spacing between the OIL mode and the cavity mode.

5.2.2 Close-Loop Characterization

Once the locking condition is selected, the loop is closed to generate the RF signal. To obtain desired phase noise performance, the whole experimental setup is packed onto a 2 ft. \times 2 ft. optical breadboard and boxed by thick foam board and plexiglass to provide temperature and vibration isolation. The pictures of the actual setup are shown in Figure 5.18.

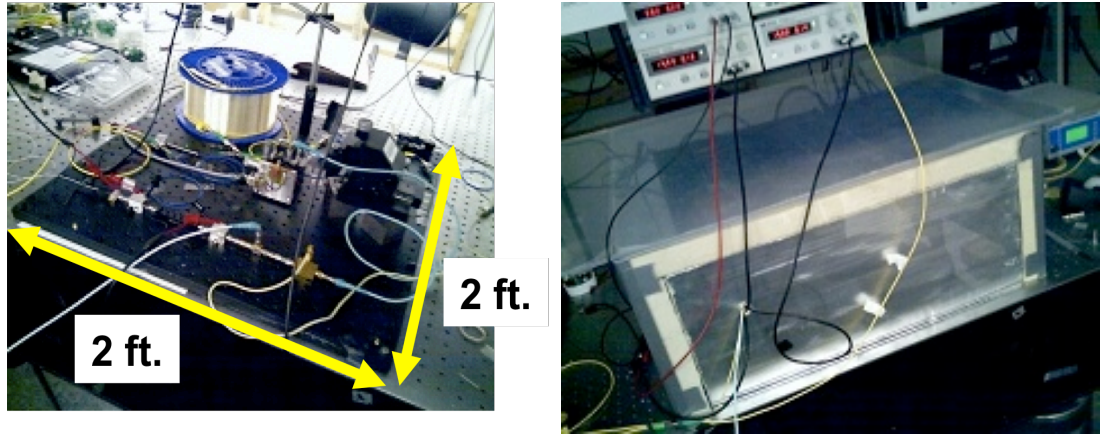


Figure 5.18 Pictures of the actual experimental setup. Foam board and plexiglass are used to provide temperature and vibration isolation.

Figure 5.19 plots both the open- and closed-loop optical spectra. The open-loop spectrum shows that a locking condition with 35-dB CMSR, and a mode spacing of 20 GHz between the master and the slave cavity mode to match the RF filter center frequency is chosen. The cavity mode is enhanced dramatically after the loop is closed indicating oscillation is achieved. The phase noise measurement then is performed by Agilent 5052A and shown in Figure 5.20. Comparing with a 20-GHz signal generated by an HP 83650B synthesizer, the phase noise of the 20-GHz signal produced by an OIL OEO using VCSEL is 38 dB lower at 5-kHz offset. To achieve good phase noise performance, long fiber loop, 17 km, is employed since the phase noise is inversely proportional to the square of the loop length [69]. However, this long fiber loop will result in a very small free spectra range, which in turn introduces numerous spurious tones and mode competition. The sharp increase of the phase noise close to 10-kHz offset in Figure 5.20 is due to the adjacent mode from the fiber loop. To reduce the mode competition thus stabilizing the tone, an RF filter centered at 20 GHz with 20-MHz bandwidth is used. This helps to stabilize the signal, but also limits the frequency

tunability of the signal. An RF amplifier with 45-dB gain is also employed in the link. Since the interest is focused on the signal stability and purity, the RF amplifier is not optimized for the minimum gain operation. A thorough study on RF threshold gain reduction for OEO using OIL DFB laser is reported in [77]. Ideally, threshold-less oscillation is desired so that the RF amplifier can be completely eliminated because it is found that the noise from high-power RF amplifier will be the ultimate limit of the phase noise performance of an OEO system. OIL OEO utilizes the optical amplification provided by the slave laser cavity as an alternative to possibly reduce the demand on RF amplification. However, the phase noise performance and limitation of such a system is still unclear and systematic theoretical study is still undergoing. In addition, note that the center frequency jitter (large spikes at 100-Hz) offset may be due to laser frequency instability or any fluctuation in the ambient environment. Overall, a stable RF signal at 20 GHz with -116 dBc/Hz phase noise at 5-kHz offset is generated by an OIL VCSEL OEO, which shows performance significantly better than a commercial RF synthesizer. This proves that OIL OEO can be the technique to achieve RF signals with high-speed and high spectral purity at the same time.

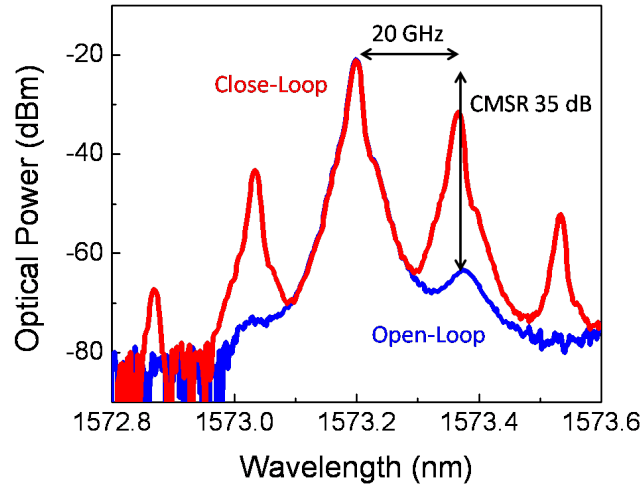


Figure 5.19 Optical spectra of open-loop and close-loop operation. The open-loop spectrum shows a locking condition with 35-dB CMSR, and a mode spacing of 20 GHz between the master and the slave cavity mode to match the RF filter center frequency. Cavity mode is enhanced dramatically when oscillation is achieved.

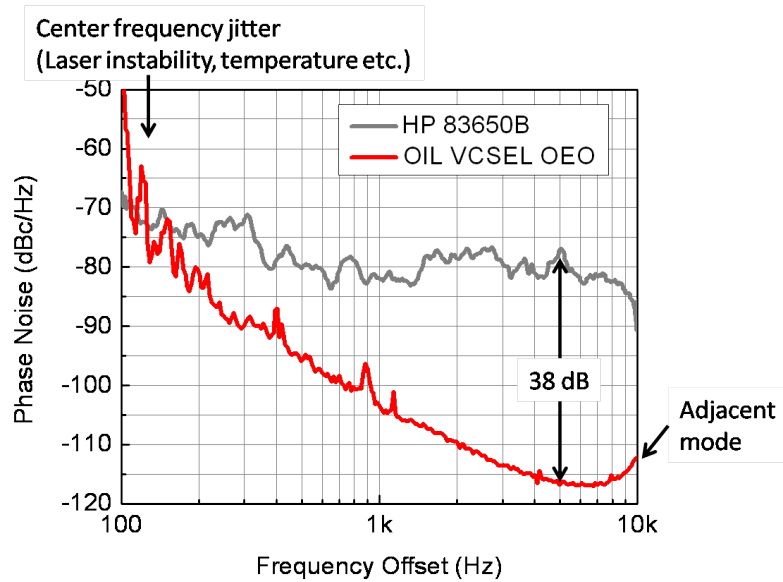


Figure 5.20 Measured phase noise performance of an OIL-OEO generated signal and an HP 83650B generated signal with center frequency at 20 GHz by Agilent 5052A. Phase noise of the 20-GHz signal produced by an OIL VCSEL OEO is 38 dB lower at 5-kHz offset.

5.3 SLOW LIGHT

Recently, there has been tremendous interest in variable all-optical delay lines and buffers for applications in optical communications, phased-array antennas and optical signal processing [79-82]. Circumventing optical-electrical-optical (OEO) conversion has the potential for increased capacity and throughput, and reduced latency in future optical networks. The key towards implementations of compact optical buffers lies inherently in achieving controllable ultraslow propagation of high-frequency modulated optical signals. Over the last couple of years, slow light has been demonstrated in a variety of systems using approaches based on material or waveguide dispersion [83-86]. While differing in their underlying physical mechanisms, the approaches share fundamental limitations with respect to the maximum achievable delay-bandwidth product. In addition, most demonstrations exhibit limited bandwidth not suited to accommodate broadband signals in the GHz-range, as required in most communications applications. This is one main reason why, up to this point, all-optical buffers still do not exist in practice. We have reported the use of a VCSEL operated as Fabry-Perot (F-P) amplifier [87] to achieve tunable group delays for broadband signals at room temperature. We demonstrate up to 100 ps tunable delay of a 2.8 GHz modulated signal. Given the VCSEL active region of 30 nm, this delay corresponds to a slow down factor of 10^6 . The delay-bandwidth product is 0.36. The setup of this experiment is similar as injection locking, however, the VCSEL is biased below threshold and the gain profile of the VCSEL amplifier is utilized. Therefore, the slow down of the group velocity is achieved according to the Kramers-Kronig relation of the gain profile. In this subsection, we present a novel master-modulated injection locking on a CW slave VCSEL, which shows

interesting frequency response and a full 2π RF phase shift over a bandwidth of a few GHz that can be effectively a slow/fast light medium and potentially useful to achieve tunable RF delay as well as optical delay.

5.3.1 Master-Modulated Injection-Locked VCSELs

The experimental setup is shown in Figure 5.21. Two 1.55- μm VCSELs [41] are used in the experiment as both master and slave lasers. A polarization maintaining (PM) EDFA is used to adjust the power of the master VCSEL. The master VCSEL, directly modulated by a network analyzer (HP 8270B), injection-locks the slave VCSEL through a PM fiber circulator. A small amount of the output light goes into an OSA to monitor the locking process, while the majority of the light goes to a receiver and then back to the network analyzer. Therefore, the small-signal amplitude and phase frequency response (S21 in both amplitude and phase formats) of a modulated-master OIL VCSEL are measured.

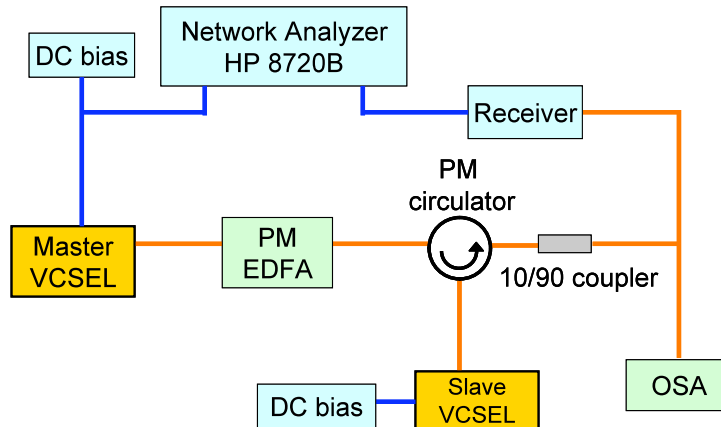


Figure 5.21 Experimental Setup. (PM: Polarization Maintaining, EDFA: Erbium-Doped Fiber Amplifier, OSA: Optical Spectrum Analyzer)

The amplitude response at various wavelength detuning values ($\Delta\lambda = \lambda_{\text{master}} - \lambda_{\text{slave}}$) is shown in Figure 5.22. Figure 5.22(a) shows the raw data taken by the network analyzer.

The black curve shows the unlocked master frequency response including all parasitics, which lead to an overall roll-off at frequencies > 6 GHz. The modulated-master OIL VCSEL frequency response is shown at different $\Delta\lambda$, and color-coded as $\Delta\lambda$ increases (the master moves from the blue to the red side relative to the slave wavelength). A dip is observed at a critical frequency f_c , which is 9.2 GHz in this injection power condition, and followed by a peak at a higher frequency, ~ 13 GHz. As $\Delta\lambda$ is increased, the depth of the dip first increases with detuning until a certain value (0.206 nm in this case), and subsequently decreases with further increasing detuning. The peak, on the other hand, drops monotonically with increasing $\Delta\lambda$. To better illustrate these features induced by injection locking; these frequency response curves can be simply calibrated by subtracting out the unlocked master laser S21 response. The calibrated response is shown in Figure 5.22(b). More pronounced dips and gain peaks could be seen. Gain as high as 18 dB is demonstrated at this injection power level.

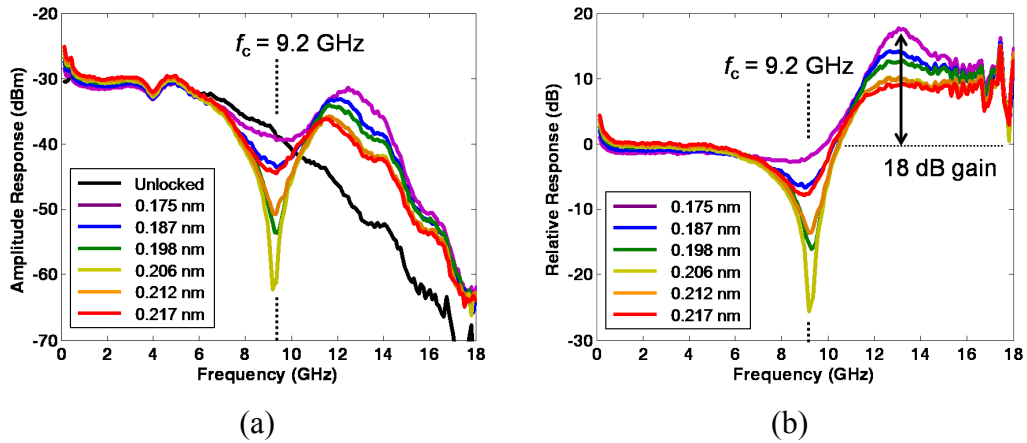


Figure 5.22 Amplitude frequency response of a modulated-master OIL VCSEL under a fixed injection power at various detuning values. (a) Raw data. (b) Calibrated data reference to the free-running frequency response.

Figure 5.23 shows the corresponding phase change response of the same modulated-master OIL VCSEL. Phase change response presents the locked phase response calibrated with the unlocked one, thus showing only the phase shift induced by injection locking. An interesting feature is that at f_c , a phase change, φ , flip occurs at the detuning value corresponding to the maximum dip. At frequencies greater than f_c , a phase shift of 2π can be achieved over a bandwidth as large as 8 GHz. The phase change can also be easily tuned by just simply tuning $\Delta\lambda$ between the master and the slave laser. The slope of the phase change response curve, $d\varphi/d\omega$, represents the delay time τ . Centered at f_c with a frequency bandwidth of 2 GHz, $d\varphi/d\omega$ changes from negative (0.2 ns) to positive (-0.2 ns) value with increasing the detuning. Hence, effectively, we can tune the slave laser medium from a slow to a fast light medium, with a total delay of ~ 0.4 ns. Since the VCSEL contains 5×6 -nm quantum wells (QWs) and the slow/fast light effects occurs in the active region, a slow down factor S (speed up for the fast light case) can be obtained as large as 2×10^6 . For frequencies above f_c , $d\varphi/d\omega$ is always negative, which always results in slow light with an effective $S \sim 4\times 10^5$. The slow/fast light effect shown here is different from those using semiconductor optical amplifiers where carrier density pulsation was the primary cause for the slow/fast light [87, 88]. However, it is similar to [89], where the VCSEL was biased below threshold and used as a narrow-band amplifier.

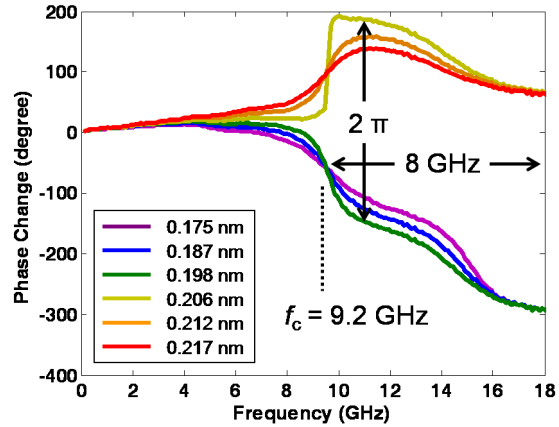


Figure 5.23 Phase change response of a modulated-master OIL VCSEL under a fixed injection power at various detuning values. For a bandwidth of ~ 2 GHz centered at f_c , the slope $d\phi/d\omega$, equivalent to the delay time τ for each detuning, changes from -0.2 ns to 0.2 ns, representing slow and fast light regimes.

Although the slave VCSEL here is biased well above threshold, and under a strong external light injection, it acts like a narrow-band amplifier as described in Chapter 2. In this case, the slow/fast light occurs at a frequency several GHz away from the master laser frequency. Therefore, utilizing it as an optical buffer for a train of light pulses requires subcarrier modulation at or above f_c . Nevertheless, the tunable phase shift is also intriguing to achieve a flexible phase control of a narrowband RF signal.

Figure 5.24 shows both the amplitude and phase response at a fixed detuning but various master injection power levels. All the features are still well maintained, while f_c increases as the injection power is increased. This shows that RF gain and phase change is possible for even higher frequencies with higher injection power levels.

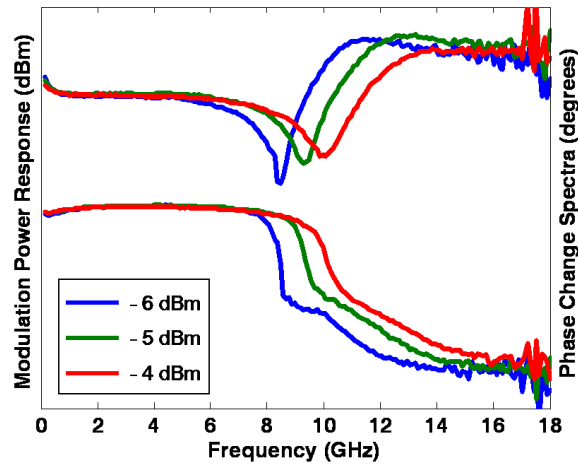


Figure 5.24 Amplitude and phase change response of a modulated-master OIL VCSEL at a fixed detuning but at three different injection power levels. RF gain and phase change is possible for even higher frequencies with higher injection power levels.

To show that these observations are a general trend of modulated-master OIL VCSELs and not due to any peculiar characteristics of any particular device or artifacts during the measurement, the same experiment is performed using different VCSELs for the master and slave lasers. Table 5.2 shows the amplitude and phase change response for three different device combinations at various injection power levels as well as detuning values. All of them show similar features and behaviors with detuning.

For the case of VCSEL 4 as master laser and VCSEL 5 as slave laser, experiments are also performed at three different power levels -10.70 dBm, -4.65 dBm and -2.27 dBm as shown in Table 5.3. At each power level a set of curves for various detuning conditions are presented. All these results show that the features of the frequency response of modulated-master OIL VCSELs are quite repeatable.

Table 5.2 Amplitude and phase change frequency response of different modulated-master OIL VCSELs.

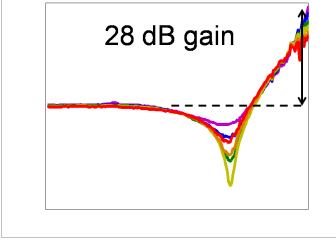
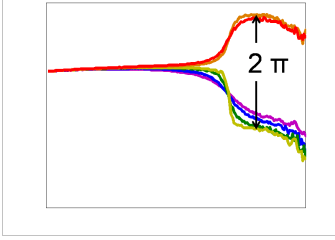
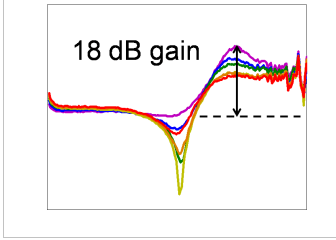
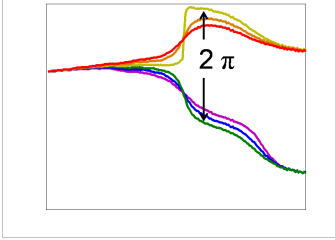
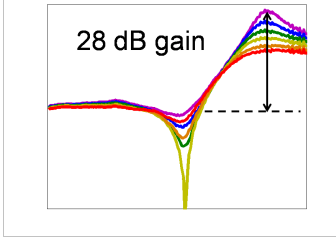
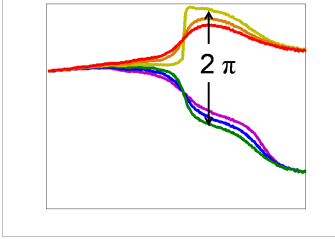
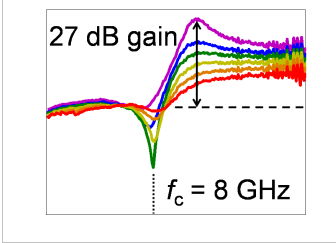
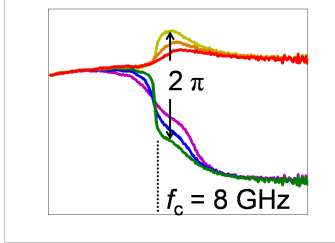
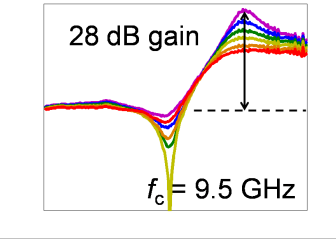
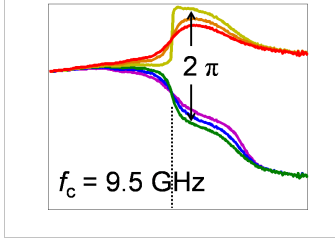
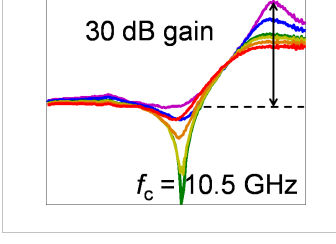
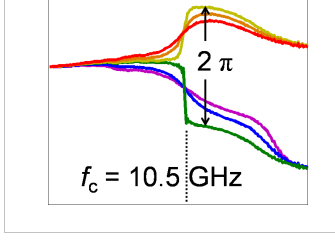
Device (Master-Slave)	Y axis: Amplitude -30 to 30 dB X axis: Frequency 0 to 18 GHz	Y axis: Phase Change -400° to 200° X axis: Frequency 0 to 18 GHz
VCSEL 1-2		
VCSEL 3-4		
VCSEL 4-5		

Table 5.3 Amplitude and phase change frequency response at various detuning values using VCSEL 4 as master and VCSEL 5 as slave at three different power levels.

Injection Power	Y axis: Amplitude -30 to 30 dB X axis: Frequency 0 to 20 GHz	Y axis: Phase Change -400° to 200° X axis: Frequency 0 to 20 GHz
-10.70 dBm		
-4.65 dBm		
-2.27 dBm		

RF phase shift can also be measured in the time domain as shown in Figure 5.25. Figure 5.25(a) shows the phase change response at two different detuning conditions. The blue one has negative phase shift at frequencies greater than f_c , while the green one has positive phase shift. The time-domain measurement is performed by modulating the master laser at single tones 14 GHz, 15 GHz and 16 GHz separately, while keeping the same detuning conditions as shown in Figure 5.25(a). The oscilloscope traces are shown in Figure 5.25(b). The same amount of phase delay and advancement are observed for

both cases at those single-tone frequencies as compared with the frequency-domain measurement.

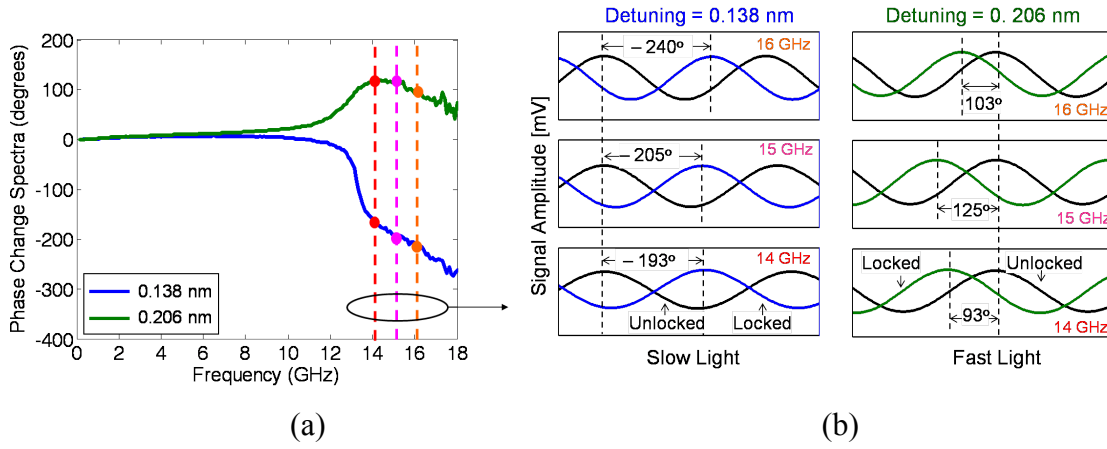


Figure 5.25 (a) Phase change response at two different detuning values with single-tone modulation frequencies indicated. (b) Time-domain traces at two detuning conditions showing both slow and fast light at three single-tone modulating frequencies.

This interesting phenomenon described here can be qualitatively understood by the hybrid amplifier model established in Chapter 3. The detuning-dependent dip shown in Figure 5.22 is possibly due to the phase cancellation between the two sidebands after detection, especially when the RF signal comes from the direct modulation of a master VCSEL that exhibits large frequency chirp. And amplitude response with dips typically associates with phase response that has sharp transitions, which in turn represents the cancelation (thus resulting in dips) on the amplitude response.

This interesting behavior may find application as tunable RF gain for all-optical communications or switching. We also demonstrate slow and fast light on single-tone signals with total RF phase shift of 2π beyond 10 GHz. This device may be useful for narrow band RF applications, such as phase shifters, phase-array antennas and beam

steering. It may be also used as an all-optical time delay in subcarrier-multiplexed networks.

Chapter 6

Digital Applications of Injection-Locked VCSELs

The recent surge in bandwidth demand, driven by fast-growing video-on-demand services and emerging applications such as network gaming, peer-to-peer downloading in addition to the global broadband data services and advanced Internet applications have been revitalizing the optical communication industry with focuses on both the access networks [90] and the long-haul transport infrastructure [91].

Access networks have been traditionally called last-mile networks as they serve as the last segment connection from service providers' central office (CO) to the end users. Access networks are typically widely implemented by either twisted copper pairs (telephone lines) connecting to each individual household or residential co-axial cable drops from Community Antenna TV (CATV) service providers. Ethernet is also a popular technology commonly deployed by private sectors, government agencies and educational institutions to form a local area network (LAN). Wi-Max is another type of access technology that uses wireless radio signals for last-mile connectivity. Typically, optical fibers are widely used in backbone networks due to their huge available bandwidth and extremely low loss. Although fiber has been proposed and researched as the next generation access technology for a long time, it was not until the beginning of this century that fiber finally saw its growing commercial importance as the technology

for last-mile connection. After more than 20 years of active research, passive optical network (PON) based broadband optical access systems are finally seeing rapid large scale commercialization in Asia and North America [90]. Among all the available technologies, wavelength-division-multiplexing (WDM) increases system capacity by transmitting multiple wavelengths on a single fiber, which can provide various services efficiently.

For backbone networks, the desire for higher per-fiber transport capacities and, at the same time, the drive for lower costs per end-to-end transmitted information bit has led to optically routed networks with high spectral efficiencies. Among other enabling technologies, advanced optical modulation formats have become key to the design of modern WDM fiber systems [91].

Therefore, in this chapter, how injection-locked VCSELs can be used as upstream transmitters in WDM-PONs along with important technical and design issues such as Rayleigh backscattering, extinction ratio, and fiber fault monitoring will be discussed.

6.1 WAVELENGTH-DIVISION-MULTIPLEXED PASSIVE OPTICAL NETWORK (WDM-PON)

The wavelength-division-multiplexed passive optical network (WDM-PON) has long been recognized as an attractive upgrade solution for current access networks due to its large capacity, ease of upgradeability, and security guarantee. In that respect, laser transmitters in WDM-PONs are required to emit transmission wavelengths fixed to the WDM grid. This key requirement is to ensure minimal crosstalk with other wavelengths and transmission loss at the wavelength multiplexers and demultiplexers, e.g., arrayed waveguide gratings (AWGs) [92]. Wavelength-specific distributed feedback (DFB) lasers, distributed Bragg reflector lasers, and tunable lasers are considered the most

expensive types of optical network unit (ONU) upstream transmitters. Active temperature control and wavelength feedback monitoring, e.g., using Fabry–Pérot (F-P) etalons and Bragg filters, are necessary to maintain emission wavelengths at their designated wavelengths, thus leading to large power consumption, significant system complexity, and more importantly, high cost.

A promising alternative to achieving low-cost wavelength-specific sources in a WDM-PON is to use VCSELs. VCSELs are well known for their excellent single-mode behavior and potential for low-cost manufacturing and electronics integration as introduced in Chapter 1. In this section, a novel scheme that exploits the use of injection-locked VCSELs for operation as stable, directly modulated, and potentially uncooled ONU transmitters is proposed and experimentally demonstrated. OIL allows the VCSEL wavelength to be matched to that of the master laser and dense WDM (DWDM) grid within a certain detuning range, and thus, is locked onto the specific AWG port provided by the central office (CO) without additional wavelength locking or stabilizing elements [93]. Therefore, using OIL VCSELs as upstream transmitters expands the wavelength tolerance of the ONU and compatibility with various vendors and systems with slightly different DWDM grid. The proposed scheme does not require external injection-locking sources and external upstream modulators. At the CO, DFB lasers that carry downstream signals also serve a second function as master lasers to injection-lock ONU slave VCSELs onto the WDM grid. A similar work proposed in [94] uses downstream signals in differential phase shift keying (DPSK) format to injection-lock F-P lasers, but at the expense of an external phase modulator for each wavelength channel at the CO and a DPSK demodulator at each ONU. In our work, both downstream and upstream data are

intensity modulated and directly detected using standard components. The slave VCSEL is shown to respond only strongly to the wavelength but not the data from the master DFB laser, with good upstream transmission performance obtained over 25-km fiber. Thus, while the downstream laser's carrier wavelength is used to lock the upstream VCSEL, its data do not influence the upstream information. It will also be shown that this proposed scheme provides a platform for an easy diagnosis of fiber failure in a rather complex PON topology with fault monitors only added to the CO without modifying the ONU.

6.1.1 Injection-Locked VCSELs as Upstream Transmitters

Figure 6.1 shows the proposed WDM-PON implementing OIL VCSELs. At the CO, master DFB lasers either directly or externally modulated with downstream data, are temperature-tuned to emit distinct wavelengths on the DWDM grid. At each ONU, an optical splitter divides the optical power of the demultiplexed downstream signal to feed a downstream receiver and to injection-lock a slave VCSEL. The splitting ratio must be carefully chosen to satisfy error-free detection at the downstream receiver while maintaining stable locking of the VCSEL. The OIL VCSEL is directly modulated with upstream data and transmits them back to the CO. For colorless operation, identical tunable VCSELs may be placed at each ONU [95]. Since the slave VCSEL emission wavelength is typically dependent on its bias current or heat sink temperature, a "training" session may be required to find the lockable wavelength regime, with the assistance of a look-up table, or by forming a feedback loop with measurements of the slave VCSEL reflected power through Port 3 of the optical circulator in Figure 6.1, or its junction voltage while sweeping the slave VCSEL wavelength. The training session

needs to be done only once when the ONU is started up or infrequently as is necessary, similar to rebooting of a personal computer.

Since the modulated master DFBs and slave VCSELS have the same emission wavelength, unidirectional fibers were implemented in the work so that the injection-locked behavior and transmission performance (of the VCSEL) can be evaluated without the influence of Rayleigh backscattering. In practice, bidirectional transmission is typically employed due to the consideration of fiber cost and management. The effects of Rayleigh backscattered light on the proposed scheme is, therefore, of interest and will be investigated in detail in the next subsection.

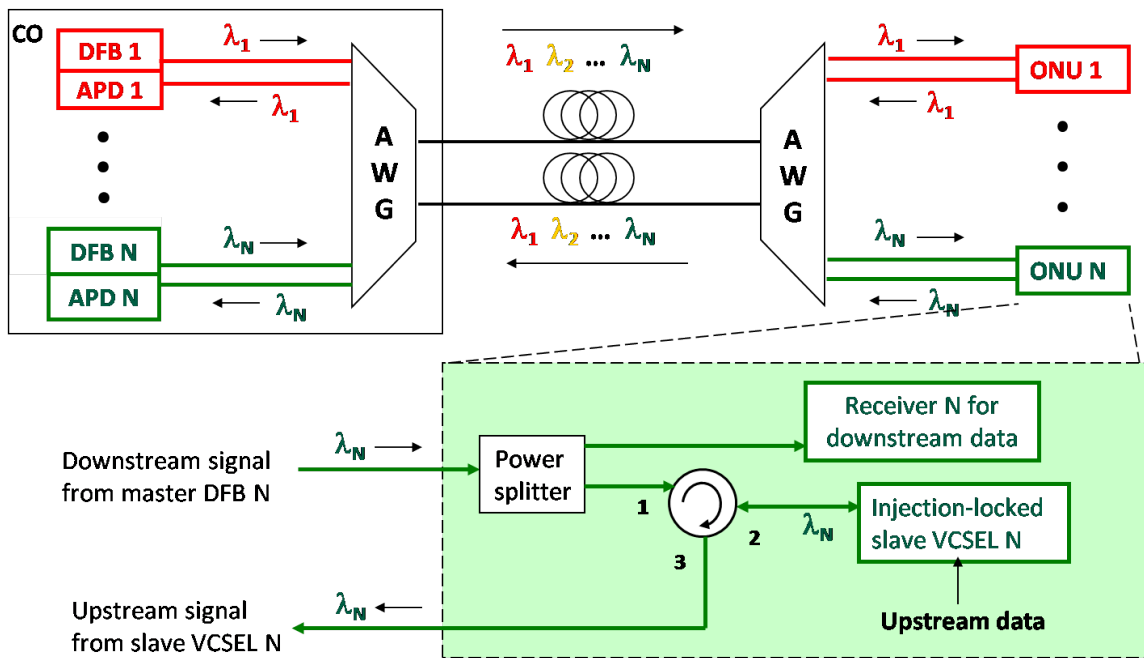


Figure 6.1 Proposed scheme of WDM-PON using directly modulated OIL-VCSELS as upstream transmitters. Each slave VCSEL is injection-locked by modulated downstream signal transmitted from a master DFB laser located at the CO.

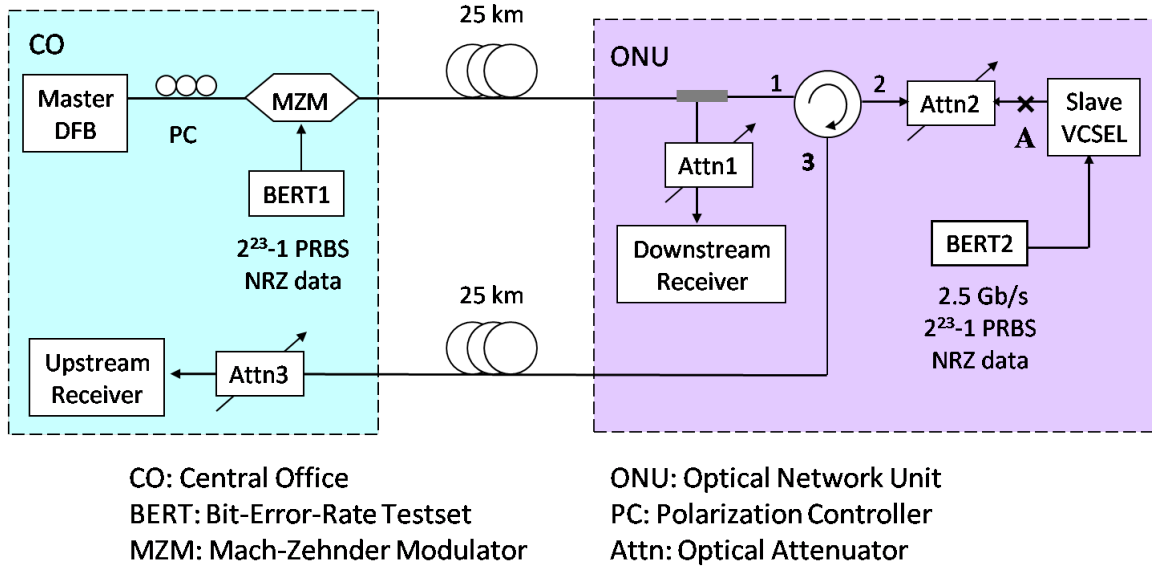


Figure 6.2 Experimental setup of single channel demonstration.

The characterization and evaluation of the OIL VCSEL scheme were performed with a non-polarization-maintaining (non-PM) single-channel experiment with the setup shown in Figure 6.2. At the CO, the continuous-wave (CW) light from a DFB laser was externally modulated with 2^{23} -1 pseudorandom bit sequence (PRBS) non-return-to-zero (NRZ) data from a bit-error-rate testset (BERT). The modulated signal was either connected directly to a 3-dB coupler for back-to-back measurements or through 25 km of fiber. At the ONU, a 3-dB coupler was used to split the downstream modulated signal between a downstream receiver and a 1.55- μ m VCSEL. The VCSEL used here is the same type of devices shown previously [41]. The VCSEL was biased at 5 mA (\sim 1 mW output power) and modulated with 2.5-Gb/s 2^{23} -1 PRBS NRZ data from a second BERT. The modulated output from the VCSEL was sent upstream and detected using a 2.5-GHz avalanche photodiode (APD) receiver at the CO after traversing 25 km of fiber. Optical attenuators (ATTN) were used to vary the received optical power at the receivers and the

injection power incident on the VCSEL. Note that in the setup, the VCSEL was free-space coupled to a fiber connected to ATTN2 at location A, incurring a coupling loss of ~ 8 dB. The absolute injection power incident on the VCSEL was, therefore, the measured power at A $- 8$ dB of coupling loss. In a practical network, lower coupling losses (~ 1 dB) can be easily achieved by deploying packaged VCSELs with a more sophisticated design or structure such as lensed-fiber so that system loss of 15–20 dB can be accommodated.

Since both the master and the slave laser will be under modulation in the PON configuration, it is necessary to characterize the dynamic locking stability first. The master DFB injection power and wavelength detuning, forming the stability plot, is used to characterize the locking stability. Figure 6.3 shows the stability plot of a CW VCSEL injection-locked by a master DFB laser modulated at 1.25 Gb/s. The range of injection powers (non-calibrated) was chosen based on practical launching powers (~ 5 dBm) and system loss (15–20 dB). Results show that there exists an optimal injection power that yields the largest locking range, and therefore, the best stability performance. The locking range is small at high injection powers because of a stronger modulated signal on the injection-locking carrier wavelength, and also at low injection powers is due to insufficient optical power to injection-lock the VCSEL. The locking range decreases even further with the modulation of the slave laser, with the smallest locking range of approximately 0.015 nm observed when both master and slave laser line-rates are identical. Though such a small locking range may lead to unstable injection-locking performance, uncooled operation may still be achieved through means of effective heat sinking for wavelength stabilization, regular in-line calibration steps, and/or use of a

look-up table. This is because single-mode VCSELs do not mode-hop due to a very large free spectral range (FSR) of 20 to 50 nm. In addition, their emission wavelengths also have well-behaved temperature and aging dependence ($0.05 - 0.1 \text{ nm} / ^\circ\text{C}$). The locking range can be significantly increased up to 0.46 nm at 13-dBm injection power by matching the polarization of the downstream signal to that of the VCSEL. However, to demonstrate the feasibility of the proposed OIL VCSEL scheme under non-optimized conditions, no PM components were used in the experiments.

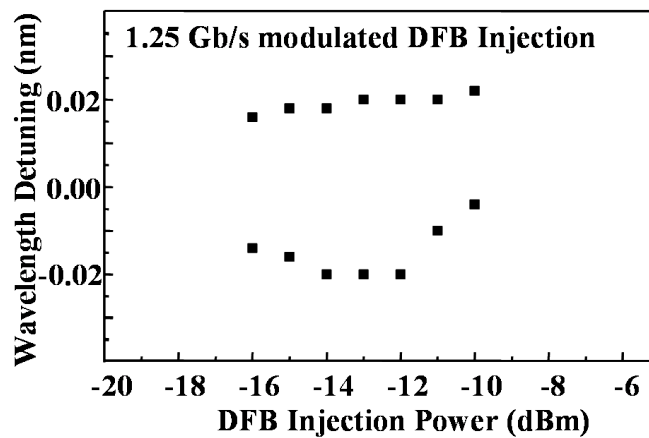


Figure 6.3 Stability plot for a CW VCSEL injection-locked by a master DFB laser modulated at 1.25 Gb/s.

Figure 6.4 shows the superimposed optical spectra of an externally modulated master DFB laser at 2.5-Gb/s and a directly modulated VCSEL at 2.5-Gb/s when it is free-running and injection-locked by the modulated DFB. Although the master and slave lasers are modulated at the same line-rate for a worst-case performance, the injection-locked optical spectrum indicates good performance with a narrower linewidth than that of the free-running VCSEL, and is shifted slightly to the longer wavelength matching that of the master laser.

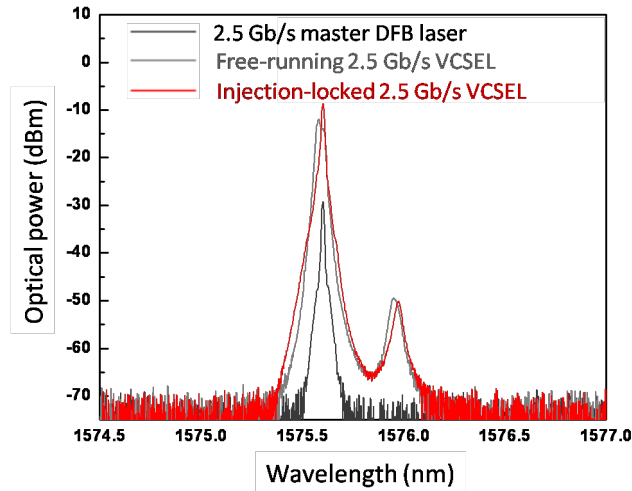


Figure 6.4 Superimposed optical spectra of an externally modulated master DFB laser at 2.5-Gb/s and a directly modulated VCSEL at 2.5-Gb/s when it is both free-running and injection-locked by the modulated DFB.

The BER of the 2.5-Gb/s upstream signal from the VCSEL, injection-locked by the master DFB laser with different line-rates and injection power levels, was evaluated. Figure 6.5 plots the BER curves measured for two injection power levels, -20 and -23 dBm (with coupling loss calibrated), and the master laser operated under CW condition, 1.25 Gb/s, and 2.5-Gb/s line-rates modulation. BER measurements from a 2.5-Gb/s modulated free-running VCSEL are also plotted in Figure 6.5 as a performance comparison. The performance of the VCSEL is clearly improved with OIL mainly due to the chirp reduction. These results were obtained with the upstream and downstream optical extinction ratio fixed to an identical and arbitrarily chosen value of 4.5 dB, enabling the OIL VCSEL upstream performance to be studied only as a function of optical injection power and downstream bit rate. The influence of the downstream optical

extinction ratio on the upstream performance also requires in-depth study and will be presented in the next subsection.

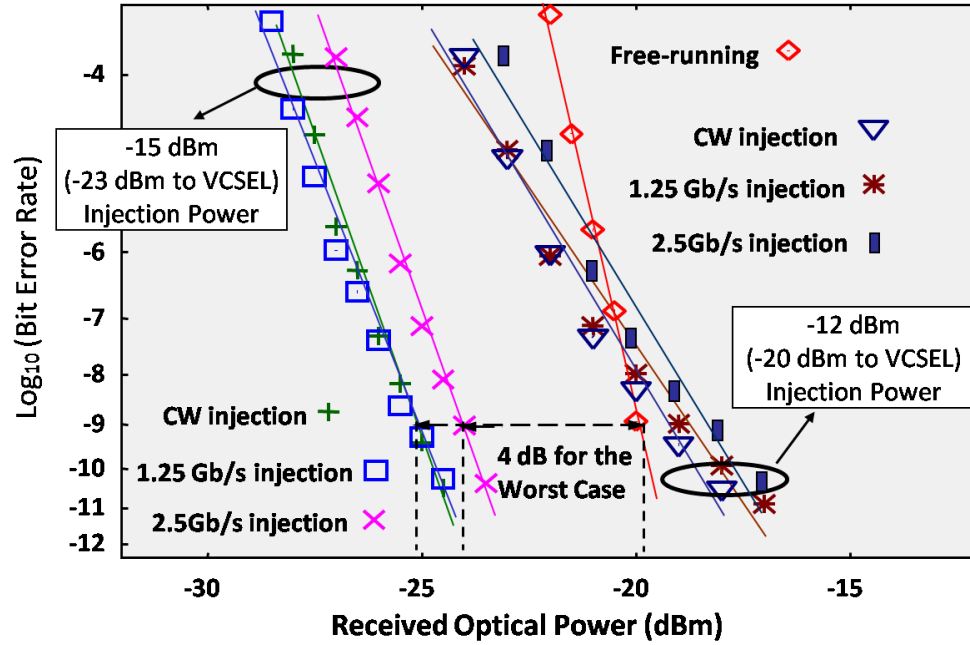


Figure 6.5 Upstream BER of a VCSEL in free-running mode and injection-locked by a CW, 1.25- and 2.5-Gb/s modulated master laser with -23 and -20 -dBm absolute injection power levels.

Even though results in Figure 6.5 show the feasibility of transmitting upstream data from the free-running VCSEL, the setup is a single channel experiment that neglected the potential high transmission losses and out-of-band crosstalk arising from misalignment of the free-running VCSEL wavelength with the AWG passband. With injection locking at an absolute power of -20 dBm, an improvement in upstream transmission performance over the free-running case is observed but only at high BER measurements, a feature applicable to networks implementing forward-error correction. As for the case of -23 -dBm injection power, a major improvement of $4 - 5$ dB at $\text{BER} = 10^{-9}$ was obtained over the free-running case, allowing an increased power margin in the network. With both

injection power levels, the performance degrades with increasing master line-rate. Further, an interesting observation arises with the VCSEL injection-locked by the master laser under CW operation. Even though no modulation exists on the optical carrier at CW, transmission performance is observed to degrade as injection power is increased. This characteristic can be attributed to the fact that high injection power can result in high CW reflection from the surface of the VCSEL due to its high reflectivity top mirror, thereby degrading the extinction ratio, and hence the transmission performance. Compounding the issue is that high injection power can possibly excite another non-lasing polarization mode of the VCSEL, which in turn can degrade the transmission performance due to mode hopping or competition.

These results, therefore, indicate that our proposed scheme benefits from stable injection locking with low injection power, which also benefits the detection of downstream signals at the ONU. The power splitter ratio can then be easily designed to maximize the performance at both the downstream receiver and the OIL VCSEL upstream transmitter.

In addition, the proposed scheme can be applied to 850- and 1330-nm VCSELs used in in-house communication with multimode fiber links. It eliminates costly components such as external broadband or narrowband light sources for injection locking, and external upstream signal modulators. Furthermore, potential uncooled operation through effective heat sinking may eliminate the need for temperature control and monitoring circuits. These features make OIL VCSELs highly desirable for broadband low-cost WDM-PONs.

6.1.2 Rayleigh Backscattering and Extinction Ratio Study

In practice, bidirectional optical networks are much preferred in PON due to reduced management and fiber costs. However, with optical injection locking in the proposed WDM-PON scheme, the master (downstream) and slave (upstream) wavelengths are identical, resulting in upstream performance degradation at the receiver in the CO caused by Rayleigh backscattered-induced intensity noise of the master DFB laser [96]. In this subsection, we study the performance dependence of OIL VCSELs on Rayleigh backscattering effects in a 25-km bidirectional optical link, and on the modulated downstream data of the master DFB laser. We evaluate the BER of the modulated upstream signal against the upstream signal to Rayleigh backscattering ratio (SRR) as well as the optical extinction ratio (ER) of the modulated downstream signal at a constant injection power. The results show that error-free performance in a bidirectional network is easily achieved with an SRR of > 13.4 dB, and with a small linear dependence on the downstream ER. Further, the small-signal frequency response of the OIL VCSEL exhibits a high-pass filter characteristic that suppresses the modulation of the downstream master carrier, achieving stable injection locking of the slave VCSEL.

Switching from the unidirectional configuration to the bidirectional configuration, the experimental setup needs to be modified accordingly with slightly more complexity. Figure 6.6 shows the revised non-PM single channel experimental setup. Same devices and operation conditions are used as before. At the CO, CW light from a DFB laser was externally modulated with 2.5 Gb/s $2^{23}-1$ NRZ PRBS from BERT1. The degree of Rayleigh backscattering, and hence the value of SRR, was set by adjusting the optical power of the downstream signal via the optical attenuator, ATTN1, whereas the

downstream ER was varied by changing the modulating data amplitude of BERT1. The downstream signal was coupled into a 25 km span of fiber using an optical circulator. At the ONU, a configuration comprising two optical circulators, a 3-dB coupler, and ATTN2, was used at the ONU to receive and optically attenuate the downstream signal to yield an absolute injection power of only -25 dBm into the VCSEL. Conversely, the upstream signal from the OIL VCSEL bypasses the 3-dB coupler and ATTN2 so that the output power from the ONU is maximized, since there is $8 \sim 10$ dB coupling loss from the VCSEL to ATTN2. Throughout the experiments, the VCSEL was modulated with 2.5 Gb/s $2^{23}-1$ NRZ PRBS from BERT2 and the upstream signal was detected at the CO, where SRR is calculated using the following equation:

$$\text{SRR (dB)} = 10 \log_{10} (\text{upstream signal power} / \text{Rayleigh backscattering power}).$$

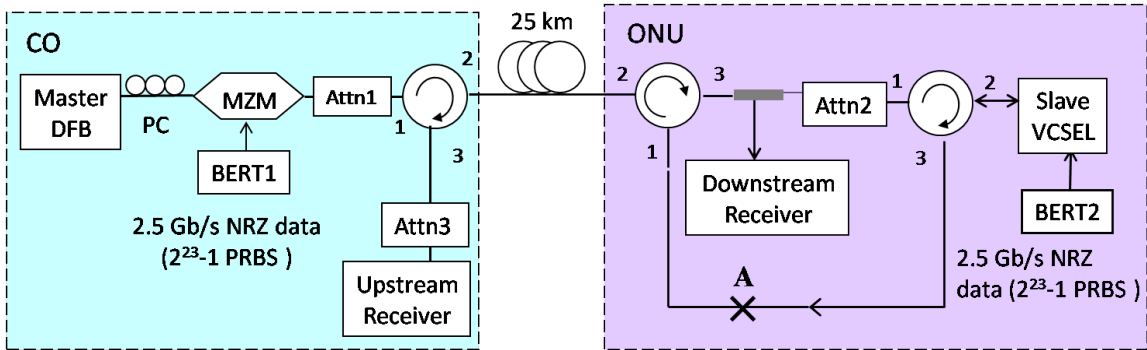


Figure 6.6 Single-channel experimental setup to study upstream performance dependence on Rayleigh backscattering and downstream optical extinction ratio in bidirectional WDM-PON using a $1.55\text{-}\mu\text{m}$ OIL VCSEL as upstream transmitter.

At the CO, the upstream signal power was measured in the absence of the downstream signal, while Rayleigh backscattering power from the downstream signal was measured with the VCSEL biased below threshold and with the fiber at location **A** disconnected. To ensure that only Rayleigh backscattering and not back reflections from

fiber end-facets and connections was considered, angled connectors were used in the setup along with optical circulators to provide further isolation.

We first analyzed the Rayleigh backscattering effects by adjusting the downstream and upstream ERs to a constant 4.5 dB while varying the SRR. Figure 6.7(a) shows BER measurements of 2.5 Gb/s upstream signals from the VCSEL optically injection-locked by 2.5 Gb/s downstream signals for different values of SRR.

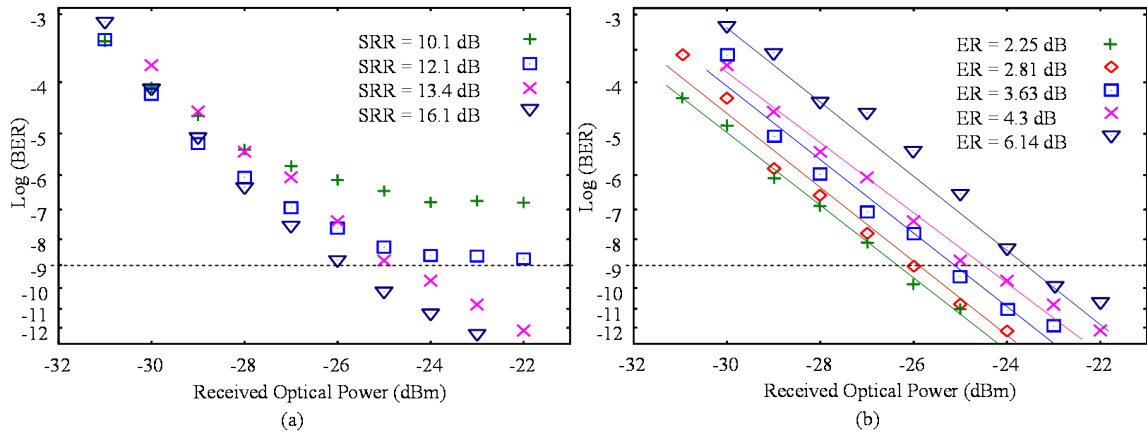


Figure 6.7 Upstream BER curves for different values of (a) SRR at a constant downstream ER of 4.5 dB and (b) downstream ER at a constant SRR of 13.4 dB.

The upstream BER degrades with decreasing SRR, inducing power penalties and error floors. Nonetheless, results show that the influence of Rayleigh backscattering can be drastically reduced to achieve error-free transmission (at $BER < 10^{-9}$) if the SRR is higher than 13.4 dB. This is easily achievable within the design limits of a practical system using lensed-fiber pigtailed VCSELs with < 1 dB coupling loss, thereby significantly increasing upstream signal power at the CO. Maintaining the SRR and upstream ER at 13.4 and 4.5 dB, respectively, the downstream ER was then varied with the corresponding upstream BER curves shown in Figure 6.7(b). While error-free

transmission is achieved in all cases, the increase in downstream ER degrades upstream performance. In the worst-case scenario, an increase in downstream extinction ratio from 2.25 to 6.14 dB incurs ~3 dB degradation on the upstream BER.

Figure 6.8 plots the minimum power required to achieve error-free versus downstream ER for both upstream and downstream signals. The solid color lines represent the relative optical ER dependencies of both upstream and downstream signals in a bidirectional network with 25-km fiber and unidirectional back-to-back setup (i.e. no Rayleigh backscattering or transmission penalty). Results show a power penalty of < 2 dB from 25 km of transmission and Rayleigh backscattering, but more importantly, a linear and small dependence of the upstream signal on the downstream ER compared to high exponential dependence of the downstream signal on the downstream ER.

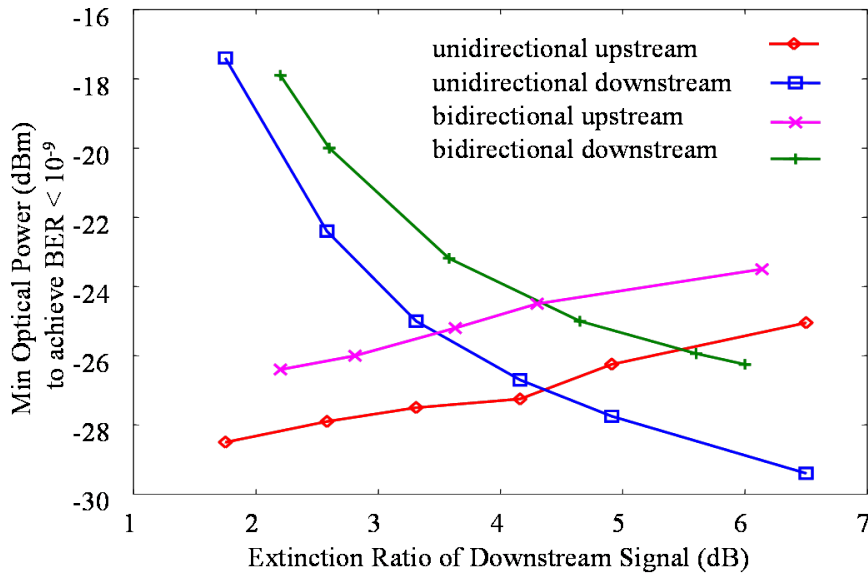


Figure 6.8 Characteristics of received optical power at error-free versus downstream extinction ratio in both unidirectional and bidirectional network configurations.

Finally, to study why the modulation data on the downstream master light does not significantly interfere with the upstream data imposed onto the VCSEL after OIL, small-signal frequency response of the OIL VCSEL under similar injection power as in the transmission experiment are taken at various detuning values, namely at -0.012, 0.018, 0.036 nm is shown in Figure 6.9. In this case, the master DFB carries the modulation while the VCSEL is under CW operation and injection-locked by the master light. The response curves are analogous to that of a high-pass filter with a cutoff frequency of 8 GHz, and show an increase in damping with increasing on the detuning value. These results indicate that the high-pass filter characteristic of the OIL VCSEL provides suppression of the 2.5 Gb/s modulation on the downstream master carrier, thereby effectively injection-locking the VCSEL as though it is a CW carrier. Note that suppression of the 2.5 Gb/s incoming downstream signal will not affect the directly modulated 2.5 Gb/s upstream signal as they undergo different processes inside the VCSEL. The former interacts with the VCSEL through photon carrier exchange while the latter directly modulates the VCSEL carriers.

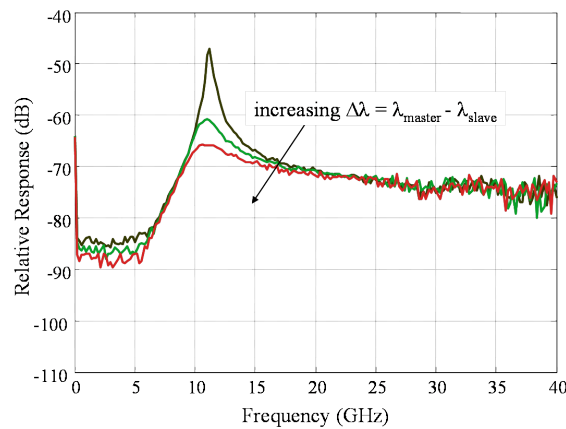


Figure 6.9 Small-signal frequency response of OIL VCSEL while the master laser is externally modulated at various detuning values, namely at -0.012, 0.018, 0.036 nm.

Therefore, The upstream performance of a 1.55- μm slave VCSEL optically injection-locked by a modulated downstream signal in a bidirectional network is shown to be minimally dependent on the downstream ER, and exhibits error-free performance with an SRR > 13.4 dB, an easily achievable value in a practical network. The frequency response of the OIL-VCSEL shows a high-pass characteristic that suppresses the master modulated downstream signal, which is highly desirable for the WDM-PON scheme discussed here.

6.1.3 Fault Monitoring and Localization Scheme

As the WDM-PON is expected to be first deployed by business customers with high capacity information in both upstream and downstream directions, real-time knowledge of a fiber fault and the location of the fault will ensure rapid rectification and restoration of transmission [97]. However, despite all its advantages, a typical WDM-PON architecture does not allow for easy diagnostic of fiber failures due to its tree and branch topology. The feeder fiber from the CO to the AWG in the remote node (RN) can be considered as the trunk of the tree network whilst the distribution fibers from the RN to the end user at the ONUs can be equated to branches of the tree network. Conventional optical time-domain reflectometry (OTDR) based on a single wavelength source at the CO is not applicable in a WDM-PON due to the wavelength-routing characteristics of the AWG in the RN [98]. Likewise, OTDR with a broadband optical source is unsuitable because reflections from different distribution fibers after the AWG will overlap back at the CO thus making the reflected pulses from different distribution fibers indistinguishable. Solutions based on tunable OTDR methods adds cost and complexity due to the requirement of a tunable laser source at the CO and the need to schedule

OTDR pulse transmission sequentially in a round-robin fashion amongst the branches of the WDM-PON [99]. An alternative proposal uses the optical transmitter at the CO to transmit an OTDR pulse upon detecting the absence of upstream signals [100].

Aside from OTDR methods, two solutions have been proposed recently that exploits the combination of a broadband source in the CO and optical reflectors at the ONU [101, 102]. For fiber fault monitoring, a broadband source (e.g. super-luminescence light emitting diode (LED), semiconductor optical amplifier (SOA) or EDFA) is employed in the CO to emit broadband light towards the RN. The broadband light is centered at waveband different than that of the upstream and downstream wavelengths. At the RN, the AWG slices the broadband light into narrowband slices, each corresponding to a distribution fiber and ONU. Each sliced light can be considered a monitoring channel in which light is reflected at the input of an ONU via an optical reflector comprising of either a wavelength dependent component such as a fiber Bragg grating [101] or a combination of a wavelength coupler and a wideband mirror centered on the emission waveband of the broadband source [102]. The reflected light is then detected back at the CO via an OSA or an optical tunable filter connected to a power meter. The former allows for simultaneous monitoring of all monitoring channels, whereas sequential monitoring is achieved in the latter. Thus, depending on presence or absence of a monitoring channel and its associated upstream channel, failures pertaining to one or more distribution fibers, feeder fiber and upstream transmitter can be monitored. Nonetheless, both schemes require the output power of the broadband source to be high due to losses from spectral slicing and bidirectional traversing of the monitoring channel in the outside plant. Additional costs are also associated with the OSA or the tunable

filter with an integrated optical power meter. More importantly, to install the fault monitoring and localization feature in an already deployed WDM-PON requires an upgrade of all ONUs whereby a wideband optical reflector or a wavelength dependent filter is required to be added. Ultimately, this feature should be provided without requiring any changes to be made at the ONU side. Since the access network segment is particularly cost-sensitive due to the relatively small number of end users it services without the benefits of large cost-sharing, minimizing the costs especially at the ONU end while having the ability to provide added features is very important for network operators.

In this subsection, it will be seen that a simple and cost-effective fault monitoring and localization scheme using a low bandwidth and low output power fault monitor in an OIL VCSEL WDM-PON scheme is possible. Without requiring additional narrowband/broadband injection-locking sources in the CO, the VCSELs are optically injection-locked by modulated downstream signals from the CO to align the upstream wavelengths to that of the downstream, and hence to the WDM grid without active temperature control. The fault monitor is added only to the CO without modifications to the ONUs. Once the monitor is in place, monitoring can be implemented individually and on-demand by each customer depending on their service level agreement. Here we propose and show the proof-of-concept demonstration of using the inherent mirror structure of VCSELs to provide monitoring and localization of fiber and device faults in a PON. We will demonstrate the feasibility of the proposed scheme with characterizations of the fault monitor that function reliably with high sensitivity (~ -67 dBm), low output power (~ -7 dBm) and low bandwidth (~ 2 kHz) requirements. We also show that the

addition of the monitoring scheme to an existing infrastructure incurs a negligible penalty (~ 0.5 dB) on the upstream transmissions of the WDM-PON.

Figure 6.10 shows the schematic of a WDM-PON implementing the proposed fault monitor comprising a low-power broadband source, a lock-in module, and a series of low-bandwidth detectors. The broadband light source is centered on a waveband distinct from the downstream and upstream wavelengths of the network and is modulated with an AC signal at a reference frequency, f_{req} , from a lock-in module. In the downstream direction, the spectral and cyclic properties of the arrayed waveguide grating, AWG2, at the remote node slices the broadband light source into multiple monitoring channels, each directed towards a different ONU along with the pre-assigned downstream channel. At the ONU, the downstream signal is detected, and also used to injection-lock the VCSEL upstream transmitter. As long as the monitoring channel does not coincide with the lasing wavelength of the VCSEL, it will be reflected by the DBR mirrors of the VCSEL with $\sim 99.5\%$ reflectivity. Back at the CO, the upstream and reflected monitoring channels from each ONU are separated by a coarse WDM (CWDM) filter at the output port of AWG1. The monitoring channel is detected with a low-bandwidth detector (bandwidth $\approx f_{\text{req}}$) and fed back into the lock-in module for measurement. The lock-in module singles out the DC component of the detected signal at f_{req} and rejects noise signals at all other frequencies, thus allowing robust detection of very small AC signals in wideband noise background. The power level of all monitoring channels can be determined from their respective lock-in measurements and in turn, can be used to determine the status of the feeder and distribution fibers, and also the VCSEL transmitter.

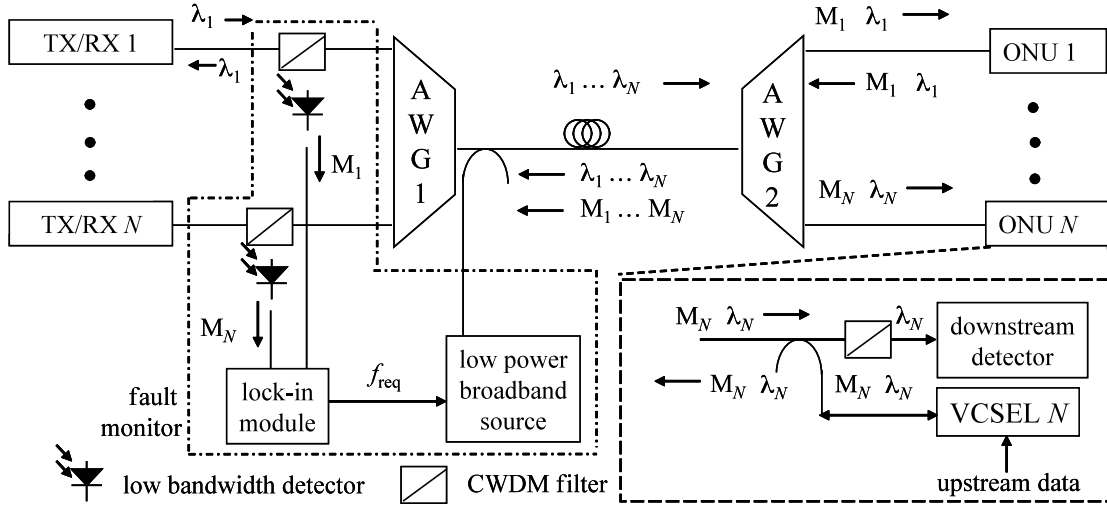


Figure 6.10 Novel fault monitoring and localization scheme in a WDM-PON with OIL VCSELs and lock-in-amplifiers.

The experimental setup used to investigate the feasibility of the proposed scheme and for characterization of the fault monitor is schematically shown in Figure 6.11. At the CO, CW light at 1576.1 nm from a DFB laser is externally modulated with $2^{23}-1$ NRZ PRBS data from a BERT. The downstream signal is coupled with broadband light from an EDFA and directed towards an optical circulator, 20 km of feeder fiber, AWG and 2.2 km of distribution fiber. The broadband light which is modulated with $f_{\text{req}} = 2$ kHz from a commercial lock-in module is sliced into narrowband monitoring channels by the cyclic AWG. The channel spacing and 3-dB pass-band of the AGW are 0.8 nm and 0.5 nm, respectively. At an ONU, the downstream channel optically injection-locks a 1.55- μm VCSEL, while the monitoring channel is reflected by the top DBR mirror of the VCSEL.

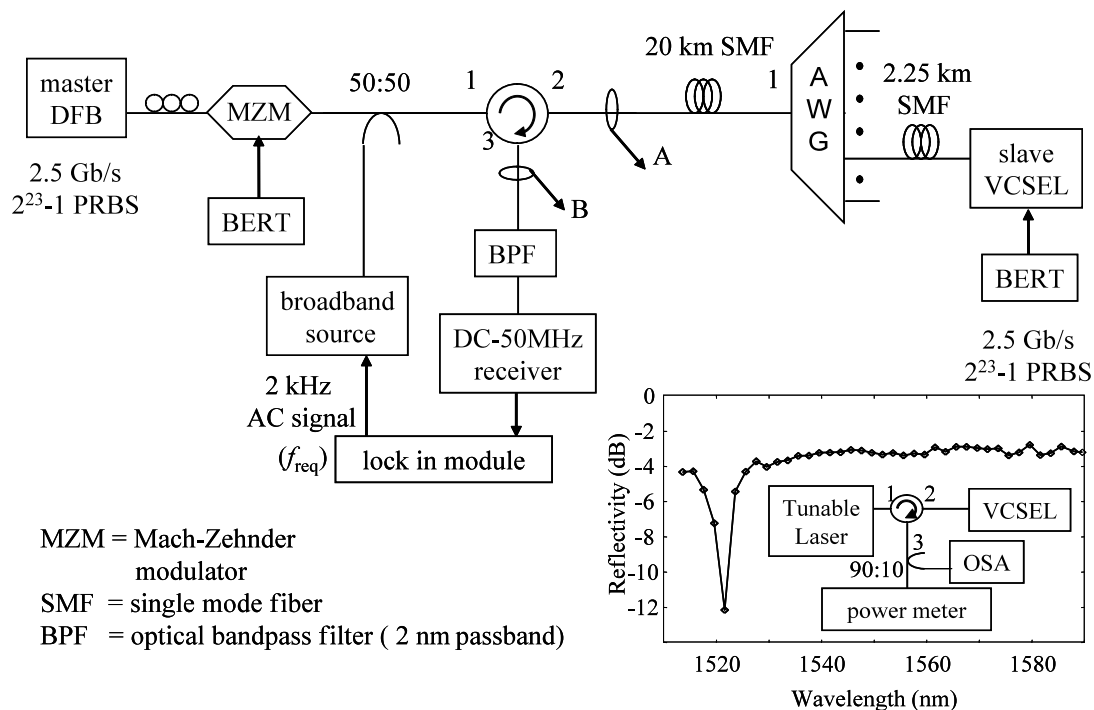


Figure 6.11 Experimental setup. Inset is the reflection spectrum of a tunable laser beam from the VCSEL top mirror when the VCSEL is off.

The inset of Figure 6.11 shows the reflection spectrum from the VCSEL top distributed Bragg reflector (DBR) mirror when the VCSEL is switched off. Only the short wavelength side of the spectrum of the DBR (reflectivity vs. wavelength) could be measured, as the tunable laser used was limited in wavelength tuning range. Further, note that since the VCSEL is free-spaced coupled to Port 2 of the optical circulator, the reflection spectrum is only a relative measure of the input power at Port 2 and the reflected output power at Port 3. Nevertheless, the reflection spectrum indicates a stop-band that is wider than the broadband optical spectrum of the EDFA, allowing all monitoring channels to be reflected. The stop-band and band edge of the VCSEL top mirror can be designed accordingly by changing the composition of the DBRs while the

reflectivity can be increased by changing the number of DBR layers. Throughout the experiment, the VCSEL was biased at 6.32 mA (~ 1 mW output power) and modulated with 2.5 Gb/s $2^{23}-1$ NRZ PRBS from a second BERT. Along with the reflected monitoring channel, the modulated output from the VCSEL that is aligned to the wavelength of the downstream channel is then sent back upstream towards the CO. At the CO, the monitoring channel is detected using an optical band-pass filter, a coarse WDM filter, a low bandwidth (DC ~ 50 MHz) detector and the lock-in module. The optical band-pass filter with a 2 nm pass-band was implemented in place of an AWG at the CO.

To visually demonstrate the feasibility of the monitoring scheme, the optical spectra of the downstream, upstream and monitoring channels were observed at locations **A** and **B** of the experimental setup in Figure 6.11. The optical spectra of the modulated downstream signal and broadband monitoring source measured at location **A** are shown in Figure 6.12(a), while that of the reflected monitoring channel and the upstream channel from the OIL VCSEL in a network without failures measured at location **B** are shown in Figure 6.12(b). It should be noted that the low peak powers of downstream and upstream signals are attributed to the low resolution of the OSA measuring over a large wavelength span. Further, the two reflected monitoring channels, spaced apart by the FSR of the AWG, are caused by the broadband source having a bandwidth larger than the AWG's FSR. For these measurements, the launching power of the broadband source was intentionally increased to +9 dBm and all other ports of the AWG were properly terminated to enable only the monitoring channel(s) on the specific output port connected to the VCSEL to be clearly observed on the OSA. At system initialization in the absence of network failures, the power level of the monitoring channel for each ONU is recorded.

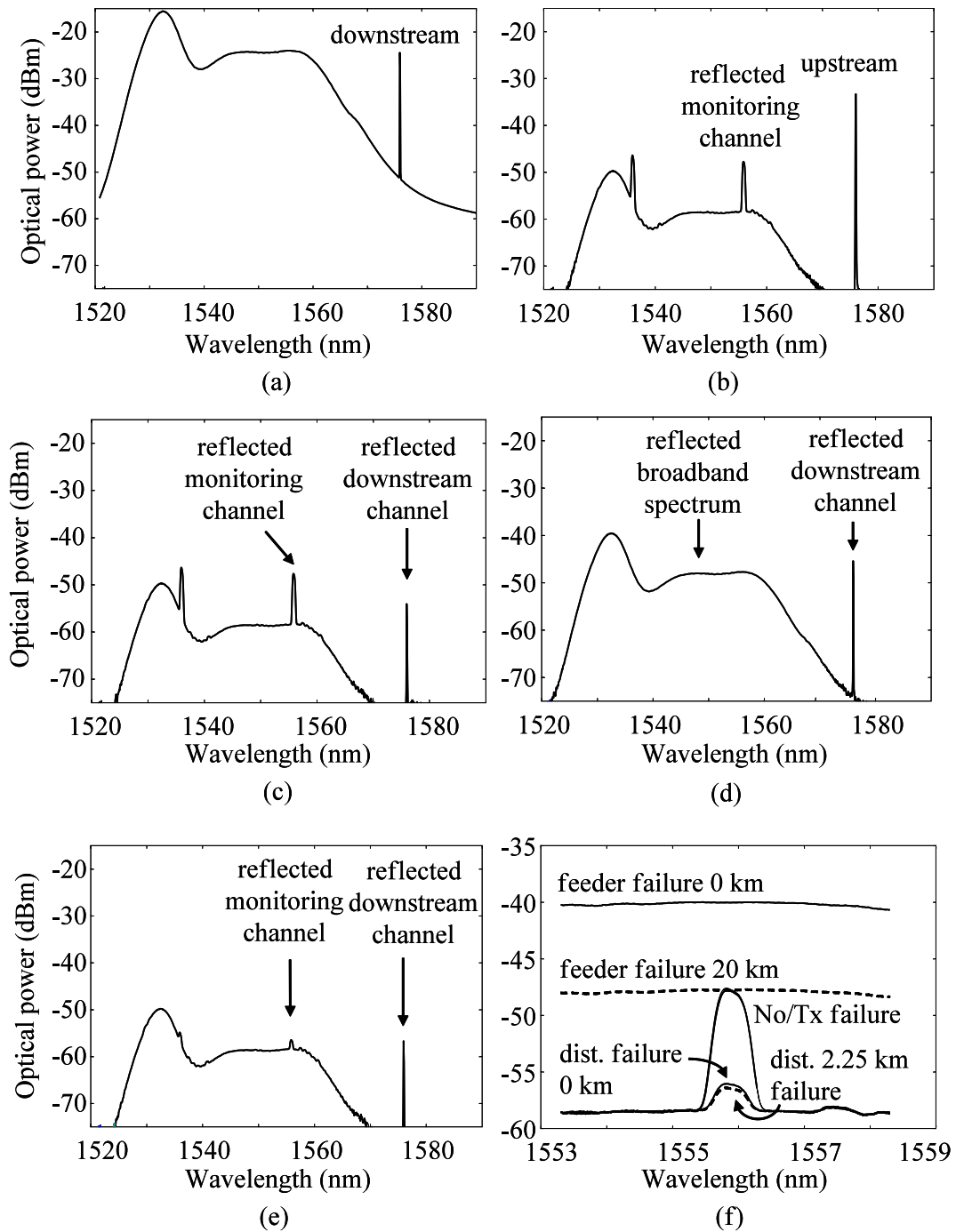


Figure 6.12 Optical spectra measured at locations **A** (Fig. 3(a)) and **B** (Fig. 3(b)-(f)) of the experimental setup in Figure 6.11: (a) broadband light + downstream channel (b) no failure (c) transmitter failure (d) feeder fiber failure at 20 km (e) distribution fiber failure at 2.25 km after AWG (f) monitoring channel in detail.

Figure 6.12(c)-(e) show the optical spectra measured at location **B** for the following network conditions: in the event of VCSEL transmitter failure; feeder fiber cut at 20 km; and distribution fiber cut at 2.25 km from the AWG, respectively. We simulated the VCSEL transmitter failure by biasing the device below threshold under non-lasing condition. In the monitoring scheme, transmission failures are diagnosed with the presence of a monitoring channel at the non-failure power level *AND* in the absence of the associated signal in upstream receiver. Distribution fiber failures are diagnosed with an optical power level of the monitoring channel being lower than the non-failure power level, with the lowest power recorded for a distribution fiber cut located just before the input to the ONU (i.e. at 2.25 km away from the AWG in our setup). Likewise, feeder fiber failures are diagnosed with a power level of all monitoring channels being above the non-failure power level.

Figure 6.12(f) shows the power level of the monitoring channel (1555.8 nm) in detail, measured at location **B** under different conditions of fiber and transmitter failures. In particular, the distribution fiber breaks at 0 km and 2.2 km away from the AWG are clearly discernable allowing the exact location of the fiber fault to be determined. Even at lower launching powers of the broadband source, the monitoring scheme is able to determine the exact location of the fiber fault due to its capability to differentiate small amounts of changes in the optical power levels using the lock-in measurements, as evident from our measurements of the lock-in DC signal as a function of received optical power at the low-bandwidth detector.

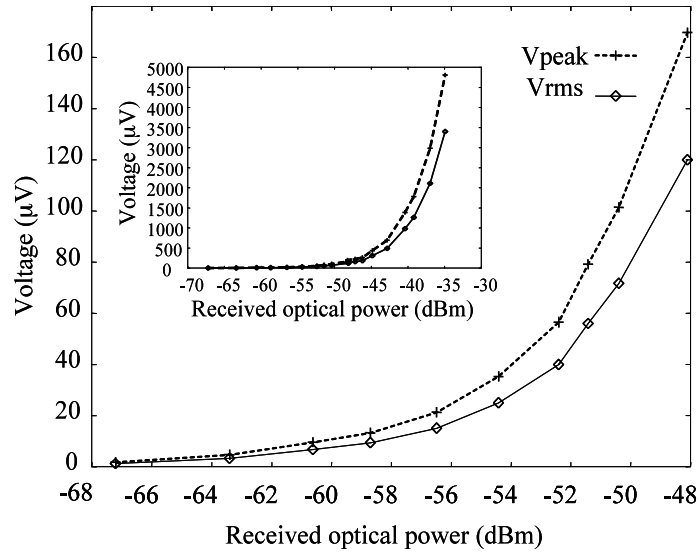


Figure 6.13 DC signal of monitoring channel measured at lock-in amplifier as a function of optical power received at the low bandwidth receiver. The inset shows DC measurements over a wider range of received optical power from -67 dB to -35 dB in this case, highlighting the ability to detect signals over a large dynamic range.

The DC signal of the monitoring channel measured at the lock-in amplifier is plotted in Figure 6.13 as a function of optical power received at the low bandwidth receiver in the monitor. The detection rate is measured to be $5 \mu\text{V}_{\text{rms}} / 1 \text{ nW}$, with stable DC measurements down to $1.3 \mu\text{V}_{\text{rms}}$ or -67 dBm. Taking into consideration the spectral slicing and roundtrip propagation losses incurred by the monitoring channel in a typical WDM-PON (i.e. Figure 6.10) and the results in Figure 6.13, our monitoring scheme can accommodate a broadband source with a total launch power of as low as -7 dBm, allowing a lower cost alternative such as an LED rather than an EDFA to be used. In a worst case that the distribution fiber breaks at 2.25 km away from the AWG, a reflected monitoring signal with power of -67 dBm can still be detected by the lock-in module. The sensitivity of the monitor can potentially be increased by using a detector with an even

lower bandwidth, ideally at 2 kHz. Likewise, the upper limit in the received optical power is limited only by the maximum tolerable input power of the low bandwidth receiver. The inset of Figure 6.13 shows DC measurements over a wider range of received optical power (from -67 dB to -35 dB in this set of measurements), highlighting the ability to detect signals over a large dynamic range.

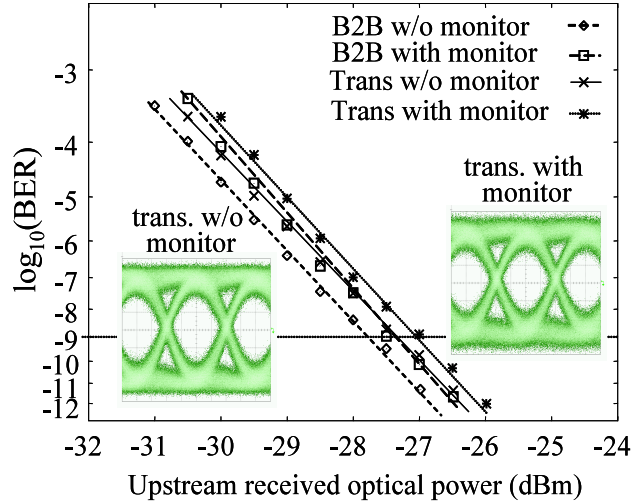


Figure 6.14 BER of upstream signals, repeated for experiments in back-to-back (B2B) and 22.25 km transmission configurations, with and without implementing the monitoring scheme. The eye diagrams measured at $\text{BER} = 10^{-9}$ for the 22.25 km transmission case are shown as insets.

BER measurements of a 2.5 Gb/s upstream signal from the OIL-VCSEL is performed to investigate the power penalty incurred by the monitoring scheme. It is essential that the added feature of monitoring and localization of faults is non-intrusive to the signals on the network and also the injection-locking performance of the VCSEL. To detect the upstream signal, we tuned the BPF to the upstream wavelength of 1576.1 nm and detect the optical signal using a 2.5 Gb/s APD. The BER measurements obtained for the back-to-back (B2B) and transmission configurations, with and without implementing the monitoring scheme are shown in Figure 6.14. The eye diagrams for the transmission

case with and without the implementation of the monitoring scheme at $\text{BER} = 10^{-9}$ are shown as insets. Results in both B2B and transmission cases show a 0.5 dB power penalty at $\text{BER} = 10^{-9}$, demonstrating the monitoring scheme to have minimal impact on the transmission and OIL performance of the VCSEL.

In summary, this is a novel scheme of fault monitoring and localization in a WDM-PON with a wavelength-dependent passive tree and branch topology. Using a highly sensitive but low-cost monitor comprising a low output power broadband source and low bandwidth detectors, in conjunction with the high reflectivity mirror of VCSELs, the monitoring channel can be fed back and detected with high sensitivity at the central office. Experimental investigations indicate that the added benefit of implementing the proposed fault-monitoring scheme imposes minimal cost associated with upgrades to the network, and also minimal penalty to data transmissions on the network.

Chapter 7

Optical Injection Locking of Multimode VCSELs

Recently, there has been growing interests and research on developing 100Gb/s Ethernet LAN [103] and 60-GHz radio-over-fiber (RoF) systems [104] using multimode (transverse mode) VCSELs due to the tremendous bandwidth optical fiber provides over electrical cables, and the cost-effective manufacturing and performance advantages of multimode VCSELs. However, it is well known that multiple modes lasing at different wavelength of a laser, such as Fabry-Perot (F-P) lasers, would introduce mode competition noise and modal dispersion, which prevent these devices from being used for high-speed or long-distance transmission [105]. On one hand, this led to the active research and development on single-mode lasers in the early 80s, which are now widely deployed in long-haul and high-performance transport networks in spite of their expensive cost. On the other hand, OIL was experimented in the same era on F-P lasers with the aim of creating a single-mode device by selectively locking a particular longitudinal mode of the F-P laser [7]. However, the small FSR (~ 0.1 nm) between different cavity modes of the F-P laser greatly confines the tuning and locking range, thus limiting the stability and the dynamic performance improvement OIL can provide [106]. For multimode VCSELs, on the contrary, due to very small cavity length (~ 1 μm) the FSR is large enough to emit only a single longitudinal mode. However, large device

aperture size is typically designed to have enough current injection and reasonable output power, but at the same time it supports multiple transverse modes emission, which typically exhibit 1 to 2-nm mode spacing. Therefore, there are two major advantages of OIL on multimode VCSELs compare to F-P lasers. First, the much larger mode spacing would allow large detuning, thus larger locking range for a selected mode. Second, other than frequency selection, spatial mode profile matching is an extra degree of freedom that one can utilize to accomplish locking preferentially on a particular (especially higher-order transverse) mode. Our study and demonstrations on injection-locked single-mode VCSELs show much improved performance in many aspects as discussed in the previous chapters. Hence, it is straightforward to expect that similar improvement could be seen on injection-locked multimode VCSELs as well, possibly with some slight variation on the parameter values. OIL on multimode VCSELs has been studied before, but only in the weak injection regime with no dynamic performance (e.g. modulation characteristics) reported [107, 108].

In our work, we are interested in exploring the possibility of using OIL to improve the direct modulation response of multimode VCSELs by leveraging the unique properties of these devices with both spatially and spectrally well-separated modes. We hope this technique will provide an important solution to low-cost upgrades of existing embedded LANs and future 60-GHz RoF for indoor distributed wireless networks.

In this chapter, I will show preliminary results on experimentally improved frequency response, data transmission performance as well as numerically simulated stability performance of injection-locked 1.55- μm multimode VCSELs. Important issues that require further study in the future are also discussed.

7.1 EXPERIMENTAL RESULTS OF SMALL-SIGNAL FREQUENCY RESPONSE

The experimental setup of OIL on a multimode VCSEL is essentially the same as the one for a single-mode VCSEL, except that the device used in this case is multimode with an aperture size of typically 10 ~15 μm (as opposed to single-mode device with an aperture of $< 6 \mu\text{m}$). The lasing threshold is $\sim 6 \text{ mA}$ and maximum output power is $\sim 5 \text{ mW}$ at bias current of 25 mA. Single-mode lensed-fiber is still used in the experiment to inject and collect light from the VCSEL due to the single-mode nature of the master laser. Therefore, because of the substantial size mismatch between the laser aperture and the core of the single-mode fiber, coupling loss of 5 ~ 10 dB is usually present.

7.1.1 Resonance Frequency and Bandwidth Enhancement

For the small-signal frequency response measurement, the VCSEL is biased at 10 mA with 1.2-mW output power. This condition is chosen with an aim at obtaining both multimode operation on the device as well as an optimized RF response, i.e. maximizing the modulation bandwidth enhancement, because the number of modes increase with the bias current, but keeping a high injection ratio (lower slave laser bias) would help obtain larger modulation bandwidth. Under this condition, the VCSEL emits both the fundamental and the first-order transverse mode including two polarization modes that are at wavelength 1.5 nm shorter than the fundamental mode (with higher frequency). If one examines the case in the frequency domain, OIL employs a master laser to frequency lock the slave laser, so either the fundamental or the higher-order mode can be locked since they are at different wavelengths. Indeed, this was demonstrated previously [109]. By optimizing the injection ratio, detuning, and the spatial mode overlap between the master and slave lasers, a regime with plausible locking efficiency and stability can be

found. Locking occurs easily when the master laser wavelength is tuned to preferentially lock to the fundamental mode, which usually has the highest output power (but not significantly higher than other modes since the device is multimode). Locking on the higher-order mode by controlling the spatial mode overlap is also possible and will be discussed in the next subsection.

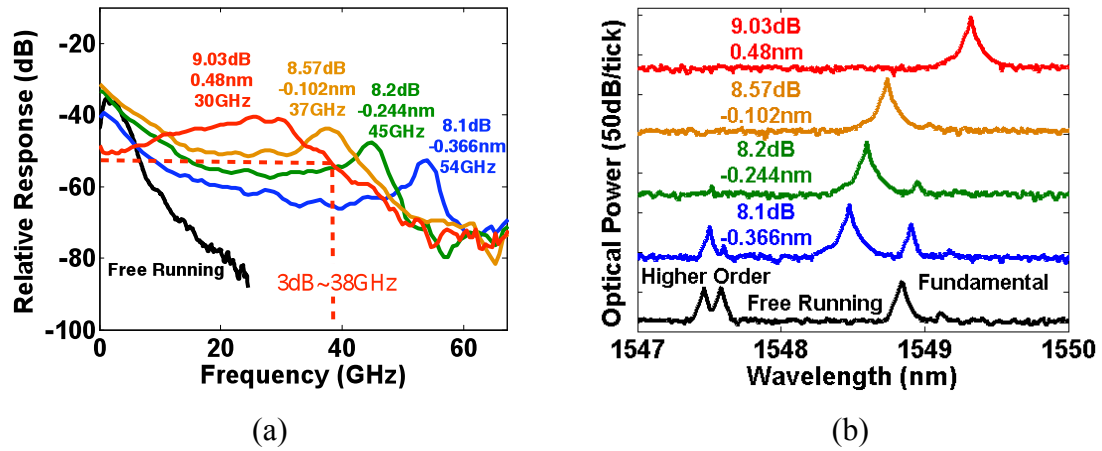


Figure 7.1 Frequency response and optical spectra of a free-running and the corresponding OIL multimode VCSEL with aperture size of $10\ \mu\text{m}$ at various injection ratio and detuning conditions. (a) Small-signal frequency response. Resonance frequency increases from 3 GHz up to 54 GHz and 3-dB bandwidth of 38 GHz is obtained. Response can be tailored by adjusting the locking parameters. The system parasitic is included such as the electric probe (40 GHz), photo-detector (50 GHz) and the bias-Tee (50 GHz). (b) Optical spectra. Master laser locks on the fundamental mode. The higher-order (1st) transverse modes are suppressed under external light injection.

Once stable locking on the fundamental mode is achieved with the higher-order modes greatly suppressed, small-signal frequency response under various master power and detuning conditions are tested. Figure 7.1 shows the response curves and the optical spectra of a multimode VCSEL with and without OIL. Same as in the single-mode case, the data presented here is raw data including VCSEL RC rated at 10 GHz and measurement system parasitics such as the electric probe (40 GHz), photo-detector (50

GHz) and the bias-Tee (50 GHz). In Figure 7.1(a), the free-running VCSEL has a modulation bandwidth of only 3 GHz. However, if it is injection-locked by a master laser, a resonance frequency as high as 54 GHz can be obtained. As it was demonstrated before on a single-mode VCSEL, the frequency response can be tailored by adjusting the injection ratio and the wavelength detuning, similar behavior exhibits on OIL multimode VCSEL as well. When the master laser injecting at the slave laser with higher power (9.03 dB) and farther red detuned (0.48 nm), a flat response is achieved with a 3-dB bandwidth of 38 GHz, which can be potentially used for a 40-Gb/s system.

Figure 7.1(b) shows the corresponding optical spectrum for each locking condition. The black trace is the free-running spectrum showing both the fundamental mode and the first-order mode at bias current of 10 mA. Two polarization modes can also be seen for the first-order mode. Once the fundamental mode is injection-locked, the higher-order mode is greatly suppressed, and the fundamental mode is lasing at the master wavelength. However, this preliminary demonstration is limited by the available master laser power since a multimode VCSEL requires additional power to suppress the higher-order mode.

To test if OIL works for highly multimode VCSELs, two devices with aperture size of 15 μm are also injection-locked independently at the fundamental mode using the same lensed-fiber for coupling at various detuning conditions. Due to the larger aperture the coupling loss is increased to 12 dB, thus lowering the achievable injection ratio. This lowered injection ratio limits the resonance frequency enhancement to ~ 30 GHz from a 3 GHz free-running resonance as shown in Figure 7.2(a) and 7.3(a). A higher power master laser or better coupling mechanism (possibly fiber with larger core size) would allow for enhancement similar to the 10- μm VCSEL. The corresponding optical spectra in Figure

7.2(b) and 7.3(b) show the higher-order mode suppression similar to the 10- μm VCSEL even though more than two groups of higher-order modes are present in the free-running condition.

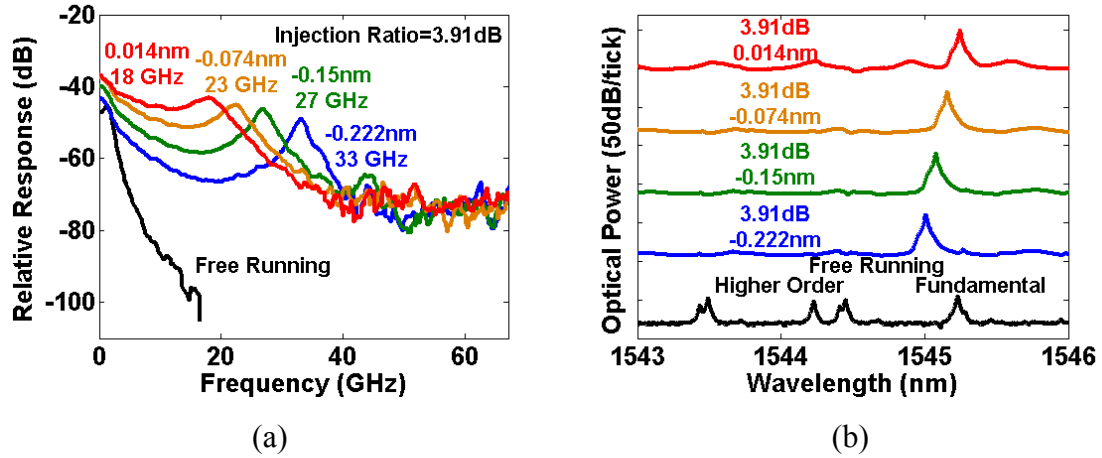


Figure 7.2 Frequency response and optical spectra of a free-running and the corresponding OIL multimode VCSEL with aperture size of 15 μm at various injection ratio and detuning conditions. (a) Small-signal frequency response. Smaller enhancement observed results from the reduced injection ratio caused by larger coupling loss. (b) Optical spectra. Master laser locks on the fundamental mode. The higher-order transverse modes are suppressed under external light injection.

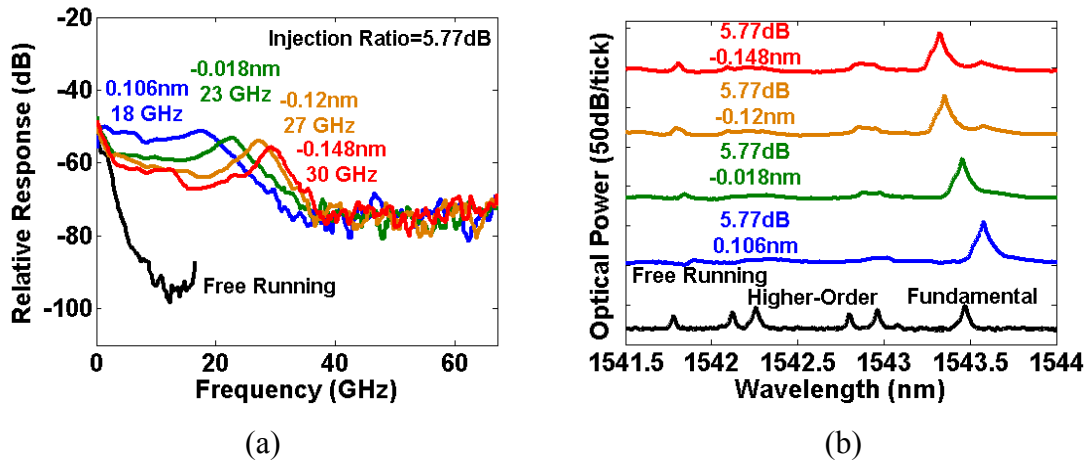
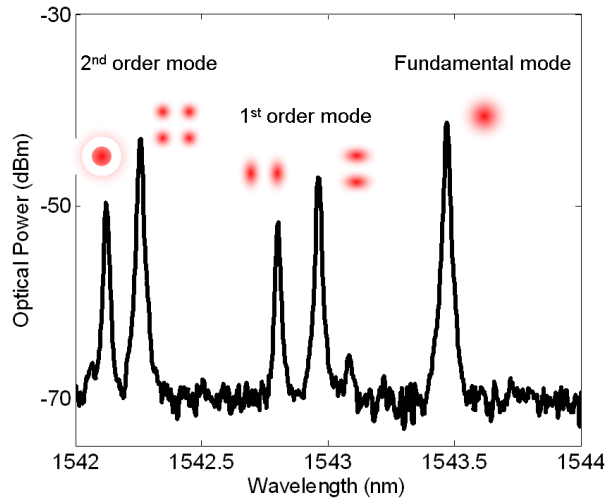


Figure 7.3 (a) Frequency response and (b) optical spectra of another free-running and the corresponding OIL multimode VCSEL with aperture size of 15 μm at various injection ratio and detuning similar as shown in Figure 7.2.

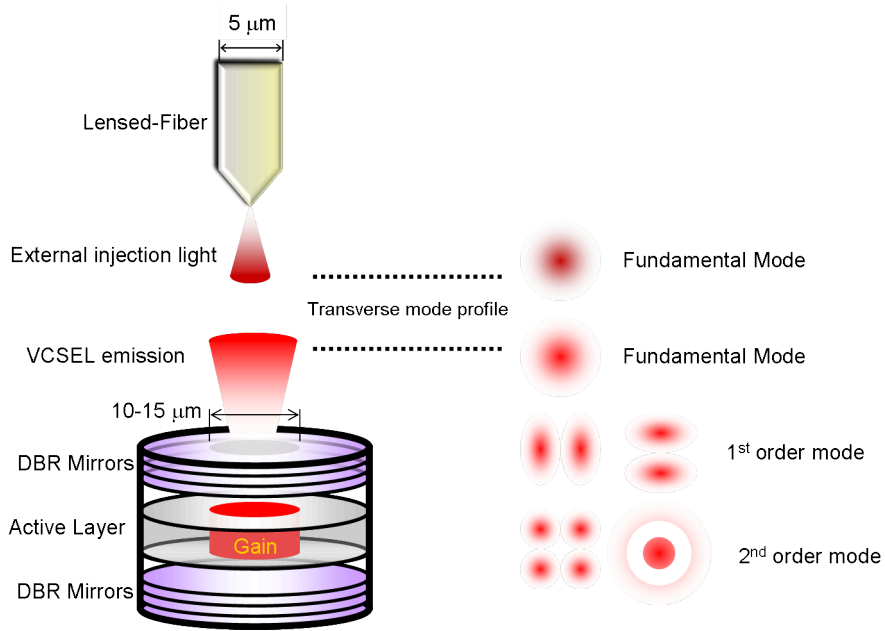
7.1.2 Spatial Detuning

As pointed out earlier in the chapter, multimode VCSELs provide an extra degree of freedom on tuning for the master laser to preferentially select a mode to lock using spatial transverse mode profile. This idea is illustrated schematically in Figure 7.4.

A multimode VCSEL with aperture size of $10 \sim 15 \mu\text{m}$ usually emits the fundamental mode, the 1st order and possibly the 2nd order transverse modes, which are also spectrally separated, as verified by measured optical spectra shown in Figure 7.4(a). Since the master laser emits only the fundamental transverse mode (DFB laser in our case), the lensed-fiber can thus be spatially moved in the horizontal plan to maximize the spatial overlap between the master laser and the preferred mode for injection locking in addition to the frequency selection by tuning the master wavelength. For example, the fundamental mode will be easily locked if the lensed-fiber is coupled to the center of the VCSEL aperture where the fundamental mode has the strongest emission. However, Locking would occur more easily on the higher-order modes if the lensed-fiber is moved to the edge of the aperture, where higher-order modes emit with stronger intensity. By doing so, locking can be achieved more effectively and more robust than by adjusting the detuning only, especially in the case of locking on a higher-order mode, which does not overlap with the master mode profile by default alignment.



(a)



(b)

Figure 7.4 (a) Optical spectrum of a multimode VCSEL with 15- μm aperture size. The spatial profile of each transverse mode is labeled. (b) Schematic showing spatial mode selection by moving coupling lensed-fiber.

The same 15- μm VCSEL used for the measurement shown in Figure 7.3 is examined again here for spatial detuning study. By tuning the lensed-fiber, the 1st order mode can be selected as the favored mode for injection locking. This is shown in Figure 7.5(b) by

the free-running optical spectrum with the 1st order mode being the strongest now among all lasing modes compare to the one shown in Figure 7.3(b). Then injection locking is performed on the 1st order mode. Similar improved modulation response is achieved as shown in Figure 7.5(a). It is interesting to note that a double-resonance is observed due to the presence of two polarization modes both belonging to the 1st order mode. This can be clearly seen on the free-running spectrum in Figure 7.3(b) where no displacement occurs on the lensed-fiber. This double-resonance is similar as the one previously shown in Chapter 3 (Figure 3.9) except that both modes can be actively lasing in this case.

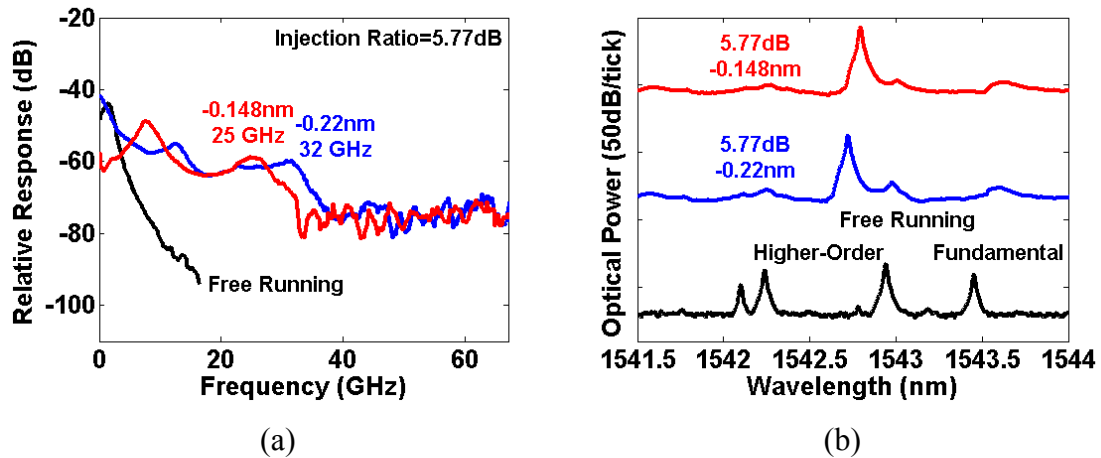


Figure 7.5 shows (a) frequency response and (b) optical spectra of the same 15- μm VCSEL used for the measurement shown in Figure 7.3 but with locking occurs on the 1st order mode. Double resonance is observed in the frequency response due to two polarization modes belonging to the 1st order mode.

7.2 EXPERIMENTAL RESULTS OF LARGE-SIGNAL MODULATION, CHIRP REDUCTION AND TRANSMISSION CHARACTERISTICS

Since injection-locked single-mode VCSELs show much-improved performance on large-signal modulation, chirp reduction and transmission distance enhancement as demonstrated in the previous chapters, and injection locking makes a multimode VCSEL

emit only at one particular mode, similar improved performance from an injection-locked multimode device can be expected if the multimode VCSEL is modulated by large-signal data.

7.2.1 Large-Signal Modulation

A highly multimode VCSEL with a 15- μm aperture is used first to demonstrate large-signal data modulation. When biased at 25 mA, approximately 3X above lasing threshold, four to five modes are lasing simultaneously. For OIL, the device is biased at 12 mA with 3-dBm injection power. Once it is injection-locked, single-mode emission is achieved. Both the modulation index and the bias current of the VCSEL are optimized separately for free-running and injection-locked conditions in order to obtain the best BER performance.

Figure 7.6 shows the optical spectra of both the free-running and the injection-locked VCSEL under 10-Gb/s PRBS modulation. It is obvious that OIL narrows the spectral width greatly, which is a strong indication of significant chirp reduction as will be shown in the next subsection.

The eye diagrams of the same device under free-running and injection-locked conditions are shown in Figure 7.7(a) and (b), respectively. In the free-running case, beating between different modes and frequency chirp result in large intersymbol interference, which almost closes the eye. However, at the same receiver power level, when the VCSEL is injection-locked, the single-mode emission opens up the eye.

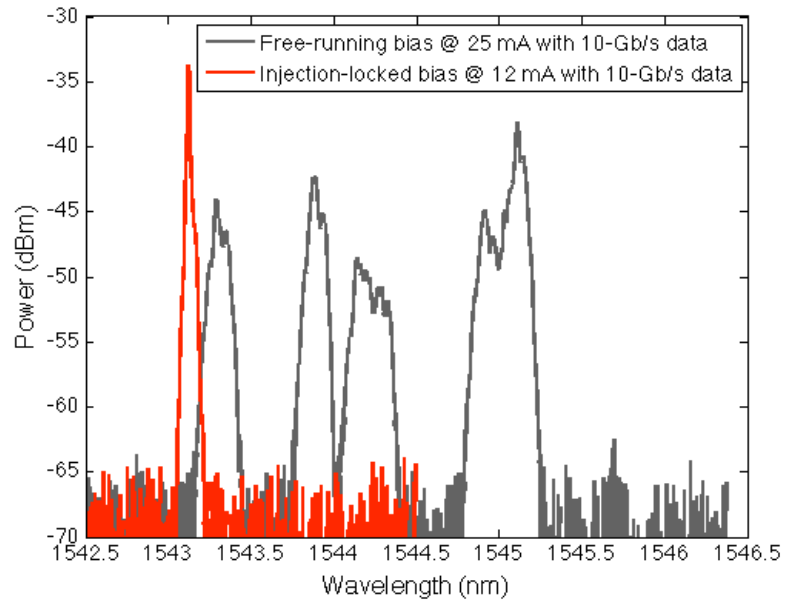


Figure 7.6 Optical spectra showing highly multimode device becomes a single-mode device after injection locking. 10-Gb/s PRBS modulation is applied directly to the VCSEL.

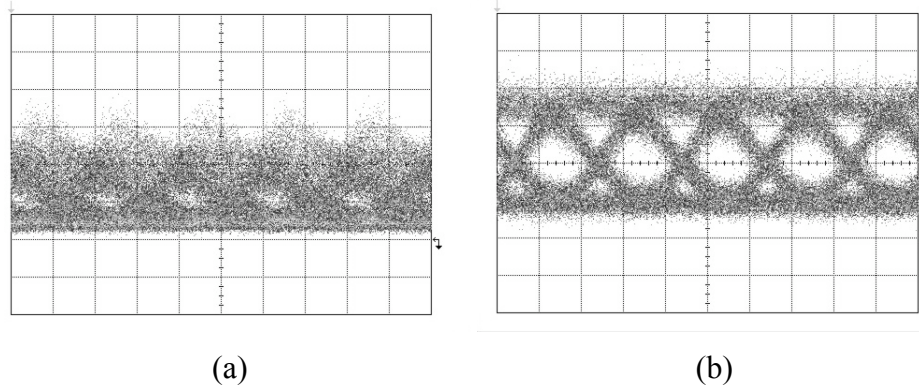


Figure 7.7 Eye-diagrams taken at the same oscilloscope settings and receiver power when the multimode VCSEL is modulated with 10-Gb/s $2^{15}-1$ PRBS. (a) Free-running condition. The nearly closed eye indicates inter-symbol interference caused by beating noise between different modes. (b) Injection-locked with 3-dBm injection power. The single-mode emission results in much cleaner eye-opening.

BER performance is tested at a few different injection power levels. As shown in Figure 7.8, there is 1.5-dB power penalty when the VCSEL is locked by 3-dBm injection power compare to the free-running case, but 1-dB and 2-dB power penalty reduction when the injection power increases to 4 dBm and 6 dBm, respectively. A possible intuitive explanation is that the 3-dBm injection power is not yet strong enough to completely stabilize the locking condition though the spectrum already shows single-mode emission. Therefore, the modes are still competing internally for lasing especially with large-signal direct modulation, which helps excite all the possible modes. However, higher injection power will strongly support the selected mode but suppress the other modes, hence a more stable locking condition, which results in better BER performance. Similar as mentioned before for single-mode VCSELs, one would expect the power penalty goes high again at some point if the injection power keeps increasing. This is due to the extinction ratio degradation from the reflected CW master light. Unfortunately, it could not be demonstrated here because of the limited output power from the tunable laser used as the master laser in the experiment.

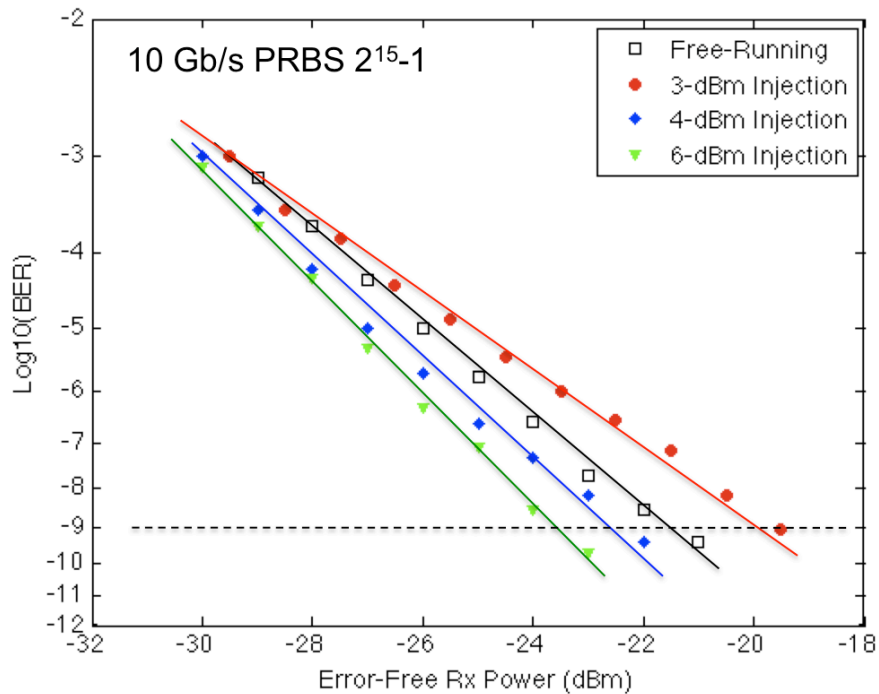


Figure 7.8 Back-to-back BER showing performance improvements as a function of injection power levels.

7.2.2 Chirp Reduction and Negative Chirp

Since the much-narrowed optical spectrum of an injection-locked multimode VCSEL suggests significant chirp reduction, the time-resolved chirp waveform is taken and shown in Figure 7.9. Figure 7.9(a) shows the signal pattern and corresponding chirp waveform of the free-running VCSEL as a reference. This device possesses peak-to-peak transient chirp of ~ 10 GHz and adiabatic chirp of ~ 4 GHz. Figure 7.9 (b-d) are the chirp waveforms of the same device but injection-locked with 3-dBm, 4-dBm and 6-dBm injection power. Same signal patterns exhibit in all these cases and no data inversion occurs. Therefore, zero adiabatic chirp and positive transient chirp with peak-to-peak value of 5 GHz, 4 GHz and 3 GHz is observed for the above three injection power levels, respectively. The results here are consistent with what has been shown in Chapter 4 for

single-mode VCSELs – the transient peak-to-peak chirp decreases as the injection power increases.

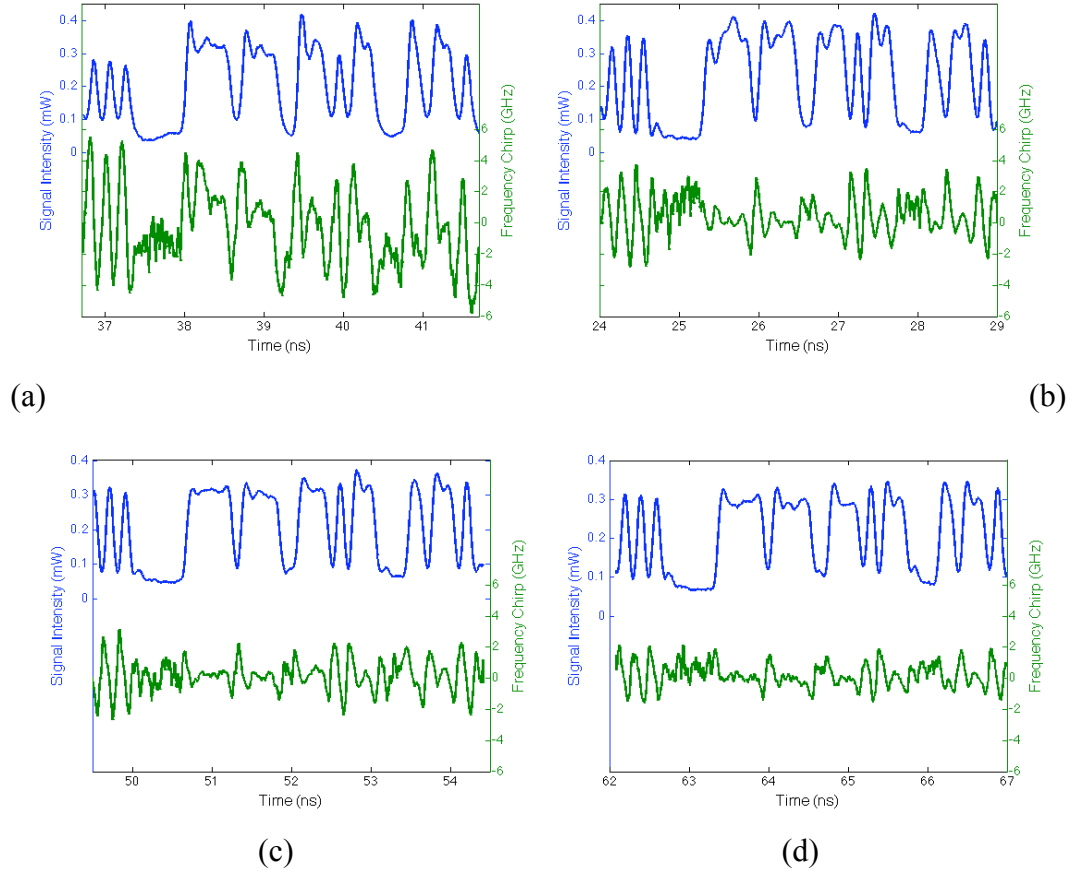


Figure 7.9 Chirp reduction by OIL on a 15- μm aperture multimode VCSEL without data pattern inversion. (a) Free-running with 10-GHz peak-to-peak positive chirp and non-zero adiabatic chirp. (b) OIL at 3-dBm injection power with 5-GHz peak-to-peak positive chirp and zero adiabatic chirp. (c) OIL at 4-dBm injection power with 4-GHz peak-to-peak positive chirp and zero adiabatic chirp. (d) OIL at 6-dBm injection power with 3-GHz peak-to-peak positive chirp and zero adiabatic chirp.

Data pattern inversion and negative chirp should also be expected on the same device if the gain level of the VCSEL is suppressed by either adjusting the detuning value or increasing the injection power, as described in Chapter 4. Since this device is a highly multimode device with 15- μm aperture size, more injection power is required to reach the

loss regime for data inversion. Again, due to the limited output power from the master laser, the tuning range is also limited, which prevent getting data inversion on this VCSEL.

To achieve data inversion and negative chirp with the present setup, another VCSEL with 10- μm aperture size is used, which emits fewer modes, thus requiring less injection power to reach loss regime. The free-running signal pattern and chirp waveform of this device is similar as shown in Figure 7.9(a). So Figure 7.10(a) and (b) shows the inverted signal pattern and negative chirp from this device when it is injection-locked with 3-dBm and 6-dBm injection power. As one could imagine, higher injection power results in smaller transient chirp. Again, zero adiabatic chirp is obtained as well.

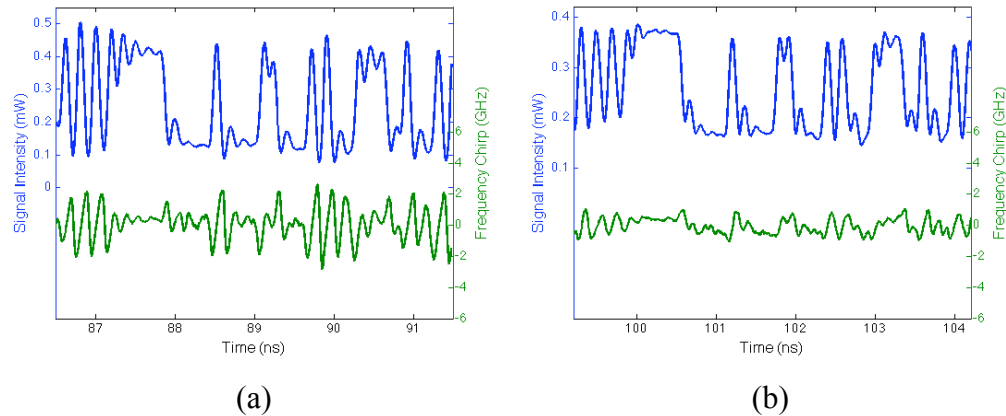


Figure 7.10 Reduced negative chirp by OIL on a 10- μm aperture multimode VCSEL. (a) OIL at 3-dBm injection power with 4-GHz negative chirp. (b) OIL at 6-dBm injection power with 2-GHz negative chirp.

7.2.3 Transmission Distance Enhancement

The much-reduced positive and negative chirp is expected to provide much-enhanced transmission distance over standard single-mode fiber (SSMF) [105]. The small positive chirp would still broaden the optical pulse of a bit through interaction with the

fiber chromatic dispersion but with much slower speed, which equivalently increases the distance the pulse could travel. The small negative chirp would compensate the fiber chromatic dispersion to compress the pulse first. And then after propagating through the optimal distance where the accumulated dispersion effect completely cancels with the amount of the negative chirp, the pulse starts to broaden again. But the overall transmission distance will be greatly lengthened.

The transmission characteristics are presented in Figure 7.11. The power penalty in the vertical axis is calculated using the free-running 15- μm VCSEL back-to-back error-free receiver power. The distance of a multimode VCSEL is severely limited to no longer than 2 km due to the mode beating and chirp. However, as the chirp is reduced by OIL, the transmission distance is enhanced. For positive chirp, the penalty increases monotonically with the distance, and smaller chirp value (higher injection power) results in slower penalty increase with distance. As shown in Figure 7.11, the transmission distance is enhanced to 20 km and 40 km with injection power of 3 dBm and 6 dBm, respectively. For negative chirp, the compensation between chirp and dispersion accounts for the penalty reduction in the beginning of the propagation. After transmitting over certain distance, the penalty increases with distance very slowly. Therefore, a shallow dip exhibits in the transmission characterization curve. The bottom of the dip, presenting minimum power penalty, is the distance where the optical pulse is compressed the most. The total transmission distance in this case can be greater than 100 km. This significant transmission distance enhancement together with the existing advantages on yield, manufacturing and cost make multimode VCSELs even more attractive for all various kinds of digital and analog applications.

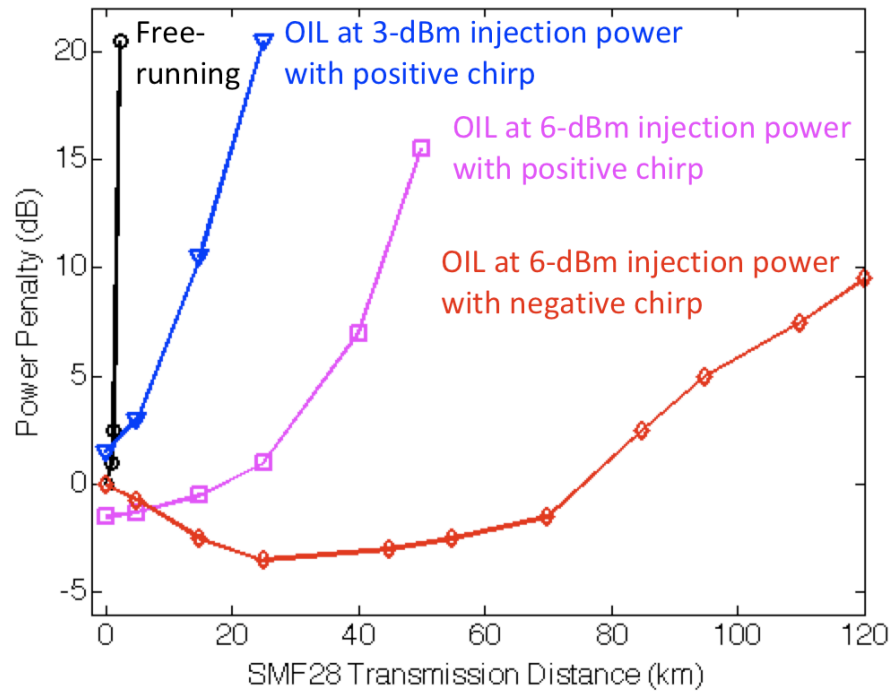


Figure 7.11 Transmission characteristics comparison between free-running and injection-locked multimode VCSELs with different values of peak-to-peak positive as well as negative chirp.

7.3 NUMERICAL SIMULATIONS OF INJECTION-LOCKING DYNAMICS OF A TWO-MODE VCSEL

It is necessary to create a theoretical framework to guide the experiments for exploring more meaningful demonstrations since OIL of multimode VCSELs is a fairly new topic to investigate. Modeling of the dynamics of such a system can be established without much hassle by adopting the OIL rate equations with extension to multiple modes.

There are different approaches to model multimode VCSELs presented in literatures before, even though they all used rate equations. The first approach [107] is to explicitly include spatial dependence of both carrier diffusion and the electric field profile, whereas the second one [109] treats different transverse modes similar as longitudinal modes by

lumping the difference between modes into the photon lifetime term and the gain compression factors, since different modes all share the same carrier reservoir as gain media. The second approach provides a comprehensive model to study injection locking on a multimode VCSEL including mode competition and nonlinear effect. It also exhibits great similarity to the single-mode OIL rate equations, hence is much simpler in terms of computational complexity. Therefore, we adopt this approach for our study.

To simplify the simulation process but without losing the generality of the modeling, only two modes are considered. The free-running rate equations are listed below. The parameters listed in Table 7.1 are chosen such that both modes are lasing notably with one mode slightly dominating the other.

The LI curves of the laser are shown in Figure 7.12. Mode 1 is the dominant mode that has a lower threshold. Once mode 2 is turned on at about 2-mA bias current, the slope efficiency of mode 1 is reduced due to the existence of mode 2.

$$\begin{aligned}
\frac{dS_1}{dt} &= \left[\Gamma v_g \frac{g_n(N - N_{tr})}{V_a(1 + \varepsilon_{11}S_1 + \varepsilon_{12}S_2)} - \frac{1}{\tau_{p1}} \right] S_1 + \frac{\beta B}{V_a} N^2 \\
\frac{dS_2}{dt} &= \left[\Gamma v_g \frac{g_n(N - N_{tr})}{V_a(1 + \varepsilon_{21}S_1 + \varepsilon_{22}S_2)} - \frac{1}{\tau_{p2}} \right] S_2 + \frac{\beta B}{V_a} N^2 \\
\frac{dN}{dt} &= \frac{I_{bias}}{q} - \frac{N}{\tau_N} - \frac{\Gamma v_g g_n(N - N_{tr})}{V_a(1 + \varepsilon_{11}S_1 + \varepsilon_{12}S_2)} S_1 - \frac{\Gamma v_g g_n(N - N_{tr})}{V_a(1 + \varepsilon_{21}S_1 + \varepsilon_{22}S_2)} S_2
\end{aligned}
\tag{7.1 a-c}$$

Table 7.1 Parameter values for free-running VCSEL simulation.

Γ	0.03	Mode confinement factor	v_g	8.3 cm/ns	Group velocity
g_n	$6 \times 10^{-16} \text{ cm}^2$	Differential gain	τ_N	1/0.22 ns	Carrier lifetime
V_a	$3 \times 10^{-12} \text{ cm}^3$	Active region volume	N_{tr}	$1.5 \times 10^{18} \times V_a$	Transparency carrier #
B	$8 \times 10^{-20} \text{ cm}^3/\text{ns}$	Recombination coefficient	β	1×10^{-4}	Spontaneous emission rate
τ_{p1}	$3 \times 10^{-3} \text{ ns}$	Mode 1 photon lifetime	τ_{p2}	$2.99 \times 10^{-3} \text{ ns}$	Mode 2 photon lifetime
ε_{11}	2×10^{-7}	Self-gain-saturation coefficient of mode 1	ε_{22}	2×10^{-7}	Self-gain-saturation coefficient of mode 2
ε_{21}	0.5×10^{-7}	Cross-gain-saturation coefficient	ε_{12}	0.5×10^{-7}	Cross-gain-saturation coefficient

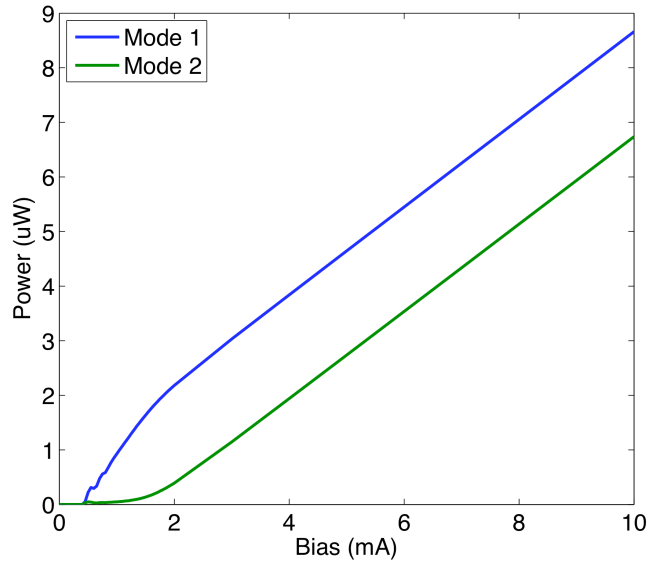


Figure 7.12 Simulated LI curves of a two-mode VCSEL using the parameters listed in Table 7.1. See Appendix A1.7 for MATLAB code.

To simulate OIL, one needs to add extra injection terms to the photon number equations, and include phase equations as well. An ideal case is to consider only one mode of the two is stably locked and the other is greatly suppressed, which leads to a set of simplified rate equations with external injection term added only to one mode (either mode 1 or mode 2). In reality, even though this is the observation once locking occurs on the selected mode, however, it ignores the fact that both modes experience the external injection from the master laser, and locking is finally achieved on one of them after mode competition. Therefore, to simulate the dynamics more accurately, we add injection terms to both modes, and employ different values for the coupling rate κ_1 and κ_2 to emulate spatial detuning. The rate equations are shown below with most of the parameter values listed in Table 7.1, except the linewidth enhancement factor $\alpha = 5$.

$$\begin{aligned}
\frac{dS_1}{dt} &= \left[\Gamma v_g \frac{g_n(N - N_r)}{V_a(1 + \varepsilon_{11}S_1 + \varepsilon_{12}S_2)} - \frac{1}{\tau_{p1}} \right] S_1 + \frac{\beta B}{V_a} N^2 + 2\kappa_1 \sqrt{S_{inj}S_1} \cos(\phi_1(t) - \phi_{inj}(t)) \\
\frac{d\phi_1}{dt} &= \frac{\alpha}{2} \left[\Gamma v_g \frac{g_n(N - N_r)}{V_a(1 + \varepsilon_{11}S_1 + \varepsilon_{12}S_2)} - \frac{1}{\tau_{p1}} \right] - 2\pi\Delta f_1 - \kappa_1 \sqrt{\frac{S_{inj}}{S_1}} \sin(\phi_1(t) - \phi_{inj}(t)) \\
\frac{dS_2}{dt} &= \left[\Gamma v_g \frac{g_n(N - N_r)}{V_a(1 + \varepsilon_{21}S_1 + \varepsilon_{22}S_2)} - \frac{1}{\tau_{p2}} \right] S_2 + \frac{\beta B}{V_a} N^2 + 2\kappa_2 \sqrt{S_{inj}S_2} \cos(\phi_2(t) - \phi_{inj}(t)) \\
\frac{d\phi_2}{dt} &= \frac{\alpha}{2} \left[\Gamma v_g \frac{g_n(N - N_r)}{V_a(1 + \varepsilon_{21}S_1 + \varepsilon_{22}S_2)} - \frac{1}{\tau_{p2}} \right] - 2\pi(\Delta f_1 - 190) - \kappa_2 \sqrt{\frac{S_{inj}}{S_2}} \sin(\phi_2(t) - \phi_{inj}(t)) \\
\frac{dN}{dt} &= \frac{I_{bias}}{q} - \frac{N}{\tau_N} - \frac{\Gamma v_g g_n(N - N_r)}{V_a(1 + \varepsilon_{11}S_1 + \varepsilon_{12}S_2)} S_1 - \frac{\Gamma v_g g_n(N - N_r)}{V_a(1 + \varepsilon_{21}S_1 + \varepsilon_{22}S_2)} S_2
\end{aligned} \tag{7.2 a-e}$$

The injection ratio and detuning values are measured referred to mode 1. If mode 1 is the fundamental mode and mode 2 is the higher-order mode, the schematic showing the frequency detuning calculation for both modes is in Figure 7.13. Since the typical mode

spacing between the fundamental and the first order mode is ~ 1.5 nm (from experimental spectrum), which is equivalent to ~ 190 GHz at 1550 nm, the detuning of the second mode can be expressed in terms of the detuning of mode 1 and the mode spacing as shown in Figure 7.13.

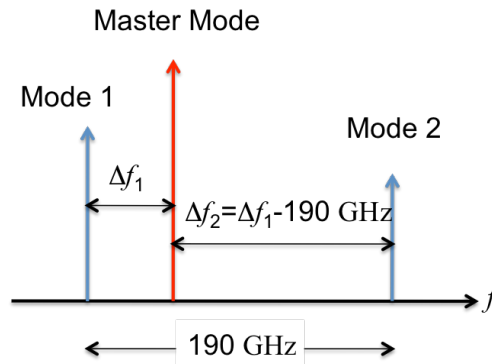


Figure 7.13 Schematic showing frequency relations between master laser and the two modes for calculating frequency detuning values.

There are 4 possible outcomes from solving the rate equation set (7.2) – (i) unstable, (ii) stable but locking on mode 1, (iii) stable but locking on mode 2, and (iv) stable but locking on neither of the modes. These conditions can be determined by measuring the photon density output of the two modes after injection locking is applied over an enough long period of time (~ 10 ns in the simulation). In the unstable case, the simulation does not converge, while in the stable locking case, the simulation converges. The threshold we set to categorize various locking condition is as follows. If mode 1 power is 10 times greater than it of mode 2 after locking, we assume locking occurs on mode 1 and the same rule applies to mode 2. If both modes are lasing with considerable amount of power but no one is significantly greater than the other, we assume no locking happens.

Locking stability plot is simulated using the time-domain method by solving the rate equation set (7.2) at various spatial detuning conditions by choosing different combinations of κ_1 and κ_2 . The results are shown in Figure 7.14. Different colors represent different locking conditions stated above with one-to-one correspondence: black – (i) unstable, red – (ii) stable locking on mode 1, blue – (iii) stable locking on mode 2, and green – (iv) stable but no locking.

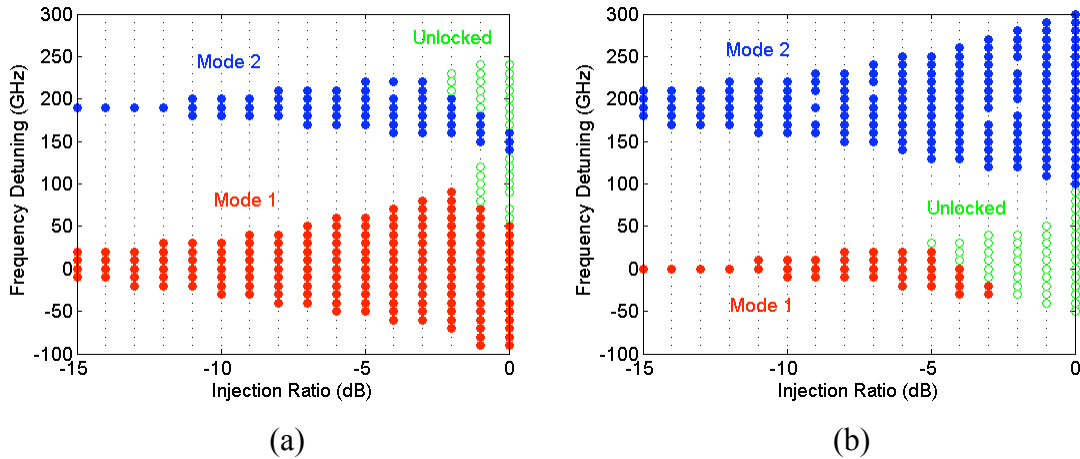


Figure 7.14 OIL stability plots of a two-mode VCSEL at different spatial detuning conditions. (a) $\kappa_1 = 0.7 \times 10^{12} \text{ s}^{-1}$ and $\kappa_2 = 0.3 \times 10^{12} \text{ s}^{-1}$ (b) $\kappa_1 = 0.3 \times 10^{12} \text{ s}^{-1}$ and $\kappa_2 = 0.7 \times 10^{12} \text{ s}^{-1}$. Different colors represent different locking conditions: black – unstable, red – stable locking on mode 1, blue – stable locking on mode 2, and green – stable but no locking. See Appendix A1.8 for MATLAB code.

Figure 7.14(a) shows the result when $\kappa_1 = 0.7 \times 10^{12} \text{ s}^{-1}$ and $\kappa_2 = 0.3 \times 10^{12} \text{ s}^{-1}$. The locking range of mode 1 is reduced on the large frequency detuning side due to the existence of mode 2 shown by the green area. Since mode 1 dominates in the free-running condition, in such a case that the spatial detuning does not favor mode 2 strongly, the stable locking range of mode 2 is very small as a result of mode competition shown by the blue area. In Figure 7.14(b), $\kappa_1 = 0.3 \times 10^{12} \text{ s}^{-1}$ and $\kappa_2 = 0.7 \times 10^{12} \text{ s}^{-1}$, which

emulates the situation that mode 2 (higher order) is being preferentially selected to be locked by adjusting the spatial detuning. As one could expect, in this case, the locking range of mode 2 is significantly enlarged, along with the reduction of the locking range of mode 1. Mode 2 also wins in the mode competition as the green area migrates towards mode 1 locking range. These results are consistent with the experimental observation.

7.4 OUTLOOK

We have demonstrated preliminary results on multimode VCSEL injection locking in this chapter. The experimental small-signal and large-signal measurements show encouraging results on both modulation bandwidth and transmission distance enhancement. In order to attain more guidance on further study of OIL dynamics of multimode VCSELs, we build a theoretical framework to simulate locking behaviors of a two-mode device.

However, there are still many issues and interesting problems unclear, which require further investigation, and I would like to point out a few of them here. First, experimentally, more detailed characterization on the transverse mode nature of a multimode VCSEL [110] can be performed to improve our understanding of the device itself, which can in turn help improve the modeling accuracy of the device. For example, if more modes or details of the modes such as polarization, spatial profile need to be considered in the model. Next, the numerical simulation is only performed in CW condition without any modulation dynamics incorporated so far. Small-signal modulation certainly can be included to study the dynamic behavior of multimode VCSELs under OIL, such as frequency response, linearity, noise etc. Experimental calibrations on these properties should follow up to verify the prediction of the simulation. Furthermore, an

important problem to be solved is the coupling loss induced by the mismatch between the multimode device and the single-mode coupling fiber. Since master laser is usually a single-mode laser, the incoming fiber from the master laser to the VCSELs needs to be single-mode to ensure an effective injection. However, the single-facet emission of VCSELs would not allow a separate multimode fiber to be used to collect the output from the device. Therefore, a possible solution is to design a fused single-mode / multimode fiber coupler, which could potentially efficiently collect both single-mode and multimode emission. Also, it is seen from the experiments that master laser with higher power is desired to improve the VCSEL performance even more. Tunable laser may be a choice for the master laser in the future, because a feedback loop circuit can then be integrated with the tuning mechanism of the master laser to assure stable locking even in some harsh environment, e.g. huge temperature variation. In this case, high power can be achieved by tagging an EDFA after the laser. Finally, although the demonstration is on 1550-nm VCSELs, the technique is readily feasible for 850-nm and 980-nm devices as well. In fact, 850-nm multimode VCSELs has the biggest commercial market.

Chapter 8

Conclusion and Future Work

Optical injection locking on semiconductor lasers has been studied more than two decades since the very beginning of the telecommunication revolution. Although it has not yet become a commercialized technique to be widely deployed, it is still a lively and active research topic and actually attracts more and more attention not only in the academic community but also in industry. Compare to the earlier OIL experiments and work published by other groups, we try to go beyond the original frequency locking and nonlinear coupling nature of this problem, and try to investigate the dynamic modulation properties of OIL lasers with the interests of discovering new physics as well as innovate new applications out of it. And this is also what this dissertation has been trying to deliver. We have reviewed the physics of the injection-locking technique and the performance of injection-locked lasers. One has seen that the characteristics of a directly modulated laser can be drastically changed when it is locked to a master laser through coherent nonlinear interactions, resulting in superior device performance for various applications. Even though most of the results presented in this dissertation obtained from a VCSEL injection-locked by a master DFB laser, there is no apparent restriction on the type of lasers to be used for either the slave or the master laser.

Due to the rapid development and application needs of high-speed lasers, our main focus has been on the performance improvement of directly modulated semiconductor lasers using OIL for both analog and digital fiber-optic communications. The demonstrated improvement includes chirp and noise reduction, resonance frequency, modulation bandwidth, RF link gain, and SFDR enhancement. Preliminary improvement is also observed on multimode VCSELs.

Based on the superior performance of injection-locked diode lasers, they can be utilized in various systems. We have discussed OIL VCSELs used as laser transmitters in PON. It is also appealing to transmit analog signals for RoF and wireless sensor networks. Furthermore, it can be an alternative approach to construct an OEO system for low phase noise microwave signal generation. In addition to the applications we have presented here, OIL was demonstrated to have advantages in many other microwave photonic applications. Just to name a few, for example, optical injection phase-locked loop (OIPLL) combining phase locking technique and injection-locking technique has been shown to improve the phase noise performance [111]. All optical regeneration, as a critical function in high-speed photonic networks, has been widely investigated by using an OIL-DFB laser [112] and a two-mode OIL FP laser [113]. Injection locking has also been proposed and demonstrated as one of the techniques for optical generation of millimeter-wave signals with low phase noise [114, 115], which would be crucial in a RoF system.

Despite all the intriguing device performance and system applications demonstrated already, there are still many new ideas and novel applications requiring further investigation.

OIL on multimode VCSELs apparently is the topic only partially studied in this dissertation. The last section in Chapter 7 summarizes the important issues that require further study.

For OIL OEO discussed in Chapter 5, it is also necessary to establish a detailed theoretical framework to study the phase noise limit. Comparing with the conventional OEO system that employs a MZM, the OIL OEO phase noise might be severely RIN-limited rather than RF amplifier noise limited. It will also be challenging to push the OEO generated RF center frequency to 60-90 GHz in the unregulated high-speed wireless transmission band. Fast tuning of the center frequency within this frequency band will also be an intriguing feature to add by taking advantage of the great tunability of the resonance frequency of an injection-locked laser.

When data inversion was discussed in Chapter 4, a transition state where only spikes at the rising and falling edges on the waveform showed up was presented in Figure 4.9 but was not studied or explained in detail. This state can be used for edge detection and clock recovery as a strong RF tone at the clock frequency exhibits in the RF spectrum when the device is modulated by PRBS. The same state can also be used as an optoelectronic technique to generate ultrawideband (UWB) signal (3.1 – 10.6 GHz) for wireless communication [116, 117]. If the electrical data is programmed to generate a “1” bit in every eight bits at 10 Gb/s, so the periodic pulse will generate a so-called monocycle optical pulse with pulse width of ~ 50 ps (similar as shown in the middle of Figure 4.9, but with higher bit-rate, hence narrower pulse width). Preliminary study shows encouraging results for both the clock recovery and the UWB signal generation, but further characterizations are certainly necessary.

A critical step to find a cost-effective solution to WDM-PON, as discussed in Chapter 6, is to innovate the technology for colorless operation. A tunable VCSEL will be the enabling device for our proposed OIL WDM-PON system to achieve colorless. All ONUs will universally employ the same type of tunable VCSELs and each ONU needs to tune the laser to their specified channel wavelength. Our group has recently successfully demonstrated a nano-electromechanical optoelectronic (NEMO) tunable VCSEL using an ultra-thin (145 nm) electrostatically actuated high-index contrast subwavelength grating (HCG) as the top mirror [118], which boosts up the tuning speed by more than 2 orders of magnitude [119]. Therefore, applying OIL on these devices and integrating them into the WDM-PON system will be a promising and exciting direction to pursue.

Finally, to ensure the commercial use of OIL for future optical communication systems, low cost integrated device – an integrated OIL laser transmitter – is one important direction to pursue [120]. Due to the lack of chip-based integratable isolator with acceptable insertion loss, this is currently a very challenging goal. It will require more brainstorming and experimenting to seek a solution to achieve unidirectional locking, which is the prerequisite of stable locking hence securing all the dynamic performance improvement. However, in any respect, we hold the belief that the OIL lasers will become one of the key technologies in the next generation high-speed fiber-optic networks if continuous effort and intelligence is devoted to this research area.

Appendix 1

MATLAB Code

A1.1 Single-Mode OIL Stability Plot – Frequency Domain Method

```
% solve for stability plot using frequency domain method
% rate equations analytically solved in steady state
% see Erwin Lau's paper in JQE vol. 44 No.1 Jan. 2008 for details
clc;
clear;
%----- constant -----
gamma = 0.03; % confinement factor
vg = 8.3; % group velocity cm/ns
gn = 6e-16; % differential gain cm2
Va = 3e-12; % active region volume cm3
G0 = gamma*vg*gn/Va; % gain coeff. 1/ns
taop = 3e-3; % photon lifetime ns
Ntr = 1.5e18*Va; % transparency carrier #
Nth = Ntr+1/G0/taop; % threshold carrier #
gammaN = .22; % carrier decay rate 1/ns
gammaP = 1/taop; % photon decay rate 1/ns
Jth = gammaN*Nth; % threshold current rate 1/ns
k = 1e3; % coupling rate 1/ns
alpha = 5; % linewidth enhancement factor
J = 2*Jth;
%----- expressions -----
inj_ratio = [-40:.5:-25];
R = sqrt(10.^(inj_ratio/10)); % field injection ratio R = Ainj/A0
det_f = -60:2:20;%[-100:5:100]; % detuning in GHz
det_w = 2*pi.*det_f; % detuning in angular frequency
for i = 1:length(R)
    for j = 1:length(det_w)
        phi_0 = asin(-det_w(j)/k/sqrt(1+alpha^2)/R(i))-atan(alpha);
        det_N = -2*k/G0*R(i)*cos(phi_0);
        Afr = sqrt((J-gammaN*Nth)/gammaP);
        A0=sqrt((Afr^2-gammaN/gammaP*det_N)/(1+G0*det_N/gammaP));
        z = k*R(i);
%-----find eigenvalues of linearized rate equations-----
        mAA = z*cos(phi_0);
        mAp = z*A0*sin(phi_0);
        mAN = -1/2*G0*A0;
        mpA = -z*sin(phi_0)/A0;
        mpp = z*cos(phi_0);
        mpN = -alpha/2*G0;
        mNA = 2*A0*(gammaP-2*z*cos(phi_0));
        mNN = gammaN + G0*A0^2;
%---p is the polynomial to be solved-----
        p(1) = 1; % coeff for 3rd order term
        p(2) = mAA + mpp + mNN; % coeff of the 2nd order term
```

```

        p(3) = mAA*mpp + mAA*mNN + mpp*mNN - mAp*mpA - mAN*mNA; % coeff
of the 1st order term
        p(4) = mAA*mpp*mNN + mAp*mpN*mNA + mAp*mpA*mNN - mAN*mNA*mpp; %
coeff of the 0 order term
        s = roots(p);
        damp = real(s);
        if (damp(1) < 0 && damp(2) < 0 && damp(3) < 0)
            stable(i,j) = 1;
        else
            stable(i,j) = 0;
        end
    end
end
%-----plot stability plot-----
lambda = 1550e-7; % lasing wavelength in cm
c = 30; % speed of light in cm/ns
det_lam = - lambda^2/c*det_f/1e-7; % wavelength detuning
figure;
for i=1:length(inj_ratio)
    for j = 1:length(det_lam)
        if stable(i,j)==1
            plot(inj_ratio(i),det_lam(j),'ro','MarkerFaceColor','r');hold on;
        else
            plot(inj_ratio(i),det_lam(j),'k.','MarkerSize',1);hold
on;
        end
    end
end
xlabel('Injection Ratio (dB)'); ylabel('Wavelength Detuning (nm)');
%-----plot locking range defined by rate equations-----
upperbound = k*lambda^2/(2*pi*c)*sqrt(1+alpha^2)*R/1e-7;
lowerbound = -k*lambda^2/(2*pi*c)*R/1e-7;
plot(inj_ratio,upperbound, inj_ratio,lowerbound,'-b','LineWidth',2);

```

A1.2 Single-Mode OIL Stability Plot – Time Domain Method

```

% transient behavior of an injection-locked single-mode laser with
nonlinear gain effects
% locking range is simulated - stable locking in detuning_freq vs.
injection ratio 2D plan
clc;
clear;
%-----solve single-mode rate equations for master laser-----
options = odeset('AbsTol',1e-6,'RelTol',1e-6,'Stats','on');
tspan= 0:10; % ns, time span of interest
y0 = [0 0 0]; % initial values for s1, s2 and N
master_bias = 10e-3; % bias in mA
[t_master,y_master]=ode45(@singlemode,tspan,y0,options,master_bias);
Sinj0 = y_master(length(t_master),1);
% initial injection power, will keep constant
index = find(t_master > 3);
% time for phase to be stable

```

```

phi_fit=polyfit(t_master(index),y_master(index,2),1);
% curve-fitting master phase
%initial master phase changing with time, so put into rate equations
%-----solve single-mode rate equations for slave laser-----
options=odeset('AbsTol',1e-6,'RelTol',1e-6,'Stats','on');
tspan= 0:10; % ns, time span of interest
y0 = [0 0 0]; % initial values for s1, s2 and N
slave_bias = 2e-3; % bias in mA
[t_slave,y_slave]=ode45(@singlemode,tspan,y0,options,slave_bias);
S_0 = y_slave(length(t_slave),1);
phi_0 = y_slave(length(t_slave),2);
N_0 = y_slave(length(t_slave),3);
Y_inj0 = [S_0, phi_0, N_0];
%-----Solve for Injection locking-----
%initial values for locking
inj_ratio = -30:-10; % injection ratio in dB
inj_coeff = 10.^(inj_ratio/10)*S_0/Sinj0; % injection ratio is relative
to the slave initial value
det_f = -150:4:150; % detuning frequency in GHz
% indices for results in stability plot
for i=1:length(inj_coeff)
    S_inj = inj_coeff(i)*Sinj0;
    for j = 1:length(det_f)
        options=odeset('AbsTol',1e-6,'RelTol',1e-3,'Stats','on');%----
test if this point is in the locking range, stably locked,
        inputs = [S_inj,det_f(j),phi_fit(1),phi_fit(2),slave_bias];
        tic;% start measuring the time of solving this locking condition
        [T_try,Y_try] = ode23(@singlemodeOIL,[10,20],Y_inj0,options,inputs);
        t_solver=toc
        if t_solver > 2
            stable(i,j) =0;
        else
            index1 = find(T_try<12);index2=find(T_try > 18);
            v1=var(Y_try(index1,1));
            v2=var(Y_try(index2,1));
            if (v1/v2 > 1e2)&&(Y_try(end,1)>Y_try(1,1))
                stable(i,j) = 1;
            else
                stable(i,j) = 0;
            end
        end
    end
end
end
%----plot transient at one locking condition-----
figure; plot(T_try, Y_try(:,1)); xlabel('Time (ns)'); ylabel('Photon
Number');
figure; plot(T_try, Y_try(:,2)); xlabel('Time (ns)'); ylabel('Phase');
figure; plot(T_try, Y_try(:,3)); xlabel('Time (ns)'); ylabel('Carrier
Number');
%-----plot stability plot wavelength detuning vs. injection ratio-----
lambda = 1550e-7; %wavelength in cm
c = 30; % speed of light cm/ns
det_lam = lambda^2/c*det_f/1e-7; % wavelength detuning in nm
figure;
for i=1:length(inj_ratio)

```

```

for j = 1:length(det_lam)
    if stable(i,j)==1
        plot(inj_ratio(i),det_lam(j),'ro','MarkerFaceColor','r');hold on;
    else
        plot(inj_ratio(i),det_lam(j),'k.','MarkerSize', 1);hold on;
    end
end
end
end

```

```

singlemode.m
%single-mode free-running rate equations
function dy = singlemode(t, y, bias)
%-----constants-----
gamma = 0.03; % mode confinement factor
vg = 8.3; % group velocity cm/ns
gn = 6e-16; % differential gain cm2
Va = 3e-12; % active region volume cm3 (length=1e-4 cm, mesa=10*10um2)
G0 = gamma*vg*gn/Va; % gain coeff. 1/ns
Ntr = 1.5e18*Va; % transparency carrier #
eps11 = 2e-7; % self-saturation coeff. cm3 for model
tao1 = 3e-3; % photon lifetime of model ns
B = 8e-20; % recommbination coeff. cm3/ns
beta = 1e-4; % spon. em. rate
gammaN = .22; % carrier recommbination rate ns-1
q = 1.6e-10; % electron charge A/ns
alpha = 5; % linewidth enhancement factor
% differentail equations y(1) = photo number (s), y(2) = phase, y(3) =
N
% creat a column vector which is required by ode solver
dy = zeros(3,1);
% photon # equation
dy(1) = (G0*(y(3)-Ntr)/(1+eps11*y(1))-1/tao1)*y(1)+ beta*B/Va*y(3)^2;
% phase equation
dy(2) = alpha/2*(G0*(y(3)-Ntr)/(1+eps11*y(1))-1/tao1);
% carrier # equation
dy(3) = bias/q - gammaN*y(3) - G0*(y(3)-Ntr)/(1+eps11*y(1))*y(1);

```

```

singlemodeOIL.m
% single-mode injection locking rate equations
function dy = singlemodeOIL(t, y, inputs)
% inputs from the main program inputs(1) = Sinj, inputs(2) = det_f,
inputs(3)=phi_inj1,inputs(4) = phi_inj2, inputs(5) = slave_bias
%-----constants-----
gamma = 0.03; % mode confinement factor
vg = 8.3; % group velocity cm/ns
gn = 6e-16; % differential gain cm2
Va = 3e-12; % active region volume cm3
G0 = gamma*vg*gn/Va; % gain coeff. 1/ns
Ntr = 1.5e18*Va; % transparency carrier #
eps11 = 2e-7; % self-saturation coeff.
tao1 = 3e-3; % photon lifetime ns
B = 8e-20; % recommbination coeff. cm3/ns
beta = 1e-4; % spon. em. rate
gammaN = .22; % carrier recommbination rate ns-1
q = 1.6e-10; % electron charge A/ns

```

```

alpha = 5;          % Linewidth enhancement factor
k = 1e3;           % coupling rate ns-1
% differentail equations y(1) = s1, y(2) = phi1, y(3) = N
dy = zeros(3,1); % creat a colum vector which is required by ODE solver
% photon # equation
dy(1) = (G0*(y(3)-Ntr)/(1+eps11*y(1))-1/tao1)*y(1) + beta*B/Va*y(3)^2 +
2*k*sqrt(y(1)*inputs(1))*cos(y(2)-inputs(3)-inputs(4)*t);
% Phase equation
dy(2) = alpha/2*(G0*(y(3)-Ntr)/(1+eps11*y(1))-1/tao1)-2*pi*inputs(2)-
k*sqrt(inputs(1)/y(1))*sin(y(2)-inputs(3)-inputs(4)*t);
% carrier # equation
dy(3) = inputs(5)/q - gammaN*y(3) - G0*(y(3)-Ntr)/(1+eps11*y(1))*y(1);

```

A1.3 Fabry-Perot Amplifier Model for Frequency Response

```

% use amplifier model to sketch out the frequency response
clear; clc;
%----- define constants-----
r1 = 0.995; % top mirror field reflectivity
r2 = 0.999; % bottom mirror field reflectivity
l = 1e-6; % cavity length
alpha_i = 1e3; % distributed material loss m-1
lambda_0 = 1.55e-6; % emission wavelength
detuning = [-0.35, -.15, 0]*1e-9; % wavelength detuning
kappa = 1e12; % coupling rate
alpha = 6; % linewidth enhancement factor
R_inj = 0.65; % field injection ratio
g0 = 3e-20; % differential gain in m^2
c = 3e8; % speed of light
vg = 8.3e7; % group velocity of the wave inside the slave laser
cavity, index ~ 3.6
gamma_th = alpha_i - log(r1*r2)/l % threshold gain of the laser
Nth = gamma_th / g0 % threshold carrier density
mod_stop = [3.5,2.5,2]; % stop frequency scanning for optical and
electrical response
%-----steady state solution-----
m=1;
figure;
for j=1:length(detuning)
    %- steady state solution
    % steady state phase
    phi_0 =
asin(2*pi*c/lambda_0^2*detuning(j)/kappa/sqrt(1+alpha^2)/R_inj)-
atan(alpha)
    % carrier density reduction under OIL
    del_N = - 2*kappa/(vg*g0)*R_inj*cos(phi_0)
    N = Nth + del_N; % electron density
    gamma = g0*N;
    % cavity resonance shift in wavelength
    del_cav_lambda = - lambda_0^2/(2*pi*c)*alpha*vg*g0*del_N/2;
    % cavity resonance shift in Hz
    del_cav_f = abs(alpha*vg*g0*del_N/2/2/pi)
%-----reflectivity and frequency response calculation-----
%-----expression of modulation sidebands-----

```

```

fm = 0:1:(mod_stop(j)*del_cav_f/1e9); % modulation frequency in GHz
lambda_m = fm/100*.8*1e-9; % modulation frequency in nm
% spacing between lower sideband (longer wavelength)and cavity
resonance
l_sb = del_cav_lambda - detuning(j) - lambda_m;
f_l = l_sb/0.8*100*1e18; % l_sb in frequency
% spacing between upper sideband (shorter wavelength)and cavity
resonance
u_sb = del_cav_lambda - detuning(j) + lambda_m;
f_u = u_sb/0.8*100*1e18; % u_sb in frequency
%----- calculate reflectivity and sideband detection-----
phase_l= -2*i*(2*pi*f_l/vg)*1; % phase of the lower modulation sideband
% field reflectivity of lower sideband
ref_l = (1-r1^2)*r2*exp((gamma-alpha_i)*1)*exp(phase_l)./(1-
r1*r2*exp((gamma-alpha_i)*1)*exp(phase_l))-r1;
phase_u= -2*i*(2*pi*f_u/vg)*1; % phase of the upper modulation sideband
% field reflectivity of upper sideband
ref_u = (1-r1^2)*r2*exp((gamma-alpha_i)*1)*exp(phase_u)./(1-
r1*r2*exp((gamma-alpha_i)*1)*exp(phase_u))-r1;
% relative frequency response in dB, electrical intensity
response = 40*log10(abs(ref_l + ref_u));
%-----plot optical spectrum & frequency response-----
slave = lambda_0*1e9; % slave wavelength in nm
slave_x = slave*ones(1,25); slave_y = 1:25;
master = (lambda_0 + detuning(j))*1e9; % master wavelength in nm
master_x = master*ones(1,40);
master_y = 1:40;
lambda_m = fm./100*0.8; % modulation sidebands in nm
cav_scan = master + lambda_m; % the x-axis for the cavity gain
%-----optical spectrum-----
subplot(3,2,m);plot(cav_scan,20*log10(abs(ref_l)), 'm', 'LineWidth',
3);hold on;
plot(master_x, master_y, 'r', 'LineWidth', 3);
plot(slave_x, slave_y, 'k', 'LineWidth', 3);
xlim([1549.3,1551.5]);
ylim([0,50]);
if j == 2
ylabel('Optical Gain (dB)');
end
if j == 3
xlabel('Wavelength (nm)');
end
%-----frequency response-----
subplot(3,2,m+1);plot(fm,response, 'b', 'LineWidth', 3);
xlim([0,110]);
if j == 3
xlabel('Frequency (GHz)');
end
ylim([0,30]);
if j == 2
ylabel('Relative Response (dB)');
end
m = m+2;
end

```

A1.4 Parasitic De-embedding from Measured Frequency Response

```

%Plot s21 curve with curve-fitting
clear; %clear workspace
%-----Set constants-----
plot_diff=0; % if plot the difference fitting results 1 or 0
plot_para=0; % if plot average parasitics 1 or 0
plot_raw=0; % if plot raw data 1 or 0
plot3dB=1; % if plot 3dB points on the graph
plot_log=0; % if plot the result in log scale 1 or 0
plot_title= 'my de-embedded s21 plot';
fig_name= 'my de-embedded s21'; % name of saved file
% p(i)= fz_1, fp_1, fr_1, gamma_1, magnitude_1, const.offset(1-2),
fz_2, fp_2, fr_2, gamma_2, magnitude_2
p0_diff=[100,10,15,10,10,0,100,15,36,10,10];
% lower boundary for curve-fitting the difference
lb_diff=[1,1,1,.1,0,-15,1,1,1,.1,0];
% upper boundary for curve-fitting the difference
ub_diff=[50000,1000,40,100,20,15,50000,1000,40,100,20];
% initial values: p(i)=fz, fp, fr, gamma, magnitude, const.offset
p0_k=[100,10,30,1,10,0]; % injection-locked
p0_f=[0,0,6,25,10,0]; % free-running
% lower boundary for curve-fitting each file
lb_single=[0,0,1,.1,0,-100];
% upper boundary for curve-fitting locked file
ub_single=[100,100,40,100,20,100];
%upper boundary for curve-fitting free running
ub_single_f=[1,1,12,100,20,100];
err_tol=500; % set error tolerance
detunings=[99,1,2,3,4]; % detuning of each file from left to right
% frequency interval of removing the noisy part for difference curve-
fitting
f_min=1; f_max=38;
% frequency interval of removing the noisy part for curve-fitting
f_st=1; f_sp_free=20; f_sp_lk=38;
% frequency at which stop plotting the parasitic removed free running
data
f_cutoff_free=22;
% frequency at which stop plotting the parasitic removed locked data
f_cutoff_lock=38;
freq_add=1; % if add 10GHz or longer frequency axes 1 or 0
freq_add_stop=50;
f_3db_free=8; % set search start point for 3dB bandwidth
f_3db_lk=[42,34,30,23];
%-----Set files-----
filename='yourfilename';
file_num=[0,1,2,3,4]; % free running at first
for i=1:length(file_num)
    files{i} = strcat(filename,num2str(file_num(i)),'.s21');
end
%-----calibration the DC power due to EDFA gain saturation-----
% DC drop due to EDFA gain saturation
DC_drop=-7.8843 - [-14.4849,-14.3984,-13.9727,-14.4175];
% order is the same as filename, calibration value(real DC gain)
DC_locked=[-79.17,-79.00,-78.67,-79.67];

```

```

% calibration is done in function files:s21-curve-fitting and fitting
difference
DCshift=DC_locked + 84.67 + DC_drop;
%-----Curve-fitting of the difference-----
count=0;
%fit difference of two injection locked curves(no free running)
for i=2:(length(file_num)-1)
for j=(i+1):length(file_num)
[parasitic,error,p]=s21_curve_fitting_difference('file1',char(files(i))
,'file2',char(files(j)),'fit_plot',plot_diff,'delimiter','\t','p0',p0_d
iff,'f_min',f_min,'f_max',f_max,'lb',lb_diff,'ub',ub_diff,'call',DCshif
t(i-1),'cal2',DCshift(j-1));
if error < err_tol;
count=count+1;
parasitics(:,count)=parasitic;
errors(count)=error;
parameters(count,:)=p;
end
end
end
%-----Get average of all parasitic-----
parasitic_avg=0;
for i=1:count;
parasitic_avg = parasitic_avg + parasitics(:,i)/errors(i);
end
parasitic_avg = parasitic_avg ./ sum ( 1 ./ errors );
%parasitic_avg = parasitic_avg ./ count;
%-----Curve-fitting of each file-----
%-----fitting free running-----
f_cut_min = f_st; f_cut_max = f_sp_free;
[parms,f,f_add,s21_raw,s21_sub,s21_fit]=s21_curve_fitting(0,char(files(
1)),'\t',parasitic_avg,p0_f,f_cut_min,f_cut_max,freq_add,freq_add_stop,
lb_single,ub_single_f,0);
s21_raws(:,1) = s21_raw;
s21_subs(:,1) = s21_sub;
s21_fits(:,1) = s21_fit;
para_each(1,:)=parms;
fr(1)= parms(3);
%-----fitting locked-----
%get noise free part for injection locked

f_cut_min = f_st; f_cut_max = f_sp_lk;
for i=2:length(file_num)
[parms,f,f_add,s21_raw,s21_sub,s21_fit]=s21_curve_fitting(1,char(files(
i)),'\t',parasitic_avg,p0_k,f_cut_min,f_cut_max,freq_add,freq_add_stop,
lb_single,ub_single,DCshift(i-1));
s21_raws(:,i) = s21_raw;
s21_subs(:,i) = s21_sub;
s21_fits(:,i) = s21_fit;
para_each(i,:)=parms;
fr(i)= parms(3);
end
%-----Plot out the result-----
%-----Plot of averaged parasitics-----
if plot_para==1

```

```

figure;
plot(f,parasitic_avg,'LineWidth', 2.5); %grid on;
title('Parasitic');
xlabel('Frequency (GHz)');
ylabel('Relative Response (dB)');
end
%-----Set color system-----
color=[0.23189431811233    0.23931256446899    0.04975448407125
        0.07838407477005    0.64081540987002    0.19088657039756
        0.84386949887436    0.17390024846178    0.17079281374168
        0.99429549051392    0.43979085694638    0.34004794885569
        0.61421731054403    0.26507838692867    0.69323955120646
        0.59152520374645    0.11974661695181    0.03812879676737
        0.45859795466496    0.86986735040701    0.93423651891762
        0.26444916614927    0.16030033919718    0.87285525701963
        0.43788030773557    0.44583124997499    0.16688742090893];
%-----plot raw data-----
if plot_raw==1
figure; %raw data
    set(gcf,'DefaultAxesColorOrder',color);
    plot(f,s21_raws,'LineWidth',2);
    title('Raw data');
    xlabel('Frequency (GHz)');
    ylabel('Relative Response (dB)');
    grid on;
end
%-----Make a legend-----
legendstr='legend(';
for i=1:length(file_num)
    legendstr=strcat(legendstr,'');
    if detunings(i)==99
        legendstr=strcat(legendstr,'free-running')
    else
        detune=num2str(detunings(i));
        legendstr=strcat(legendstr,'detuning= ',detune,'nm');
    end
    legendstr=strcat(legendstr,'');
    if i < length(file_num)
        legendstr=strcat(legendstr,', ');
    end
end
legendstr=strcat(legendstr,',2)');
%-----Plotting-----
%-----linear scale-----
%-----search for 3dB point-----
if plot3dB==1
    flat_resp=s21_fits(30,:);
    three_db=flat_resp-3
    for i=1:length(file_num)
d2=100; flag=1;
if i==1
f_3db_inx_free=find(f_add>f_3db_free);
j=f_3db_inx_free(1);
else
    f_3db_inx_lk=find(f_add>f_3db_lk(i-1));

```

```

        j=f_3db_inx_lk(1);
    end
    while flag==1
        d1=abs(s21_fits(j,i)-three_db(i));
        if d1<=d2
            f_3db(i)=f_add(j);
            s21_3db(i)=s21_fits(j,i);
        else
            flag=0;
        end
        d2=d1;
        j=j+1;
    end
end
end
%-----plot-----
figure;
set(gcf,'DefaultAxesColorOrder',color); %curve-fitted data
plot(f_add,s21_fits,'LineWidth',1.3);
if plot3dB==1
    hold on;
    plot(f_3db,s21_3db,'+','MarkerSize',11);
    title(plot_title);
    disp('fz, fp, fr, Gamma, A, offset'); %place fitted parameters

    for i=1:length(file_num)
        disp(num2str(para_each(i,:)));
        text(f_3db(i)-2*i-2,s21_3db(i)-5*i+5, strcat(num2str(f_3db(i)), 'GHz'));
        text(2,-70-i*6, num2str(para_each(i,:)));
    end
end
xlabel('Frequency (GHz)');
ylabel('Relative Response (dB)');
grid on;
eval(legendstr);
ylim([-120,40]);
hold on;
f_int_f=find(f<f_cutoff_free);
freq_f=f(f_int_f);
s21_p_rem_f=s21_subs(f_int_f,1);
f_int_l=find(f<f_cutoff_lock); %eliminate the noise
freq_l=f(f_int_l);
s21_p_rem_l=s21_subs(f_int_l,2:length(file_num));
set(gcf,'DefaultAxesColorOrder',color);
%parasitic removed data
plot(freq_f,s21_p_rem_f,':',freq_l,s21_p_rem_l,':','LineWidth',2.5);
%saveas(gcf,fig_name,'fig');
%saveas(gcf,fig_name,'jpg');
%-----plot in log scale-----
if plot_log==1
    figure;
    %curve-fitted data in log scale
    set(gcf,'DefaultAxesColorOrder',color);
    plot(log10(f_add),s21_fits,'LineWidth',1.3);
    title(plot_title);

```

```

xlabel('Frequency (dB)');
ylabel('Magnitude (dB)');
grid on;
eval(legendstr{1});
ylim([-150,5]);
    hold on;
plot(log10(freq_f),s21_p_rem_f,':',log10(freq_l),s21_p_rem_l,':','LineW
idth',2.5);    %parasitic removed data in log scale
saveas(gcf,strcat(fig_name,'-log'),'fig');
saveas(gcf,strcat(fig_name,'-log'),'jpg');
end

```

s21_curve_fitting_difference.m

```

% curve-fitting the difference of two transfer functions
function [parasitic,resnorm,p]=s21_curve_fitting_difference(varargin)
%curve-fitting program of s21
%first curve-fitting the difference of two curves to get the fitting
parameters
%then use the optimized parameters to get the curve-fitted result
%subtract the curve-fitted result from the raw data to get parasitic
%average the parasitic got from two curves
%return the average parasitic of the two files and the curve-fitting
error value
%-----Input arguments-----
%Totally 12 inputs, every two stand for the same thing, first is
meaning of the argument, second is the value of the argument
for i=1:2:nargin
    varargin{i};
    switch varargin {i}
        case 'file1'
            file1=varargin{i+1}
        case 'file2'
            file2=varargin{i+1}
        case 'fit_plot'
            fit_plot=varargin{i+1}
        case 'delimiter'
            delimiter=varargin{i+1}
        case 'p0'
            p0=varargin{i+1}
        case 'f_min'
            f_cut_min=varargin{i+1}
        case 'f_max'
            f_cut_max=varargin{i+1}
        case 'lb'
            lb=varargin{i+1}
        case 'ub'
            ub=varargin{i+1}
        case 'call1'
            DCshift1=varargin{i+1}
        case 'cal2'
            DCshift2=varargin{i+1}
    end
end
%-----Import files-----
file_raw_1 = dlmread(file1,delimiter);    %import file_1

```

```

file_raw_2 = dlmread(file2,delimiter); %import file_2
f = file_raw_1(:,1)./1e9; %get frequency
value and change the frequency unit to GHz
s21_raw_1=file_raw_1(:,3) + DCshift1; %get response
value and do calibration
s21_raw_2=file_raw_2(:,3) + DCshift2;
f_num = find(f>f_cut_min&f<f_cut_max); %eliminate the
noisy part
f_int = f(f_num);
s21_raw_1_int=s21_raw_1(f_num);
s21_raw_2_int=s21_raw_2(f_num);
%-----Make a difference of the two raw data-----
s21_diff = s21_raw_1_int - s21_raw_2_int;
%-----Curve-fitting the difference-----
%---fitted parameters p(i)= fn_1, f0_1, fr_1, gamma_1, const.offset(1-
2), fn_2, f0_2, fr_2, gamma_2
[p,resnorm,residual,exitflag,output]=lsqcurvefit(@difference_of_two_tra
nsfer_function,p0,f_int,s21_diff,lb,ub,optimset('MaxIter',1e3,'MaxFunEv
als',1e7,'TolFun',1e-16,'TolX',1e-
7,'MinAbsMax',1e52,'Display','final'));
p,resnorm
if exitflag < 0;
    disp('Did not converge on a solution');
%inform failuar of curve-fitting
end
diff_fit = difference_of_two_transfer_function(p,f);
%get curve-fitted plot of the difference
s21_fit_1 = injection_locked_transfer_function([p(1:5),0],f);
%get curve-fitted plot of file_1 without const.offset
s21_fit_2 = injection_locked_transfer_function([p(7:11),0],f);
%get curve-fitted plot of file_2 without const.offset
parasitic_1 = s21_raw_1 -
injection_locked_transfer_function([p(1:5),(mean(s21_raw_1)-
mean(s21_fit_1))],f);
parasitic_2 = s21_raw_2 -
injection_locked_transfer_function([p(7:11),(mean(s21_raw_2)-
mean(s21_fit_2))],f);
parasitic = (parasitic_1 + parasitic_2)/2;
%get averaged parasitic from every two files
%-----Plot the fitting result-----
color=[0.61421731054403    0.26507838692867    0.69323955120646
        0.59152520374645    0.11974661695181    0.03812879676737
        0.45859795466496    0.86986735040701    0.93423651891762
        0.26444916614927    0.16030033919718    0.87285525701963
        0.43788030773557    0.44583124997499    0.16688742090893]
if fit_plot==1
    figure;
    set(gcf,'DefaultAxesColorOrder',color);
    plot(f_int,s21_diff,':','LineWidth',3.5); hold on;
    plot(f,diff_fit,'LineWidth',1.5);
    grid on;
    title('Curve-fitted difference');
    figure;
    set(gcf,'DefaultAxesColorOrder',color);
    plot(f,s21_fit_1,'LineWidth',1.5);

```

```

    grid on;
    title('one time curve-fitted s21')
end

```

injection_locked_transfer_function.m

```

% injection-locked laser transfer function
function [y]=injection_locked_transfer_function(p,f)
%This is the analytical injection locked transfer function
%p is the vector holding parameters in the function
%p(1) = fz, p(2) = f0, p(3) = fr, p(4) = gamma, p(5) = magnitude, p(6)=
const.offset
y = p(6) + 10*log10 ( ( 1 + (f ./ p(1) ).^2 ) ./ ( 1 + ( f / p(2) ) .^2
) ./ ( ( 1 - ( f./ p(3) ) .^2 ) .^2 + (( p(4)/2/pi./p(3)).^2) .* (
f./p(3) ).^2 ) );

```

difference_of_two_transfer_function.m

```

% difference of two injection-locked laser transfer functions
function [y]=difference_of_two_transfer_function(p,f)
%The difference of two injection locked transfer functions fixed the
magnitude
%p is the vector of parameters in the two functions
%p(1) = p(1) = fz_1, p(2) = fp_1, p(3) = fr_1, p(4) = gamma_1, p(5) =
magnitude_1, p(6) = const.offset, p(7) = fz_2, p(8) = fp_2, p(9) =
fr_2, p(10)= gamma_2, p(11)=magnitude_2
y = p(6) + 10*log10 ( ( 1 + ( f./ p(1) ).^2 ) ./ ( 1 + ( f / p(2) ) .^2 )
./ ( ( 1 - ( f./ p(3) ) .^2 ) .^2 + (( p(4)/2/pi./p(3)).^2) .* (
f./p(3) ).^2 ) ) - 10*log10 ( ( 1 + (f ./ p(7) ).^2 ) ./ ( 1 + ( f / p(8)
) .^2 ) ./ ( ( 1 - ( f./ p(9) ) .^2 ) .^2 + (( p(10)/2/pi./p(9)).^2) .*
( f./p(9) ).^2 ) );

```

free_running_transfer_function.m

```

% free-running laser transfer function
function [y]=free_running_transfer_function(p,f)
%This is the analytical injection locked transfer functionp
%p is the vector holding parameters in the function
%p(1) = fz, p(2) = fp, p(3) = fr, p(4) = gamma, p(5) = magnitude, p(6)
= const. offset
y=p(6) + 10*log10 ( 1 ./ ( ( 1 - ( f./ p(3) ) .^2 ) .^2 + ((
p(4)/2/pi./p(3)).^2) .* ( f./p(3) ).^2 ) );

```

s21_curve_fitting.m

```

% curve-fitting single de-embedded s21
function
[p,f,f_add,s21_raw,s21_sub,s21_fit]=s21_curve_fitting(f_lk,file,delimit
er,parasitic,p0,f_cut_min,f_cut_max,freq_add,freq_add_stop,lb,ub,DCshif
t)
%curve-fitting each s21 file using the average parasitic got from all
the files
%-----Import file-----
s21_file = dlmread(file,delimiter); %import file
f = s21_file(:,1)./1e9; %get frequency and change unit
%try to eliminate the noisy part then do curve-fitting
f_num = find(f>f_cut_min&f<f_cut_max);
f_int = f(f_num);
s21_raw = s21_file(:,3) + DCshift; %get response and calibrate

```

```

%-----Subtract the parasitic from raw data-----
s21_sub = s21_raw - parasitic;
s21_sub_int = s21_sub(f_num);
%-----Curve-fitting the parasitic-removed data-----
if f_lk==1 % locked fitting
    % p(i)=magnitude, f0, fr, gamma, const.offset
    [p,resnorm,residual,exitflag]=lsqcurvefit(@injection_locked_transfer_fu
nction,p0,f_int,s21_sub_int,lb,ub,optimset('MaxIter',1e3,'MaxFunEvals',
1e7,'TolFun',1e-16,'TolX',1e-7,'MinAbsMax',1e52,'Display','final'));
    if exitflag < 0;
        disp ('Did not converge on a solution');
    end
    p,resnorm
else %free_running fitting
    %p(i)=fn, f0, fr, gamma, magnitude, const.offset
    [p,resnorm,residual,exitflag]=lsqcurvefit(@free_running_transfer_functi
on,p0,f_int,s21_sub_int,lb,ub,optimset('MaxIter',1e3,'MaxFunEvals',1e7,
'TolFun',1e-16,'TolX',1e-7,'MinAbsMax',1e52,'Display','final'));
    if exitflag < 0;
        disp ('Did not converge on a solution');
    end
    p,resnorm
end
%-----Curve-fitted result-----
if freq_add==1
    f_add=f;
%plot in a longer scale of frequency for curve-fitted data
for i=1:(freq_add_stop-40)/10
    f_len=length(f_add);
    add=find(f_add>20+i*10&f_add<30+i*10);
%increas 10GHz every time
    f_add(f_len+1:f_len+length(add))=f_add(add)+10;
end
else
    f_add=f;
end
if f_lk==1
    s21_fit = injection_locked_transfer_function(p(1:6),f_add);
%curve-fitted locked result
else
    s21_fit = free_running_transfer_function(p(1:6),f_add);
%curve-fitted free running result
end

```

A1.5 Amplifier Model for Data Pattern Inversion

```

%- use amplifier model to simulation data pattern inversion
clear; clc;
%- define VCSEL constants
r1 = 0.99; % top mirror field reflectivity
r2 = 0.995; % bottom mirror field reflectivity
L = 1e-6; % cavity length
alpha_i = 1e3; % distributed material loss m-1
detuning = [0.05 0.355 .8]*1e-9; % wavelength detuning

```

```

kappa = 1e12; % coupling rate
alpha = 4; % linewidth enhancement factor
R_inj = 0.3; % field injection ratio
g0 = 2e-20; % differential gain in m^2
c = 3e8; % m/s - speed of light
vg = 8.3e7; % group velocity of the wave inside the slave laser
cavity, index ~ 3.6
gamma_th = alpha_i - log(r1*r2)/L % threshold gain of the laser
Nth = gamma_th / g0 % threshold carrier density
%-----constants for QW gain calculation-----
e = 1.6e-19; % C - electron charge
nr = 3.6; % refractive index
h_b = 1.05e-34; % Js
eps0 = 8.8542e-12; % F/m - vacuum dielectric const.
m0 = 9.1e-31; % kg - free electron mass
me = 0.041*m0; % electron effective mass
mlh = 0.05*m0; % light hole effective mass
mhh = 0.56*m0; % heavy hole effective mass
mh = (1/mlh + 1/mhh)^-1; % hole effective mass
mr = (1/me + 1/mh)^-1; % reduced mass
Eg = .75*e; % J - bandgap adjusted to emit at 1550 nm
Lz = 5e-9; % m - quantum well thickness 5 nm
QW = 7; % layers of quantum wells for the gain
Ep = 20.7*e;
Mb = m0/3*Ep; % QW momentum matrix element
kBT = 26.5e-3*e; % J - Boltzmann constant * room temp.@300K
Ee1 = h_b^2/(2*me)*(pi/Lz)^2/15; % 1st subband in c band, energy
reference is the top of the valence band
Eh1 = -h_b^2/(2*mh)*(pi/Lz)^2/15; % 1st subband in v band, factor
1/15 used to adjust from ideal infinite well model
E_tran = (Eg + Ee1 - Eh1)/e % intersubband transition energy
% emission wavelength
del_E = Eg + Ee1 - Eh1;
lambda = h_b*2*pi*c/del_E;
W = 2*pi*c/lambda;
% parameters in the gain spectrum
C0 = pi*e^2/(nr*c*eps0*m0^2*W); % constant
p2D = mr/(pi*h_b^2*Lz)/100; % density of states of 2D structure,
adjusted from ideal model
%- modulated carrier density
N0=4e22; % carrier modulation amplitude
t=[.6:1/1e2:7.6]; % two periods of square wave
data = square(pi*t, 30); % square wave with amplitude of N0 and period
of 2 ns - 1 Gb/s pulse
rise = [-1:.1:1];
fall = [1:-.1:-1];
l=1;
while l < length(data)
    if (data(l)-data(l+1)) < 0
        data = [data(1:(l-1)),rise,data((l+2):end)];
        t = [t(1:(l-1)), [t(l):1/2e3:t(l+1)],t((l+2):end)];
        l=l+1+length(rise);
    end
    if (data(l)-data(l+1)) > 0
        data = [data(1:(l-1)),fall,data((l+2):end)];

```

```

        t = [t(1:(l-1)), [t(l):1/2e3:t(l+1)], t((l+2):end)];
        l=l+1+length(fall);
    end
    if (data(l)-data(l+1)) == 0
        l=l+1;
    end
end
%dc = 1e10; % offset chirp frequency 10GHz
N_m = N0*data;
t_chirp = 5e-12*diff(N_m); % transient chirp induced by carrier
modulation
t_chirp(length(t_chirp)+1) = 0;
m=1;
figure;
for j=1:length(detuning)
    %- steady state solution
    phi_0 =
asin(2*pi*c/lambda^2*detuning(j)/kappa/sqrt(1+alpha^2)/R_inj)-
atan(alpha) % steady state phase
    del_N = - 2*kappa/(vg*g0)*R_inj*cos(phi_0) % carrier density
reduction under OIL
    N = Nth + del_N + N_m; % electron density
    P=N; % hole density
    % quasi Fermi levels
    Fc = Ee1 + Eg + kBT*log(exp((N*pi*h_b^2*Lz)/(me*kBT))-1); % energy
reference is the top of valence band
    Fv = Eh1 - kBT*log(exp((P*pi*h_b^2*Lz)/(mh*kBT))-1);
    Fc_Fv = Fc/e - Fv/e; % Fermi Energy difference (compare with
intersubband transition)
    % Fermi-Dirac distribution
    fc = 1./(1+exp((Eg + Ee1 - Fc)/kBT));
    fv = 1./(1+exp((Eh1 - Fv)/kBT));
    gamma = QW*C0*p2D*(fc-fv)*2*Mb; % amplifier gain
    %g = g0*gamma/gamma_th; % rescale differentail gain (slope of
gain) at different amplifier gain level
    del_cav_lambda = - lambda^2/(2*pi*c)*alpha*vg*g0*(del_N+N_m)/2; %
cavity resonance shift in wavelength
    del_cav_f = abs(alpha*vg*g0*(del_N+N_m)/2/2/pi); % cavity
resonance shift in Hz
%-----Phase and reflectivity calculatio-----
    del_lambda = del_cav_lambda - detuning(j); % spacing between master
mode and cavity resonance
    del_f = - del_lambda/0.8*100*1e18; % above spacing in frequency
    phase = 2*i*(2*pi.*(del_f + t_chirp)./vg)*L; % optical phase of
the master mode
    Refl = abs((1-r1^2)*r2*exp((gamma-alpha_i)*L).*exp(phase)./(1-
r1*r2*exp((gamma-alpha_i)*L).*exp(phase))-r1).^2; % intensity
reflectivity of the master
%- plot original modulation signal
    subplot(3,2,m);plot(t,gamma/100,'b','LineWidth', 2.5); % plot
gain in cm^-1
    xlim([t(1),t(length(t))]);
    if j == 3
        xlabel('Time (ns)');
    end
end

```

```

        ylim([-300,120]);
        if j == 2
            ylabel('VCSEL Gain (cm-1)');
        end
%-----plot optical intensity of the master-----
        subplot(3,2,m+1);plot(t,Refl,'r','LineWidth', 2.5);
        xlim([t(1),t(length(t))]);
        if j == 3
            xlabel('Time (ns)');
        end
        if j == 2
            ylabel('Relative Output Intensity (a.u.)');
        end
        m = m+2;
    end
end

```

A1.6 Spectrogram Plotting

```

% Plot spectrogram by definition from measured data
% Similar as FROG traces, see FROG introduction as references
clear;
filename = 'import_chirp_data.chp';
data=dlmread(filename, ',', 8, 0);
time=data(951:1150,1)/1e-9;    % in ns
inten=data(951:1150,4)/1e-3;  % in mW
chirp=data(951:1150,5)/1e9;   % in GHz
N = 200;    %number of data points. An even number makes it easier
width =time(N)-time(1);    %pulse duration in ns
dt = width/N;    %sampling time interval
t = (-N/2:N/2-1)*dt;    %new time sequence - time delay center at 0
df = 24.3/N; % chirp step for y-axis labeling
f = (-N/2:N/2-1)*df;    %frequency sequence for FFT
f0=0;%3e8/1.5e-6/1e9; %center frequency
intensity = inten;    %pulse intensity
phase = cumsum(chirp)*2*pi*dt+f0;
E_sig = sqrt(intensity).*exp(-j*phase); % electric field of the signal
gate = exp(-(t/.032).^2);    % gate pulse - change the width of the
gate pulse, to make the spectrogram look better (0.004 for FR)
XF = XFROGTRACE(gate,E_sig); % get spectrogram by definition
XF_inten=XF./max(max(XF)).*max(max(intensity));
figure;
imagesc(t,f,XF_inten); axis xy; colormap(jet); colorbar;
xlabel('Time Delay (ns)'),ylabel('Frequency Chirp (GHz)')

```

CalcEsigOP.m

```

function [E]=CalcEsigOP(G,P)
% Calculate E_signal (time domain complex form of FROG trace) using
Outer PProduct
error(nargchk(2,2,nargin))
N = length(P);
E = G(:)*P(:).';
for i = 1:N
    E(i,:) = circshift(E(i,:),[0,i-1]);
end

```

XFROGTRACE.m

```
function SHG = CALCSHG(gate,pulse);
SHG = CalcEsigOP(gate,pulse);
SHG = fftshift(fft(SHG)); % fftshift swap the upper/lower half, and
left and right half of the matrix
SHG = abs(SHG).^2;
```

A1.7 LI Curve of a Two-Mode VCSEL

```
% LI curves of a free-running two-mode
clc; clear;
h = 6.63e-34; % Planck constant
nu = 3e8/1550e-9; % photon frequency
taop1 = 3e-12; % mode_1 photon lifetime in s
taop2 = 2.99e-12; % mode_2 photon lifetime in s
R = 0.998; % top mirror reflectivity
%----solve two-mode rate equations-----
options=odeset('AbsTol',1e-6,'RelTol',1e-6,'Stats','on');
tspan= 0:10; % ns, time span of interest
y0 = [0 0 0]; % initial values for s1, s2 and N
bias = [0.1:.1:2,3:10]*1e-3; % bias in mA
for i = 1:length(bias)
    [t,y]=ode45(@twomode,tspan,y0,options,bias(i));
    output(i)=y(length(tspan),1)*h*nu*(1-R)/taop1*1e6;
end
%-----Plot transient-----
figure; plot(t,y(:,1)); xlabel('Time (ns)'); ylabel('Photon # Mode 1');
figure; plot(t,y(:,2)); xlabel('Time (ns)'); ylabel('Photon # Mode 2');
figure; plot(t,y(:,3)); xlabel('Time (ns)'); ylabel('Phase');
%-----Plot LI curve-----
figure; plot(bias*1e3, output, 'LineWidth',2); xlabel('Bias (mA)');
ylabel('Power (uW)');
```

twomode.m

```
% 2-mode free-runnging rate equations
function dy = twomode(t, y, bias)
% bias is the input from the main program
%-----constants-----
gamma = 0.03; % mode confinement factor
vg = 8.3; % group velocity cm/ns
gn = 6e-16; % differential gain cm2
Va = 3e-12; % active region volume cm3
G0 = gamma*vg*gn/Va; % gain coeff. 1/ns
Ntr = 1.5e18*Va; % transparency carrier #
eps11 = 2e-7; % self-saturation coeff. for mode 1
eps22 = 2e-7; % self-saturation coeff. for mode 1
eps12 = .5e-7; % cross-saturation coeff.
eps21 = eps12;
tao1 = 3e-3; % photon lifetime of model1 ns
tao2 = 2.99e-3; % photon lifetime of mode2 ns
B = 8e-20; % recommbination coeff. cm3/ns
beta = 1e-4; % spon. em. rate
gammaN = .22; % carrier recommbination rate ns-1
```

```

q = 1.6e-10; % electron charge A/ns
% differentail equations y(1) = s1, y(2) = s2, y(3) = N
dy = zeros(3,1); % creat a colum vector which is required by ode solver
dy(1) = (G0*(y(3)-Ntr)/(1+eps11*y(1)+eps12*y(2))-1/tao1)*y(1)+
beta*B/Va*y(3)^2; % photon # equation for model1
dy(2) = (G0*(y(3)-Ntr)/(1+eps21*y(1)+eps22*y(2))-1/tao2)*y(2)+
beta*B/Va*y(3)^2; % photon # equation for mode2
dy(3) = bias/q - gammaN*y(3) - G0*(y(3)-
Ntr)/(1+eps11*y(1)+eps12*y(2))*y(1) - G0*(y(3)-
Ntr)/(1+eps21*y(1)+eps22*y(2))*y(2); % carrier # equation

```

A1.8 Two-Mode OIL Stability Plot With Spatial Detuning

```

% transient behavior of an injection-locked two-mode laser with
nonlinear gain effects
% locking range is simulated - stable locking in detuning_freq vs
injection ratio 2D plan
clc;
clear;
%-----solve single-mode rate equations for master laser-----
options = odeset('AbsTol',1e-6,'RelTol',1e-6,'Stats','on');
tspan= 0:10; % ns, time span of interest
y0 = [0 0 0]; % initial values for s1, s2 and N
master_bias = 10e-3; % bias in mA
[t_master,y_master]=ode45(@singlemode,tspan,y0,options,master_bias);
Sinj0 = y_master(length(t_master),1);
% initial injection power, will keep constant
index = find(t_master > 3);
% time for phase to be stable
phi_fit=polyfit(t_master(index),y_master(index,2),1); %
curve-fitting master phase
%initial master phase changing with time, so put into rate equations
%-----solve two-mode rate equations for slave laser-----
options=odeset('AbsTol',1e-6,'RelTol',1e-6,'Stats','on');
tspan= 0:10; % time span of interest
y0 = [0 0 0 0 0]; % initial values for s1, s2 and N
slave_bias = 3e-3; % bias in mA
[t_slave,y_slave]=ode45(@twomodesfull,tspan,y0,options,slave_bias);
S_01 = y_slave(length(t_slave),1);
phi_01 = y_slave(length(t_slave),2);
S_02 = y_slave(length(t_slave),3);
phi_02 = y_slave(length(t_slave),4);
N_0 = y_slave(length(t_slave),5);
Y_inj0 = [S_01, phi_01, S_02, phi_02, N_0];
%-----Solve for Injection locking-----
%initial values for locking
inj_ratio = -15:0; % injection ratio in dB
inj_coeff = 10.^(inj_ratio/10)*S_01/Sinj0;
det_f = -100:10:300; % relative to Mode 1 and in GHz
% indices for results in stability plot
for i=1:length(inj_coeff)
    S_inj = inj_coeff(i)*Sinj0;
    for j = 1:length(det_f)
        options=odeset('AbsTol',1e-6,'RelTol',1e-3,'Stats','on');
    
```

```

%---- test if this point is in the locking range, stably locked-----
    inputs = [S_inj,det_f(j),phi_fit(1),phi_fit(2),slave_bias];
    tic;
% start measuring the time of solving this locking condition
[T_try,Y_try] = ode23(@twomodes_couple,[10,20],Y_inj0,options,inputs);
    t_solver = toc
    if t_solver > 4
        stable(i,j) =0;
    else
        index1 = find(T_try<12);index2=find(T_try > 18);
        v1=var(Y_try(index1,1));
        v2=var(Y_try(index2,1));
        v3=var(Y_try(index1,3));
        v4=var(Y_try(index2,3));
        if (v1/v2 > 1e2) && (v3/v4 > 1e2) %check converge
            if (Y_try(end,1) > Y_try(1,1))&&(Y_try(end,3) <
Y_try(1,3))&&(Y_try(end,1)/Y_try(end,3)>10)
                stable(i,j) = 1; % mode 1 locked
            else
                if (Y_try(end,1) < Y_try(1,1))&&(Y_try(end,3) >
Y_try(1,3))&&(Y_try(end,3)/Y_try(end,1)>10)
                    stable(i,j) =2; % mode 2 locked
                else
                    stable(i,j)=3; % converge but both
modes lasing
                end
            end
        else
            stable(i,j) = 0;
        end
    end
end
end
end
%----plot transient at one locking condition-----
figure; plot(T_try, Y_try(:,1),'LineWidth',2); xlabel('Time (ns)');
ylabel('Photon Number Mode 1');
figure; plot(T_try, Y_try(:,2),'LineWidth',2); xlabel('Time (ns)');
ylabel('Phase Mode 1');
figure; plot(T_try, Y_try(:,3),'LineWidth',2); xlabel('Time (ns)');
ylabel('Photon Number Mode 2');
figure; plot(T_try, Y_try(:,4),'LineWidth',2); xlabel('Time (ns)');
ylabel('Phase Mode 2');
figure; plot(T_try, Y_try(:,5),'LineWidth',2); xlabel('Time (ns)');
ylabel('Carrier Number');
%-----plot stability plot-----
figure;
for i=1:length(inj_ratio)
    for j = 1:length(det_f)
        if stable(i,j)==1
            plot(inj_ratio(i),det_f(j),'ro','MarkerFaceColor','r');hold
on;
        end
        if stable(i,j)==2

```

```

        plot(inj_ratio(i),det_f(j),'bo','MarkerFaceColor','b');hold
on;
    end
    if stable(i,j)==3
        plot(inj_ratio(i),det_f(j),'go');hold on;
    end
    if stable(i,j)==0
        plot(inj_ratio(i),det_f(j),'k.','MarkerSize',1);hold on;
    end
end
end
xlabel('Injection Ratio (dB)'); ylabel('Frequency Detuning (GHz)');

```

twomodesfull.m

```

% 2-mode free-running rate equations with phase equations
% bias is the input from the main program
function dy = twomodesfull(t, y, bias)
%-----constants-----
gamma = 0.03; % mode confinement factor
vg = 8.3; % group velocity cm/ns
gn = 6e-16; % differential gain cm2
Va = 3e-12; % active region volume cm3
G0 = gamma*vg*gn/Va; % gain coeff. 1/ns
Ntr = 1.5e18*Va; % transparency carrier #
eps11 = 2e-7; % self-saturation coeff. for mode 1
eps22 = 2e-7; % self-saturation coeff. for mode 2
eps12 = .5e-7; % cross-saturation coeff.
eps21 = eps12;
tao1 = 3e-3; % photon lifetime of mode1 ns
tao2 = 2.99e-3; % photon lifetime of mode2 ns
B = 8e-20; % recommbination coeff. cm3/ns
beta = 1e-4; % spon. em. rate
gammaN = .22; % carrier recommbination rate ns-1
q = 1.6e-10; % electron charge A/ns
alpha = 5; % Linewidth enhancement factor
% differentail equations y(1) = s1, y(2) = phi1, y(3) = s2, y(4) =
phi2, y(5) = N;
dy = zeros(5,1); % creat a colum vector which is required by ode solver
dy(1) = (G0*(y(5)-Ntr)/(1+eps11*y(1)+eps12*y(3))-1/tao1)*y(1)+
beta*B/Va*y(5)^2; % photon # equation for mode1
dy(2) = alpha/2*(G0*(y(5)-Ntr)/(1+eps11*y(1)+eps12*y(3))-1/tao1);
% phase equation for mode_1
dy(3) = (G0*(y(5)-Ntr)/(1+eps21*y(1)+eps22*y(3))-1/tao2)*y(3)+
beta*B/Va*y(5)^2; % photon # equation for mode2
dy(4) = alpha/2*(G0*(y(5)-Ntr)/(1+eps21*y(1)+eps22*y(3))-1/tao2);
% phase equation for mode_2
dy(5) = bias/q - gammaN*y(5) - G0*(y(5)-
Ntr)/(1+eps11*y(1)+eps12*y(3))*y(1) - G0*(y(5)-
Ntr)/(1+eps21*y(1)+eps22*y(3))*y(3); % carrier # equation % 2-mode

```

twomodes_couple.m

```

%injection-locking rate equations, locking on both modes
function dy = twomodes_couple(t, y, inputs) % inputs from the main
program inputs(1) = Sinj, inputs(2) = det_f, inputs(3) = phi_inj1,
inputs(4) = phi_inj2

```

```

%-----constants-----
gamma = 0.03; % lateral mode confinement factor
vg = 8.3; % group velocity cm/ns
gn = 6e-16; % differential gain cm2
Va = 3e-12;% active region volume cm3 (length = 1 um, mesa = 10*10
um^2)
G0 = gamma*vg*gn/Va; % gain coeff. 1/ns
Ntr = 1.5e18*Va; % transparency carrier #
eps11 = 2e-7; % self-saturation coeff. for mode 1
eps22 = 2e-7; % self-saturation coeff. for mode 2
eps12 = 0.5e-7; % cross-saturation coeff.
eps21 = eps12;
tao1 = 3e-3; % photon lifetime of model ns
tao2 = 2.99e-3; % photon lifetime of mode2 ns
B = 8e-20; % recommbination coeff. cm3/ns
beta = 1e-4; % spon. em. rate
gammaN = .22; % carrier recommbination rate ns-1
q = 1.6e-10; % electron charge A/ns
alpha = 5; % Linewidth enhancement factor
k1 = 0.7e3; % coupling rate ns-1 for mode 1
k2 = 0.3e3; % coupling rate ns-1 for mode 2
% differentail equations y(1) = s1, y(2) = phi1, y(3) = s2, y(4) =
phi2, y(5) = N
dy = zeros(5,1); % creat a colum vector which is required by ODE solver
dy(1) = (G0*(y(5)-Ntr)/(1+eps11*y(1)+eps12*y(3))-1/tao1)*y(1)+
beta*B/Va*y(5)^2 + 2*k1*sqrt(y(1)*inputs(1))*cos(y(2)-inputs(3)-
inputs(4)*t); % photon # equation for model
dy(2) = alpha/2*(G0*(y(5)-Ntr)/(1+eps11*y(1)+eps12*y(3))-1/tao1)-
k1*sqrt(inputs(1)/y(1))*sin(y(2)-inputs(3)-inputs(4)*t) -
2*pi*inputs(2); % Phase equation for model
dy(3) = (G0*(y(5)-Ntr)/(1+eps21*y(1)+eps22*y(3))-1/tao2)*y(3)+
beta*B/Va*y(5)^2 + 2*k2*sqrt(y(3)*inputs(1))*cos(y(4)-inputs(3)-
inputs(4)*t); % photon # equation for mode2
dy(4) = alpha/2*(G0*(y(5)-Ntr)/(1+eps21*y(1)+eps22*y(3))-1/tao2)-
k2*sqrt(inputs(1)/y(3))*sin(y(4)-inputs(3)-inputs(4)*t) -
2*pi*(inputs(2)-190); % Phase equation for mode2
dy(5) = inputs(5)/q - gammaN*y(5) - G0*(y(5)-
Ntr)/(1+eps11*y(1)+eps12*y(3))*y(1) - G0*(y(5)-
Ntr)/(1+eps21*y(1)+eps22*y(3))*y(3); % carrier # equation

```

BIBLIOGRAPHY

- [1] Pikovsky, M. Rosenblum, J. Kurths, and B. Chirikov, "Synchronization: A universal concept in nonlinear sciences," Cambridge Nonlinear Science Series, Cambridge, UK: Cambridge University Press, 2003.
- [2] B. van der Pol, "Forced oscillations in a circuit with non-nonlinear resistance," *Philos. Mag.*, iii, 65–80, 1927.
- [3] R. Adler, "A study of locking phenomena in oscillators," in *Proc. IRE*, 34, 351–357, 1946.
- [4] H. L. Stover and W. H. Steier, "Locking of laser oscillators by light injection," *Appl. Phys. Lett.*, 8, 91–93, 1966.
- [5] <http://www.physics.gatech.edu/schatz/clocks.html>
- [6] S. Kobayashi and T. Kimura, "Coherence on injection phase-locked AlGaAs semiconductor laser," *Electron. Lett.* 16, 668–670, 1980.
- [7] K. Iwashita and K. Nakagawa, "Suppression of mode partition noise by laser diode light injection," *IEEE Trans. Microw. Theory Tech.*, 30, 1657–1662, 1982.
- [8] R. Lang, "Injection locking properties of a semiconductor laser," *IEEE J. Quantum Electron.*, QE-18, 976–83, 1982.
- [9] C. Lin and F. Mengel, "Reduction of frequency chirping and dynamic linewidth in high-speed directly modulated semiconductor lasers by injection locking," *Electron. Lett.*, 20, 1073–1075, 1984.
- [10] N. A. Olsson, H. Temkin, R. A. Logan et al., "Chirp-free transmission over 82.5 km of single mode fibers at 2 Gbit/s with injection locked DFB semiconductor lasers," *IEEE J. Lightw. Technol.*, LT-3(1), 63–66, 1985.
- [11] C.-H. Chang, L. Chrostowski, and C. J. Chang-Hasnain, "Injection locking of VCSELs," *IEEE J. Sel. Top. Quantum Electron.*, 9(5), 1386–1393, 2003.
- [12] T. B. Simpson, J. M. Liu, and A. Gavrielides, "Bandwidth enhancement and broadband noise reduction in injection-locked semiconductor lasers," *IEEE Photon. Technol. Lett.*, 7, 709–711, 1995.
- [13] J. M. Liu, H. F. Chen, X. J. Meng, and T. B. Simpson, "Modulation bandwidth, noise, and stability of a semiconductor laser subject to strong injection locking," *IEEE Photon. Technol. Lett.*, 9, 1325–1327, 1997.
- [14] H.-K. Sung et al., "Modulation Bandwidth Enhancement and Nonlinear Distortion Suppression in Directly Modulated Monolithic Injection-Locked DFB Lasers," in *Int. Topical Microw. Photon. Meeting*, 2003, pp. 27–30.
- [15] L. Chrostowski, X. Zhao, C. J. Chang-Hasnain et al., "50-GHz Optically Injection-Locked 1.55-mm VCSELs," *IEEE Photon. Technol. Lett.*, 18, 367–369, 2006.
- [16] X. Jin and S. L. Chuang, "Relative intensity noise characteristics of injection-locked semiconductor lasers," *Appl. Phys. Lett.*, 77(9), 1250–1252, 2000.
- [17] L. Chrostowski, C. H. Chang, and C. J. Chang-Hasnain, "Reduction of Relative Intensity Noise and Improvement of Spur-Free Dynamic Range of an Injection Locked VCSEL," in *Proc. LEOS*, 2, October 27–28, 2003. pp. 65–80.
- [18] K. Iga, "Surface-emitting laser – its birth and generation of new optoelectronics field," *IEEE J. Select. Topics Quantum Electron.*, 6(6)1201-1215, December 2000.
- [19] Y.-C. Chang, C.S. Wang and L.A. Coldren, "High-efficiency, high-speed VCSELs with 35 Gbit/s error-free operation," *Electron. Lett.* Vol. 43, 2007.
- [20] R. H. Johnson and D. M. Kuchta, "30 Gb/s directly modulated 850 nm Datacom VCSELs," post-deadline paper, Conference on Lasers and Electro-optics (CLEO), San Jose, California, USA, 4-9 May 2008
- [21] W. E. Lamb, "Theory of an optical maser," *Phys. Rev.*, 134(6A), 1429–1450, 1964.
- [22] A. Murakami, K. Kawashima, and K. Atsuki, "Cavity resonance shift and bandwidth enhancement in semiconductor lasers with strong light injection," *IEEE J. Quantum Electron.* 39, 1196–204, 2003.
- [23] E. Lau, H.-K. Sung, and M. C. Wu, "Frequency response enhancement of optical injection-locked lasers," *IEEE J. Quantum Electron.* 44, 90-99, 2008.
- [24] V. Annovazzi-Lodi, S. Donati, and M. Manna, "Chaos and locking in a semiconductor laser due to external injection," *IEEE J. Quantum Electron.*, 30, 1537–1541, 1994.

- [25] V. Kovanis, A. Gavrielides, T. B. Simpson et al., "Chaos, Period-Doubling and Reverse Bifurcations in an Optically Injected Semiconductor Laser," in Proc. IEEE Nonlinear Optics: Materials, Fundamentals, and Applications (Cat. No.94CH3370-4), New York, NY, USA, 1994, pp. 30–32.
- [26] T. B. Simpson, J. M. Liu, A. Gavrielides et al., "Period-doubling route to chaos in a semiconductor laser subject to optical injection," *Appl. Phys. Lett.*, 64, 3539–3541, 1994.
- [27] T. B. Simpson, J. M. Liu, K. F. Huang, and K. Tai, "Nonlinear dynamics induced by external optical injection in semiconductor lasers," *Quantum & Semiclassical Optics*, 9, 765–784, 1997.
- [28] C. H. Henry, N. A. Olsson, and N. K. Dutta, "Locking range and stability of injection locked 1.54 μm InGaAsP semiconductor lasers," *IEEE J. Quantum Electron.* QE-21, 1152–1156, 1985.
- [29] R. S. Tucker, "High-speed modulation of semiconductor lasers," *J. Lightwave Technol.* 3, 1180–1192, 1985.
- [30] N. Schunk and K. Petermann, "Noise analysis of injection-locked semiconductor injection lasers," *IEEE J. Quantum Electron.* QE-22, 642–650, 1986.
- [31] J. Wang, M. K. Haldar, L. Li, and F.V.C. Mendis, "Enhancement of modulation bandwidth of laser diode by injection locking," *IEEE Photon. Technol. Lett.* 8, 34–36, 1996.
- [32] G. Yabre and J. Le Bihan, "Reduction of nonlinear distortion in directly modulated semiconductor lasers by coherent light injection," *IEEE J. Quantum Electron.* 33(7), 1132–1140, July 1997.
- [33] Yariv, A. *Optical Electronics in Modern Communications* Ch. 6 (Oxford Univ. Press, New York, 1997)
- [34] X. Zhao, Y. Zhou, C. J. Chang-Hasnain, W. Hofmann, and M. C. Amann, "Novel Modulated-Master Injection-Locked 1.55- μm VCSELs," *Opt. Express* 14, 10500–10507, 2006
- [35] Y. Matsui, H. Murai, S. Arahira, S. Kutsuzawa, and Y. Ogawa, "30-GHz bandwidth 1.55- μm strain-compensated InGaAlAs-InGaAsP MQW laser," *IEEE Photon. Technol. Lett.* 9, 25–27, 1997.
- [36] O. Kjebon, R. Schatz, S. Lourdudoss, S. Nilsson, B. Stalnacke and L. Backbom, "30GHz direct modulation bandwidth in detuned loaded InGaAsP DBR lasers at 1.55 μm wavelength," *Electron. Lett.* 33, 488–489, 1997.
- [37] K. Noguchi, O. Mitomi and H. Miyazawa, "Millimeter-wave Ti:LiNbO₃ optical modulators," *J. Lightwave Technol.* 16, 615–619, 1998.
- [38] M. Lee, H. E. Katz, C. Erben, D. M. Gill, P. Gopalan, J. D. Heber, and D. J. McGee, "Broadband modulation of light by using an electro-optic polymer," *Science* 298, 1401–1403, 2002.
- [39] L. Chrostowski, X. Zhao, and C. J. Chang-Hasnain, "Microwave performance of optically injection-locked VCSELs," *IEEE Trans. Microwave Theory Tech.* 54, 788–796 (2006).
- [40] X. Zhao, E. K. Lau, D. Parekh, H.-K. Sung, W. Hofmann, M. C. Amann, M. C. Wu, and C. J. Chang-Hasnain, "107-GHz Resonance Frequency of 1.55- μm VCSELs under Ultra-High Optical Injection Locking," Conference on Lasers and Electro-optics (CLEO), San Jose, California, USA, 4–9 May 2008
- [41] W. Hofmann, N. H. Zhu, M. Ortsiefer, G. Böhm, Y. Liu and M. C. Amann, "High speed (>11 GHz) modulation of BCB-passivated 1.55 μm InGaAlAs-InP VCSELs," *Electron. Lett.* 42, 976, 2006
- [42] E. K. Lau, H.-K. Sung and M. C. Wu, "Scaling of resonance frequency for strong injection-locked lasers," *Optics Lett.* 32, 3373, 2007.
- [43] B. Faraji, L. Chrostowski, W. Hofmann, M.-C. Amann, "Dual Resonance Frequency in Injection-Locked 1.55 μm VCSELs," OFC Anaheim, CA, 25–29 March, 2007
- [44] E. K. Lau, X. Zhao, H.-K. Sung, D. Parekh, C. Chang-Hasnain, and M. C. Wu, "Strong optical injection-locked semiconductor lasers demonstrating > 100-GHz resonance frequencies and 80-GHz intrinsic bandwidths," *Optics Express*, 16, 6609–6618, 2008.
- [45] J. C. Cartledge and R. C. Srinivasan, "Extraction of DFB laser rate equation parameters for system simulation purposes," *J. Lightwave Technol.* 15, pp. 852–860, 1997.
- [46] Koch, T. L. & Bowers, J. E. Nature of wavelength chirping in directly modulated semiconductor lasers. *Electron. Lett.* 20, 1038–1040, 1984
- [47] Koyama, F. & Suematsu, Y. Analysis of dynamic spectral width of dynamic-single-mode (DSM) lasers and related transmission bandwidth of single-mode fibers. *IEEE J. Quantum Electron.* QE-21, 292–297, 1985
- [48] Linke, R. A. Modulation induced transient chirping in single frequency lasers. *IEEE J. Quantum Electron.* QE-21, 593–597, 1985
- [49] L. G. Cohen, W. L. Mammel, and S. Lumish, "Tailoring the shapes of dispersion spectra to control bandwidths in single-mode fibers," *Optics Letters*, Vol. 7, 183, 1982

- [50] A. J. Antos, D. K. Smith, "Design and characterization of dispersion compensating fiber based on the LP₀₁ mode," *J. Lightwave Technol.* 12 1739-1745, 1994.
- [51] J. H. Winters, "Equalization in coherent lightwave systems using a fractionally spaced equalizer," *J. Lightwave Technol.* 8 1487-1491, 1990.
- [52] Bickers, L and Westbrook, L. D. "Reduction of laser chirp in 1.5 mm DFB lasers by modulation pulse shaping," *Electron. Lett.* 21, 103-105, 1985
- [53] Wedding, B., Franz, B. & Junginger, B. "10-Gb/s optical transmission up to 253 km via standard single-mode fiber using the method of dispersion-supported transmission," *J. Lightwave Technol.* 12, 1720-1727, 1994
- [54] Y. Matsui, D. Mahgerefteh, X. Zheng, C. Liao, Z. F. Fan, K. McCallion and P. Tayebati, "Chirp-managed directly modulated laser (CML)," *IEEE Photon. Technol. Lett.* 18, 385-387, 2006
- [55] Mohrdiek, S., Burkhard, H. & Walter H. "Chirp reduction of directly modulated semiconductor lasers at 10 Gb/s by strong CW light injection," *J. Lightwave Technol.* 12, 418-424, 1994
- [56] Chang, C.-H., Chrostowski, L., Chang-Hasnain, C. J. and Chow, W. W. "Study of long-wavelength VCSEL-VCSEL injection locking for 2.5-Gb/s transmission," *IEEE Photon. Technol. Lett.* 14, 1635-1637, 2002
- [57] T. L. Koch and R. A. Linke, "Effect of nonlinear gain reduction on semiconductor laser wavelength chirping" *Appl. Phys. Lett.* 48, 613-615, 1986
- [58] Y. Onishi, F. Koyama, N. Nishiyama, C. Caneau, and C. E. Zah, "Nonlinear optical input-output characteristics of 1.55 mm injection-locked vertical-cavity surface-emitting lasers" *Appl. Phys. Lett.* vol. 84, pp.3247-3249, 2004
- [59] L.-S. Yan, Y. Wang, B. Zhang, C. Yu, J. McGeehan, L. Paraschis, A. E. Willner, "Reach extension in 10-Gb/s directly modulated transmission systems using asymmetric and narrowband optical filtering," *Optics Express.* vol. 13, pp. 5106-5115, 2005
- [60] A. Alping, "Radio-over-fiber for the radio access network," presented at the 6th Int. Symp. Contemp. Photon. Tech. (CPT03), Tokyo, Japan, Jan. 15-17, 2003.
- [61] X. Lu and O. Snieszko, "The evolution of Cable TV networks," *Optical Fiber Telecommunications IVB*, edited by Ivan Kaminow and Tingye Li, Academic Press 2002.
- [62] T. Nishitani, T. Konishi, and K. Itoh, "All-Optical Analog-to-Digital Conversion Using Optical Delay Line Encoders," *IEICE Trans. Electron.*, Vol. E90-C, 479-480, 2007.
- [63] K. Y. Lau and A. Yariv, "Intermodulation distortion in a directly modulated semiconductor injection laser," *Appl. Phys. Lett.*, vol. 45, no. 10, pp. 1034-1036, 1984.
- [64] R.-H. Yan, R. J. Simes, L. A. Coldren, "Analysis and design of surface-normal Fabry-Perot electrooptic modulators," *IEEE J. Quantum Electron.* Vol. 25, 2272, 1989.
- [65] D. A. Miller, D. S. Chemla, T. C. Damen, A. C. Gossard, W. Wiegmann, T. H. Wood, and C. A. Burrus, "Band-Edge Electroabsorption in Quantum Well Structures: The Quantum-Confined Stark Effect," *Phys. Rev. Lett.* 53, 2173, 1984
- [66] L. Chrostowski, X. Zhao, and C. J. Chang-Hasnain, "Microwave performance of optically injection-locked VCSELs," *IEEE Trans. Microw. Theory Tech.*, 54, 788-796, 2006.
- [67] HP 71400C and 85200B detector application guide – RIN measurement
- [68] X. S. Yao and L. Maleki, "Optoelectronic oscillator for photonic systems," *IEEE J. Quantum Electron.*, vol. 32, no. 7, pp. 1141-1149, Jul. 1996.
- [69] X. S. Yao and L. Maleki, "Optoelectronic microwave oscillator," *J. Opt. Soc. Amer. B*, vol. 13 no. 8, pp. 1725-1735, Aug. 1996.
- [70] X. S. Yao, L. Maleki, and D. Eliyahu, "Progress in the opto-electronic oscillator - a ten year anniversary review," *IEEE MTT-S International Microwave Symposium*, vol. 1, pp. 287-290 2004.
- [71] X. S. Yao, L. Davis, and L. Maleki, "Coupled optoelectronic oscillators for generating both RF signal and optical pulses," *J. Lightwave Technol.*, vol. 18, no. 1, pp. 73-78, Jan. 2000.
- [72] X. S. Yao and L. Maleki, "Multiloop optoelectronic oscillator," *IEEE J. Quantum Electron.*, vol. 36, no. 1, pp. 79-84, Jan. 2000.
- [73] D. Strelakov, D. Aveline, Y. Nan, R. Thompson, A. B. Matsko, and L. Maleki, "Stabilizing an optoelectronic microwave oscillator with photonic filters," *J. Lightwave Technol.*, vol. 21, no. 12, pp. 3052-3061, Dec. 2003.
- [74] E. Salik, N. Yu, and L. Maleki, "An Ultralow Phase Noise Coupled Optoelectronic Oscillator," *IEEE Photon. Technol. Lett.*, vol. 19, no. 6, pp. 444-446, Mar. 2007.

- [75] Z. Weimin and G. Blasche, "Injection-locked dual opto-electronic oscillator with ultra-low phase noise and ultra-low spurious level," *IEEE Trans. Microwave Theory Tech.*, vol. 53, no. 3, pp. 929-933, Mar. 2005.
- [76] S. C. Chan and J. M. Liu, "Tunable narrow-linewidth photonic microwave generation using semiconductor laser dynamics," *IEEE Journal of Selected Topics in Quantum Electronics*, vol. 10, no. 5, pp. 1025-32, May 2004.
- [77] H.-K. Sung, E. K. Lau, X. Zhao, D. Parekh, C. J. Chang-Hasnain and M. C. Wu, "Optically Injection-Locked Optoelectronic Oscillators with Low RF Threshold Gain," *Conference on Lasers and Electro-optics (CLEO)*, Baltimore, USA, 6-11 May 2007
- [78] C. J. Chang-Hasnain, P.C. Ku, J. Kim, S.L. Chuang, "Variable Optical Buffer Using Slow Light in Semiconductor Nanostructures," in *Proceedings of the IEEE Conference on Special Issue on Nanoelectronics and Nanoscale Processing (2003)*, pp. 1884-1897.
- [79] G. Lenz, B. J. Eggleton, C. K. Madsen, and R. E. Slusher, "Optical Delay Lines Based on Optical Filters," *IEEE J. Quantum Electron.* 37, NO. 4, pp.525-532 (2001).
- [80] J. Scheuer, George T. Paloczi, J. K. S. Poon, and A. Yariv, "Coupled Resonator Optical Waveguides: Toward the Slowing and Storage of Light," *OPN* 16, No.2, 36 (2005).
- [81] J. E. Heebner, P. Chak, S. Pereira, J. E. Sipe, R. W. Boyd, "Distributed and Localized Feedback in Microresonator Sequences for Linear and Nonlinear Optics," *J. Opt. Soc. Am. B*, 21, 1818 (2004)
- [82] J. P. Heritage, A. M. Weiner, and R. N. Thurston, "Picosecond Pulse Shaping by Spectral Phase and Amplitude Manipulation," *Opt. Lett.* 10, 609 (1985).
- [83] M.S. Bigelow, N.N Lepeshkin, R.W. Boyd, "Observation of Ultraslow Light Propagation in a Ruby Crystal at Room-Temperature," *Phys. Rev. Lett.* 90, 113903 (2003).
- [84] L.V. Hau, S.E. Harris, Z. Dutton, C.H. Behroozi, "Light speed reduction to 17 m/s in an ultracold atomic gas," *Nature* 397, 594-598 (1999).
- [85] H. Altug, J. Vuckovic, "Experimental demonstration of the slow group velocity of light in two-dimensional coupled photonic crystal microcavity arrays," *Appl. Phys. Lett.* 86, 111102 (2005).
- [86] Ph. Palinginis, S. Crankshaw, F. Sedgwick, M. Moewe, E. Kim, C.J. Chang-Hasnain, H. Wang, S. L. Chuang, "Ultraslow light (< 200 m/s) propagation in a semiconductor nanostructure," *Appl. Phys. Lett.* 87, 171102, 2005
- [87] X. Zhao, P. Palinginis, B. Pesala, C. J. Chang-Hasnain, and P. Hemmer, "Tunable ultraslow light in vertical-cavity surface-emitting laser amplifier," *Optics Express* 13, 7899-7904, 2005.
- [88] H. Su and S. L. Chuang, "Room temperature slow and fast light in quantum-dot semiconductor optical amplifiers," *Appl. Phys. Lett.* 88, 061102, 2006.
- [89] B. Pesala, Z. Chen, and C. Chang-Hasnain, "Tunable pulse delay demonstration using four-wave mixing in semiconductor optical amplifiers," presented at OSA Topical Meeting of Slow and Fast Light, Washington, DC, 23-26 July 2006.
- [90] *Passive Optical Networks: Principles and Practice*, edited by Cedric F. Lam, Academic Press, 2007
- [91] P. J. Winzer, R.-J. Essiambre, "Advanced optical modulation formats," *Proceedings of the IEEE*, vol.94, 952-984, 2006
- [92] A. Banerjee, Y. Park, F. Clarke, H. Song, S. Yang, G. Kramer, K. Kim, and B. Mukherjee, "WDM-PON technologies for broadband access: A review," *OSA J. Opt. Networking*, vol. 4, pp. 737-758, Nov. 2005.
- [93] L. Chrostowski, C. Chang, and C. J. Chang-Hasnain, "Uncooled injection-locked 1.55 mm tunable VCSELs as DWDM transmitter," in *Proc. Optical Fiber Communication Conf.*, Mar. 2003, vol. 2, pp. 753-754.
- [94] W. Hung, C.-K. Chan, L.-K. Chen, and F. Tong, "An optical network unit for WDM access networks with downstream DPSK and upstream remodulated OOK data using injection-locked FP laser," *IEEE Photon. Technol. Lett.*, vol. 15, no. 10, pp. 1476-1478, Oct. 2003.
- [95] W. Yuen, G. S. Li, R. F. Nabiev, M. Jansen, D. Davis, and C. J. Chang-Hasnain, "Electrically-pumped directly-modulated tunable VCSEL for metro DWDM applications," in *GaAs IC Symp. Tech. Dig.*, Oct. 2001, pp. 51-52.
- [96] W. S. Jang, H. C. Kwon, and S. K. Han, "Suppression of Rayleigh backscattering in a bidirectional WDM optical link using clipped direct modulation," *IEE Proc., Optoelectron.*, 151, (4), pp. 219-222, 2004
- [97] Y. Chung, "Challenges towards Practical WDM-PON" in *Optoelectronic Conference in Communications*, paper 6C4-1-1-, 2006.

- [98] C. L. Lin, *Broadband optical access and FTTH*, (Wiley & Sons, Ltd, 2006), Chapter 12, pp. 288.
- [99] K. Tanaka, H. Izumita, N. Tomita, and Y. Inoue, "In-service individual line monitoring on a mehto for compensating for the temperature-dependent channel drift of a WM-PON containing a AWGR using a 1.6 um tunable OTDR," in *Eur. Conf. Optical Communication*, paper 448, pp. 295-298, 1997.
- [100] K. W. Lim, E. S. Son, K. H. Han, and Y. C. Chung, "Fault localization in WDM-PON by Reusing Downstream Light Sources", *IEEE Photon. Technol. Lett.*, Vol. 17, pp. 2691-2693, 2005.
- [101] S. B. Park, D. K. Jung, H. S. Shin, S. Hwang, Y. Oh, and C. Shim, "Optical fault monitoring method using broadband light source in WDM-PON," *Electron. Lett.*, 42, pp. 239-241, 2006.
- [102] K. Lee, S. B. Kang, D. S. Lim, H. K. Lee and W. Sorin, "Fiber link loss monitoring scheme in bidirectional WDM transmission using ASE-injected FP-LD", *IEEE Photon. Technol. Lett.*, 18, pp. 523-525, 2006.
- [103] D. Vez, S. Eitel, S. Hunziker, G. Knight, M. Moser, R. Hoevel, H.-P. Gauggel, M. Brunner A. Hold, and K. Gulden, "10 Gb/s VCSELs for datacom: devices and applications," *Proc. SPIE Int. Soc. Opt. Eng.*, 4292, p. 29-43, 2003.
- [104] C. Carlsson, A. Larsson, A. Alping, "RF transmission over multimode fibers using VCSELs-comparing standard and high-bandwidth multimode fibers," *IEEE J. Light. Technol.*, 22, p. 1694-1700, 2004.
- [105] G. P. Agrawal, *Fiber-optic Communication Systems*, 3rd Edition, Wiley-Interscience
- [106] N. H. Zhu, et al., "Enhanced Modulation Bandwidth of a Fabry-Perot Semiconductor Laser Subject to Light Injection From Another Fabry-Perot Laser," *IEEE J. of Quantum Electron.*, vol. 44, no.6, June 2008.
- [107] J. Y. Law, G. H. M. van Tartwijk, G. P. Agrawal, "Effects of transverse-mode competition on the injection dynamics of vertical-cavity surface-emitting lasers," *Quantum Semiclass Opt.*, 9, pp. 737-747, 1997
- [108] Y. Hong, Paul S. Spencer, P. Rees, and K. Alan Shore, "Optical Injection Dynamics of Two-Mode Vertical Cavity Surface-Emitting Semiconductor Lasers," *IEEE J. Quantum Electron.*, 38, p. 274-278, 2002.
- [109] Y. Onishi, N. Nishiyama, C. Caneau and F. Koyama and C-E. Zah, "All-optical inverter based on long-wavelength VCSEL," *IEEE J. Selected Topics in Quantum Election.* 11, pp. 999-1005, 2005
- [110] C. J. Chang-Hasnain, J. P. Harbison, G. Hasnain, A. C. Von Lehmen, L. T. Florez, and N. G. Stoffel, "Dynamic, polarization, and transverse mode characteristics of vertical cavity surface emitting lasers," *IEEE J. Quantum. Electron.* 27, 1402-1409, 1991.
- [111] A. C. Bordonalli, C. Walton, and A. J. Seeds, "High-performance phase locking of wide linewidth semiconductor lasers by combined use of optical injection locking and optical phase-lock loop," *J. Lightw. Technol.*, 17, 328-342, 1999.
- [112] S. Yamashita and D. Matsumoto, "Waveform reshaping based on injection locking of a distributed-feedback semiconductor laser," *IEEE Photon. Technol. Lett.*, 12, 1388-1390, 2000.
- [113] S. Yamashita and J. Suzuki, "All-optical 2R regeneration using a two-mode injection-locked Fabry-Perot laser diode," *IEEE Photon. Technol. Lett.*, 16, 1176-1178, 2004.
- [114] L. Goldberg, H. F. Taylor, J. F. Weller, and D. M. Bloom, "Microwave signal generation with injection-locked laser diodes," *Electron. Lett.*, 19, 491-493, 1983.
- [115] R. P. Braun, G. Grosskopf, D. Rohde, and F. Schmidt, "Low-phase-noise millimeter-wave generation at 64 GHz and data transmission using optical sideband injection locking," *IEEE Photon. Technol. Lett.*, 10, 728-730, 1998.
- [116] J. Yao, F. Zeng, and Q. Wang, "Photonic generation of ultrawideband signals," *J. Lightw. Technol.*, vol. 11, No. 11, 2007.
- [117] J. Dong, X. Zhang, J. Xu and D. Huang, "All-optical ultrawideband monocycle generation utilizing gain saturation of a dark return-to-zero signal in a semiconductor optical amplifier," *Optics Lett.* Vol. 32, 2158-2160, 2007.
- [118] M. C. Y. Huang, Y. Zhou, and C. J. Chang-Hasnain, "A surface-emitting laser incorporating a high-index-contrast subwavelength grating," *Nature Photon.* 1, 119-122, 2007.
- [119] M. C. Y. Huang, Y. Zhou, and C. J. Chang-Hasnain, "A nanoelectromechanical tunable laser," *Nature Photon.* 2, 180-184, 2008.
- [120] X. J. Meng, T. Chau, and M. C. Wu, "Improved intrinsic dynamic distortions in directly modulated semiconductor lasers by optical injection locking," *IEEE Trans. Microw. Theory Tech.*, 47, 1172-6, 1999.